THE UNIVERSITY OF CAPE TOWN

Exploring the Application of New Telescope Technologies in the Testing of Dwarf Novae Accretion Models

Thesis Presented for the Degree of
DOCTOR OF PHILOSOPHY
in the Department of Astronomy
UNIVERSITY OF CAPE TOWN

©Mellony Spark

February 2011

THE UNIVERSITY OF CAPE TOWN
FACULTY OF SCIENCE
DEPARTMENT OF ASTRONOMY

Doctor of Philosophy

Exploring the Application of New Telescope Technologies in the Testing of Dwarf Novae Accretion Models

February 2011

ABSTRACT

In this thesis I investigate emerging telescope technologies and demonstrate, within the context of accretion in cataclysmic variables (CVs), their role in contributing to the stellar variability studies which help drive their development.

The process of small-telescope automation is demonstrated by the coordination and implementation of the hardware and software upgrade and refurbishment of the South African Astronomical Observatory's (SAAO) 0.75m reflector telescope for the purpose of remote operation. The user, telescope and instrument requirements were prescribed and online and written documentation were provided for most aspects of the project. Testing of the telescope and the University of Cape Town's CCD camera in remote mode allowed the successful acquisition of a dwarf nova light curve which served as a science demonstrator for the telescope's new observing mode. The science test-case also demonstrated that legacy CCD imaging systems and manual observing modes can no longer meet the demand for efficiency in competitive high-speed photometry science.

During the course of the upgrade a long-term campaign conducted on the 0.75m reflector, monitoring the accretion discs of the SU Ursa Majoris (SU UMa) stars OY Carinae (OY Car) and Z Chamaleontis (Z Cha), provided a test of current superoutburst theories. An analysis of 74 light curves produced from this campaign is presented.

The two competing models explaining the phenomena of SU UMa superoutbursts, the Thermal Tidal Instability (TTI) model and the Enhanced Mass Transfer model (EMT) were tested by measuring the accretion disc radii over the targets' supercycles using the location of their bright spots from the eclipse light curves. The measured radii were combined with previous measurements and compared with predictions made by the TTI and EMT models. While possessing similar binary parameters, both systems demonstrate very different behaviours. The new measurements from Z Cha's light curves suggest an increasing disc radius, which conflicts with combined published measurements showing a decrease over the supercycle. OY Car's accretion disc hardly varies over the supercycle. Both systems show variability on an orbital timescale which is comparable to the trend expected from the models for the full supercycle. Neither systems exhibit the distinctive trends predicted by model simulations of the TTI and EMT scenarios. Thus both are shown to fail to describe the essential physics governing the progression of SU UMa supercycles.

Good estimations of white dwarf masses are essential for the development of theories of CV evolution.

Estimates of white dwarf radii from photometric observations of eclipsing CVs critically depend on the shape of the emitting region which has, until now, been assumed to be spherical and unchanging. Derivative analysis of light curves can reveal the shape of the emitting boundary layer but requires high signal-to-noise ratio (SNR), fast photometry of the central, compact object. To this end, 18 light curves were obtained from high time resolution observations of OY Car taken using the Southern African Large Telescope's (SALT) imaging camera (SALTICAM). The technique of Total Variation Regularisation, adapted and applied here for the first time to astronomical time-series data, as well as the high SNR provided by SALTICAM allowed analysis of the light curves on an individual basis. This showed that the shape of the emitting region can not be taken to be constant, as previously assumed; the boundary layer emission clearly varies significantly and on a cycle-to-cycle basis. Using this result it is shown that previous analyses of data have led to overestimates in the white dwarf's radius. Nearly all of the light curves presented here did not match previously proposed models for the boundary layer's surface brightness distribution. Light curves which did match that of a spherical distribution were used to constrain the white dwarf's radius and mass; OY Car's mass and radius were determined to be $R_{wd}/a = 0.0155 \pm 0.00015$, $M_1 = 0.812 \pm 0.012 M\odot$, the latter 30% larger than previous best estimates derived from eclipse timing methods. Thus it is demonstrated that, under high SNR conditions, regularised derivative analysis of eclipse light curves provides the best means of determining white dwarf masses.

To my Mom and the memory of my Grandparents

Acknowledgements

My deepest, heartfelt gratitude goes to my supervisor, mentor and professional parent, 'Daddy D', Darragh O' Donoghue. I have been privileged to have been grown and pruned by your attention, allowed your good-humoured patience, ever-ready ear and, especially, to just to hang out in the light of your mind, soaking up your focused approach to problems, your unique perspective and steadfast stoicism. I cannot properly convey the awe and admiration I have for your self. On complaining that there seems no way in which I may repay your personal time and investment, a close friend once commented 'probably only by being a good student'. Until a better opportunity to repay the kindness presents itself, I'll try to be one for the rest of my life.

I would like to say thank you to my UCT supervisor Patrick Woudt for the careful screening of my manuscript and insightful guidance in creating a well-rounded work. Thank you to Brian 'the Guru' Warner for my first taste of CVs, many insightful, entertaining conversations and 'setting me straight' on the basics.

I owe many thanks to the staff of the electronics and mechanical departments at the SAAO especially Piet Fourie, Geoff Evans, John Stoffels, Dave Carter, Michael Rust, Jackie Dyers and Hennie Klein. Without your expert input and patient fault finding, the realisation of the 0.75 m project would have been an impossibility. I owe a special thanks to the past-and-present SAAO IT department, namely Roy Emmerich, Hamish Whittal, Chantal Fourie and Garith Dugmore, for supporting my every whim with incredible cheerfulness.

I am indebted to Richard Chartrand for taking the time to offer me help and advice. I thank the AAVSO and RASNZ observers and data managers for their on-going efforts, especially Pauline Loader of the RASNZ Variable Star Section for her cheerful and prompt supply of valuable data.

I would like to thank Dave Kilkenny for his downright nosiness, support and introducing me to the 0.75m telescope. I thank the SALT astronomers, namely Petri Vaisanen and Amanada Gulbis for their diligent nannying of my SALT campaigns. Thank you to the Sutherland hostel staff for putting up with putting my up. I thank 'Ol' Faithful', the 0.75m for being a willing, stubbornly-literal mule if there ever was one.

I thank Patricia Whitelock and Phil Charles for their continuing support over the years. I would like to thank Peter Dunsby for steering my instrumentation interests to Darragh's door. I thank Lisa 'Big Sis' Crause for her kind and unbidden interest in my stress-levels, crying-shoulder availability, general sympathies and commiserations. I acknowledge the support and sponsorship of the NRF, through various research schemes, for funding this work.

I am deeply indebted to the SAAO, staff and institute for my growth and development. Your cool corridors, creaking wood panels, beautiful buildings and green grounds have provided a safe shelter to

grow, away from the harsh realities of ‘real’ life, for the Moraea, the Leopard Toad and myself. Thank you.

I thank Bruce Cowley for his advice, kindness, incredible patience and loving support.

I thank Angus MacNeilage and numerous friends for their support, seemingly bottomless sympathies and confidence in me during initial stages of the project.

Last, but definitely not least, I thank my exceptional Mom. Thank you for expecting the unusual of me (I’m sorry I’m not raising baby dinosaurs too). I am because you are.

Preamble

This thesis engages two problems in accretion astrophysics using two new and different telescope technologies. One involved upgrading the SAAO's 0.75m reflector telescope's control system to enable remote operation and the capture of large datasets over an extended period. The other took advantage of the Southern African Large Telescope's high speed photometric capability and queue scheduled operating mode to gather extremely high signal-to-noise eclipse light curves. The characteristics of these two very different observing tools were essential to providing scrutiny sufficiently penetrating to eludicate the diverse questions found within the same astrophysical setting: within the subclass of the ultra-short period, semi-detached cataclysmic variable (CVs) stars known as dwarf novae. The established work modelling the behaviour of their accretion discs and the nature of their central sources were thus challenged. To fully exploit the high time-resolution offered by SALT, the information in the data needed to confront theory was extracted by the application, for the first time to astronomical time series data, a regularisation technique most commonly used in 2-dimensional image processing.

As such, the flow of this thesis is from technology to science: the first part, Chapters 1-3, documents the design study, refurbishment and testing of the 0.75m to enable remote operability over the internet. Chapter 4 provides an introduction to cataclysmic variables. Chapter 5 describes the observations, analysis and results of the observing campaign conducted on the SAAO's 0.75m telescope, monitoring ongoing cyclic variability in two eclipsing CV systems to compare with the predictions made by established models. Chapter 6 describes the observations, analysis and results of the SALT observing campaign which utilises the high time resolution offered by SALT's imaging camera, SALTICAM, to probe the nature of the central objects' brightness distributions in an eclipsing CV system. Finally, Chapter 7 summarises the main results of the instrumentation and research projects.

Statement of Original Work

In this statement I would like to clarify my role in this thesis and distinguish work that can be attributed to myself from the work performed by members of the South African Astronomical Observatory (SAAO) staff.

Part I: 0.75m Refurbishment and Upgrade

- **Work performed by author:**
  - Explicit identification of user requirements. Throughout the project, progress was reviewed in comparison to these requirements to ensure that each requirement was met.
  - Coordination of the staff involved in the implementation of certain stages of the upgrade.
  - Testing of the system after each installation.
  - Investigation of various techniques to remotely access the instrument and Telescope Control (TCS) systems leading to the final design and implementation of the system.
  - Set-up and testing of the TCS software (including the creation of a pointing model for the telescope). Identification of software bugs and liaison with Dr F. Melsheimer (DFM) suppliers for follow up support.
  - Provision of notes to supplement existing documentation.
  - Testing of auto-initialisation hardware.
  - Investigation into monitoring of the CCD camera. Design, coding and testing of software to remotely communicate with the CCD camera.
  - Modification of DOS UCT CCD control program `wrmwind` to help enable remote communications.
  - Investigation and testing of various methods for monitoring conditions in the dome including the purchase of the final surveillance system.
  - Provision of comprehensive online project documentation including a User's Manual, Technical Manual, all supplementary help documents, installation documents and drawings (refer to Appendix C).

- **Work performed by SAAO staff:**

Mr Geoff Evans (Head of SAAO electronics department):

- Initial investigation of what would be required for a TCS upgrade. Liaison with DFM engineering, leading to the purchase of the new TCS.
- Ordering and purchase of all necessary hardware.
- Monitoring of the implementation stages.

Mr Piet Fourie (Senior Electronics Technician):

Unless otherwise stated, the design, fabrication and installation of all necessary electronics circuits and systems were conducted by Mr Piet Fourie.

- Installation and testing of the new TCS hardware and electronics.
- Investigation of radio control of the dome leading to the purchase of the necessary hardware as well as design and installation of the necessary interface electronics.
- Installation and testing of auto-initialisation hardware.
- Design, fabrication and testing of the peripheral systems control box allowing for safety monitoring of the TCS.

Mr John Stoffels (Senior Mechanical Technician):

- Design, fabrication and installation of the mirror cover system.
- Installation and testing of auto-initialisation hardware.

Dr John Menzies (Senior Astronomer):

- Coding of software script `Remdisp` to display images on remote machine.

Work performed by supervisor Dr Darragh O' Donoghue:

- Modification of DOS UCT CCD control program `wrmwind` to help enable remote communications.

Part II: Science

Most of the content of Chapters 5 and 6 has appeared in the following:

1. Spark, M. and O' Donoghue, D., *Re-examining the Nature of Dwarf Novae Boundary Layers* (poster), 2011, Proceedings of the Physics of Accreting Compact Binaries Symposium, Universal Academy Press (in press)

2. Spark, M., O' Donoghue, D. and Woudt, P. A., *Accretion Disc Variability over the SU UMa Supercycle* (poster), 2011, Proceedings of the Physics of Accreting Compact Binaries Symposium, Universal Academy Press (in press)

3. Buckley, D. A. H., Crawford, S., Gulbis, A. A. S., McPhate, J., Nordsieck, K. H., Potter, S. B., O'Donoghue, D., Siegmund, O. H. W., Schellart, P., Spark, M., Welsh, B. Y., Zietsman, E., 2010, *Time resolved astronomy with the SALT*, SPIE, Vol. 7735, p. 174

- **Work performed by author:**
  - Acquisition, reduction and analysis of all observations used in the project (unless otherwise stated).
  - Production of all plots and diagrams using plotting programs Gnuplot, Excel and Darragh O' Donoghue's Roche lobe modeling program, `roche`. Adaption of `roche` for the needs of the analysis presented here.
  - Review of all relevant literature as cited.
  - Extension and adaptation of Dr R. Chartrand's, of Los Alamos' National Laboratory, `MATLAB` numerical differentiation code to enable p-norm regularisation (refer to Chapter 4).
  - Investigation of p-norm regularisation, subsequent application to photometric data sets and interpretation of results.
- **Work performed by supervisor Dr Darragh O' Donoghue:**
  - Creation of Roche lobe modeling and light curve synthesis program `roche`.
  - Creation of function fitting program `ephem`.

Contents

"The instruments of darkness tell us truths..."

William Shakespeare (MacBeth)

Part I

Upgrade of the SAAO's 0.75m Reflector to enable Remote Operability

Chapter 1

Introduction

The South African Astronomical Observatory (SAAO) is a national facility dedicated to optical and infrared astronomy. The SAAO's offices are situated in Cape Town, but their research telescopes are situated at the remote observing station in Sutherland, $\sim$ 400km NE of Cape Town. Research telescopes on this site include the 1.9m Radcliffe telescope, the 1.0m Elizabeth telescope, the 0.75m telescope, the 0.75m Automatic Photometric Telescope, the 0.5m telescope and the 10m-class Southern African Large Telescope (SALT). The latter achieved 'First Light' at the end of 2005. A range of externally funded telescopes are also located and managed at the site.

SALT was commissioned and built to enable competitive Southern-African-based astronomical research in an era when the 10m-class telescope is the modern standard of excellence in optical astronomical instrumentation. Astronomy has undergone a boom in instrumentation development and research in the last two decades with, at the turn of this century, more 10m-class than 4m-class telescopes in commission and operation (Mountain 1996). This has been a result of rapid technological advancements in ground-based telescope instrumentation allowing science drivers – such as planetary exploration, star and planetary formation, all-sky survey follow-ups, deep-field extra-galactic campaigns – to be reliably pursued in synergy with, or as an alternative to, costly space missions.

Thus the global trend has been a greater focus and devotion of resources to the development, maintenance and support of instrumentation for 10m-class telescopes. After the inauguration of SALT, the reduction in the availability of on-site small-telescope assistance and the minimisation of instrument changes has been implemented at the SAAO as part of a policy to conserve personnel resources. The long term goal of the observatory is to have each instrument dedicated to a particular telescope where these small telescopes are, ideally, operating in modes that would require as little supervision and maintenance as possible (O'Donoghue, private communication). Generally, the drive for competitive science and the fact that 10m-class telescopes demand a full team of astronomers, engi-

neers, technicians and support staff dedicated simply to the supervision of their operation has meant that small telescopes ($\sim$ 2m-class and below) have had to suffer a reduction in support.

This is not to say that small telescopes no longer have an important role to play in the progress of astronomical investigation; on the contrary, small telescopes are still invaluable work horses in the continuation of survey work and extended campaigns monitoring relatively bright and variable objects. This has been clearly demonstrated by the two 1.3m 2MASS (2 Micron All Sky Survey) telescopes in Arizona and Chilé, (Skrutskie *et al.* 2006), the dedicated 2.5m SDSS (Sloan Digital Sky Survey) telescope in New Mexico (York *et al.* 2000) and the Anglo-Australian Observatory's 1.2m UK Schmidt Telescope on which the 6dF Galaxy Survey was completed (Jones *et al.* 2004). Therefore the continued functioning of small telescopes as part of a balanced portfolio of observing instruments needs to be sustained and accommodated despite observatories' changing operational conditions.

In practice, operating a telescope with as little human effort or interference as possible means complete automation. The trend in technology is towards automation of systems, whether the system is designed for the monitoring and control of industrial processes or for data acquisition. Astronomy is no exception; automating the scheduling and observational process means that data are acquired as efficiently as possible (Kitt Peak's RCT upgrade provides a good case example, Gelderman *et al.* 2007) . Recently, focus on automating the data reduction process has produced very efficient data reduction "pipelines" and distribution networks for instrument users (Butler & Forde 2004, Bierwirth *et al.* 2010). All of this enables more time to be spent on the aspects of the research project requiring more expertise: the analysis and interpretation of the data.

Full automation of any of the telescopes at the SAAO's remote observatory in Sutherland, however, would involve major refurbishment, requiring time and financial resources that are unavailable at present. Remote operation provides an intermediate and less ambitious objective enroute to full automation.

Remote operation involves the operation of the telescope via a computer network connection. While a user is still required to make observations and operate the telescope for the length of the run, remote operation means that the observer is not required to be at the site. The telescope and its peripherals are controlled by the user over a network via a software interface. All the operations that were previously performed by an observer present in the dome can be completed at the click of a button over the network (see Section 1.1.4 for further detail). The Willard L. Eccles Telescope (Gajadhar *et al.* 2011) and Canada-France-Hawaii Telescope (Springer *et al.* 2011) are examples of recent telescope developments and refurbishments to enable remote operations.

Another motivation for the refurbishment of one of the SAAO's telescopes to enable remote operation is the large number of projects available which would be best suited to remote operation, in particular, variability studies. The SAAO has been conducting research in the field of variable stars for the past 35 years. The topics of research have included variability studies of almost every kind of pulsating star known: from red supergiants with periods of 2000 days or more to pulsating white dwarfs or subdwarfs with periods of about 100 seconds. Many of these variable star observations require high speed photometry, which has been successfully carried out with the use of the SAAO's and University of Cape Town's (UCT) CCD cameras mounted on any of the three larger SAAO telescopes: the 1.9m, 1.0m and the 0.75m.

A reasonable number of these observing projects only require observations of one or two hours per night, week or quarter, repeated over a long period of time. Highly variable stellar systems, or other targets needing occasional monitoring or which exhibit periodic events which reveal something of the physical nature of the system, naturally require such observations. The research project completed with the 0.75m telescope, in Part II of this dissertation, is a classic example of where a remotely-operated telescope, equipped with a dedicated instrument, would have proved invaluable to its execution. Remote operation delivers some of the desired flexibility in telescope management and allocation of observing time, while still allowing the observer direct control of the telescope control system (TCS).

An "online" telescope would have the additional benefit of making practical astronomy more accessible to the public. Prospective astronomy students, SAAO summer and winter school students need not travel to Sutherland to have their first glimpse of a working telescope in action. Honours students enrolled with the National Astrophysics and Space Science Program (Whitelock 2004) need not have to delay their observing projects for months after the start of the course, which has been the case due to the difficulty in traveling up to Sutherland during the academic term.

Description of the Project

The telescope best suited for this kind of refurbishment is the 0.75m telescope. The 0.75m telescope is large enough to produce valuable astronomy, yet small enough to be reasonably tackled as part of a postgraduate project.

Part I of this dissertation documents the processes of design and implementation governing the upgrade of the SAAO's 0.75m telescope to remote operation. When describing decisions made in the design and implementation of the project in the following chapters

(unless otherwise stated), 'we' refers to the author and the staff members of the SAAO who have supervised progress of the refurbishment, namely my supervisor Dr. Darragh O'Donoghue and the Head of the SAAO electronics department, Mr. Geoff Evans The project involved, firstly, an initial investigation into the telescope and instrument requirements and their suitability for remote operation. This is covered in Sections 1.1 and 1.2. The first stage of the refurbishment was the upgrade of the existing telescope control system (TCS) from DOS to a Windows-based application. This is detailed in Section 2.1. The next step was the procurement or design and assembly of additional electronics and hardware to allow PC control of the telescope peripherals: the dome shutter, lights and mirror cover which is described Section 2.2. The next stage was the installation of hardware to allow the telescope to self-initialise (Section 2.3). Subsequent stages involved the development of a client side software interface for the instrument and the installation of the sensory feedback systems, namely the webcam. This is covered in Sections 2.4 and 2.5.

Chapter 3 reports the testing of the system and the remote acquisition of a set of observations to illustrate the kind of science which would be best suited to remote observing. Finally, a project summary and further recommendations are given in Section 3.4.

1.1 Telescope and Instrument Requirements

1.1.1 General Description of the Telescope

The 0.75m telescope is a Grubb Parsons Cassegrain reflector with an equatorial English mount which was built in 1964. The telescope's secondary mirror delivers a Cassegrain focus with a focal ratio of f/15. A photo of the 0.75m with the UCT CCD mounted at the Cassegrain focus is shown in Figure 1.1. The right ascension (RA) drive is a single stage of worm gears driven by a stepping servo motor through two timing belts and pulley stages. The hour angle (HA) encoder is driven off the worm shaft. The declination (Dec) drive is a chain drive and the Dec encoder is driven off this via a sprocket. There is a mercury limit switch assembly mounted on the polar axis which provides hardware limits for the servo motors. This is essential for remote operation as the mercury switches interrupt power to the motors if the telescope tube assembly is driven too close to the horizon should the software limits fail. In this event a limit override key must be used on the rack and the telescope manually driven back out of the limit to recover control of the telescope.

The 0.75m telescope has been PC-controlled since its last refurbishment in 1998 by the DFM telescope engineering company. In this refurbishment, DFM provided: primary and secondary gearing for the Declination axis; a declination servo motor, motor encoder, position encoder and drive; an R.A. servo motor, motor encoder and position encoder (secondary gearing and drive provided by SAAO); a focus geared stepping motor and position encoding system; a control system including PC computer, DFM TCS control circuit board and Motor Driver Chassis (containing servo controllers, power supplies etc.) and a dome azimuth controller and position encoder. An interface card plugged into the PC controls the motor driver chassis. The chassis houses the power supplies and control logic hardware for the motors. The PC interface includes: VIAs (versatile interface adapters), Intel 8254 pulse rate generators used to produce motion commands to the motors, LSI 7166 up-down counters used to keep track of the axes positions and an AD-5744 (12 bit) analog-to-digital converter used to read the focus position potentiometer.

1.1.2 The University of Cape Town CCD (UCT CCD)

Traditionally the instrument suite of the 0.75m telescope has the Infrared Photometer MkII and the UCT Photometer (with the option of a polarimeter). Since 1995, the UCT CCD has been added (O'Donoghue *et al.* 1999) and following the refurbishment of the telescope for remote operation, the plan is for the UCT CCD camera to be exclusively dedicated to the telescope. The basic features of charge coupled devices (CCDs) will not

be described here[1]; I will only discuss the key features of the UCT CCD photometer.

The UCT CCD is a Wright Instruments Peltier-cooled camera with a 576×420 pixel, thinned, back illuminated EEV CCD. Thinning and back illumination provides a greater sensitivity to ultraviolet and blue light namely, a peak quantum efficiency of ∼70% at ∼600nm and a quantum efficiency of ∼25% at ∼350nm. The CCD is Peltier-cooled to −50 Celsius. This yields a dark count rate of ∼0.05 electrons/pix/sec which is negligible for short exposures (less than 30s). The readout noise by comparison, is 10 electrons/pix (O'Donoghue *et al.* 1999). On the 0.75m telescope, the UCT CCD has a field of view of 142×97 arcsec.

The camera was designed for high speed photometry operated in frame transfer mode. Frame transfer allows for exposure times as short as 10 seconds with no dead time for readout. Prebinning, where the light from a user-specified number of adjacent pixels is combined, allows for even shorter timed exposures. (O'Donoghue *et al.* 1999). The CCD has a charge loss of 1% for charge transferred from the diagonally opposite corner of the CCD to the output amplifier.

The camera is driven by a 486 Dos machine which runs the CCD program `wrmwind` adapted by Dr O'Donoghue from a program written by Dr J. Menzies for the 1m CCD camera. This program controls the data acquisition process, displays the images as they are read out and allows for basic image measurements to be made. The PC is linked to a Linux workstation via the Sutherland ethernet; this is the principal data storage. Online data reductions can be made on the workstation. In remote operation mode, this Linux workstation would be replaced by the observer's workstation.

1.1.3 Operation and Status of the 0.75m Before Refurbishment

At the start of the project an initial investigation was made into the operational status of the telescope and its suitability to remote operation. With respect to safety issues, the fact that the 0.75m telescope had hardware limit switches was very important in considering the telescope for control over a network. The existence of hardware limits means that there is a mechanical fail-safe that would prevent the telescope ever colliding with the pier supporting the polar axis or exceeding its horizon limit, thereby ensuring the safety of the telescope, should the software control and feedback system fail. Remote operation could not be considered without such a safety measure installed. Another feature of the 0.75m which makes it a good candidate for remote operation is that its pointing is accurate; to within a few arc minutes when initialised at the zenith and within a fraction of an arc

[1]For a basic introduction to CCDs refer to Peterson (2001)

Figure 1.1: The 0.75m telescope with the UCT CCD mounted at the Cassegrain focus (circled).

minute once the pointing zero points have been set using a bright star and the UCT CCD.

Prior to the upgrade, the telescope and instrument were operated by an observer in the dome. Switching of dome power, lights, dome tracking, telescope tracking and focus position was done manually. Opening of the shutter was done via a manual switch and the mirror cover was removed by hand. Movement of the telescope was controlled via a DOS based interface. The UCT CCD instrument was controlled via the DOS interface `wrmwind` as described above.

1.1.4 Remotely Operated Telescopes

Wilson *et al.* (2005), in their description of the design and implementation of their Telescope Automation and Remote Observing System TAROS, define three kinds of remote observing modes. These modes are the working definitions used in this document and are defined as:

Automated Observing In this mode the telescope and instruments are fully controlled by computer and observations are scheduled by the computer. Monitoring is possible from the local and remote sites.

Remote Observing In this mode an observer at a remote location has full control of the telescope and instrument, with no assistance from the staff. This mode of observing is well suited for educational purposes as access to the telescope can easily be made available to the public, schools and universities.

Assisted Observing The observer at a remote location has full control of the instrument and, optionally, the telescope with limited assistance provided by an observing assistant at the telescope site.

The first remotely operated telescope came into being in the 1960's when Kitt Peak National Observatory operated their 50-inch metal-mirror telescope from their downtown Tucson office (Maran 1967). Since then the field of automated observing has rapidly progressed with new technology advancing every aspect of the process from telescope and instrument control/access, to data transmission and distribution[2]. The advantages of automated observing, as outlined by Eaton *et al.* (2001), are summarised below.

Automated observing has become possible due to the application of inexpensive computers to the control of telescopes small enough ($\leq$ 2m) to be reliably converted. Automated telescopes are cheap to operate, making feasible, continuing competitive research

[2]See the proceedings of the Fairborn annual symposia "Automatic Photoelectric Telescopes" and "Robotic Telescopes", Fairborn 1990a and 1990b respectively, for a good background in the progress and developments that have occurred in automating observing, and its applications, leading up to the last decade.

on many objects that are now no longer the major focus of observatory programmes. They are less likely to break down if they have a dedicated instrument and produce data of a higher quality than manual telescopes. Automated telescopes can be programmed to look at objects at specific times. This means that they are well suited to making observations of periodic variables, such as eclipsing binaries, but also allow for new avenues of research to be explored which were previously prohibited due to the commitment of personal effort required. Automatic telescopes are queue scheduled using dedicated programs to maximise efficiency. Ideally, automated telescopes can be programmed to coordinate with satellite programmes to provide immediate response to special astronomical events detected by orbiting spacecraft; NASA's Infrared Telescope Facility (IRTF), which provides rapid-response support to planetary astronomy (Bus *et al.* 2009), and the 30 cm BOOTES-1B telescope, which provides optical follow-up of Gamma Ray Burst (GRB) detections (Jelínek *et al.* 2010) are working examples.

Assisted observing is the mode of operation that is implemented in this project and will be referred to simply as remote observing in the rest of this document. Refurbishing computer-controlled telescopes to allow assisted remote operation over a network is the first step towards complete automation. A good illustration of the development and implementation of this mode of remote observing at large observatories can be found in the ESO's Messenger periodicals (Raffi & Zeibell 1986, Waelkens 1988, Balestra *et al.* 1992, Zijlstra *et al.* 1995), which detail the experiences and successes of their 2.2m telescope, CAT (Coudé Auxiliary Telescope) and NTT (New Technology Telescope) at La Silla, (operated in remote modes from Garching), as well as the Australian National Observatory's TAROS (Telescope Automation and Remote Observing System) papers (Wilson *et al.* 2005, Czezowski *et al.* 2001). In the present case, assisted observing is implemented to limit the scope of the project to a manageable size. The role of the on-site assistant is to power up the telescope and instrument at the beginning of the evening and power everything down first thing in the morning. The assistant will also be expected to perform preliminary diagnostics on the health of the camera and check that communications to filter wheels and peripheral systems such as the dome and lights are all operational before handing over to the remote observer to take over for the rest of the night.

The efficient operation of an astronomical telescope over the internet by a remote user requires a high level of performance from the telescope, instruments, support facilities and the control system (Melsheimer 2005). The required performance is determined by the user requirements.

1.1.5 Requirements

User Requirements

The 0.75m is envisaged to have the UCT CCD camera dedicated to it as its science instrument so users of this system will be performing real-time direct imaging (as opposed to photomultiplier-based photometry or spectroscopy). The primary needs of the user can be summarised as the following control sequence:

1. Allow the user to log in to the control system.
2. Accept the user's commands specifying the coordinates of the first object of interest.
3. Slew the telescope to the object.
4. Provide visual confirmation from the instrument that the target has been acquired and track the object.
5. Adjust the telescope to the correct focus.
6. Set up the camera according to the user specified parameters of exposure time and desired filter. Control the integration.
7. Transmit the image data to the remote user.
8. Repeat the sequence until the time allocation expires.

This simple control sequence indirectly prescribes a whole package of requirements for the system. For the process of observation to be efficient, the control system must be user friendly, reliable and transparent to the user.

User friendliness implies that the system's interface must be intuitive and simple to use. This does not pose a problem; there are many telescope control software packages currently available which employ the modular windows based interface, facilitating simple "point-and-click" operation. These include Omega Labs ATC (Advanced Telescope Control and Auto Centre, Omega Lab 2010), Software Bisque's TheSky package (Software Bisque 2010), ATC Innovations TCS applications (ATC Innovations 2010) and Diffraction Limited's Maxim DL, MaxDome II and MaxPoint suite (Diffraction Limited 2010).

In addition to implementing the user's commands, the controls system's most important task is to provide real-time feedback on the status of the system and all of its peripherals. This renders the system "transparent" to the user and is absolutely necessary for the user to maintain full control of the telescope's operation. This feedback must include:

- Display of the telescope's status.
- Visual feedback of the telescope's position (RA, Dec, etc.) inside the dome, and conditions inside the dome. This would be best facilitated via the use of a webcam.
- Visual feedback of the telescope's position on the sky. This will be facilitated by the CCD image itself.
- Weather information.

In addition to commands and status feedback, the information system must be able to transfer data from the instrument PC to the user coherently and in real time. Online data reductions ensures the best data quality control by the user but this can be done independently of the TCS. Thus, all that is needed is the safe packaging and transmission of the raw CCD image data to the user.

Reliability prescribes that the telescope slews to the target accurately and consistently. This condition specifies the telescope performance requirements.

Telescope Requirements

The performance requirements for real-time imaging are generally stringent. This is because the object's profile is directly imaged onto an area detector, in this case a CCD detector. Due to imperfections across the detector and the fact that reduction techniques assume that the object is a point source (and not smeared across the detector), the object needs to be kept as near stationary as possible within the field of view. This imaging requirement means that the telescope needs to be able to maintain reasonable focus and track sufficiently well, open loop, throughout the run. The requirement of slewing to and acquiring a target reliably specifies the telescope's pointing performance.

Pointing performance

When a telescope is operated locally, the operator can move the telescope manually to centre an object in the field of view. The remote user may have this motion capability, but it is awkward and time consuming to perform these motions over a relatively slow data transmission line particularly when all that is seen by the way of visual feedback is a tiny fraction of the sky. There is also always the danger that the wrong target may be observed. Hence an object falling outside the field of view should be considered an unacceptable error (Melsheimer 2005). This condition translates to a pointing requirement. Telescope pointing performance is usually characterised by specifying the root mean square (RMS)

value for the pointing error on the sky, that is the root mean square of the maximum pointing errors in Right Ascension and Declination. A 30 arcsec RMS value means that the telescope is within 30 arcsec of the target 67% of the time. An RMS pointing error of about $\frac{1}{4}$ of the field of view of the camera will usually place the object within the central $\frac{1}{2}$ of the field of view, 67% of the time. This should be considered the absolute minimum pointing performance as some objects will fall at the edge or outside the field of view. A remote telescope needs to be able to point open loop to about $\frac{1}{10}$ of the field of view to avoid this problem. In the case of the 0.75m telescope coupled with the UCT CCD operating in frame transfer mode, this translates to an RMS pointing requirement of ∼26 arcsec.

Tracking performance

Tracking performance is another reason to provide accurate absolute pointing as unguided tracking is simply differential pointing (Wallace 2005). Ideally the telescope would track an object for the entire exposure with an error too small to be seen on the image, to some small fraction of an arcsec. However telescope imperfections, such as non-perfect polar alignment of the telescope, create tracking error problems. Even so, at the very least, the telescope needs to be able to track open loop sufficiently well to meet the imaging requirements.

Direct imaging requires tracking to a fraction of the seeing disk. In good seeing conditions, without optical feedback or guiding, this can mean a maximum integration time of about 10 seconds (Melsheimer 2005). Since the telescope will be used for high speed photometry, this is an acceptable limit and prescribes that the telescope should at least be able to maintain a track rate down to a sensitivity of 0.02 arcsec/second in moderate seeing conditions. In the particular case of the 0.75m, its movement is sensitive to 0.005 arcsec/second adjustments, allowing for unguided exposure times of up to 40 seconds. However, reduction techniques that analyse data over the entire length of a run typically require sensitivities of ∼0.002 arcsec/second, so as to keep the object within a 10-15 arcsec window. This, and the instrument's small field of view, means that the user will have to contend with occasionally making small track corrections throughout the run to eliminate the drift that inevitably will arise from atmospheric changes and telescope imperfections. Drift could be eliminated using auto-guiding, but providing the 0.75m with remote auto-guiding capabilities is beyond the scope of this project.

Focus stability

In order for a remotely operated telescope to operate efficiently the telescope focus must remain within an acceptable tolerance during the entire night's operation, over a range of temperatures and at different zenith distances.

For point spread function (PSF) fitting of stellar profiles, optimum focus gives a Full-Width-Half-Maximum (FWHM) of ∼2.2 pixels on the CCD for 1 arcsecond seeing. For a given seeing condition, the optimum focus prescribes the minimum spread of the stellar profile's FWHM over the chip. The 0.75m tends to remain within 5% of this optimum focus over the course of an evening, the necessary change in focus due to atmospheric changes. The focus rarely needs adjusting when atmospheric seeing is stable. If necessary, the user must be able to tweak the focus over the course of an evening, as is the case during normal on-site operation.

Imaging and Data Transmission Requirements

During the early days of automating telescopes, one of the main limits to moving remote stations further and further away from the telescope was the slow rate of data transmission links (unless the observatory had access to a full satellite channel from the observatory to the remote station). When CCD imaging came into widespread use, this meant that CCD data could not be received in real-time and suffered from reduced resolution (Hendon 1990)[3]. This situation changed in the mid-1990s thanks to the advent of the World Wide Web as well as improved transmission and data compression techniques.

The 0.75m telescope is expected to perform to the same imaging standards as its previous manually operated capabilities. The instrument will be used for high speed photometry of objects down to $\sim 18^{th}$ magnitude in the V-band. This translates to an exposure time of at most ∼20 seconds.

Data will be transfered over the SAAO network in the form of FITS (Flexible Image Transfer System, Hanisch *et al.* 2001) files to minimise any degradation of image quality. The data files are typically 0.1 MB but can have a maximum file size of 0.25 MB. The bandwidth required for remote network access can be considered negligible in comparison, so we require a file transfer rate of at most 0.25 MB/s. The SAAO network has 20 MB bandwidth, of which, 6 MB are dedicated to international connections and ∼4 MB to the Cape Town Sutherland link. Of that 4 MB, at least half will be allocated to the SALT data line, which will be used for daytime data retrieval leaving > 0.5 MB at our disposal,

[3]This also meant that the environments running the instrument and telescope had to be menu driven right up until the 1990s due to the high data rates required to interact with an X-windows system.

Table 1.1: Summary of functional and performance requirements

Maximum exposure time	optimally, 40 seconds
Pointing performance	26 arcseconds
Tracking performance	0.005 arcsec/second
Science field of view	142×97 arcsec
Time resolution	2-3 seconds using pre-binning, 10 seconds without
Image transfer rate	0.25 MB/s
Focus	FWHM $= 2.2 \pm 0.1$ pixels for 1 arcsec seeing

more than adequate for this project's needs. If necessary, shaping the network traffic will allow us to prioritise the data connection to the 0.75m telescope.

Control Software Requirements

The telescope control software (TCS) must be able to control all mechanical aspects of the telescope's subsystems and its peripherals (dome and lights). This includes start-up, initialisation and movement of the telescope. The user should thus be able to control operation of the telescope via a software interface which will implement all of the user's commands. Similarly the user should be able to control the UCT CCD instrument via a software interface which implements all the basic functions necessary for image acquisition such as: movement of the filters, setting the CCD parameters, controlling the exposure and saving the images to disc.

In addition, the telescope and instrument control software should be able to be accessed from any of the designated remote workstations. The TCS software which will be run from the telescope PC ('server' side) should allow access via the network from any designated location. The software which will be run from the observer's remote workstation ('client' side) has the main requirement that it should be portable so that it may be run on any of the designated remote workstations.

The TCS PC is a vital system which will be accessed over the network. Therefore adequate protection of the system from viruses and network invasions should be provided for.

A summary of the functional and performance requirements discussed above is given in Table B.1.

1.1.6 Operational Concepts Definition

Mode of operation

Operational times will depend on demand, but the most likely case will be that an observer will have use of the telescope for an entire evening. The sequence of procedures to be followed in remote operation mode is roughly described below. In the following the remote station refers to the observer's workstation and the 'on-site' station refers to the computer systems at the telescope:

- A user with an address designated for that session will remotely access the on-site TCS computer using a suitable program such as VNC or Remote Desktop.
- They will log in and execute the TCS program.
- A technician/telescope operator/night assistant/service observer hereafter called the "local assistant" at the Sutherland site will start up the instrument PC in remote operation mode, specifying the user's PC as the remote workstation from which to receive commands and send data. The local assistant will also power up the telescope and the motor driver chassis.
- The user launches the instrument interface program on the remote workstation.
- The user indirectly checks the status of the on-site instrument PC program via the remote instrument interface. Changes to the status of the CCD camera are continually written from the on-site machine to the remote interface which then updates the display on the remote station.
- The user checks the status inside the dome via visual feedback from a webcam stationed inside the dome. The user checks on-site weather station webpages for site conditions. The user switches off lights and opens the dome shutter from the TCS program.
- The user opens the mirror cover and sets the telescope to auto-initialise.
- The user sets the image display program on the machine running. This automatically displays the images from the instrument as they are sent to the remote station.
- The user slews the telescope from the TCS program to a bright star to check the initialisation of the telescope. If necessary, the telescope is re-initialised by the user centering the star on the CCD and setting the telescope coordinates. Visual feedback of the telescope position in the dome is provided by the webcam.

- The user sets up the camera for observations and slews to target.
- Once the target is acquired, the user enters image parameters into the remote instrument interface and initiates data acquisition. Images are sent to the user's PC. Then further targets may be acquired and be observed in the same manner.
- After the night's observations, or if weather conditions makes useful observing impossible, the user terminates the on-site data acquisition program from their remote interface and parks the telescope. The telescope is powered down and the mirror cover is replaced. After closing the dome shutter, the user logs out of the system.
- In the morning the local assistant switches off the power to the telescope.

1.1.7 Testing

Testing in the form of comparison of the telescope's operation as per the user requirements will be performed throughout the design process and at the end of each installation phase. The final test will of course be the acquisition of photometric data from Cape Town in the telescope's remote operation mode.

1.2 Initial Design Investigation

The process of operating a telescope to acquire data essentially involves two component systems - the TCS and the instrument control system. In addition the TCS must manage the peripheral devices such as the dome lights and shutter. Figure 1.2 summarises the various subsystems involved. Both the telescope and instrument control systems were investigated to establish the simplest and most cost-effective method of adapting the telescope for remote control. During these investigations a number of constraints were identified, as outlined below.

1.2.1 Design Survey

The old DOS-based TCS did not allow for direct control over the network. In addition, the system was already seven years old in 2005 and computers supporting the DOS operating systems were fast disappearing. When the 0.75m telescope remote-observing project had first been suggested in 2002, MicroSoft^{TM}had already ceased to produce DOS systems but they were still available from IBM. It would be straightforward enough to purchase a Windows^{TM}operating system to replace the DOS system. As mentioned in Section 1.1.4, there are a variety TCS packages available on the market which facilitate remote operation of a telescope. However purchasing such systems proves very expensive as one has to purchase both the client and server packages. In this case, extra costs would be incurred integrating a modern software system to the current electronics. So the next step would be to find a Windows^{TM}-based telescope control program that could be easily integrated in to the telescope's existing electronics.

The Colorado engineering company DFM upgraded the 0.75m's TCS in 1997 to its DOS-based configuration, so we decided to inquire what new systems they had available. In 2002, DFM were already running their TCS system in a DOS window on Windows^{TM}98. At that time they were working on their true windows application WinTCS, with the possibility of a LINUX version to be made available. Since DFM already had the electronic specifications of the telescope system, it seemed ideal to purchase a TCS package from them. We needed to ascertain how straightforward it would be to upgrade the old TCS system to their new system and if their system made provision for remote control over a network. In addition to moving the telescope and providing operational status, the new TCS would also have to have the capability to control, via suitable interfaces:

- Switching of dome lights
- Opening and closing of the dome shutter

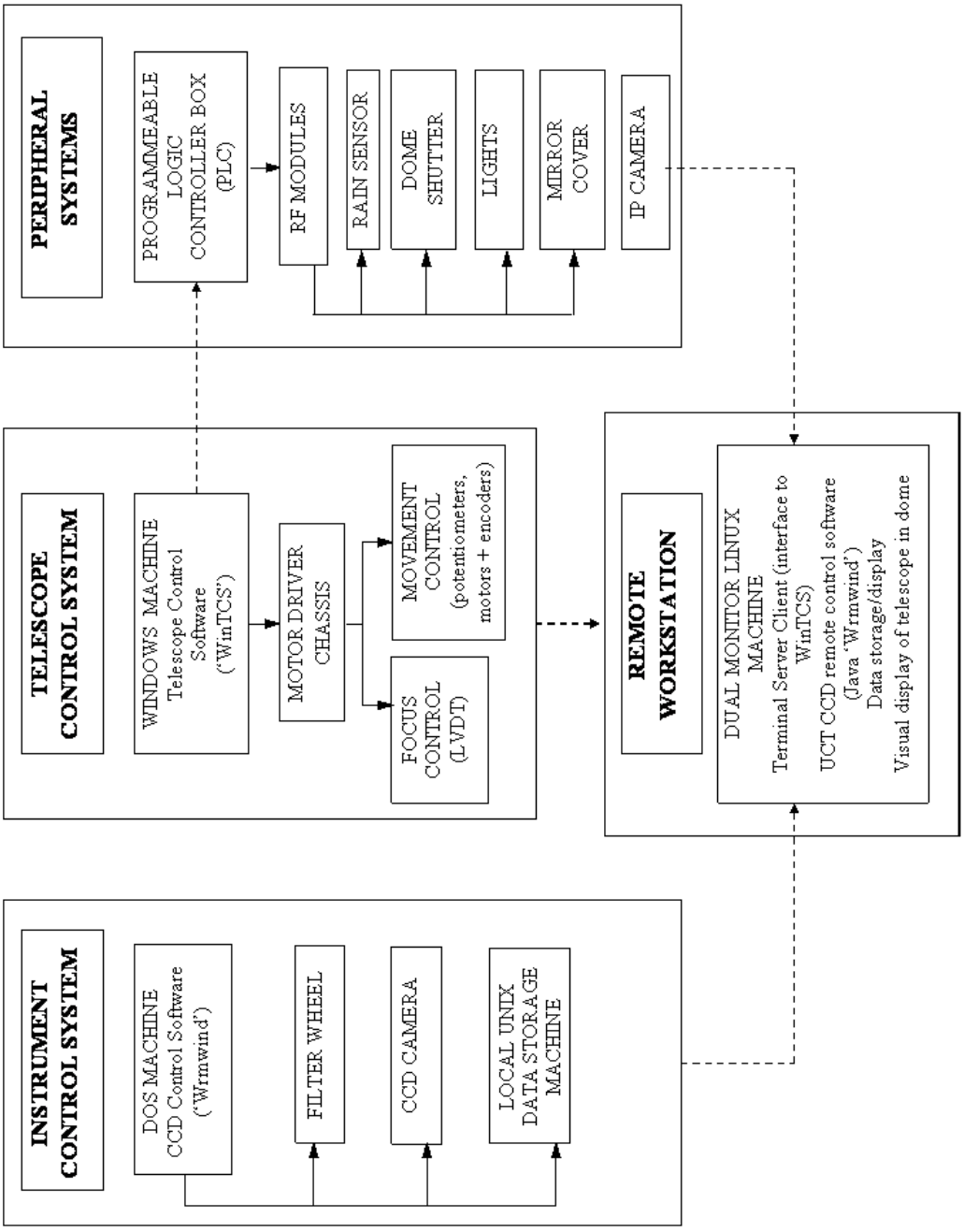

Figure 1.2: Block diagram of the various subsystems necessary for the remote acquisition of data.

- Removal and replacement of the mirror cover
- Initialisation of the telescope
- Initialisation of the dome.

The new TCS may also have to provide weather response:

- Hardware detection of rain with subsequent closing of the dome
- Hardware detection of wind speed and direction with subsequent closing and parking of the dome when the wind speed exceeds the limit for safe observing.

Ideally, the new TCS would have an integrated visual feedback system to provide visual confirmation of the telescope position as well as conditions inside the dome; separate webcam packages could be used instead if WinTCS did not provide for this.

The next concern was the remote-operation of the UCT CCD. In the past, the two systems have been kept separate to facilitate easy instrument changes; the SAAO instruments have not traditionally been dedicated to specific telescopes, but shuffled around between telescopes according to availability and observer requests. In our case we know we will have a dedicated instrument and so ideally the user would only have to deal with one software package which integrates the control of the telescope as well as the instrument. Unfortunately DFM does not provide integrated software for CCD camera control. This left the problem of how to access the existing instrument PC over the network. The instrument PC is also a DOS based machine, which meant that it would also have to be upgraded before it could be run over a network. Upgrading both machines as well as having to buy additional CCD software would prove too costly and possibly time consuming, so we had to adapt the CCD's existing PC and software for use over the network.

1.2.2 Upgrade Plan

In January 2005, SAAO confirmed with DFM that their WinTCS program enabled control of the telescope and all of its peripherals from the PC console. Additional requirements, such as interfacing to weather detection hardware, are not standard features of WinTCS, but could be accommodated for. DFM added that, to meet the self-initialisation requirements, new hardware would have to be installed, which they could provide. The required components would be new RA and Dec encoders, potentiometers and drive assemblies.

The basic user requirements for remote operation were met by DFM's WinTCS program and they were already familiar with the 0.75m telescope. Therefore their software and hardware recommendations provided the most straightforward and cost effective solution to upgrading the telescope.

This left the concern of accessing the DOS-based instrument PC over the network; a remote access program could not be used to communicate with it. However the PC can read and write information over the network, where the workstation to be written to is chosen by the user for data storage. The workstation's disk is mounted as drive f: on the DOS PC. The author of the instrument control program `wrmwind`, Darragh O'Donoghue, suggested this offered the possibility of the PC receiving commands over the network. `Wrmwind` could be modified to have the option to read commands from a specified file on the workstation disk, accessible over the network, instead of the local keyboard. A suitable local interface to accept the user's commands and write them to the designated file would have to be programmed (see Figure 1.2).

Once it was established how communication to the instrument PC would be handled and that WinTCS and necessary hardware would be purchased from DFM for control of the telescope, it was decided that refurbishment would proceed in the following stages:

Stage 1: Purchase of DFM software and upgrade of control system from DOS to Windows.

Stage 2: Purchase of any necessary dome interface hardware. Design and installation of dome interface controllers to enable PC control of dome and lights. Purchase and installation of necessary hardware and electronics for PC control of the mirror cover.

Stage 3: Purchase, installation and testing of new encoders, RA and Dec potentiometers and drive assemblies to facilitate self-initialisation of telescope.

Stage 4: Purchase and installation of sensory feedback systems, namely camera surveillance of the telescope floor, instrument monitor and rain sensors.

Stage 5: Design and programming of remote instrument interface.

Stage 6: Installation and testing of instrument program interface. Communications and data testing between the SAAO Sutherland and Cape Town sites.

Stage 7: Completion of an observing run via remote operation of the 0.75m telescope to demonstrate the intended science role of the telescope and its instrument.

A significant constraint on this plan is the need to keep the telescope fully operational for other users throughout the entire upgrade.

The first stage, the upgrading of the telescope's DOS control system to a Windows operating system, is detailed in the next chapter.

Chapter 2

Upgrade and Development of Hardware and Software Control Systems

2.1 Stage 1: Upgrade of the DOS-based TCS

2.1.1 In Cape Town - Receipt and Testing of WinTCS

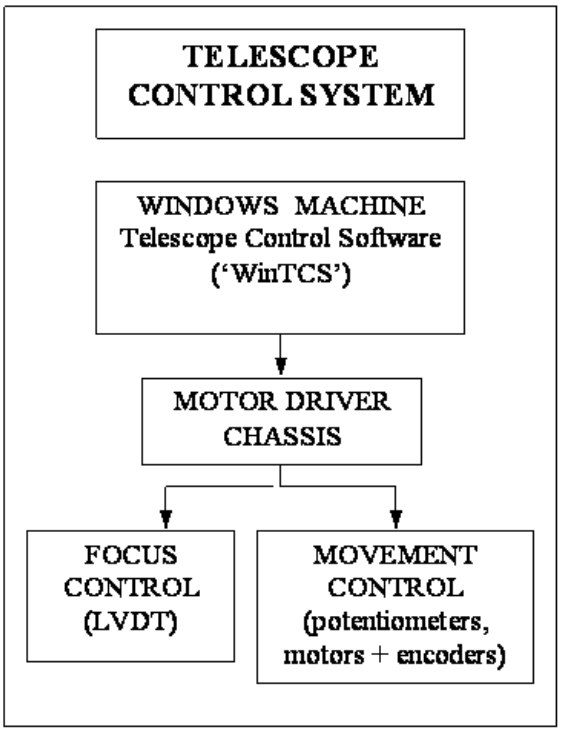

Figure 2.1: The telescope control subsystem.

The new Windows PC and TCS were received in Cape Town in June 2005. The shipment included two LCD monitors for the warm room, a more temperature resistant View-

Sonic monitor for inside the dome, all of the necessary cables and an Avocent Longview Companion extender to allow dual display and control of the PC from inside the warm room or the dome.

The computer system was set-up in the SAAO electronics laboratory in Cape Town and the functionality of WinTCS was investigated and tested. The software was found to satisfy basic user requirements but a few problems were identified.

Firstly, there was not enough feedback to adequately test the software before installation. In a few cases, when implementing user requests, the TCS system was unaware that the necessary hardware devices were not connected, making it difficult to ascertain whether the software was functioning correctly or not.

Secondly, on investigation of the IP connection it was discovered that, while DFM does make provision for control over a network via IP commands, there is no real interface available. There was only an example 'demonstrator' program interface to confirm that the IP connection was operational and that the IP commands provided were accepted and implemented by WinTCS. Ideally the capability for remote operation would have taken the form of an identical interface to the on-site TCS system. The on-site system could be configured to receive IP commands which would be sent by point-and-click operation of the remote interface. In turn the WinTCS would send real-time feedback on system status to be automatically displayed on the remote interface. The remote interface provided by DFM however, is very basic with no real-time display of telescope status. The user can only repeatedly request information on operational status. Not only is this user unfriendly, but would be too dangerous to implement as a permanent remote interface to the telescope control system.

Unfortunately, DFM expects the customer to create their own IP user interface. With no prior provision for real-time feedback, the user interface would therefore have to be programmed to send commands and continually request and display system information. A custom interface could not realistically be created with the limited command set supplied by DFM which does not encompass the full functionality of WinTCS. We decided that creating a custom interface would be redundant and inefficient as there is already a TCS interface available which could easily have been modified to send commands over the network to the remote system and should have been implemented by DFM. Modifying WinTCS ourselves would have required the source code from DFM and an unwarranted amount of time to implement.

The simplest solution is to use a remote access program such as VNC or Remote Desktop to access the TCS machine and launch WinTCS. The TCS desktop could be viewed from a remote monitor and interfaced with directly. Remote access programs such

as VNC and Remote Desktop do not require much bandwidth; our bandwidth provisions are more than adequate to eliminate any danger of stalling or 'hanging' of the display.

Finally, it was discovered that provision of the computer monitors and extenders by DFM was made on the assumption that the TCS PC would be housed inside the warm room. The rack assembly in which the PC is housed is situated on the observing floor. Booster cables were provided by the electronics laboratory to adapt the new system to the existing configuration.

2.1.2 In Sutherland - Installation, Creation of Pointing Model and Testing

The new TCS computer system and necessary cables were installed in October 2005 (refer to Figure 2.1 for a schematic of the TCS). The computer set-up in the warm room and on the dome floor are shown in Figure 2.2.

The system was tested with technical support and verification from the DFM software developer. Software and hardware modifications were made to eliminate feedback problems causing incorrect movement of the telescope and runaway. Once the system was proved to provide correct movement and control, a pointing model had to be created and fine tuned to enable accurate pointing and tracking of the telescope across the sky (refer to Appendix B for a description of pointing models).

The 0.75m's pointing model was created using the WinTCS pointing program PNTM. First, a list of telescope errors across the sky was generated by making a declination sweep and a right ascension sweep. To perform a declination sweep, the telescope is kept at hour angle zero and swept across the meridian, while for a right ascension sweep the telescope is kept at a declination equal to the site latitude and swept from East to West. In both directions, the telescope was pointed at a sequence of stars, approximately ten degrees apart. For each star, the catalogue coordinates were recorded and the telescope slewed to that star. The telescope's position was adjusted so that the star was centred on the UCT CCD and the telescope readout was recorded. It should be noted that certain coefficients in the pointing model, such as the collimation error, depend on the alignment of the optics relative to the telescope. The pointing model was optimised for East-West orientation of the CCD. Each sweep of the telescope was made as wide as the telescope limits would allow to obtain the best possible fit.

The list of catalogue coordinates and the telescope's position coordinates for each star was fed into PNTM. PNTM used the coordinates to generate four plots representing the functions of the telescope geometrical and flexure terms. Any trends or curves in the plots were eliminated manually by adjusting the model's coefficients. This is an iterative

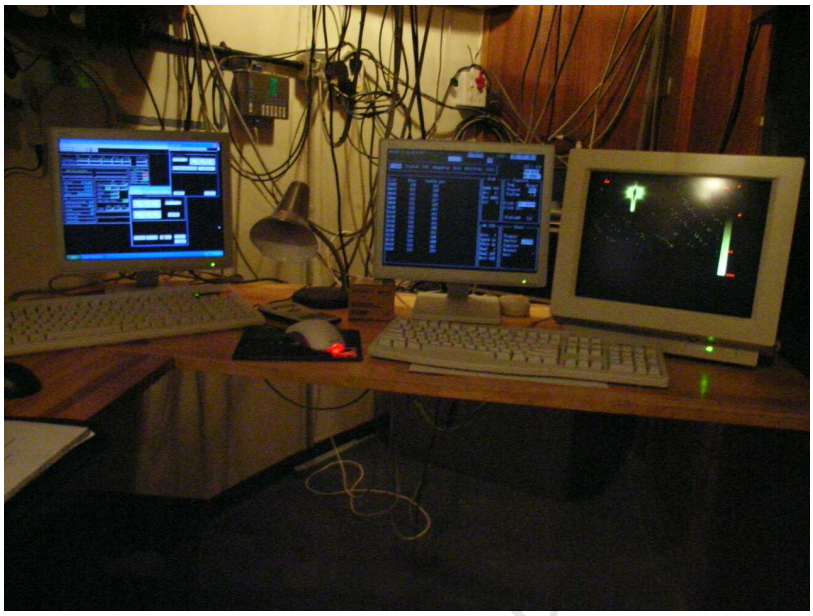

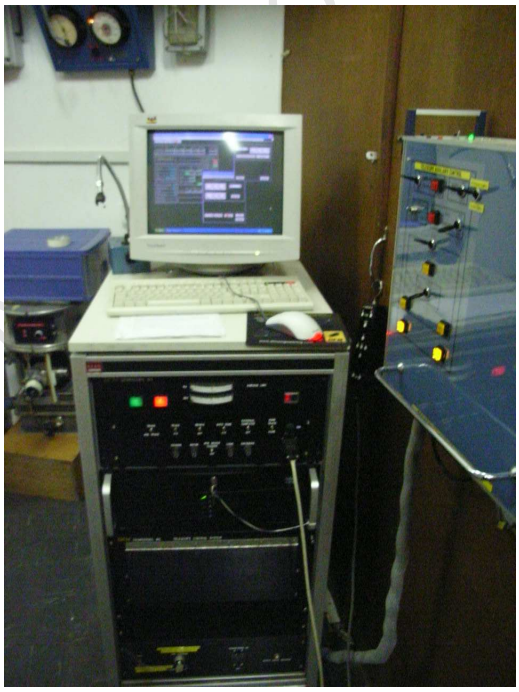

Figure 2.2: (Top) The TCS and instrument interface set-up in the warm room. The monitor on the far left is connected to the TCS computer in the dome and displays WinTCS. The two monitors on the right are connected to the instrument DOS machine (not in view) and display the CCD program `wrmwind` and the CCD pixel readout. (Bottom) The TCS computer housed in the Motor Driver Chassis in the dome. The PLC panel controlling the dome peripherals can just be seen on the right (see Section 2.2).

process as many of the telescope terms are interactive. This process is done automatically in more sophisticated pointing programs such as TPOINT, see Appendix B.

Once the RMS pointing error was reduced to the smallest possible value, a second set of star positions was taken across the declination and right ascension axes. This was done to ensure that the previously obtained values were stable and to fine-tune each coefficient.

A pointing model had to be created for both the East-side and West-side operational modes. During East-side operation the telescope is reversed, situated on the other side of the pier, changing the position of the telescope relative to the pier and dome. In addition, different components of flexure and torsion act on the tube assembly thereby necessitating a different pointing model to be created for East side operation. After fine tuning of the pointing models for each side, an RMS value of $\sim$22 arcsec was obtained for the West side and $\sim$40 arcsec for the East side. This was not surprising as the West side of the pier is where the telescope is usually situated and where it will be predominately operated. The RMS value of 22 arc seconds just falls within our pointing requirements.

In addition to correcting for the telescope's motion across the sky, the pointing model includes terms which are used by the TCS to monitor the telescope's motion within the dome. Model terms – such as the telescope's position relative to the pier, the radius of the dome and pier's placement within the dome – ensure that the telescope does not travel into the pier during slew or track motion. These telescope 'no-go' areas are the 'software limits' and are used to caution the user when the telescope is in danger of reaching them. If the telescope should reach these limits during operation, the TCS halts all motion of the telescope and only enables motion out of the limits. The TCS limits were tested for all motions and direction of movement of the telescope within the dome and the software was found to provide appropriate warning when the software limits were approached. In the majority of tests, the mechanical (mercury) limit-switches cut power to the drives before the TCS's limits were encountered but, in a few instances, the TCS stopped further movement of the telescope before the mercury switches could kick-in.

The last part of the installation process simply involved the organisation of user accounts, formulation of login procedures and restricted access and privileges. Thereafter the appropriate documentation was supplied and training of the on-site users was given.

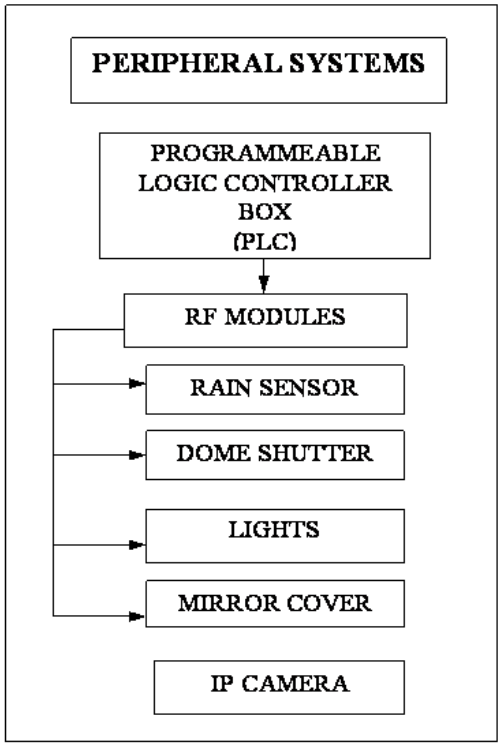

Figure 2.3: The peripheral subsystem.

2.2 Stage 2: PC Control of Dome, Lights and Mirror Cover

The upgrade software supplied by DFM allowed for PC console-control of the dome lights and shutter switches. However, as there was no existing hardware for the software to interface to, this required all the necessary hardware to be designed and built in-house, or bought and installed.

The cheapest and easiest means of controlling the dome shutter and lights is via wireless (radio frequency) communications. PC commands can be communicated via an off-the-shelf RF transceiver and antenna to an identical module situated on the dome's control box. Interfaces between the RF modules and the relevant electronics, PC and dome had to be designed and built (by P. Fourie of the electronics department). The integration of the RF modules with the dome electronics is described in this section. A block diagram showing the components which make up the peripheral subsystem is shown in Figure 2.3. A block diagram of the Client/Server interaction between the dome and the TCS PC is shown in Figure 2.4.

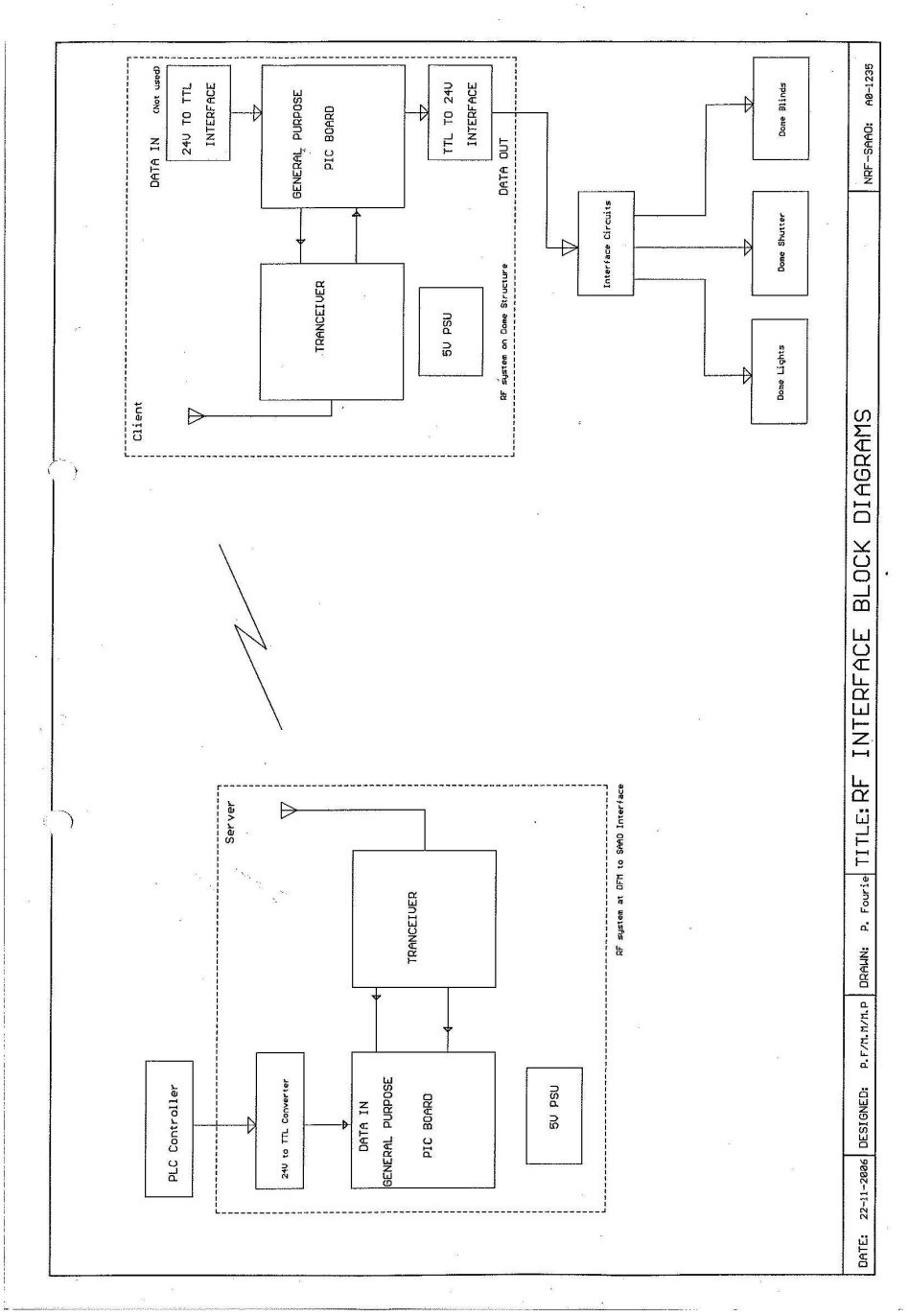

Figure 2.4: Block diagram showing the communications between the dome and TCS RF modules.

2.2.1 The Radio Frequency Modules

There is a wide variety of off-the-shelf RF products available on the market. In practice, *spread spectrum transmission* is always used in commercial industrial applications in order to reduce the problem of interference with other devices.

Frequency-hopping spread spectrum (FHSS) is a spread spectrum method of transmitting signals by rapidly switching a carrier among many frequency channels. The switching is done using a pseudo random sequence known to both the transmitter and the receiver. The overall bandwidth required for frequency hopping is much wider than that required to transmit the same information using one carrier frequency but this is countered by the fact that the signal-to-noise ratio required for the carrier relative to the background decreases as a wider range of frequencies is used for transmission. The switching sequence and the wide range of frequencies employed reduces the likelihood of signal corruption and creates virtually no interference with other devices.

The transceivers chosen for this application were the Aerocomm AC4486 868MHz OEM transceivers from RF Design's wireless communications range. All of their modules are qualified for industrial temperatures and can be used as a direct serial cable replacement, requiring no special host software (Aerocomm 2007). The AC4486 transceivers themselves (shown in Figure 2.5) boast the smallest form factor on the market, ideal for indoor applications such as this.

Brief Theory of Operation

The transceivers are operated in Client/Server mode, with the TCS PC module as the server and the dome module as the client. The transceiver clients communicate with the host via a TTL/RS485 *asynchronous* serial interface. The interface signals are defined for each pin of the transceiver, the most important for our purposes being TXD and RXD, the transmit and receive data lines respectively which transmit and accept TTL data, and CTS, the Clear-To-Send 'handshaking' pin. The CTS pin ensures that no data are sent to the transceiver while the interface buffer is full hence preventing any data loss.

2.2.2 Interfacing

Once the RF transceivers were received, suitable interfaces had to be designed to integrate them into the current system. They could not be simply linked up to the 'Dome' and 'Lights' ports on the TCS rack or on the Dome NEMA Box. The RF transceivers accept TTL RS232 serial input, while the computer rack outputs 24V parallel communications. The conversion of serial to parallel communications was to be achieved using a

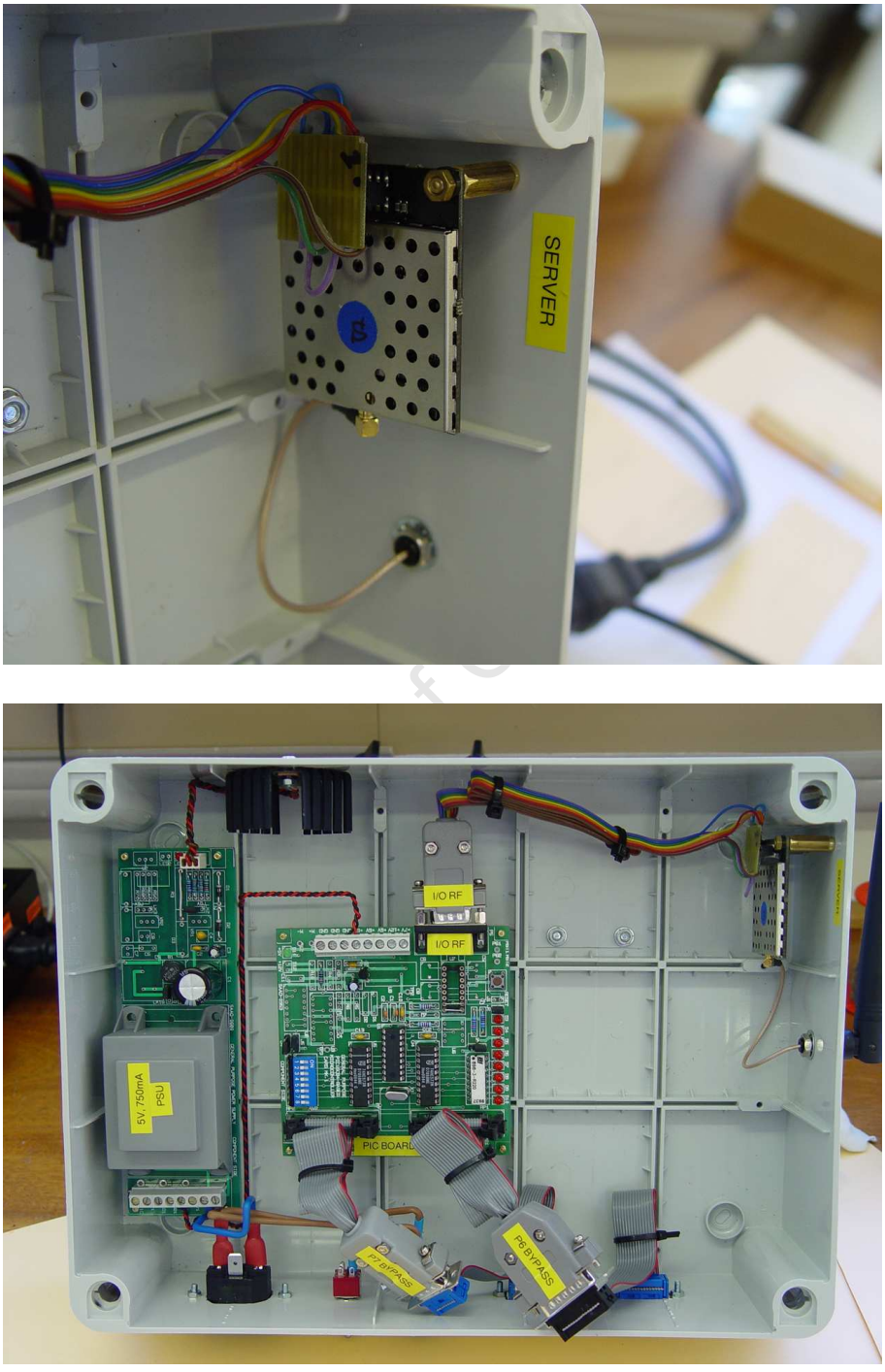

Figure 2.5: (Top) The Aerocomm AC4486 868MHz transceiver in the server module installed on the dome. (Below) Inside one of the modules. The RF I/O PIC and TTL to 24V interfaces lie on the board in the centre, on the left is the power supply unit for the module.

PIC (Programmable Interface Controller) microcontroller; a PIC was therefore required for each transceiver. Each PIC had to be programmed to control the switching between transmission and receipt of data. In addition, the PICs only accept TTL inputs, so two 24V to 5V interfaces had to be built for each PIC, one for input, one for output.

The PIC interface and testing

The PIC microcontroller chosen was the PIC16F87X 8 bit CMOS Flash Microcontrollers by Microchip. The PIC selected was the PIC16F877.

Essentially the PIC has to be programmed to read an input byte from the parallel I/O lines and place the byte on the PIC's RS232 serial TX line to the radio module. Then, after a short delay, the PIC checks if there are data on its RX line from the radio module and, if so, place the byte on the I/O lines. This process of checking and sending data between the I/O lines and the RX/TX lines has to be repeated indefinitely in a continuous loop. This process was translated into C code and programmed, by SAAO electronics internship students from the Cape Peninsula University of Technology, Molao Monaise and Laurel Pedinyane, using CCS's PICmicro7MCU compiler (Figure 2.6).

Two PICs were needed; one to interface between an RF module and the PC interface card and another to interface between the RF module situated on the dome and the dome NEMA box. Of course, it is best to test electronic modules independently of each other and, since the PICs would essentially be communicating their inputs to each other's outputs, they were first connected in this manner (without the radio transceivers) via an adapted PIC16C84-based microcontroller card.

The inputs for each PIC were connected to mechanical switches and the outputs to LEDs in order to verify that the C program to worked as intended i.e so that the PICs checked and sent data between their inputs and outputs coherently and reliably.

The next step in the interfacing process is the design and assembly of the 24V to TTL and TTL to 24V interfaces for each PIC. The circuits were designed by Piet Fourie of the SAAO and built by Molao Monaise and Laurel Pedinyane.

Once these interfaces were integrated and tested with the PICs, the RF modules were connected via a nine-way D-type connector. The RF modules were tested and found to relay the signals successfully.

2.2.3 Final Dome Integration

The final interface circuit to be built was the interface between the PIC outputs and the shutter control box which houses the 3-phase controllers for the dome shutter and the

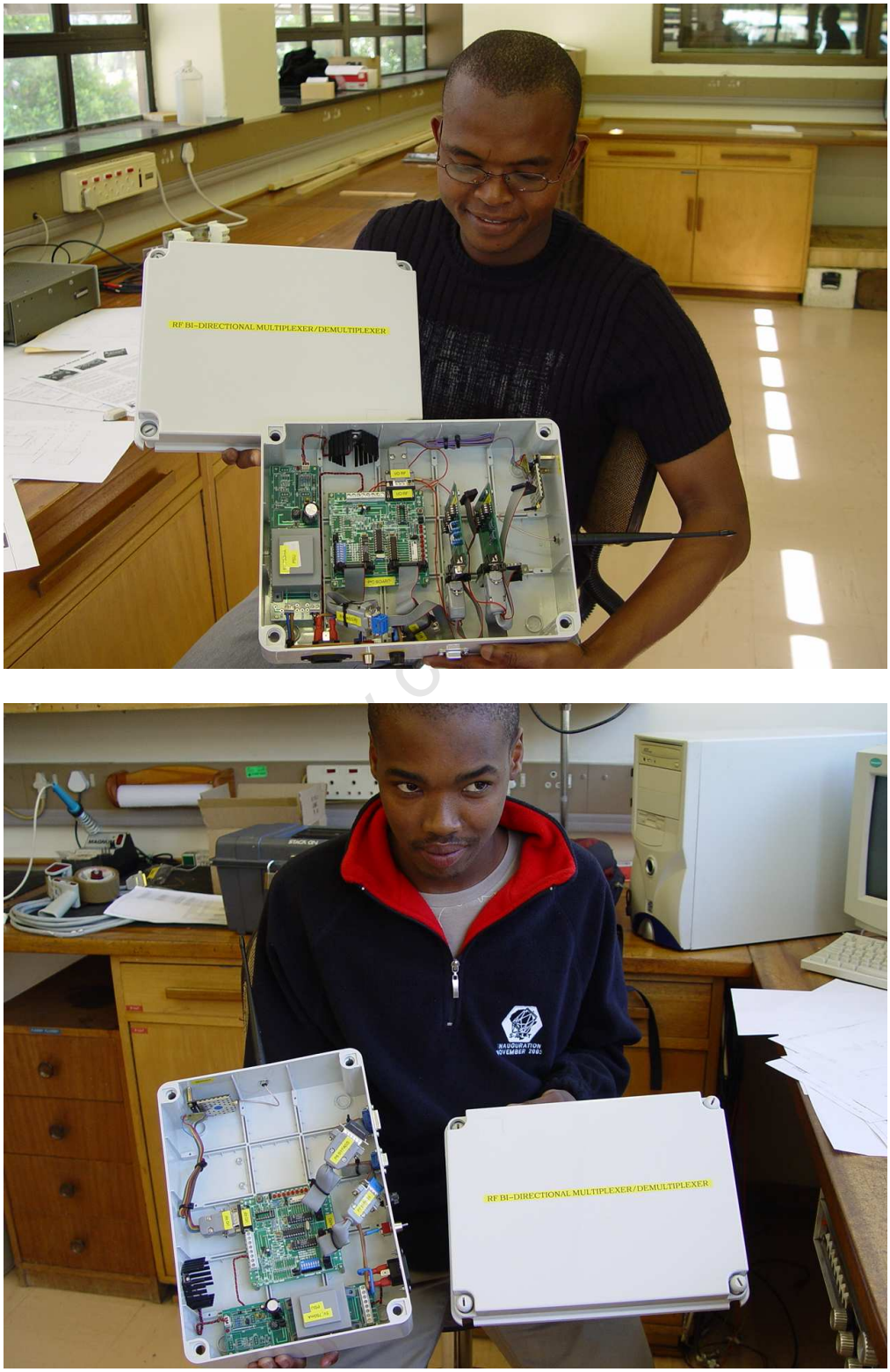

Figure 2.6: SAAO electronics internship students from the Cape Peninsula University of Technology, Laurel Pedinyane (top) and Molao Monaise (bottom), with the RF interface modules.

transformer for the lights. The outputs from the PIC situated on the dome are 'enable, logic low', 'open, logic low' and 'lights, logic high'. Since the switches for the dome shutter and the lights are mechanical, the natural choice of interface were solid state relays.

The RF modules, and their interfaces, were housed as single/demultiplexer units, while the solid state relays were housed in separate units (Figure 2.7).

The RF dome electronics were installed in January 2006. Initially, the DFM TCS program had not been correctly configured for the dome electronics, but after successive versions of the program were installed, the dome shutter and lights were able to be successfully controlled from the PC console. Automatic closing of the dome shutter on termination of the TCS program was included as an added safety precaution for remote operation.

2.2.4 The Mirror Cover

A few options for the operation of the mirror cover were considered by Piet Fourie of the SAAO electronics department and John Stoffels of the SAAO mechanics department. These are summarised below.

- **A Solid state relay running a wiper motor.**

  The advantage of wiper motors (the same sort of motors which operate windscreen wipers) is that they exert a large amount of torque. The disadvantage of this implementation is that, for a typically weighted cover, the mirror cover would require in the region of 180 Watts to operate. Typical solid state relays are 12V DC and therefore require a large amount of current, of the order of 10 amps. Therefore an additional power supply would be needed with a transformer. The resulting unit would be bulky and relatively expensive.

- **An AC motor.**

  An AC motor has the advantage of being small and would be able to run off the existing power supply. The disadvantage with AC motors is that a typical motor runs at 30-60 rpm so the cover would be jerked off in under a second. Lower rpm motors tend to be bigger and bulkier and obtaining small low rpm motors is expensive. Slowing down the motor would reduce the torque and require an additional power supply. Therefore a second stage of of gears would be needed, a rack and pinion assembly being the most suitable. Again this would increase the bulkiness of the whole unit.

- **A pneumatic actuator (compressed air piston).**

Figure 2.7: (Top) The client module installed on the dome with its solid state relay module, interfaced to the dome's control box seen on the right hand side, installed below it. (Bottom) The server module installed on the dome wall with the motor driver chassis housing the TCS machine seen in the foreground.

Another alternative was to make use of a spare pneumatic piston which was available from the mechanical workshop. The obvious advantage of incorporating this piston in an operation system was that it would be low cost. The disadvantage is that it would need a compressor to run full-time in the background to maintain the air pressure in the piston.

The 0.75m telescope building houses a compressor in the dome for routine maintenance of the dome tyres. Therefore we decided that the use of a pneumatic system to operate the closing and opening of the mirror cover would be the cheapest and easiest to implement. The pistons used would not require much air so the available compressor, a Hobby Craft 25 model with a maximum pressure of 800kpa and a duty cycle of 60%, would not have to pressurise for weeks at a time.

Two designs were considered for the cover itself; namely an accordion-style blind or an aluminium trap-door arrangement. The former would be made of a hard plastic material and would fold up in an accordion fashion run off either electric or pneumatic motors operating two rod-less pistons fixed either side of the blind. A similar arrangement is used on the Japanese IRSF telescope located at the Sutherland site. The big advantage of this design is that it would be compact and minimally reduce the amount of dust that could come in contact with the mirror. The disadvantage as it turned out was that such a system (due to the cost of rod-less pistons) is quite expensive to produce. There was also an additional concern, due to the dimensions of the telescope tubing, that the folded up cover would obscure a section of the primary mirror. The latter design involved the creation of a circular, light-weight, aluminium cover to be removed and replaced using a piston armature. The piston would be controlled using a three-way solenoid valve. The advantage of this system is that it can be manufactured at a reasonable cost. The disadvantage is that it is bulky to implement. There is also the additional concern that the pistons would jerk the cover off rapidly, particularly if the air pressure is low.

Due to budget restraints, the second design was chosen for the mirror cover. A three way solenoid valve was ordered from the pneumatic control system company Festo and a electronic control system and power supply were designed for the control of the valve. The installation is shown in Figure 2.8. The aluminium lid has been since coated with a black, non-reflective paint so as to minimise the reflection of stray light into the light path of the telescope. The basic operation is described below.

Figure 2.8: The mirror cover. Top right shows a close up of the Festo valve which directs air-flow in and out of the piston.

Basic operation of mirror cover and control electronics

A control card for the control of the solenoids was designed and built by Piet Fourie of the SAAO electronics department. The card is equipped for both remote and manual control to accommodate both modes of operation. The command to open the mirror cover is logic 1, logic 0 to close.

The switching of the solenoids is controlled via a solid state relay. When the mirror cover is commanded to open (logic 1) the solid state relay is switched on. The relay then switches power to the 'open solenoid'. When the solenoid is energised it pulls a shunt within the valve which directs air from the compressor to the top of the piston. Air from the bottom of the piston is let out through one of two exhausts in the valve. The piston then pulls up the cover until an arm on the cover hits the 'open limit' switch situated on the telescope tube. The limit switch, which is connected in series with solenoid, then interrupts power to the solenoid. The shunt is then released to a 'stop' position where the air within the tubing to the front of the piston is kept in place. A similar process follows for the closing of the cover: logic 0 switches off power to the relay. The relay then releases the power switch to the 'open solenoid' so the 'close solenoid' is switched on. This solenoid pulls the shunt in the opposite direction, allowing air from the front of the piston to escape through the second exhaust while air from the compressor is redirected to the bottom of the piston thereby pushing the cover down. Again, power to the 'close solenoid' is interrupted when the close limit, situated below the cover and connected in series with the 'close solenoid', is reached by the cover.

This arrangement has the advantageous feature of providing feedback control should the cover shift from its position during slewing of the telescope. If the cover should slip from its open position then the 'open limit' switch will be released. However since the 'open solenoid' is still energised (as the relay is still registering the TCS 'mirror cover open' command and therefore still switched on), the solenoid will resume forcing air into the piston until the open limit is reached again. Of course, the reverse is true for the 'close limit' switch. The one disadvantage of this arrangement is that if power to the solid state relay or the TCS PC fails, then the mirror cover is likely to open or close unbidden. For this reason, the solid state relay was put on UPS. The problem of the event of a PC failure is discussed below in the next section.

24V unregulated and 5V regulated power supplies for the solenoids and the solid state relay respectively, were designed and built by Geoff Evans, head of the SAAO electronics

department.

2.2.5 Safety Control of Peripherals

During a snow storm in August 2006, power to the Sutherland telescopes failed and most systems were offline for a few hours as the back-up generator was frozen. Later in the day it was noticed that the 0.75m dome shutter was open. The cause of this was unknown until, later in the month, the TCS computer automatically rebooted in the early hours of the morning after downloading and installing Windows OS updates. The rebooting of the PC caused the dome shutter to open and the lights to switch on. It was since determined that the dome shutter opens as the PC is shut down and the lights switch on as the PC restarts. We managed to ascertain that, as long as the power to the telescope/dome motors was off, then the dome shutter could not open when the TCS PC is shut down.

Even so, the opening of the dome shutter and switching of the lights after a shut down of the PC remained a great concern. While the problem did not occur when power to the building was switched off, there was still always the possibility that, since the remote user will not have the capability to switch on/off the building power, that the problem could arise after a remote observing run. The event of the snowstorm in August showed that we could have the possible scenario of a user parking the telescope and logging out at the onset of a snow storm. The storm disrupts the power to the TCS PC and as the PC shuts down the dome and mirror cover open during the storm. In addition, not allowing the TCS PC to reboot meant that all automatic software updates to the Windows OS had to be suspended. Roy Emmerich, SAAO's head IT administrator expressed concern at this even though the PC lies behind the SAAO firewall; Windows XP is notorious for being an insecure OS. Electronic safeguarding of the dome and lights would have been provided by DFM's dome *NEMA* box. However purchasing of the box proved to be too expensive at the time. The need for safe-guarding against TCS or power failure prompted the electronics department to design and build a control system for monitoring of the dome.

An Omron CPM2C programmable logic controller (PLC) was purchased from a Yelland control distributor to coordinate and control the switching of the lights, dome shutter and mirror cover. In addition to providing the safeguards to address the safety concerns outlined above, incorporating a PLC to manage the existing peripheral system allowed the functionality of a PLC controlled wind-blind and automated rain-sensing to be added.

Management of the telescope peripherals and the operation of the safeguards provided by the PLC are described below[1].

Safeguarding the peripheral system against system failure

The most important feature provided by the PLC is to prevent unsolicited switching of the dome shutter, mirror cover and lights during a TCS reboot or system failure. Preventing this is achieved by exploiting the fact that the telescope drives are switched off whenever power to the TCS is disrupted. If the PLC is able to detect when the drives are switched off then it can be programmed in that event to ignore any commands coming from the TCS PC. This arrangement required the installation of a sensor to detect whether the telescope drives are receiving power and some careful programming of the PLC by Piet Fourie of the SAAO Electronics department.

The operation of PLC's system monitoring can be summarised as below:

- All TCS and manual commands are re-routed to the PLC.
- The controller monitors the status of the TCS PC.
- When WinTCS is closed down, it immediately interrupts power to the drives.
- In the event of a PC shut down, the controller monitors the drives.
- If the drives are switched off then the controller prevents the dome, lights and mirror cover from receiving any signals until the TCS PC is fully rebooted. This involved the addition of a timer to the Dome circuit board. This ensures that the radio transmitter module will ignore any commands to the dome, lights and wind blind for 10-15 seconds after system start-up to allow for the TCS/radio system to settle and prevent any erroneous commands from the TCS being actuated.

The PLC was also programmed to implement an Emergency Shutdown routine. This can be selected in either auto or manual mode[2] and has the highest priority. When selected the dome shutters and mirror cover are closed and cannot be reactivated until Emergency Shutdown is switched off.

Programming of the PLC

The above control logic were implemented using a form of PLC programming known as Ladder Logic. Ladder Logic is a graphical language used to program PLCs by imple-

[1] See Manly (1990) for a similar implementation and discussion on observatory controllers in general.

[2] The peripheral system can be switched to be operated in either manual or auto mode where 'manual' is direct switching at the PLC control panel and 'auto' is receiving commands straight from the TCS PC.

menting ladder diagrams. Ladder diagrams are electrical logic schematics drawn using the rules of Ladder Logic, so called because the schematics resemble ladders with two vertical 'rails' and a sequence of rungs between them (Kuphaldt 2009).

The diagrams can be seen as a series of connections (an 'instruction line') between 'logical checkers' (contacts) on the left rail and actuators on the right. Along the instruction lines are placed conditions which lead to other instructions on the right hand side. The logical combinations of these conditions determine when and how the instructions on the right hand side are executed (OMRON 2003). If a path can be traced between the inputs on the left side of the rung and the output on the right side of the rung, through "closed" contacts, the rung or instruction line is true and the output bit is asserted true (Kamen 1999). Each contact (input) or actuator (output) corresponds to the status of a single bit in the PLC's memory. In this case the contacts and actuators correspond to physical devices such as limit switches, push-buttons and toggle switches[3].

Ladder notation is best suited to control problems such as this, where only binary variables serve as inputs/outputs and where the sequencing of a series of binary operations is required.

2.2.6 Control of the Peripheral System

The operation of the various peripherals is summarised below.

Mirror Cover

If manual control is selected the mirror cover can be opened and closed from the PLC panel. The TCS controls the mirror cover in auto mode only if the telescope is powered (in AUTO mode). The mirror cover electronics were modified to accommodate the new system. The current system has two separate relays, one for each solenoid, switched by the PLC. The limit switches were originally in series with the solenoids, thereby cutting power to the relays when the cover reached either its closed or open limits. The current system now has the limits detected by the PLC which then switches off the appropriate open/close command. The internal mirror cover switch became a toggle switch so that if the cover should move from its position (thereby opening a limit switch), the previous open/close command will be read by the PLC which will then actuate the corresponding solenoid, reverting the cover to its previous position.

[3]This does not have to be the case. In bigger systems the inputs may be internal storage bits or the results of outputs generated elsewhere within the program or in another embedded system.

Dome Lights

The TCS lights control is wired in parallel with the manual control, allowing switching of the lights between the two (both the TCS signal and the manual switch must be off for the lights to be off). The TCS can only switch on the lights if there is power to the telescope.

Dome Shutter

The dome shutter can be opened either manually from the PLC panel or from the TCS when in AUTO mode. The TCS can only open the shutter when the PLC senses there is power to the telescope drives. Emergency Shutdown disables all control of the shutters.

The Rain Sensor

A rain detector was added as part of the upgrade to the peripheral system. This was deemed necessary as the remote user will only be able to monitor environmental conditions indirectly by checking the Sutherland weather stations' websites. The detector essentially consists of a series of conductance probes which have a voltage potential across them. The conductor is made of a non-erosive metal, in this case aluminium. The circuit is closed when the surface becomes wet. In this case the circuit switches the Emergency Shutdown routine implemented by the PLC. Transistors behind the conductance mesh keeps the plate warm to prevent false alarms being implemented due to condensation and to speed up drying of sensor after the rain has stopped.

When the rain sensor is triggered the mirror cover and shutter can not be opened, not even manually, without first powering down the telescope and restarting the system.
The PLC interface system was installed near the TCS PC rack inside the dome and tested to perform to spec in April 2007.

2.3 Stage 3: Installation of Auto-Initialisation Hardware

Before the upgrade, the on-site astronomer had to initialise the telescope manually. This is done by positioning the telescope using a laser pointer situated at the base of the telescope tube. The telescope is driven until the laser pointer is centered with markings situated on the west wall – this points the telescope directly at the zenith and the position encoders are intialised to this position via the TCS. This process provides a rough initialisation for the pointing system. Fine positioning is achieved by searching for and identifying a bright star using the UCT CCD to provide an absolute position. Due to the very small FoV afforded by the UCT CCD, the rough initialisation rarely produces the bright star on the chip. The process usually requires a few iterations of slewing and exposing before the star is found. As outlined in Section 1.2, this process of absolute positioning is simply unacceptable for remote observing.

2.3.1 Telescope Auto-Initialisation

Automation of the telescope initialisation process means that, at the request of the user, the TCS software positions the telescope at a preset coordinate then sets its software coordinates to this position. The software would have to do this reliably and consistently using feedback from suitable rotary movement counters otherwise known as encoders.

Encoders

An encoder is a sensor paired with a transducer and a scale to translate or encode a position into a code of electronic pulses.

There are three main types of encoders: optical (or photoelectric), magnetic and mechanical. Optical encoders are the most common type of encoder in use today. These are highly accurate, very reliable and relatively low cost encoders. Optical encoders operate on the principle of the photo-electrical scanning of very fine gratings. Optical encoders are classified into two types: rotary and linear encoders. For our purposes only rotary encoders are of interest and will be described here.

Rotary encoders operate by transducing angular motions into electrical signals for either display, automation and/or numerical control (Korte 1997). Rotary encoders consist of a disc marked with radial lines. An optical switch (photodiode) generates a pulse of light whenever one of the line rotates into its field of view. Rotary encoders are classified

as either incremental or absolute encoders which measure absolute position depending on whether they provide measurement of relative or absolute angular position. Absolute encoders are very expensive and can be cumbersome; for our purposes, we would need an encoder disc the ∼size of the mirror to achieve the desired resolution. Therefore incremental encoders were chosen for this system. Unlike absolute encoders, which produce a unique digital code for each distinct angle of the shaft, incremental encoders can only measure the change in angle relative to some arbitrary datum, such as the shaft's position at the time when the power was switched on (Soloman 2009). This is why, before the refurbishment for auto-initialisation, it was necessary for the telescope always to be parked at the zenith before the TCS was switched on. The TCS could then assume that the telescope was at the zenith and set the position encoders to this value. Increments would then be counted from this 'zero' value.

Operation of the Auto-Initialisation System

As previously described, a remote observer will not have the ability to centre and initialise the telescope at the zenith. This necessitates the addition of a second sensor to sense when the telescope has passed its zero position. This is what has been implemented in this case. The additional sensors are in the form of potentiometers. The potentiometers are able to provide a rough absolute position for the telescope, once they have been calibrated using the TCS. The encoders used in this system are designed with 'fiducial' or reference lines. As the encoder shaft rotates, a single differential index line (TTL) output is fed to the motion control processor once per revolution when the fiducial line is detected. The zero reference position that the TCS will use to set the telescope's position is set to coincide with the detection of a fiducial. Thus when the telescope is requested to auto-initialise, the TCS uses feedback from the potentiometers to move the telescope to roughly the absolute zero position. This should be within one revolution of the encoder's fiducial. Then the TCS will request the telescope to track until the fiducial line is detected, thus the encoders provide fine positioning of the telescope. On detection, the telescope's position is set to the TCS's internally stored value.

2.3.2 Installation and Testing of Auto-Initialisation Hardware

The necessary HA and Dec potentiometers and drive assemblies to facilitate self-initialisation of the 0.75m were received and installed in May 2006. The potentiometers and drive assemblies were tested to provide correct movement and control. The pointing of the telescope was also corrected for and WinTCS was modified to allow the new potentiometers

to provide a rough absolute position.

When the telescope was tested for auto-initialisation in September 2006 it was found that WinTCS could not detect the HA fiducial on the new encoder. After performing a series of tests suggested by Mark Kelley (the DFM WinTCS software developer) with the help of the on-site electronic assistance, we believed that the problem did not lie with the encoders themselves or within the cables. This left the PC I/O card or WinTCS as the source of the problem. We were able to rule out problems with the I/O card when we were able to detect both the Dec and the HA fiducial signal coming from the encoders. As it turned out the problem lay with WinTCS not having being given the capability to detect the HA signal. In January 2007, when testing the auto-initialisation it was noticed that the Dec coordinate was consistently incorrectly set to a value offset from the true Dec position. This offset was rectified by Mark Kelley the same week.

As already mentioned, during initialisation, the TCS slews the telescope to a rough position, an hour angle of ∼0.5 hr East of the zenith, then slowly moves the telescope in positive HA while the TCS looks for the fiducial. When the fiducial is found, the telescope tracks back in negative HA until the signal is detected again and then stops at what should be the previously determined, and internally stored, fiducial position. However in July of 2007 it was discovered that the TCS did not consistently find the HA fiducial in the correct position. It seemed that the telescope was not consistently being slewed to lie within one encoder revolution of the initialisation position[4]. If the telescope was set by the potentiometers to a start position which just missed the correct fiducial position then TCS would only detect the signal on the next turn of the encoder (2 arcmin later) but still initialise the telescope to the previous fiducial position (as this is the value stored in the TCS). This resulted in the telescope, once 'initialised', frequently finding targets at either plus or minus 2 arc minutes.

For the most part of 2008, intermittent tests seemed to suggest that the problem was a balancing issue where slight imbalancing of the telescope was causing it to over-shoot/under-shoot the ∼0.5 HA start point. The far-from-ideal solution was procedural; in order to conduct remote tests, part of the 'on-site' telescope assistant's start-up duties would have to be to initialise the telescope manually before logging out and allowing the remote user to take-over. The inability to auto-initialise posed a serious disadvantage to operating remotely; should the remote user lose pointing at any point during the run then they would not be able to recover the telescope without on-site assistance.

[4]This would be the stored values of the particular HA and Dec at which the fiducials were found during the initialisation of the encoders.

It was not until January 2009, when the HA potentiometer was damaged and required replacing, that the real source of the auto-initialisation problem was correctly identified. Detailed and systematic testing of different pot-assemblies clearly indicated that the TCS slewed the telescope to two distinct start positions, depending on the direction it was coming from, before beginning to search for a fiducial. The repeatability over a range of HA suggested that the the difference in start positions could not be due to any mechanical play in the system or uncertainty due to lack of A/D resolution; the problem must have lain in software resolution.

On communication with Mark Kelley on the results of the hypothesis testing and elimination procedures, his inspection of the TCS code confirmed the author's firm suspicion; the software window for the fiducial-search start position was set too large (the equivalent of a rounding error). Thus, while the TCS, on auto-initialising, would stop slewing the telescope once the ∼0.5 HA condition for the start position was met, this loose approximation meant the start position would be HA = -0.4789 h or HA = -0.5093 h depending on the direction of slew (i.e. which value was encountered first).

After the necessary correction was made and the TCS software re-installed, the auto-initialisation procedure performed to specification. Once the telescope is auto-initialised, stars between +1 and -4 in HA and -80 and +20 degrees in Dec (nearly the full range of the telescope in Dec) can be successfully found to fall within the field of view when the telescope is slewed from the zenith. Slewing to targets which lie at greater than +1 HA can be achieved by performing successive re-initialisations on bright stars, 'star-hops', in ∼1 HA steps approaching the target.

The auto-intialisation trouble-shoot is an excellent illustration of why any software installation process should ideally have the source code and/or the developer available on site during the testing phase.

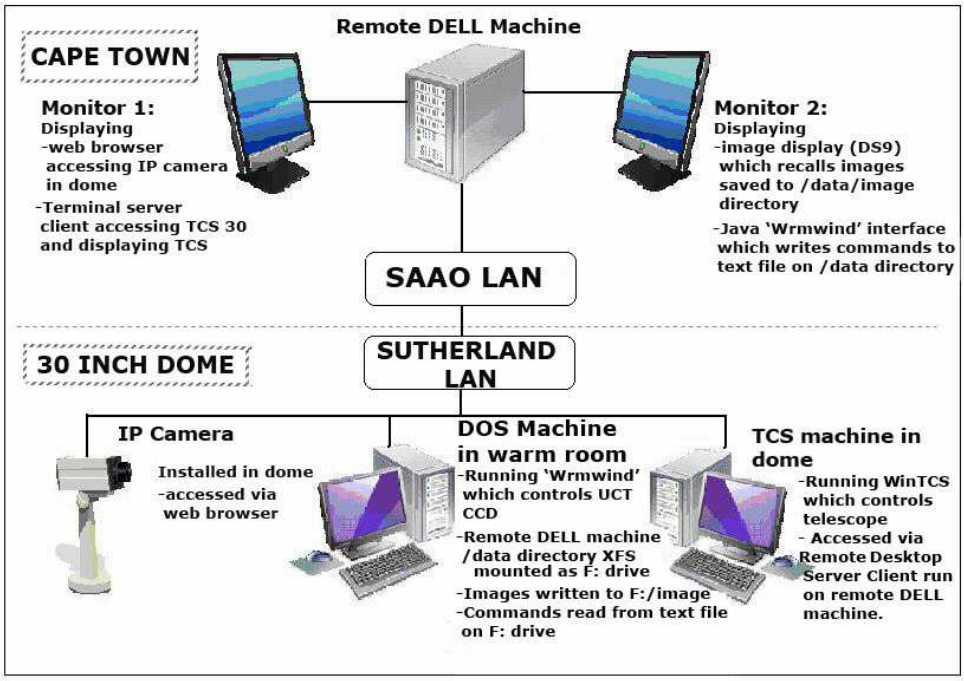

Figure 2.9: Schematic of communications, via the SAAO and Sutherland networks, between the on-site telescope and instrument control computers and the remote workstation.

2.4 Stage 4: Development of Remote Instrument Software Interface

The user requirements, as outlined in section 1.1, specify that the user interface be as simple to use as possible and 'transparent' i.e. providing realtime feedback on the status of the system. The off-the-shelf system implemented for the TCS fulfills these requirements; the parallel instrument control system should do the same as far as possible within the limits of the existing system.

As discussed in section 1.2, the fact that the PC controlling the UCT CCD is a DOS operating system presented the problem of how to access it remotely over a network. The solution to this was proposed by the co-author of the instrument control program, `wrmwind`, Darragh O'Donoghue. The idea was to have `wrmwind` modified so that it would read its commands, over the network, from a text file on the data storage PC, instead of the local keyboard. This required a local user interface to be designed and programmed to write the user's commands to this text file (refer to Figure 2.9 for a schematic of the communications). This section describes the design and programming of this user

interface.

2.4.1 Remote User Implementation

As mentioned in section 1.1, the easiest and simplest user interfaces are graphical windows based applications which implement a "point-and-click" interaction. Therefore it was decided that the remote CCD control program would be an updated "windows" based GUI display, instead of a simple command line series of prompts. The GUI would model the interaction of the DOS based program as far as possible, displaying the selected instrument control parameters but only providing the commands sufficient for the control of the camera.

The GUI is run on the Unix data storage machine. The GUI is intended to emulate the DOS based program `wrmwind` by providing the basic commands and features used for CCD photometry, presented in a similar layout to the original program. Each command selected is written to a text file on the Unix machine, and available for reading by the DOS machine, simulating keystrokes that would normally be entered on the keyboard at the telescope by the local operator. The DOS-based program continually reads from this file, thereby implementing the user's commands. This set-up was first tested in Cape Town in January 2006, when the UCT CCD was at the electronics lab for image testing. `Wrmwind` was modified to continuously read from the ('flip') text file on the Unix workstation that the camera was writing to. A command set was written to the file and read by the camera. Each of the commands were executed as expected, proving the feasibility of the procedure.

Transparency stipulated that the user be able to receive real-time feedback of the system status. As discussed before, the user will not be afforded this information via remote access of the instrument Desktop. One suggested remedy for this was the use of an IP camera to provide visual feedback of the instrument status. The IP camera would be trained on the DOS machine's monitor thus, while the GUI would display user selected system parameters, the user was expected to monitor the state of the system via the visual feedback system.

However tests made at the offices of the electrical appliances and video surveillance retailer, Eagle Technology, demonstrated that this solution was not feasible, as the size of the text was too small and the image quality too poor to be easily legible over the network. The next alternative investigated was to convert the signal to the DOS monitor from VGA to video, then from video to IP using an IP server thus making the monitor's output addressable and, therefore, accessible over the internet. However tests made at Eagle Technology in December 2006 again showed that the quality of the image over the

server was too poor to be used for late night observations. There had to be another solution to accessing `wrmwind`'s screen output.

The DOS `wrmwind` output to screen is sectioned into three panels; a menubar, a panel to display the current parameters of the camera (display panel) and a scrolling panel to display `wrmwind`'s responses to user commands. The most important information that the user needs to be able to access is output to the scrolling panel. The remote user interface has been programmed to keep track of the camera control parameters, but ideally the user would also be able to see the output to the DOS display panel as well. This would be most important in the situation where a command to the camera is not implemented due to hardware failure or connection to the SAAO internet server being disabled. For instance the user may send a command to the filter wheel to move to a new position when communications to the filter wheel have failed. The command would still be sent to the DOS PC and the new position reflected on the remote machine, giving the user the impression that a new filter is in position. Hence communication to the camera remotely without feedback is unacceptable. Therefore Dr Darragh O'Donoghue suggested that the DOS `wrmwind` version be modified so as to write its updates to the display panel and the scrolling panel to a text file which could then be *read in* by the remote `wrmwind` GUI (hereafter referred to as Wrmwind_II) and displayed. Thus the user would have indirect two-way communication with the DOS machine controlling the camera.

2.4.2 Design of the Interface

The interface was designed to be similar in layout to the original DOS version but with the presentation of modern windows based applications. The layout of the original design was modified as little as possible so as to allow users an easy transition from viewing the system in one mode and working in another, the originally intended mode of viewing. Therefore the appearance of the GUI consists of three panels, similar to the DOS version; one menu bar, a display panel showing the current parameters of the camera and an input panel (instead of the DOS's informative scrolling panel) from which to receive the user's commands.

The programming of the interface had to involve as little cost as possible, particularly since it would simply be used as a user interface to relay commands to the DOS programme which would actually be implementing the commands. The desirability of a modern 'look-and-feel' meant that a relatively new programming package would have to be used.

2.4.3 The Programming Language

At first programming the graphical user interface (GUI) in C was considered, provided that an open source GUI package for C could be found. Some investigation of C programming packages revealed the X-Forms Library, an open source GUI package created in C and easily downloaded over the internet. The Forms Library uses the services provided by Xlib and should therefore be compilable on any machine that has X installed.

The X-forms library provides a simple procedure to create a basic user interface. A form is defined on which different types of objects, such as input fields, buttons or boxes can be placed. The painting of the form and all the associated objects is done by a single routine which also handles the detection of a user interaction with any of the objects on the form. On detection of a user event, control is returned to the program which can then take the appropriate action. This implementation makes creating a simple application relatively straightforward.

However consultation with other software programmers and the SAAO system administrator gave rise to concerns over portability issues. Ideally the interface should be able to run on any machine or operating system with consistent results. The X-forms library, while based on Xlib, is still an open source library of C routines and is not guaranteed to perform in this manner. However a programming language designed to provide consistent performance and presentation on a variety of operating systems is the high-level language Java. After confirming that all of the systems installed on the SAAO network were equipped to run Java programmes and that the environment is relatively simple to set-up, it was decided to switch to programming in Java.

The Java programming language was designed to optimise portability and security as its key features. This has been achieved by having the Java environment run inside a virtual machine, the Java Virtual Machine (JVM), instead of on the operating system directly. The JVM is written in a fast natively compiled language such as C or C++ allowing Java programs to be run on any platform (Unix, PC or Macintosh) with consistent results, removing the need to produce alternative versions of the same program.

The GUI was designed using Swing, Java's user interface toolkit. The toolkit is reasonably flexible and allows for simple interfaces to be quickly coded, compiled and run. The GUI was coded using Java's Object Orientated methodology (Niemeyer & Knudsen 2005). Object orientated programming refers to the encapsulation of GUI components as objects[5] with associated methods which are only linked together at runtime by the main

[5]Objects being instants of a defined class.

program.

2.4.4 Coding, Implementation and Operation of the GUI

The program contains only one public class, the GUI itself. This class contains the objects imported from the Java Swing Toolkit which make up the interface, e.g labels, textfields and buttons. Each Swing object has associated methods and attributes which can be modified to create and customize the look and feel of the interface. The individual Swing objects generate events in response to user actions, which have to be handled appropriately, as opposed to the C Forms Library where any action by the user is detected by a single routine. In this case, smaller private classes were created to model the response of the original DOS `wrmwind` to various user commands.

At runtime the main public class is instantiated as a GUI object by the main method after which control of the program is effectively handed over to the GUI object's main method. This method 'listens' for a user action, or event. Once an event is received, the method detects the source of the action (i.e. which command the user wishes to implement) and hands over the action to an instance of the appropriate private class to deal with. The private class will send off the command (i.e. write it to the textfile) and, depending on the nature of the command, adjust the display value or request further information from the user. Methods were created for the main public class for the sending of data and retrieval of information from the user.

Operation of the GUI

Interaction of the remote user with the interface can be described as below:

- On starting Wrmwind_II a dialog box appears. This requests the desired directory path for the file that will contain the commands for the remote machine to be written to. The program will not proceed without this user defined path.
- The Wrmwind_II panel opens up as displayed in Figure 2.10 The camera settings displayed in the panel on the right hand side are set to the same default values as the DOS version, with the exception of the run number which the user is expected to change.
- The user selects commands by selecting various Menu items. The menu items can be selected using the mouse or the accelerator keys such 'Shift' and 'Alt'.
- Before any commands can be sent to the DOS machine the user must first select 'Remote Channel open' under the 'Remote' menu. This ensures that the correct

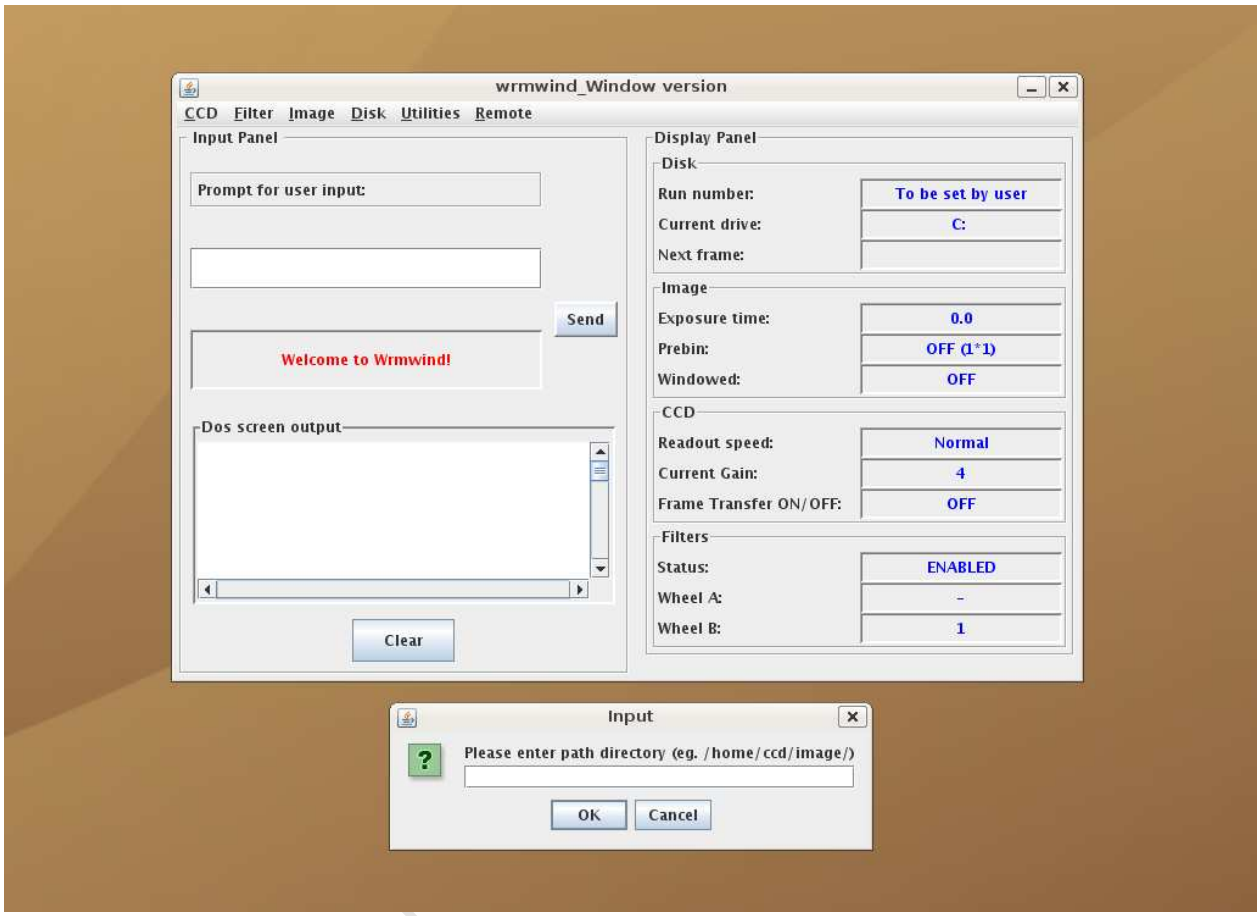

Figure 2.10: The view of the Java version of `wrmwind`, Wrmwind_II on start-up.

command/information files are available to be written to or read from. If these files are not detected (perhaps indicating that the DOS machine has not been set to operate in remote mode) then Wrmwind_II displays an appropriate error (Figure 2.11a).

- If an item is selected which does not require further information (e.g. toggling frame transfer mode) then the corresponding command is written straight to the text file.

- If an item is selected that does require further user information (e.g. changing the run number) then the label above the textfield requests the relevant information. The user is expected to enter the relevant information in the textfield and, on completion, press the 'Send' button, upon which the information is retrieved from the textfield and written to the text file.

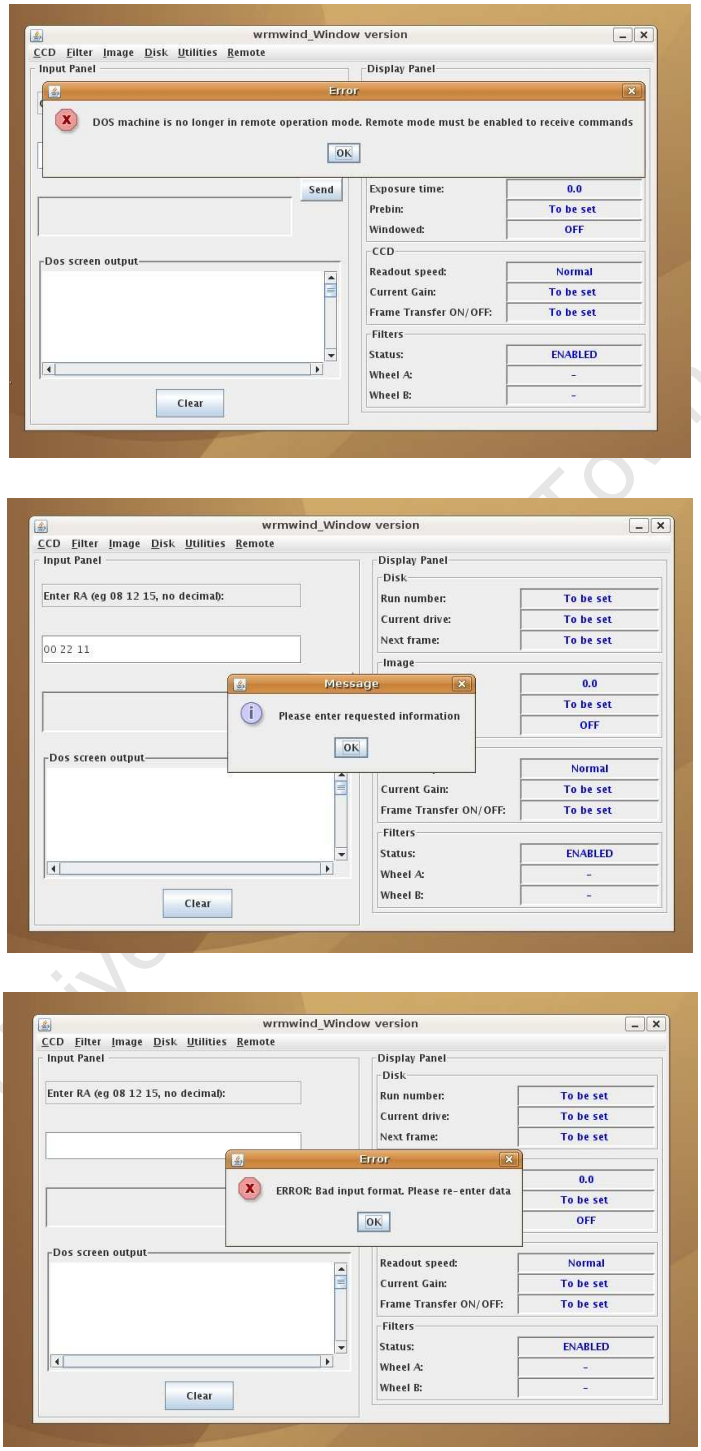

Figure 2.11: Some of the error messages displayed by Wrmwind_II: (top) if there is a problem detected with the remote connection (or it hasn't been opened), (middle) prompting the user to enter information after a long delay and (bottom) informing the user that the information entered is of the incorrect format.

- If the textfield remains empty after the user is asked for information, then dialog boxes appear every thirty seconds prompting the user to enter the appropriate information. The menu bar is disabled pending the user's response to prevent other commands being sent while the DOS machine is waiting for further information. Figure 2.11b

- Before the input from the textfield is retrieved (on registering the 'Send' button being pushed) it's first checked to see if the value is in a valid format according to the information requested. For instance if RA nd Dec coordinates are required then the user's input must be of the format +/-## ## ## where # indicates that the input must be a digit. If the input is not of the correct format then the user will not even be able to enter it into the textfield. If an empty data field is sent then a dialog box prompts the user to enter the information correctly (Figure 2.11c). Only then is the information retrieved and sent.

- The GUI's response to commands that require a whole sequence of information to be entered, such as the initiation of a high speed photometry run, was programmed to emulate the DOS responses.

- On the execution of a command, a panel below the textfield, termed the comment box, informs the user of the commands implemented.

- On exiting Wrmwind_II the command to exit is sent to the remote PC and all the command text files are deleted

Coding Challenges

There were two major challenges posed in programming the GUI. The first was caused by the fact that many of the commands to be implemented initiate a sequence of exchanges between the user and the program. Of course the program cannot proceed in requesting the next item of information from the user before the previous item has been entered, retrieved and scanned for errors before being sent. This means that the program has to be in a waiting state while the user enters the information. However it was found that the main program could not be in a waiting state and still register the user event of pressing the 'Send' button; the main window became unresponsive, even if the main program was coded to check, periodically, for the 'Sent' condition. This kind of issue is known as a concurrency problem in programming, and in Java the solution is supposed to be

the appropriate use of 'threads'[6]. In this case the problem was circumvented by creating individual objects (the private classes) to handle the responsiveness of each menu and the commands that fell under it. The objects are run in separate threads and 'wait' for the user's information to be entered thereby allowing the main program to be free to receive the 'Sent' action.

The second issue involved checking that the user's information was in the appropriate format. Of course the appropriate format depends on the requested information, whether it be a new filter number or a set of coordinates. Ideally the information is scanned at the entry point, in this case a textfield, before it's even retrieved. Java accommodates this kind of format checking but assumes that only one kind of information will be entered in a given textfield, while in this case all of the users information is received through a single textfield. This problem was overcome by redefining the existing Java formatting objects attached to textfields and overriding some of the methods to force a change of format as and when needed.

2.4.5 Testing of the GUI in Cape Town

The UCT CCD and DOS control camera was sent down to Cape Town for integration with the Java GUI. A new Dell computer was acquired to be the dedicated remote machine. The Dell machine has the Linux based 'Ubuntu' package as its operating system and was installed with the full Java JDK development suite and JRE runtime environment to allow running of the GUI interface.

Communication between the GUI and the CCD camera

A directory on the Dell machine is allocated for the use of the DOS machine. This directory is XFS-mounted onto the DOS machine's f: drive when the remote machine is selected as the destination for the images. Communication between the two programs is implemented using text files. When DOS `wrmwind` is switched to remote observation mode then it immediately begins checking the f: drive for indication that a command has been written to the drive. This is done by looping through the following sequence:

1. Once a command is received by the GUI it is first written to a text file, called 'flipfile'.
2. When the write operation is completed the GUI creates another textfile, called 'flip'. This is the indication to the DOS program that there is a command to be received.

[6]Threads are parallel processes which can be created and run concurrently with the main program, then terminated when their task is completed

3. Once DOS `wrmwind` detects the existence of 'flip' it opens up the 'flipfile' text file and reads in the command it should implement. Once it has done so, the DOS machine switches to looking for the presence of the next flag file.

4. The next command issued from the GUI is written to the text file 'flopfile'.

5. When the write operation is completed the GUI creates another textfile, called 'flop'. This is the indication to the DOS program that there is a command to be read in from the 'flopfile' text file.

6. On detection of 'flop', DOS `wrmwind` opens up 'flopfile' and reads in the command to be implemented.

7. This constitutes one I/O cycle between the remote GUI and DOS `wrmwind`. After a command has been read from 'flopfile' DOS reverts to scanning for the 'flip' file again and so on.

This 'handshaking' sequence of read back and forth between 'flipfile' and 'flopfile' was created to prevent I/O errors such as instructions being written to the command file before the previous instruction has been read.

Testing of Communications

The transmission and implementation of the user's actions was tested to perform as per the control sequence outlined in the previous section. After minor adjustments, all of the menu commands were received and implemented as expected. After performing basic image tests the following modifications were made to improve the transparency of the system and safeguard against possible system failures:

- DOS `wrmwind` was modified so as to indicate when it is remote enabled. When remote operation mode is selected then `wrmwind` creates a 'remote' file on the f: drive which is deleted when remote mode is disabled. If this file is not detected by the remote GUI then no instructions are written to the command file.

- A basic handshaking process was created to ensure that all previous commands are read by the DOS machine before the next one is written to the drive. This was done to compensate for the faster writing speed of the Dell machine and achieved by enabling the DOS `wrmwind` to delete the flag files 'flop' and 'flip' once commands were read from 'flopfile' or 'flipfile'. If a flag file is still present before a command is to be sent by the GUI then the GUI waits until the relevant flag file is deleted (indicating that

DOS is ready to receive commands) before sending the user's command. This also indicates if the DOS machine may have hung or rebooted during remote operation.

- Direct confirmation that the commands are successful is required to guard against the possibility of hardware failure. Hardware failure is detected by the DOS interface thus DOS `wrmwind` was modified so that responses to user commands would be be written to a text file. The information to be updated, as well as the position on the DOS screen to which the information is to be displayed, is written to the text file. The text file is read by the remote GUI and, from matching the screen position to internally stored parameters (such as exposure time, read-out speed etc.), the appropriate parameter is updated and displayed. A scrolling display screen was added to the GUI to display the DOS scrolling screen's responses to commands. Communication between the two interfaces was tested to be successful during the week leading up to the test remote run in August 2007.

2.5 Stage 5: Purchase, Installation and Testing of Sensory Hardware

2.5.1 Internet Cameras for Dome surveillance

Safe movement of the telescope requires visual feedback of conditions inside the dome. After investigation of modern surveillance technologies available on the market, two solutions presented themselves. Remote viewing of the dome could be accomplished using either:

- A Network IP camera
- An analog camera combined with an IP server

Before the advent of web camera technology the most common way of implementing visual surveillance would have been via closed circuit television, or CCTV. CCTV uses analog cameras for image capture, coaxial cable for transmission, video tape recorders for image storage and TV monitors for display. Over the last decade the video surveillance industry has slowly moved towards digitising the entire system. First CCD technology allowed the digitising of images, then Digital Video Recorders (DVRs) replaced VCRs for more efficient image storage and retrieval. Finally PCs were introduced to display the images via modem or network connection to a DVR (Networkcamerareviews.com 2007) Then small portable web cameras were developed for the consumer market primarily to satisfy the need for long distance audio with visual communications. However the technology was not taken seriously for industrial applications, mainly because typical PC web cameras are not robust enough for industrial conditions. This shortcoming was solved by the Network IP camera. An IP camera is a robust camera for industrial applications which incorporates all the features of a digital video system using onboard processors and built in web server software allowing surveillance over the Internet. The web server software allows easy access to images from anywhere using a standard web browser over a LAN network or the Internet.

An alternative to using an IP camera is the combination of an analog camera with an IP server. Video IP servers were introduced to give existing CCTV systems the benefit of network access while protecting investments in analog cameras (Networkcamerareviews.com 2007). IP servers effectively turn video cameras into IP cameras by converting the analog images to digital then making them available over a network using web server software to make each camera addressable. Using an analog camera combined with an IP server

has the advantage of increasing flexibility of system design as the established variety of analog cameras allow one to tailor the surveillance system to requirements.

Two entry-level cameras were tested at the commercial CCTV vendor, Eagle Technology. While both provided good image quality at moderately low light-levels ($\sim$ 1 lux), neither were suitable for very low-level light conditions. Night vision IP cameras are relatively expensive and most operate using infrared illumination, which is undesirable as the UCT CCD is sensitive to infrared. However the IP cameras did demonstrate the ease of setting up IP surveillance systems.

Having a surveillance system that could not operate in the dark conditions of the dome would mean in effect that the dome shutter would have to be closed and the lights switched on every time the user wished to either slew the telescope or either confirm that the telescope was in the correct position and in line with the slit. This unacceptable mode of operation prompted us to consider the alternative of an analog camera combined with an IP server.

The first analog camera tested was a board camera obtained from RF Concepts Ltd, based in Belfast, Ireland. Board cameras are the simplest cameras available consisting only of a lens, image sensor (CCD or CMOS in this case) and support electronics. Board cameras provide live video outputs and have the desirable feature of being able to produce images in very low level light conditions. This particular camera is certified to operate down to 0.003 lux. However modifying the camera by including a gain amplifier allowed the camera to operate at even lower light conditions.

Comparing this camera, the 1000XA model, to the best low lux cameras offered by Eagle Technology showed that the modified 1000XA provided a brighter image, but at lower image resolution. However the streamed image could be viewed in a web browser from the IP server which was small enough in size such that the difference in image resolution over the range of cameras hardly changed the picture quality over the network. For the purposes of this project, having a brighter image and being able to modify a camera to provide one was more important. Therefore it was decided to purchase the 1000XA board camera to be coupled with a Vivotek IP server from Eagle Technology.

The new camera arrived in May 2007. A suitable housing was designed by Willie Koorts of the SAAO electronics department to insulate the camera from the low temperatures and possibly high humidities within the dome.

The next issue to consider was where in the dome the camera should be mounted. What needs to be checked is if the telescope is aligned with the dome slit and that there is

nothing obstructing movement of the telescope. After testing various camera positions, it was decided to place the camera underneath the telescope, so the telescope could be seen outlined against the sky. Despite the low light conditions that the board camera could operate at, the telescope could still not be seen in total darkness, say, at new moon. But the 1000XA is also sensitive to near infra-red light. While illumination of the dome by typical infra-red cameras was not acceptable due to the sensitivity of CCD cameras, a little infra-red illumination in the form of LEDs was deemed tolerable as long as the LEDs were not directly in the light path of the telescope.

The camera and IP server were tested at the telescope in June 2007. First the camera was tested under various light conditions. Virtually nothing of the telescope could be seen without some form of illumination in the dome. LEDs placed at the base of the telescope were not sufficient for determining which direction the telescope is pointing in. There are two sets of lights within the dome: fluorescents affixed to the dome ceiling, which the observer can switch remotely, and a set of wall lights. Further investigation showed that red 40W light bulbs placed in the wall lights provided more than sufficient illumination for the telescope and everything within the dome to be seen. It was suggested by Mr Geoff Evans that there be a switch within the dome installed to allow input to the TCS to be toggled between the dome lights and the wall lights. Then in remote mode, the 'lights' input to the TCS would be the dome wall lights fitted with red 40W bulbs, which could be safely turned on during the observation run with the dome shutter still open without compromising the work of other observers on the plateau. This would save the inconvenience of having to close the dome shutter every time the telescope needed to be slewed or the observer need to check its position relative to the dome.

The camera was also tested from various positions within the dome (Figure 2.12) and with different lens mounts. The best configuration was found to be mounting the camera in the NW corner of the dome using the original lens (in red light conditions, Figure 2.13). The images shown are the screenshots of the Internet Explorer web browser displaying the camera views over the SAAO network.

Lastly an appropriate housing was ordered and fitted to the camera. The network camera was finally installed in July 2007.

Operating the telescope while using the camera exclusively for surveillance of the dome was tested in July 2007. Use of the camera during that run demonstrated that the perspective view of the camera makes it difficult to judge whether the dome slit is always in line with the telescope. However a camera is required in this position to see whether there are obstacles in the way of the slewing telescope. A second IP camera, situated at the corner of the telescope tube and set pointing upwards so the view would be of the

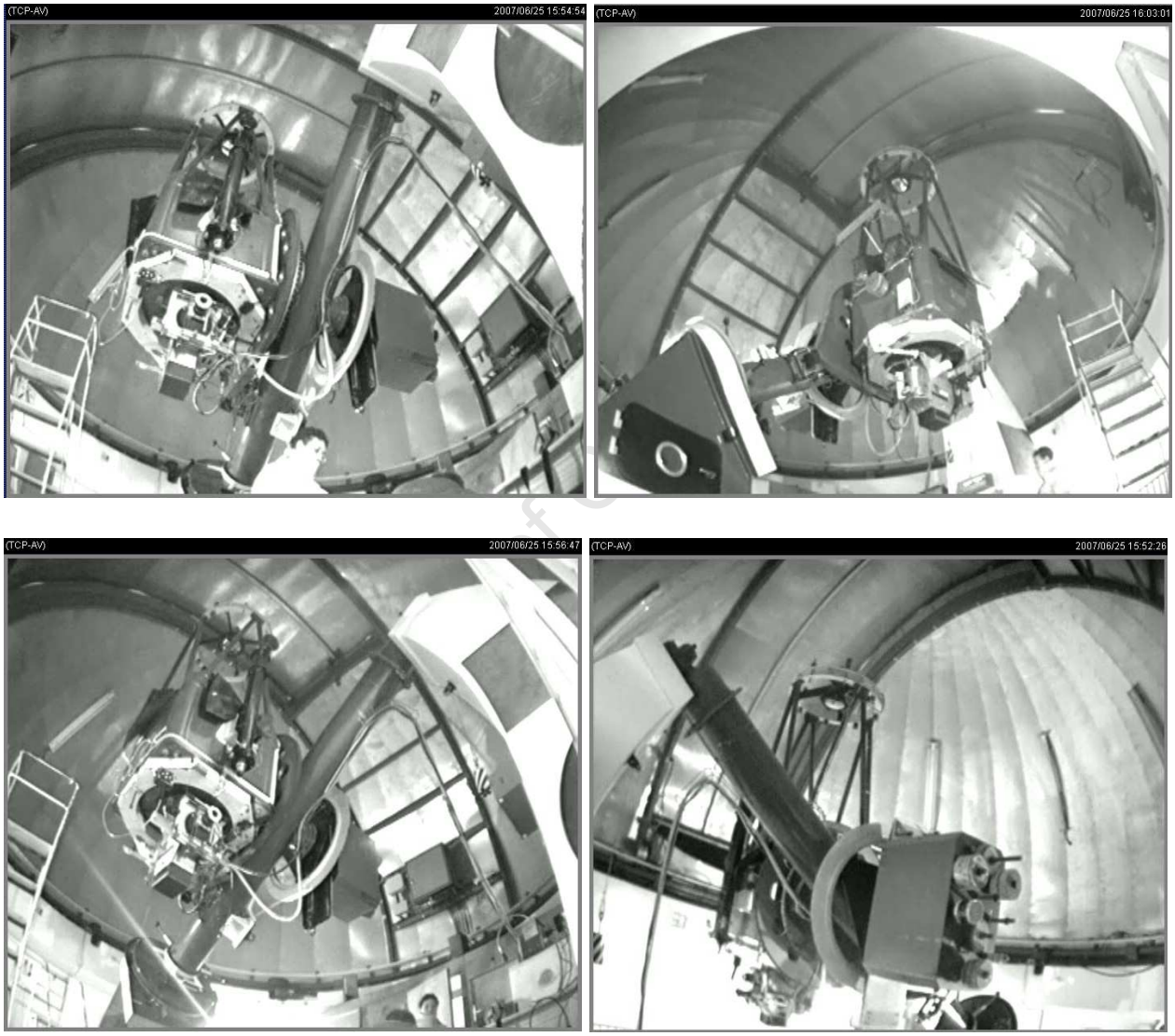

Figure 2.12: Camera view from the base of the pier (top left), camera view from North-West corner of the dome (top right). (Bottom left) View from the railing South-West in the dome, (bottom right), view from top of the warm room roof.

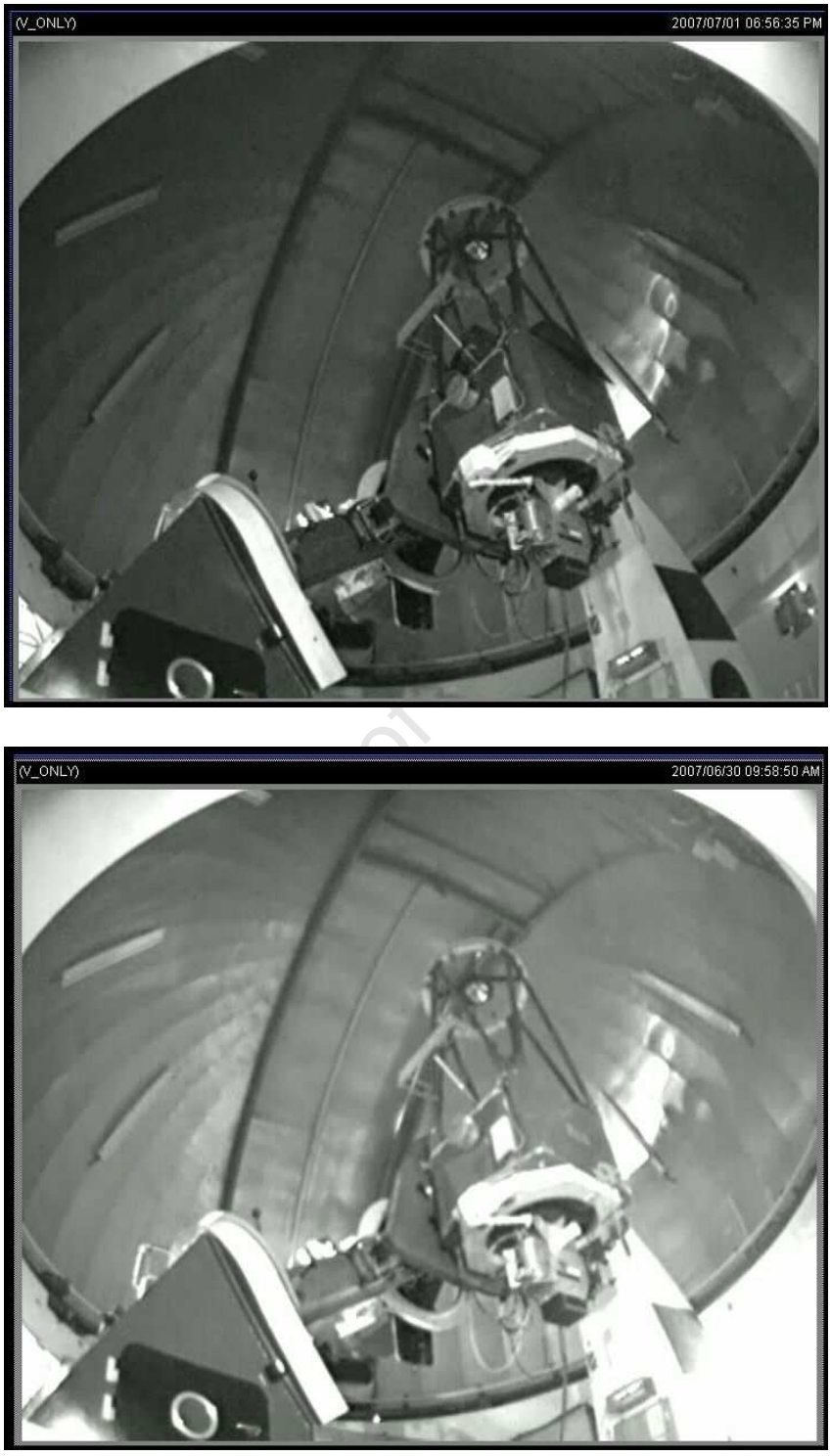

Figure 2.13: (Top) View inside the dome in red light conditions. (Bottom) View inside the dome under fluorescent lights.

telescope tube outlined against the dome slit, would remedy this. The images provided in low level red-light conditions were of good enough quality to be able easily identify all objects in the dome and the frame rate (40 frames/sec) allowed motions of the telescope and dome to be tracked easily. The camera's microphone has been tested but has yet to be installed and enabled. The additional feature of being able to hear the sounds made by the telescope and dome as they slew will provide warning of problems (e.g. sluggish dome rotation) and add a touch of realism to the remote observing experience.

Chapter 3

Testing of Remote Capabilities

It was decided that initial testing of the TCS in remote operation mode would be conducted on-site. The testing would start from within the telescope's dome, in order to identify possible problem areas and to determine a remote viewing procedure, then later from the electronic technicians' offices on the observing plateau within 20 metres of the telescope.

In July 2007 the remote machine, hereafter remote30, was installed in the dome warm room to test control of the TCS. remote30 was able to log onto the TCS machine and launch WinTCS via the Terminal Client Server Remote Desktop application. All motions of the telescope were viewed via a web browser accessing the IP camera. All telescope movements were successfully carried out in this mode of operation. The view of the TCS and the IP camera from the remote machine are shown in Figure 3.1.

Telescope time was booked to test operation of telescope and instrument from a remote machine during $8^{th} - 14^{th}$ of August and 28^{th} November - 4^{th} December 2007. The first remote run to be performed from the Sutherland electronic technicians' offices, was scheduled for the end of the August week. The time leading up to the August run was spent resolving communication problems between the instrument interfaces, debugging the remote software and identifying the cause behind the telescope auto-initalisation problems.

The working version of the remote interface was installed on remote30 and tested within the dome during the second half of the August run.

3.1 Preliminary Testing: Trial run within the dome

In order to demonstrate the feasibility of a remote run, the remote system set-up had first to be operated within the dome and shown to meet with the following basic user requirements:

- Auto-initialisation of the telescope.

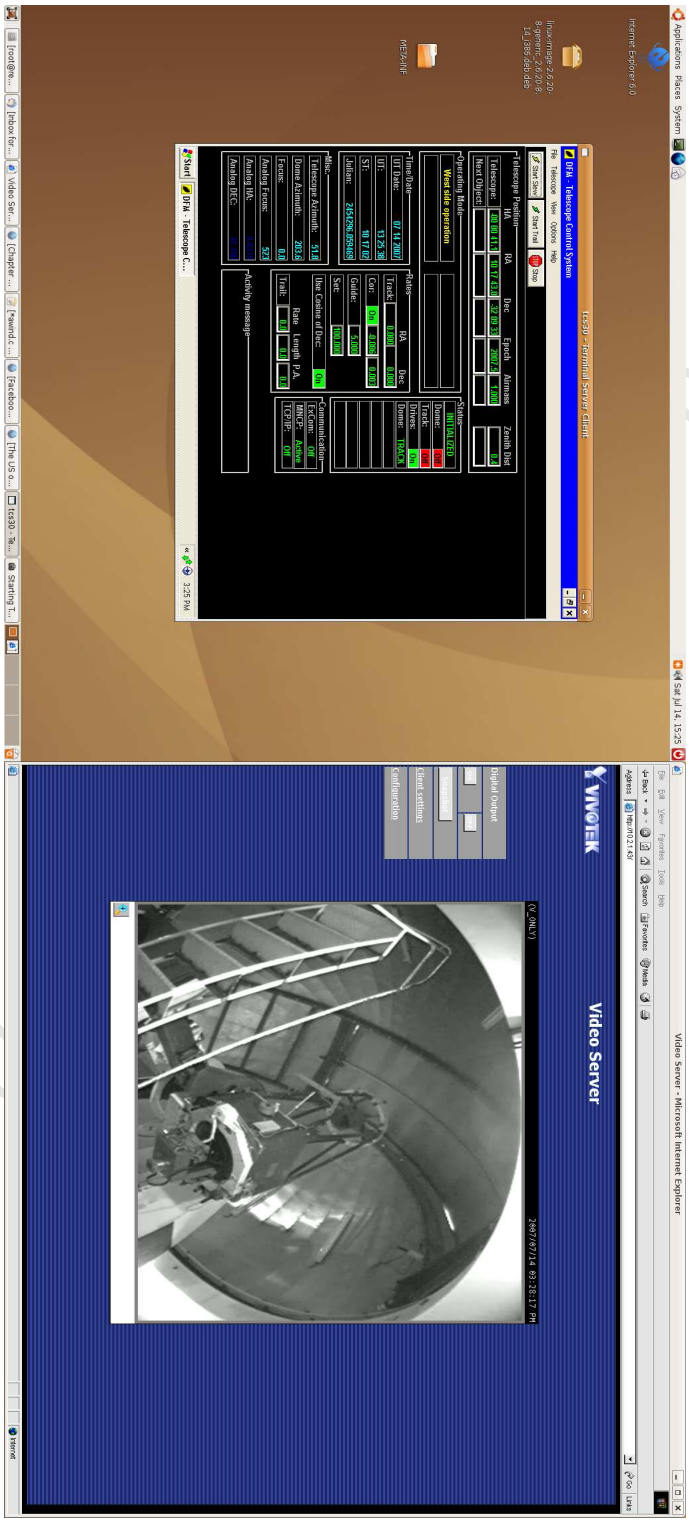

Figure 3.1: Screenshot of the two remote machine monitors displaying the IP camera's view in the dome and the remote terminal shell logged into the TCS machine. The terminal shell is full size.

- Slewing to and acquisition of, a bright star for fine position tuning.
- Slewing to and acquisition of, a focus star for focus tests.
- Slewing to and acquisition of, the target star.
- Commencement and control of data acquisition.

For pointing checks, fine position tuning and acquisition of targets, frequent visual feedback of the telescope position on the sky is desired. On the DOS machine, this is facilitated by a video-viewing mode implemented by `wrmwind` where snapshots of the sky are displayed at user-specified intervals on an RGB monitor. Of course the remote observer will not be able to view this monitor and hence make use of this facility.

Hence a script was developed by SAAO astronomer, John Menzies, for the purpose of viewing images on remote30 in a similar video-mode manner. The script runs the image display program ds9. ds9 is an open source astronomical software program designed to display images in FITS file format. ds9 allows for basic measurements to be made on the image, useful for making focus tests since the remote observer will not have the image diagnostic subroutines provided by the original DOS `wrmwind` at their disposal. ds9 also has the advantage of direct access to the Digital Sky Survey (DSS) server. This means that an image of the field surrounding a target can be recalled from the server and displayed alongside the images being received from the UCT CCD to facilitate easier identification of targets. This is illustrated in Figure 3.2 which shows a snapshot of one of remote30's monitors during remote testing.

Starting with a user specified frame and run number, the script, called RemdispX, runs through the image files stored on disk and displays them in ds9. This produces a similar effect to viewing the sky fields at the local machine in video mode where continuous snapshots of the sky are taken and read straight to screen. In remote-viewing high-speed photometry mode, the image files take a few seconds to download and stabilise once they have been transferred to the Unix storage machine. Waiting for the images to stabilise while displaying them in sequence means that a backlog of images to be viewed builds up on the remote machine. To prevent this, the script requests that ds9 only display every nth image as specified by the user. This way the user can be assured of viewing the most recent image, necessary for monitoring the tracking of the telescope.

During remote performance tests from within the dome, the remote observation procedure, for both the would-be local assistant and the remote observer, was formulated. This is briefly summarised below:

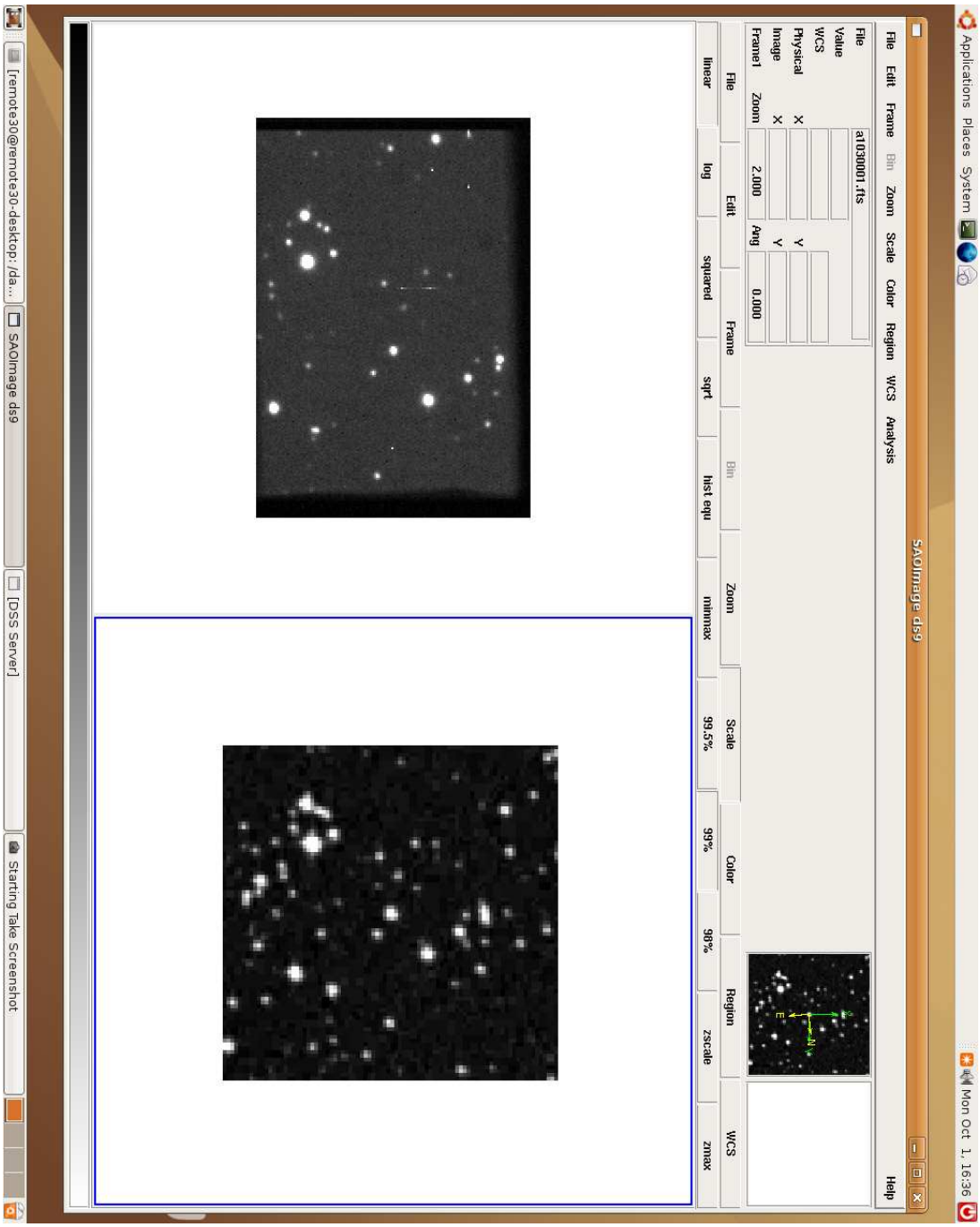

Figure 3.2: The image display program ds9 showing an exposure of OY Car from the UCT CCD (left) and an image of OY Car recalled from the DSS Server (right).

Remote observing procedure for the Sutherland assistant

- **Setting up the Telescope Control System**
  - During the afternoon, test that the rain sensor is working correctly and initiates the automated shut-down procedure once triggered.
  - In the evening, power up the telescope and set all the toggle switches to 'Auto' on the Motor Driver Chassis which controls power to the telescope and dome motors. Set the dome and telescope to track (the telescope will not track unless WinTCS is open).
  - Set all switches on the peripheral systems panel, which controls the lights, dome shutter and mirror cover, to 'Auto'.
  - Check that the TCS CPU time is in time with the Sutherland time server 'stime' (as this is what the TCS uses to calculate UT and sidereal time).
  - Make sure that all users are logged out of the TCS (otherwise the remote user will not be able to log in).
  - The telescope should be parked at the zenith.
  - Finally switch on the camera and IP server and confirm that video images of the dome can be viewed from a web-browser.
- **Setting up the UCT CCD**
  - During the afternoon, check the filter positions within the filter wheel and note them for the remote user.
  - Start up the DOS UCT CCD program `wrmwind`. Make sure that the filter positions as logged by `wrmwind` are correct.
  - Test communications to the filter wheels and camera. Run routine diagnostics on the CCD.
  - At the start of the remote observing run, once the remote user has established control of the telescope and is ready to test communications to the camera, set `wrmwind` running in remote operation mode. Confirm with the user that they are able to communicate with the CCD.

Remote observing procedure for the remote user

- **Setting up the Telescope Control System and Camera**

- Log into remote30 and run the Terminal Server Client application 'Remote Desktop'. Log into the TCS machine and start up WinTCS.
- Check that all the telescope and dome drives are switched on. Switch on the lights.
- Open up a web browser and type in the IP address of the dome camera's IP server. A view of the inside of dome should be displayed.
- Set the telescope to auto-initialise. Open the dome and mirror cover, set the track rate to an appropriate value and slew the telescope to the nearest bright star.
- Start up the local UCT CCD interface, Wrmwind_II. Confirm that both input and output files are available and establish a connection with the UCT CCD.
- Initiate high speed photometry mode so that the images are saved to the remote machine. The CCD parameters should be set to allow the fastest possible readout.
- Set the image recall program RemdispX running on the remote machine. The image frames should start to be recalled and displayed in a ds9 shell.
- Apply telescope offsets until the star is centred on the image and re-initialise the telescope.
- Slew the telescope to an E-region focus star. Use ds9's analysis tools to examine the profile of the target and adjust the focus to obtain the best profile (i.e. the narrowest FWHM for the brightest intensity). The telescope and CCD are now set-up for observations.

On the last two evenings of the 2007 August observing run, the system was scheduled to be tested to perform to meet the basic user requirements as outlined above. On both nights, on-the-fly adjustments were made to the two CCD programs (remote and on-site) to improve interaction between the two, increasing functionality in the case of the remote program. The on-site program had to be modified to allocate memory dynamically for the functions added to enable remote operation. This is because the high rate of access to the memory buffer, required to operate in high speed photometry mode, write screen updates to disk *and* read commands from file proved too much for the DOS machine to execute using pre-runtime static memory allocation.

Finally the system was tested to meet the user's requirements of telescope control and target acquisition satisfactorily.

3.2 Preliminary Testing: Sutherland Electronics Offices

On the last night of the 2007 August observing run the remote machine was moved to the site electronics technicians' offices. During the afternoon the TCS's rain detector system was tested to execute it's emergency shut-down procedure as a precaution (in fact it was discovered that the mirror cover was not programmed to close during automated shut-down, which has since been rectified). In the evening the telescope was setup for remote operation as per the procedure for the local assistant outlined in the previous section. Then the remote user, the author, logged onto the remote machine and executed the procedure for setting up the telescope for remote observations. The remote user was able to initialise the telescope and slew to a selection of targets over the sky. The user was also able to execute a short focus run before bad weather forced the run to be terminated in the early hours of the morning.

Unfortunately, the rise in humidity marked the arrival of one of Sutherland's winter snow storms. Hence a data set of SDSS J0155, the target selected for observation, could not be obtained remotely.

A similar procedure of testing was followed (preliminary testing of the system executed from within the dome followed by testing of the system from the on-site electronics offices) during the 2007 December observing run. During this period new issues regarding the DOS machine's ability to execute in remote mode surfaced. On this occasion it was the runtime memory that struggled to handle the saving of images to disk while performing high speed photometry during remote operation (leading to stalling/crashing of the machine). This indicated that the DOS machine operates near the limits of its capacity in remote operation mode. Again the week leading up to the remote run was spent modifying and testing successive versions of the DOS `wrmwind` program to restrict its memory allocation processes to be as conservative as possible.

After a week plagued by bad weather, remote operation of the telescope and instrument was tested to work to reasonable satisfaction on the very last night of the observing run. After automatically intialising the telescope and focussing the instrument on suitable 9th magnitude stars, the target Z Cha was successfully acquired and observed remotely on the 4th of December 2007. Again, unfortunately, heavy cloud descended just as the target was acquired in the field of view. The light curve is presented in Figure 3.3 (just recognisable as an eclipse curve).

While this particular light curve is unsuitable for scientific analysis, it demonstrates that the capability of making such observations remotely, with-

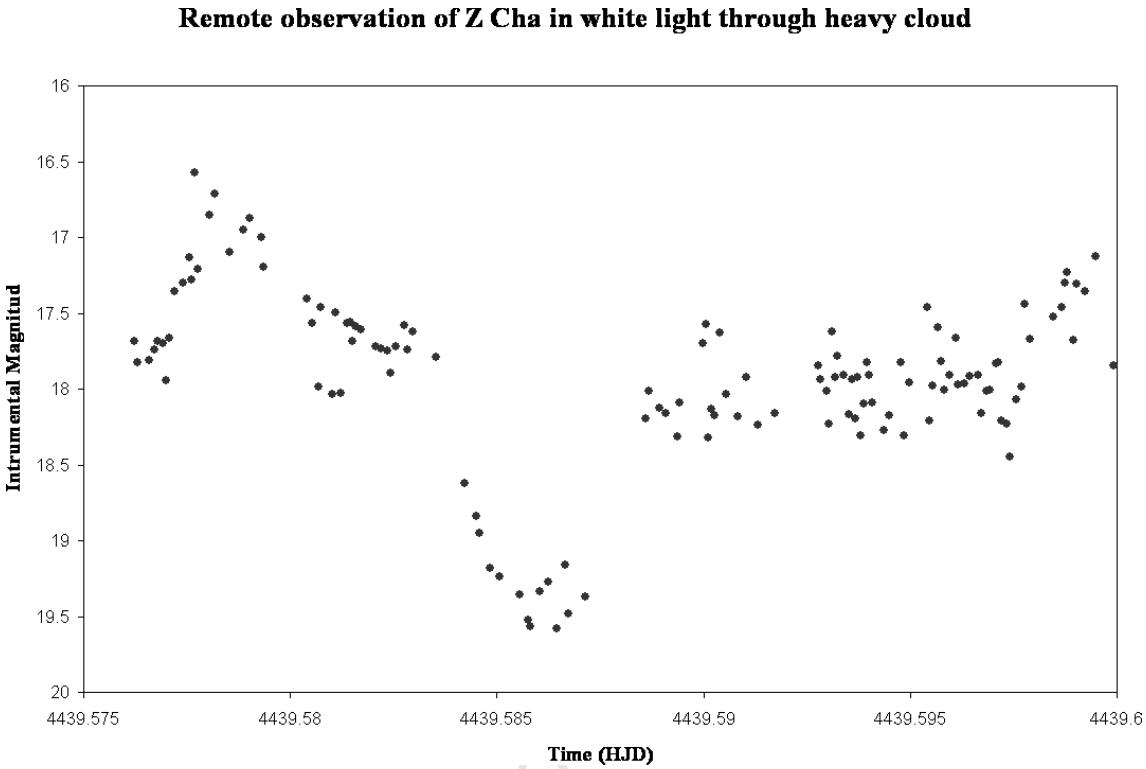

Figure 3.3: Light curve of Z Cha taken remotely on the 4th of December 2007, from the electronic office located on the Sutherland site. The exposures were taken through heavy cloud with no filter and an exposure time of 6 seconds.

out the requirement of the observer being present at the telescope, has been achieved.

3.2.1 Remote System Performance

Comparison to Operational Concepts Definition

Comparing the observing procedures for the local Sutherland assistant and the remote user to the Operational Concepts Definition (section 1.1), we can see that, in practice, the telescope's operational procedure in remote mode closely follows the Operational Concepts Definition. Perhaps the only significant difference is that the local assistant will have to play a more active role than anticipated in the setting up of the telescope and camera for an evening of remote use. This should not pose any great difficulty provided the local assistant is sufficiently trained in the procedure.

Comparison to Functional Performance Requirements

The final assessment of the system's performance lies in determining how well the system met the functional performance requirements. These were outlined in Section 1.1:

- **Pointing and tracking performance**

  As noted in Section 2.4, once initialised, when the telescope was slewed from the zenith to stars between +1 and -4 h in HA and -80 and +20 degrees in Dec, the targets were successfully found to consistently fall within the central half of the field of view. The RMS pointing error within this range was found to be ∼30 arc seconds, just outside of the pointing requirement. A full sky test, slewing from the zenith to targets down to + 4HA, would yield a much greater error. If the poor pointing at high HA is indeed due to a balancing problem, then fine-tuning the pointing model to accommodate this will only degrade the pointing for lower HA. As been described in Section 2.4, poor pointing at high hour angles can best be remedied by successive initalisation on bright stars nearing the target.

  A pointing model could be created to optimise the pointing within the range that the telescope will be most often be slewed to, within the range +1 to -4 HA. This would bring the RMS error within the pointing requirement. However, the extent to which this would make slewing to targets far West of the pier less accurate would have to be determined. It would be unacceptable to require a remote user to have to slew and re-initialise the telescope at more than one or two bright stars each time they wished to acquire a target far West of the pier.

  As in local user mode, tracking adjustments are made through the WinTCS interface, therefore there was no notable change in the tracking performance of the telescope. Minor adjustments to the telescope's track rate had to made every 1-2 hours (depending on the declination of the telescope) as normal.

- **Exposure Time**

  During the remote mode tests it was necessary to recall images as quickly as possible to provide close to real-time feedback of the sky, necessary for checking the pointing of the telescope and running focus tests. As mentioned, continuous image acquisition is facilitated by operating the CCD in high speed photometry mode. This meant that the UCT CCD was operated at short exposures and high binning to reduce readout speed. The system was not tested for exposures > 10 seconds, so how well the system performs at longer integration times has yet to be determined.

From what has been determined for shorter exposures, the system operates optimally at the shortest exposure times allowable for a given pre-binning. This is because the DOS `wrmwind` program can only read commands from the remote machine between exposures; therefore short exposure times mean better responsiveness. The readout speed limits the exposure times for a given binning value; the next exposure cannot be taken while the previous image is being read out. There was a small concern that the extra I/O traffic would mean increased readout time (as the images are being read out straight to disk) so that the minimum integration times for a given binning would increase, but this did not seem to be the case. The system performs to its previous standard of minimum integration times of 2-3 seconds using 3×3 pre-binning, 10 seconds without.

When video-viewing mode is selected on the DOS machine a faster readout speed is used. This produces images of lower quality but good enough for, say, adjusting the pointing of the telescope. Enabling this rapid readout speed to be employed when using high speed photometry during remote runs would allow for faster interaction between the two interfaces.

- **Image Transfer**

  As mentioned above, the image transfer rate was not significantly affected by operating the instrument remotely. However remote operation has only been tested within the Sutherland network; the image transfer rate and subsequent affect on remote performance must be tested across the Sutherland and SAAO networks.

  The main disadvantage to viewing the images remotely is the fact that the FITS files are slow to stabilise once they have been written to the remote DELL machine. This means that after the image file has been written to disk, it takes a few seconds before the DELL operating system recognises there is a new a file to read. The consequences are, depending on the rate at which the user is viewing the images as compared to the rate they are being acquired, after a few hours of observation the user will be in one of two situations: either a backlog of images will have gradually built up, so that the user will only be aware of a change in sky/telescope conditions after a few minutes, or the ds9 script will be in a state of waiting for the next nth image to be transferred with a similar result. Neither situation is ideal and means, effectively, that the user will not have real-time feedback of the sky conditions or of the performance of the optics.

  There is no straightforward remedy to this. At present it seems the problem can best be addressed by acquiring images at the highest acceptable binning, to reduce file

size, and to match, as closely as possible, the rate at which the images are called up by ds9 ('remote-view rate') to the rate at which images are stabilising on the remote machine ('image-capture rate', determined by the size of the file).

In practice this requires that the observer will have to adjust the remote-view rate every 1-2 hours to maintain close to real-time feedback. Since this is roughly the frequency of adjustment made to other control parameters, such as the telescope's track rate, this does not pose an exceptional constraint.

- **Focus Control**

  The focus control is not as sensitive when actuated through the WinTCS interface as opposed to through the 'handpaddle' consoles in the dome; a large offset to the focus position is needed to change the displayed readout from the A to D converter. This makes adjusting the focus fiddly to get correct, and it is estimated that the uncertainty in focus position can make a difference of ∼5%. This could be formally tested by making observations on a few standard stars over two nights with similar conditions (sky brightness and humidity). In remote operation mode focus adjustments are made hourly using the WinTCS interface, in local user mode the adjustments are made using the handpaddles. In both cases measurements are made using ds9 analysis software. Plotting the measured FWHM of the profiles for different seeing would reveal any significant difference in the two methods of focus adjustments.

  However, this uncertainty in focus should not significantly affect observations of faint stars taken with the camera operating with binned pixels. In addition, performing differential photometry (even if the focus may not be strictly uniform over the field) helps reduce the effects of slight de-focussing. Since these are the conditions under which the telescope will be expected to operate in remote operation mode, the focus performance proves satisfactory for requirements.

- **The Control Software**

  It was determined during the remote access runs initiated in the dome and from the Sutherland electronic technicians' office that the TCS system, WinTCS, combined with the Terminal Server Client 'Remote Desktop' interface, enabled complete remote control of the telescope and its peripherals with no compromise on the TCS's local performance. The TCS system can be accessed from any workstation which implements 'Remote Desktop' and is given permissions to access other workstations within the Sutherland/SAAO firewall.

  The remote instrument interface was designed to implement only the basic commands

necessary for high speed photometry. In this respect the interface allows full control of the key functions necessary for image acquisition from the camera. The remote performance was only limited by the speed at which the local DOS machine can read commands and transfer images.

The fact that the remote interface is a 'client-side' application reduces its ease of portability. Any workstations wishing to implement it would have to be able to install and run the Java Runtime Environment (version 1.5.0 minimum). At present the interface has yet to be tested on a non-Unix platform and needs to be packaged into an easy to extract-and-install executable file. It may be desirable to upgrade the existing local data storage workstation (within the warm room) to meet these requirements and have this local machine run the Java instrument interface. Then remote users could access this machine from any workstation in much the same way as the TCS machine. This way only one machine need have to run the program in a consistent manner and the 'Remote Desktop' client would be left the task of handling the display and interaction between the remote workstation and the local one. However 'Remote Desktop' does not allow a full screen view of the desktop being remotely accessed to be seen (as can be seen from Figure 3.3). This means that the images recalled and displayed on the local machine (which is mounted onto the DOS drives as the data storage machine) by the script RemdispX would not be easily seen. The relative advantages of portability versus ease of remote operation will have to be assessed.

3.3 Formal Testing: Testing from SAAO Cape Town

The remote performance of the system was scheduled to be tested from the SAAO head offices in Cape Town during 2008. Before this could be achieved further tests were made from the Sutherland site in order to determine any modifications to the instrument interface or user procedure to optimise control. In addition, training runs with the on-site assistants were needed in order to familiarise the local assistants with the set-up procedure and obtain their input. Unfortunately, remote observing attempts in 2008 and 2009 showed that the UCT CCD's PC and control software proved inadequate for the task for the following reasons:

- As a 486 machine, the processor was simply too slow to handle instrument control, status feedback, CCD readout, and network data transfers in the time available for the execution of these tasks (namely, the image integration time).

- The instrument control software uses a complex scheme for memory management (due to the 640 Kb limit of DOS). This scheme was not reliable in the current application.

Fixing these problems would have necessitated a revamp of both instrument P.C. and software which was beyond the scope of this thesis project. Thus, full commissioning of remote operation was not possible.

In Section 3.4, the overall ease of using this arrangement to acquire data remotely will be discussed, as well as the feasibility of getting the system fully commissioned.

3.4 Project Summary and Further Recommendations

3.4.1 Project Summary and Current Status

Project Summary

This project documented the modification and refurbishment of the SAAO's 0.75m telescope's TCS and instrument (UCT CCD) control system to facilitate remote operation over the internet with limited on site assistance. There were two main motivations for the initiation of this project: First, remote operation is an intermediate step towards the ultimate goal of complete automation of the 0.75m which forms part of the SAAO's ongoing efforts to reduce the personnel resources spent on the management of the smaller telescopes. Second, remote capability facilitates the more efficient operation of stellar variability studies which meet the following criteria: (i) CCD photometry is required, (ii) only a few observations per night, week or quarter are needed and (iii) with repetition over a long period of time.

In the next section the outcomes of the project are summarised, the system's performance is compared to the original project requirements and, finally, recommendations are made for the future of the project, to address issues that arose during the testing phase.

Review of Project Outcomes

The outcomes achieved during the course of this project can be summarised as follows:

1. The upgrade of the 0.75m's previous DOS-based TCS to a Windows^{TM}-based TCS allowed for straightforward remote access to the telescope control system.

2. The installation of a new position encoding system has enabled self-automated intialisation of the telescope. This is useful in local on-site observing mode, should the telescope lose pointing during observations, and is essential for remote observing.

3. The addition of a PLC to manage the telescope peripheral subsystem allowed for:

   - PC control of the dome shutter, lights and mirror cover,
   - safeguarding of the peripheral subsystem from behaving unpredictably following power outages or TCS failure,
   - the addition of a rain sensor to initiate an emergency shut down procedure on detection of rain.

The last two features provide extra safeguards against the risk of damage to the telescope when used in local observing mode, and are absolutely essential for use of the telescope in remote observing mode.

4. The development of a Java-programmed user interface allowed remote control of the UCT CCD control PC and demonstrated the possibility of running command driven DOS programs remotely.

5. The remote acquisition of first-science observations, which illustrated the typical kind of project that a remote telescope would be best suited to. The results of monitoring the accretion discs in the dwarf novae, presented in Section 5.2.5, produced interesting results which pose new challenges to the currently accepted theory of dwarf nova outbursts. The fact that the scheduling of the observations was so critical to the results presented motivates the need for a remote system to form part of any observatory's suite of research telescopes.

3.4.2 Review of System Performance and Further Recommendations

System Performance

The trial runs made in August 2007-January 2009, which tested the remote operability of the telescope from the Sutherland electronics technicians' office, demonstrated how well the system performed to the user requirements.

Overall the telescope control system does fulfill the user defined requirements and operational concepts definition outlined in Section 1.1. Concerning the performance of the system, some requirements have been compromised in the telescope's pointing performance and the image acquisition from the camera. In the case of the pointing performance, imprecision in the telescope's movement and positioning sub-system leads to a minor compromise in observing efficiency; at high HA, the telescope has to be re-initialised on bright stars within a few hours of the science target before slewing to the target.

In the case of the image acquisition from the camera, real-time visual feedback of the sky is limited by the camera readout speed and how quickly the data storage system can log and display the image. This renders the feedback response to changes in sky conditions or telescope alignment less than ideal, but still tolerable, and still within the limits of concern for telescope safety.

Both of these issues arise from having to adapt existing hardware systems to the more demanding requirements specified by remote operation. Neither issue compromises the

performance of the telescope significantly enough to render this mode of operation too awkward to utilise. The telescope changes were largely successful.

There is, however, a more serious issue which calls into question the robustness of the instrument control system and its suitability to being operated in remote mode. This is the problem of the DOS machine's limited memory capacity which affects its ability to write images and system information to disk in high speed photometry mode while at the same time continually checking for new commands on the disk to read and implement. Both the DOS machine's pre-runtime stack memory and runtime heap memory are heavily accessed and utilised while performing high-speed photometry, even more so if it is in remote mode. In the event of the read/write processes exhausting the memory buffer, the conflict leads to a system crash which can only be resolved via a hard re-boot of the machine (which can only be performed by the on-site assistant). These are obviously an unacceptable operational circumstances. Possible solutions to this problem are proposed in the next section.

Further Recommendations

This final section concludes with a proposed list of further recommendations for the telescope control and the instrument control systems.

Recommended additional features for the telescope control, sensory feedback and peripheral systems

The TCS, sensory feedback and peripherals subsystem could benefit from the following additional features to improve functionality, ease-of-use and safeguarding of the system:

- Increased weather sensing functionality
  - Ideally the 0.75m should be fitted with a complete weather detection system. This would include a wind sensor and a cloud/humidity sensory system, with feedback control to enable automatic shutdown for wind speeds > 60km/hr or humidity levels above $\sim 85\%$. Such a weather detection system is already employed by the planetary detection program SuperWASP, which sites its automatic robotic telescope SuperWASP-South on the Sutherland observing plateau just 20 metres from the 0.75m dome. As the 0.75m remote observing procedure currently stands, the remote user is directed to the SuperWASP weather station's website to monitor wind speeds and humidity levels. The possibility has been suggested that the command for shut-down initiated by SuperWASP's weather

sensors could also be directed to the 0.75m PLC peripheral subsystem to initiate emergency shut-down. This possibility should be investigated as a solution as it would prove more practical and, possibly easier to implement, than assembling and integrating additional wind and humidity sensors into the existing system.

- Remote switching of telescope power
  - The present TCS arrangement does not allow for the remote user to switch the power to the dome and telescope motors off at the end of their remote run. Adding this functionality would simply act as an extra precaution against the dangers of having the telescope motors powered when there is no-one present in the dome (as the on-site assistant will not be able to check the status of the telescope until later the next morning) e.g. the telescope continuing to track if the remote user should fail to turn off the tracking before logging out (although, as mentioned previously there are mechanical limits on the telescope to prevent the telescope from being driven too far over), or an electrical fault presenting a fire hazard.
- Improved focus control
  - As briefly mentioned in Chapter 3, the user does not have accurate focus control (to within $\sim 5\%$ of optimum focus) when focus adjustments are actuated through the WinTCS interface (as they must be in remote observing mode). Further consultation must be made with the SAAO electronics department to ascertain the exact cause of this, but it is felt that the reason could be that WinTCS is having to actuate a motor to adjust the focus with an LVDT as feedback. The A/D conversion is an imprecise measure of the focus. In that case the best solution would be to replace the LVDT with a focus encoder.
- Independent movement of the dome
  - In certain parts of the sky, the dome tracking and movement is not perfect and on rare occasions the dome can obscure a small fraction of the mirror for a few minutes before it is given the instruction from the WinTCS to move over. If the telescope is at very low Dec, WinTCS can fail to move the dome to the correct position altogether. Unfortunately the effect is not constant at all angles or positions of the telescope and the problem is not due to a constant dome offset. On these occasions, in local observing mode, it is possible to switch off power to the dome, move it manually using a handpaddle and then re-initialise the dome

to its new position before switching its power back on. However it is not possible to move the dome position (independent of the telescope) in remote observing mode. This can only be made possible with the addition of a fiducial position encoder assembly for the dome. The design and acquisition of such an assembly, and subsequent modification to the TCS software, would have to be negotiated with DFM.

- Addition of an extra IP camera to monitor dome shutter/telescope alignment
  - The currently installed IP camera allows a remote user to determine if the telescope is moving, if the dome is tracking it, if there are any obstacles in the way of the slewing telescope and if the lights are on. However, it is not easy to determine from the perspective view presented by the camera, whether the telescope is perfectly aligned with the centre of the dome shutter. Therefore the installation of a second IP camera is recommended, situated either on the telescope truss or just to the side of the dome shutter, which would enable the remote user to determine whether the dome shutter is aligned with the telescope.
- Remote auto-guiding capabilities to facilitate long integration times
  - As previously noted in Chapter 3, the remote user has to make regular adjustments to the tracking speed to maintain the targets at roughly the same positions on the CCD. This is unsatisfactory for observations which require long integration times (of say 200 seconds or more). If the 0.75m will eventually be expected to accommodate science applications which require long exposures then this will necessitate the acquisition of an auto-guider system which could be remotely accessed.

    One suggestion for addressing this issue may be to install a relatively inexpensive amateur-market telescope on the existing finder-scope. The most straightforward procedure would be for this guide camera to issue pointing tweak-ups to the TCS's existing handpaddle-guiding inputs. With existing dense star catalogues such as UCAC-3, the guide-telescope could even be used to auto-find target fields.

Two solutions for the improved control of the instrument

The problem of the instrument remote control reliability (stemming from the current configuration's limited speed and memory capacity, briefly mentioned at the beginning

of this chapter), can be solved either by upgrading the current PC from a DOS 486 to a DOS 686 and/or streamlining the current memory allocation setup, or simply replacing the existing CCD instrument. Both solutions (and the steps required for implementing each one) are discussed below.

1. Stream-lining of the instrument control program and DOS memory allocation

   - During the August and November 2007 observing runs, only the subroutines relating to the execution of high speed photometry and reading/writing remote commands were analysed and streamlined for improved memory allocation. This significantly improved the reliability of the DOS machine's performance but it was still prone to crashing during the remote tests. If the current method of remote access to the control PC is to be maintained, then the efficiency of the control program's memory allocation (and perhaps the DOS machine's management of memory in general) will have to be further improved, as recommended below:
     - The rest of the subroutines used by the instrument control software `wrmwind` should be streamlined to use dynamic, instead of static, memory allocation wherever possible.
     - The investigation into the possibility of acquiring a compatible expanded memory expansion card or, alternatively, installation of a memory manager such as QEMM (Quarterdeck Expanded Memory Manager by Quarterdeck Office Systems), which enables DOS programs which require a lot of conventional memory to be loaded into the upper memory blocks of the PC memory's architecture (see web references Fuchs 2001 and Tzen 1998).
     - Testing the results of replacing the existing DOS 486 control PC with a 686 in order to expand the available memory plus (moderately) extend the capability for memory expansion cards.
     - Investigation into the possibility of rebooting the DOS machine remotely in the event of a system crash. Consultations with the SAAO's Head of IT Division suggest that this may be possible.
     - Modifications should be made to the remote Java interface and to the DOS machine's local program `wrmwind` to enable, after a system re-boot in the event of a crash, the two software interfaces to return to common parameter state.

2. Acquisition of a new CCD instrument

- This is the straightforward solution to the problem of reliably controlling the remote instrument PC. However it is by far the most expensive. This is because the EISA expansion cards which are supplied with the CCD camera and which interface between the DOS machine and the instrument controllers are only compatible with a DOS machine's computer bus. Hence they cannot be inserted into a 5^{th} generation (Pentium and above) processor which would run a Linux or Windows^{TM}operating system. Acquiring or designing and programming interface cards that would be compatible with Pentium processors would be near impossible, therefore the only option would be to obtain a new CCD instrument, complete with controllers and interface cards. In addition to the expense of acquiring the CCD camera itself, there would be the added effort of having to program a suitable user interface to communicate with the PCI cards, unless the camera came replete with the necessary software, in which case this would significantly add to the cost of purchasing a new system. The advantages to purchasing a new system, however, would be:
  - The observer would have easy, direct remote access to the new instrument PC and control software using the same Remote Desktop software that is currently used to access the TCS PC. This would improve the response of the remote interaction as there would be no lag time spent waiting for the PC to process the previous command before being able to read and implement the next.
  - There would be no need for the on-site assistant to start up the instrument control program and test the state of the CCD camera before a remote run as the remote observer would be able to do this.
  - The system could be trusted to be generally reliable as the new PC would not be running at the limits of it capability. In addition, image frames could be saved to the local PC, saving bandwidth and, possibly, network lag. The most recent sky image could be viewed remotely on the local (on-site) desktop, possibly as an integrated feature of the instrument control software, without the need to run a separate image viewing program such as ds9, and the data could be retrieved after the high speed photometry run was complete.
  - A new instrument PC, and hence the capability for new high performance software, would offer the prospect of integrating a remotely operable auto-guiding system for long exposures.

– The new PC would also offer the possibility of users outside the SAAO network of being able to access the telescope and instrument. Users outside of the network could be allocated a random login name and password and granted temporary access to the network and use of the telescope. This would provide a valuable cost-saving resource to foreign astronomers, who would have the opportunity to run the telescope from their own country, possibly during office hours. In addition, outside access could open up the 0.75m telescope to be offered as an educational resource to local schools who do not have the financial support to be able to send students to Sutherland and see a working research telescope in action.

If the recommendations put forward by the first solution successively address and resolve the problem of the instrument performing reliably in remote mode, then option one will provide a satisfactory short-term solution to the project of remote operation. However, as a long term solution, the first option is not ideal; investigations should be made into the acquisition of a new instrument system, particularly if complete automation is the end-goal of the project. Moreover, maintenance of the DOS based system is questionable. As previously mentioned, Micro Soft™ has stopped producing DOS, considering the operating system now to be obsolete. The SAAO's Automatic Photometric Telescope has already been shutdown for refurbishment after its DOS telescope and instrument control systems finally collapsed. The re-development of DOS based control systems is simply no longer viable

Future projects planned by the SAAO offer the promise that the second solution could be feasibly implemented within the next couple of years. The SAAO currently has one CCD47-20 (1024×1024 pixel) chip in its possession which is waiting to be built into a Peltier-cooled camera system. A working camera could be available by April 2011, following a collaboration between the SAAO and the National Astronomical Observatory of Japan which will see the delivery of a Peltier camera developed by RAL (Rutherford Appelton Laboratory) complete with SDSU[1] software and controller. This CCD-camera system is intended for use on the Radcliffe 1.9m telescope. However, it will serve as a model for the Peltier-cooled system that the SAAO technical staff will design and build for the CCD47-20 chip. This second CCD-camera system will be available for use on the smaller telescopes. The instrument control software for the cameras has yet to be programmed so additional features needed to optimise remote use could easily be added in the design process. In addition, as of November 2010, an unexpected boost to the financial resources

[1] Named after their origins at San Diego State University.

available to the SAAO's instrumentation department, offers the exciting prospect of two additions to the complement of existing imaging cameras in the form of off-the shelf purchases. One is an Andor EMCCD, optimised for high speed photometric studies, the other an Andor DW 436, offered by Keele University's SuperWASP exo-planet team, the latter with the view to using the 0.75m as a remote follow-up photometry telescope. Upgrades and additions to the suite of 0.75m accessories include an Apogee aquisition camera, a new filter system and an SBIG tip/tilt adaptive optics system.

This is an ideal situation which could see the exciting prospect of having a reliable, remotely-operable instrument, form part of the SAAO's ensemble of research telescopes in the near future.

Part II

Testing Accretion Theory using Variability of Dwarf Novae Accretion Features

Chapter 4

Introduction

Many of the well-established small telescopes still currently in operation such as the 0.75m reflector, the key tool of the previous investigation, were built during an era in the last century where the science demanded of them was broad in scope and foundational in principle. As a consequence they were general-purpose-built, with comparatively less demands made on their performance, scope and, therefore, specifications. In contrast to this tradition of general-purpose built telescopes which serve a broad range of scientific concerns, modern astronomical technology is increasingly targeted at solving specific astronomical problems. The telescopes are designed around acquiring data sets which will address specific unsolved questions. Science instruments are matched to the design constraints of the telescope in order to take best of advantage of its observational niche. These niches include (among others): high-speed (up to 10 Hz) time resolved imaging photometry, polarimetry, spectroscopy and spectropolarimetry. In particular, 10-m class telescopes such as SALT, with high time resolution sampling capability, allow the time-domain equivalent of high resolution spectroscopy.

Stellar variability studies (particularly those associated with high-energy processes) are fields in which high time resolution is opening up a new dimension of astrophysics to scrutiny. On the other hand, monitoring of longer baseline variations continues to throw up new challenges to established stellar models. One of the specialised stellar-variability fields which makes the most of observations at both ends of the temporal scale is the study of cataclysmic variable stars (CVs). Thus the next part of this thesis reports on science questions addressed by the availability of the facilities at the SAAO which can exploit this aspect of CVs.

As the term implies, cataclysmic variables make up some of the most highly variable objects in the sky. Their variability and unpredictability has attracted attention from many astronomers, amateur and professional alike. This is because detailed study, using even a comparatively short number of observations, reveals a wealth of information

which can have application to a diverse range of fields; from the study of X-ray binaries (XRBs) and star formation, to the processes which power some of the brightest objects in the universe: active galactic nuclei (AGNs). The reason for this is that the study of cataclysmic variables is essentially the study of accretion – the process by which matter is transferred onto the surface of a star from the surrounding environment. This process is responsible for the highly variable brightness fluctuations observed in CVs which make up their defining characteristics. Variations occur on time scales from seconds to decades and even longer. Thus, unlike XRBs or AGNs, these timescales are easily accessible to study.

Many of the key questions in the astrophysics of these binaries requires investigation of the long term behaviour, i.e. over hundreds or thousands of orbital cycles. As discussed in Chapter 1, the on-going monitoring campaigns conducted on small telescopes (now increasingly conducted in remote or fully automated mode, see Section 1.1.4) still offer meaningful contributions to long-term behavioural studies where the characteristics in question are observed in relatively bright systems. Thus, one of the studies presented in this work reports on a 2005-2008 observing campaign, conducted on the SAAO's 0.75m telescope, following two examples of a particular class of CVs. These systems (termed 'SU UMa' stars) exhibit long-baseline variational behaviour – repetitive on a period of $\sim$ hundreds of days – which provide invaluable insights into the accretion mechanism. Further motivation for this study, the data acquisition, analysis and final results are all given in Chapter 5.

At the other end of the temporal scale, the second investigation presented here reports on an observing campaign which exploited the high-time resolution capability of SALT's imaging camera, SALTICAM. The camera, operated in its fastest photometry mode, allows probing of the nature of the central source in an SU UMa-type CV system with unprecedented signal-to-noise. The data, their analysis – using the latest 1-dimensional-data statistical techniques – and results are presented in Chapter 6.

The outcome of both investigations provide fresh challenges to the present understanding of SU UMa-type stars and prompt a review of some of the fundmental theories of these systems.

4.1 Overview of Cataclysmic Variables

4.1.1 Introduction to Cataclysmic Variables

The shape of the stars in a close binary is key to understanding them. They can be described by a series of nested volumes whose surfaces define loci of equal effective potential. These pseudo-potentials are approximations to gravitational equipotentials which include centrifugal terms (Chanan *et al.* 1976). These surfaces are known as Roche equipotentials (Kopal 1959). Matter within a particular equipotential, centred on the centre of mass of a component star, is gravitationally bound to that star. The largest closed equipotential which contains the mass of a star is known as its Roche lobe and defines the upper limiting volume that each star can occupy. The apex of this surface is called the inner Lagrangian point which lies on the line of centres between the two stars. A more detailed description of Roche lobe geometry is given in Section 5.3. Semi-detached binaries are close binary stars where one component fills its Roche lobe while the other lies within its Roche lobe. Figure 4.1 shows a sketch of the Roche equipotentials in a semi-detached binary.

Cataclysmic variables (CVs) are semi-detached binaries comprising a white dwarf primary and a Roche-lobe filling evolved secondary. Most often the secondary is an M dwarf but in rare cases may be G or K main sequence stars or a helium-rich, low mass white dwarf (a class of objects known as AM CVn stars). Close cousins include systems with a neutron star primary (the Low Mass X-Ray Binaries) or a giant secondary (symbiotic stars).

In CVs, matter is transferred from the secondary to the primary through the inner Lagrangian point, L_1 in a process known as accretion. Their orbital periods are short, in the range 1-13 hours for hydrogen-rich systems, and the energy liberated through accretion is at least equal to, and usually dominates, the intrinsic luminosity of the component stars. Figure 4.2 is an artist's illustration of a typical CV.

If they have large inclination, i, the eclipses in their light curves are unequivocal evidence of their binary nature. As a result, the orbital period is usually the most precisely known parameter of a CV, especially if it is an eclipsing system. Eclipsing systems are particularly valuable because analysis of the eclipse can reveal the physical features of the system, providing estimates of the vital statistics of the binary such as the orbital separation, orbital inclination, presence of an accretion disc, rate of mass transfer and the relative masses of the components. Analysis of the light curve can also reveal features that give insight into the physics of the system such as the rotation of the primary, the presence of magnetic fields and the origins of rapid brightness variations such as dwarf

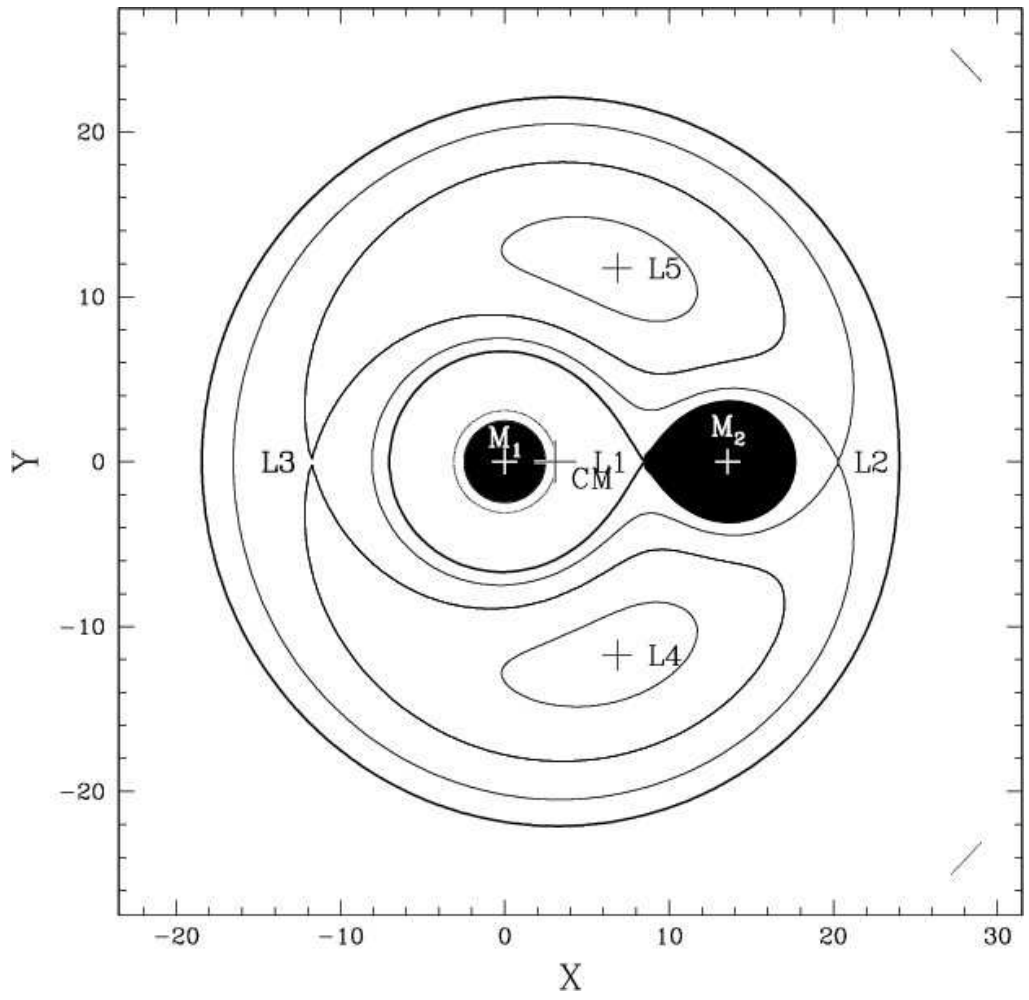

Figure 4.1: Roche equipotentials for a semi-detached system (cross-section in the orbital plane). Contour lines join points of equal potential. M_1, M_2 denote the masses of the primary and secondary respectively and CM is the binary's centre of mass. L_{1-5} are the Lagrangian points, where L_1 joins the lobes of the critical equipotential, outside of which matter is disassociated from either of the masses, known as the Roche lobes. Note that M_2 fills its Roche lobe but M_1 does not, thus L_1 is also the point through which matter leaves the Roche lobe of the secondary and enters the primary's Roche lobe, see Section 5.3 for further details.

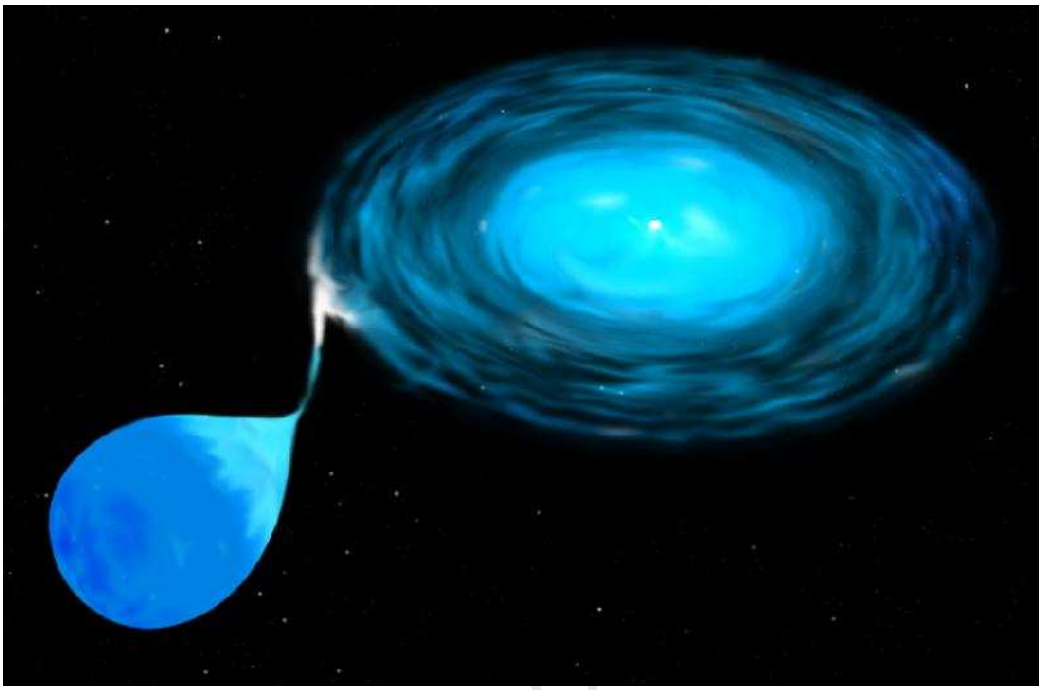

Figure 4.2: Artist's impression of a cataclysmic variable (courtesy of NASA/JPL-Caltech).

nova oscillations (DNOs).

4.1.2 Formation and Evolution of Cataclysmic Variables

The evolution of CVs, during and post their formation phases, has minimal relevance to the work presented here but, because of its importance to the formation of all sorts of ultra-compact binaries and for identifying supernova type Ia progenitors, the field is currently a hot topic in CV astrophysics. A brief, qualitative description of CV formation and evolution is presented here but for a more detailed summary, see Ritter (2008) and the comprehensive reference list supplied therein.

CVs originate from detached binary systems with initial periods of hundreds of days. The more massive companion evolves more rapidly, its main sequence lifetime $\propto 1/M^{2.5}$ (where M is its mass). Once the more massive star has exhausted its hydrogen supply in the core, it expands to become a red giant until it begins to overflow its Roche lobe. The tenuous outer layers of the red giant transfer to the less massive companion through the L_1 point. This mass flow occurs away from the centre of mass therefore, to conserve angular momentum, the orbital separation decreases slightly. This in turn decreases the size of the primary's Roche lobe so that a positive feedback loop of rapid mass transfer is

created and runaway mass transfer takes place. This results in the entire envelope of the more massive star being lost to the binary on the timescale of just a few years (Paczyński & Sienkiewicz 1972, Taam & Sandquist 2000).

Meanwhile, the less massive companion is unable to accommodate the sudden influx of material which forms a "fluffy" common envelope around both stars. The resulting drag from the envelope acting on the binary drains angular momentum from the binary, causing the orbital separation to decrease from ~ 100 $R_\odot$ to $\sim 1R_\odot$ in the order of 10^3 years (Hellier 2001, Ritter 2008). The angular momentum is taken up by the common envelope which is completely expelled from the system leaving an exposed white dwarf and its companion.

At this stage the binary is detached. To form a CV from this system, the orbital separation must decrease, which implies the loss of angular momentum. The mechanism for this angular momentum loss is believed to be 'magnetic braking', described further below. This 'pre-CV' phase terminates when the secondary comes into contact with its Roche lobe and mass transfer, now *from* the secondary *to* the primary, commences.

To detect cataclysmic variables in significant numbers, sustainable mass transfer from the lower mass secondary to the primary is required. Mass transfer from the secondary to the primary, towards the centre of mass, results in a loss of angular momentum, causing the orbital separation to increase slightly to compensate. This should halt further mass loss for $q \leq 5/6$ (Warner 1995), where q is the mass ratio defined as $q = M_2/M_1$, the relative masses of the primary (M_1) and secondary (M_2). Yet steady mass transfer is observed in lower q systems suggesting that either mass and/or angular momentum cannot be conserved in these systems. The rate of mass transfer through stellar winds from the secondary is not sufficient to account for the observed rate of mass transfer; there has to be a mechanism for removing angular momentum from the system altogether. The standard paradigm is that there are two main mechanisms which can achieve this: gravitational radiation and magnetic braking.

Magnetic braking is thought to be the primary method of angular momentum removal for pre-CVs and CVs with periods greater than 3 hr. The concept of magnetic braking relies on the combination of the secondary star's stellar wind and its weak magnetic field. Since the charged particles of the stellar wind are forced to travel along the red dwarf's field lines, they are forced to corotate with the red dwarf out to a considerable distance, thereby taking a substantial amount of the angular momentum of the red dwarf with them. The synchronous rotation of the red dwarf means that ultimately, the angular momentum is supplied by the orbital motion thus shrinking the orbital separation (Meyer & Meyer-Hofmeister 1979, Spruit & Ritter 1983, Andronov *et al.* 2003). Mag-

netic braking is thought to be an effective means of draining angular momentum from the system as red dwarfs in CV systems are thought to be highly chromospherically active.

At orbital periods of ∼3 hr magnetic braking is disrupted/switches off and halts mass transfer (for reasons which still remain the topic of intense research – see below). The CV remains faint and detached until it has evolved, via gravitational radiation, down to an orbital period of ∼2 hour after which contact is re-initiated and mass transfer can resume. Gravitational radiation is the dissipation of energy from a binary system caused by the two masses periodically warping space-time as they orbit each other. Gravitational radiation becomes significant for binary systems which have either very high masses, such as X-ray binaries, or very short orbital periods. The latter applies to CVs below the 2-3 hour period range such as Z Chameleontis (Z Cha) and OY Carinae (OY Car), the systems under investigation in this thesis. For CVs with orbital periods shorter than 2 hours, it is thought that the primary mechanism for angular momentum removal is gravitational radiation. Gravitational radiation continues to drive angular momentum loss of the binary, and mass loss of the secondary, until hydrogen-burning is terminated in the secondary. The secondary is termed a brown dwarf from here on. The binary period shortens until the secondary becomes fully degenerate. At this stage further mass loss from the degenerate secondary causes expansion of the binary separation and a period minimum is reached from where the binary is expected to evolve towards longer periods, a feature known as the *period bounce*. Though highly evolved CV systems longward of the period minimum should make up the vast majority of all CVs, the very low accretion rates present in these systems make them faint and very difficult to detect. However, notable recent results from the Sloan Digital Sky Survey (SDSS, Szkody *et al.* 2009) – which presents the most unbiased sample of CVs to date due to its unprecedented deep-sky, multi-colour and spectroscopic coverage (Gänsicke 2005) – has resolved the expected accumulation of faint, short period systems near the period minimum known as the 'period spike' (Gänsicke *et al.* 2009) and revealed the possible detection of the elusive post-minimum population (Littlefair *et al.* 2008).

Disrupted magnetic braking is the standard explanation for the reduction in numbers of non-magnetic systems observed within this 2-3 hour range, otherwise known as the period gap (Howell *et al.* 2001 and references therein). However details of the mechanism are unclear, with current prescriptions predicting the efficiency of the angular momentum loss differing by up to 4 orders of magnitude (Schreiber *et al.* 2010). Neither is the origin of the magnetic braking cut-off at ∼3 hr well understood (Ritter 2009 and references

therein). For primaries with large magnetic fields ($\sim 10^7 - 10^8$G), computational analysis shows that the combined field structure of the binary prevents any outflow of wind from the system (Li, Wu & Wickramashinge 1994, Zhang *et al.* 2009). Thus the magnetic braking model does not apply and there is no period gap seen in such systems (known as "polars"); all of the mass transfer is driven by gravitational radiation, as the observed mass transfer rates observed in polars confirm (Warner 1995, Tovmassian *et al.* 2004).

Progress in the study of CV evolution critically depends on the accurate determination of the component masses of a large number of compact binaries which, in turn, depends on the accurate determination of binary mass ratios and component radii. Photometric techniques using eclipsing systems for the determination of these parameters shall be investigated as part of the studies presented in the coming chapters.

4.1.3 Matter Transfer in Non-Magnetic Systems

In non-magnetic systems (where the white dwarf's magnetic field $\leq 10^5$ Gauss) the movement of gas from the secondary to the primary is determined predominately by dynamical and hydrodynamical flows. From the inner Lagrangian point, pushed by the pressure of the secondary's atmosphere where the speed of sound in the gas is $\sim$ 10 km s^{-1}, the particles proceed on a free-fall trajectory towards the primary. The inner Lagrangian point is also orbiting the primary, so this additional orbital angular momentum causes the stream of particles to swing into orbit around the primary instead of falling directly towards it. At this point the particles reach supersonic speeds and the stream expands. Pressure forces then become negligible so the stream can be modeled as the trajectories of individual particles. When the stream swings around the primary, it begins to climb out of the primary's gravitational well towards the perimeter of the Roche lobe. The Roche lobes can be considered to be zero velocity surfaces. The particles therefore reach zero velocity and fall back towards the primary, looping back to cross the stream's earlier path. The resulting turbulent shocks dissipate energy and the material settles into the lowest energy state, a circular orbit (Warner 1995, Hellier 2001).

The Accretion Disc

If the resulting ring of material is free of viscosity, its radial extent will be small and the mean radius will be given by the so-called *circularisation radius* given by (Hessman & Hopp 1990):

$$\frac{R_r}{a} = 0.0859q^{-0.426},$$

where R_r is the circularisation radius, a is the orbital separation and q is the mass ratio which falls within the range $0.05 \leq q < 1$. This is considered to be the minimum outer radius that a disc can have. At this radius, the material has the same specific angular momentum as the gas at the inner Lagrangian point.

On the other hand, if viscosity within the gas orbiting at the circularisation radius is significant, there will be energy dissipation and transfer of angular momentum within the material. From Kepler's second law, we know that a particle in orbit around a central mass moves more slowly with increasing distance from the mass, but has larger specific angular momentum. The effect of viscosity is to transfer angular momentum from more rapidly moving gas at smaller radii to more slowly moving gas at larger radii. It also releases gravitational potential energy from gas at smaller radii which allows it to accrete on to the central mass, dissipating energy in the process, half of which is thermalised and radiated away. A consequence of these processes is that the inner radius of the disc decreases as most of the gas accretes on to the white dwarf and the outer radius of the disc increases, as some of the gas carries away the excess angular momentum, thereby forming a disc (Lynden-Bell & Pringle 1974).

Under the action of viscosity the disc expands until tidal interactions with the secondary prevent its outer edge from spreading beyond the tidal radius (Ichikawa & Osaki 1994), defined in equation 4.1. These tidal interactions, thought to be caused by the phase lag between density perturbations in the disc and the orbit of the secondary (Paploizou & Pringle 1977), transfers the excess angular momentum from the disc into orbital motion.

Much of the groundwork for modelling accretion discs was made in the 1970s. The foundation for nearly all accretion disc models is the work of Shakura & Sunyaev's seminal paper (1973) which provided the first theoretical calculations for the model of a steady-state, stationary accretion disc. The model, commonly know as the α prescription, characterises the mechanism of angular momentum transport through the disc via the paramaterisation:

$$\nu = \alpha H c_s$$

where ν is the viscosity within the disc, H is the scale height and c_s is the speed of sound in the orbiting gas. This standard model has since been extended to the case of time dependent accretion rate variations through the disc (Lipunova & Shakura 2000). The α prescription, and most of the extensions to it, assume that gas pressure and viscosity

in the disc is small so that the disc can be well modelled by simple particle trajectories occupying circular Keplarian orbits (Lynden-Bell & Pringle 1974, Lubow & Shu 1975, Flannery 1975).

Many theoretical constraints can be deduced from such models including limits on the size of the disc (Paczynski 1977). Extensive numerical modelling by Truss (2007) confirmed Whitehurst and King's (1991) assertion that, for $0.03 < q < 1$, the maximum radius to which a disc can expand before tidal interactions restrict its expansion is $R_d(max)/a \approx 0.9R_{L1}/a$ where R_d is the disc radius and R_{L1} is the primary Roche lobe radius as given by Eggleton (1983)[1]. That is:

$$\frac{R_d(max)}{a} = \frac{0.45}{0.6 + q^{2/3}\ln(1 + q^{-1/3})} \tag{4.1}$$

The disc is maintained by the continuous stream of particles flowing from the secondary. When the stream of free-falling gas from the secondary collides with the outer edge of the disc, the resulting turbulent shocks release enough energy so as to form a bright spot on the disc. In some systems, this collision region emits ∼30% of the total light of the system (Hellier 2001).

The accretion disc, and its process of accretion, are the defining characteristics of a non-magnetic cataclysmic variable. Their features dominate the lightcurves of CVs and are critical in the classification of CVs.

4.1.4 Dwarf Novae

"The Dwarf Novae are arguably the most valuable of objects for the study of accretion discs" (Warner 1995)

Dwarf novae (DN) are CVs which show rapid and semi-regular brightenings (outbursts or eruptions) over their observed lifespan. A luminosity increase of 2-5 magnitudes during an outburst event is typical, although low mass transfer systems, such as WZ Sge, can reach ∼7-8 magnitudes (Patterson *et al.* 2002). The events last for intervals of the order of a few days, though the recurrence times and duration of outburst are variable.

The most useful insight provided by eclipsing systems which undergo dwarf nova eruptions, is into the process of accretion. As previously mentioned, accretion has important applications in other fields of astronomy such as star formation (where accretion discs

[1]Note that the tidal truncation radius and the primary Roche lobe radius are given in Whitehurst and King (1991) and Eggleton (1983), respectively, with errors in the powers of q.

enable gas clouds to collapse into stars), quasars and black holes at the centre of active galactic nuclei where accretion discs power these energetic systems. However, details of the accretion processes which drive these phenomena are difficult to study, either because the objects are vast distances away or because they are obscured by dust and gas. Cataclysmic variables afford the opportunity to study these processes close up and phenomena which take place in accretion discs such as dwarf nova (DN) outbursts, give us additional insight into the physics of discs.

The repetitive outbursts of dwarf novae lead to the inference that their accretion discs are not in a steady state. The most popular explanation for dwarf nova outbursts is the disc instability (DI) model, first suggested by Osaki (1974) to support the conclusion from observations that dwarf nova outbursts are centred on the primary and accretion disc (Warner 1995) and therefore initiated by some kind of instability in the disc[2]. The model holds that if, at quiescence, the rate of mass transfer from the secondary is greater than the rate of mass transfer through the disc, then material piles up in the disc. The resulting increase in viscous reactions increases the temperature in the disc until the material becomes partially ionised. When the temperature of the disc is high enough to allow partial ionisation, the disc becomes opaque to radiation. In this state, the addition of more heat in the disc, from viscous heating and increasingly trapped radiation, creates more ions, rather than heating the disc. The rate of ionisation rapidly increases until the disc is completely ionised. The disc is thus flipped from a cold (neutral), low viscosity state to a hot (ionised), high viscosity state. The disc is said to have gone into outburst, typically increasing the luminosity of the system by 2-5 magnitudes. In addition, the high rate of mass transfer through the disc during outburst increases the rate of accretion onto the primary, further boosting the luminosity of the system. When the disc is in its high viscosity, fully ionised state, magnetic field interactions become important, accelerating the transport of material through the disc so that the inward flow of material through the disc exceeds the mass transfer rate from the secondary. Thus the system cannot maintain this high luminosity state for long and the disc eventually returns to quiescence once its temperature begins to drop below the critical temperature. The interval between outbursts can be from $\sim$10 days to tens of years, with each object having a recurrence timescale that is approximately constant (Warner 1995).

The DI model is supported by the observation that accretion disc features dominate the

[2]Robinson (1976) gives a good review of the observations, made during the preceding decade, which influenced the development of standard dwarf novae models.

light curves of dwarf novae during outburst. The model also predicts that the increased viscosity at the onset of outburst causes the disc to expand. During quiescence, the addition of more material from the accretion stream (which has lower angular momentum than material at the edge of the disc) causes the disc gradually to shrink until the next outburst. This has been supported by observations (Smak 1984, Wood *et al.* 1986, 1989a, 1989b, Wolf *et al.* 1993), although more extensive measurements, particularly at the onset of outburst, would be beneficial. This is especially so in light of the fact that, since the 1990's, the DI model has come under fire for not being able to satisfactorily explain all of the observed phenomena. For example, there are observations of DN systems where the disc is seen to shrink on the onset of outburst (Baptista *et al.* 2007); where mass transfer rates through the disc during outburst are found to be identical to the transfer rate through the bright spot, both many orders of magnitude higher than at quiescence (where the DI model predicts that mass transfer through the bright spot should be unchanging, Smak 2008); and the failure of the DI model to explain the appreciable differences between the observed light curves of different systems as well as within a single system during the outburst cycle (Schreiber *et al.* 2005). A more detailed discussion on extensions to the DI model, and subsequent comparisons to observations, is presented in Chapter 5.

Dwarf novae are divided into three subtypes and one category, the SU Ursa Majoris (SU UMa) stars, is relevant to this work. These are stars that, in addition to normal outbursts, undergo superoutbursts which have a maxima of $\sim$0.7 magnitudes brighter than normal outbursts. They have the additional features of hump-shaped modulations, which may appear near superoutburst maximum ('early'), during the plateau phase or during superoutburst decline ('late'), known as superhumps. Superhumps are periodic with a period slightly longer than the orbital period. Superhumps are thought to be caused by the disc becoming elliptical during outburst and precessing about the primary. The interaction between the orbital period and the precession period produces superhumps at a period equal to the beat period between the orbital and precession periods. Z Cha and OY Car are examples of such systems classified as SU UMa stars and are of particular interest in this thesis.

4.1.5 Light Curve Characteristics of Non-Magnetic CVs

Unless a CV is seen to go into outburst, blue colours or spectroscopic measurements are the usual means of discovery. This can be confirmed by analysis of the light curve. Some light curves display features which are unique to the physics of CVs and for this reason a brief outline of those features which are relevant to this project will be given. For detailed

light curve analysis specific to CVs, see Hellier (2001) and Warner (1995).

Orbital Humps

As already mentioned, the bright spot situated on the outer edge of the disc can emit up to 30% of the total luminosity of the system. To the Earth-based observer, the emission in high inclination CVs is observed to be strongest just before conjunction of the two stars. This is because the free-fall velocity of the particle stream towards the primary and the orbital velocity of the secondary results in the bright spot lying slightly ahead of the line of centres of the two stars. For this reason, orbitals humps in eclipsing systems are most prominent in the light curve just before eclipse. The light curve of IY UMa (Uemura *et al.* 2000) is a good example of this effect, see below for further discussion.

The Eclipse Light Curve

Eclipses are seen if the system is at a high enough inclination (between 70° and 90°). Eclipse light curves are very distinctive as their variation is not at all slow or smooth. This is due to the high luminosity of the accretion disc and the primary star, causing the overall luminosity of the system to drop dramatically during eclipse. Eclipsing systems are invaluable as their light curves contain information about the binaries' characteristics. The light curves of IY UMa (Uemara *et al.* 2000, Steeghs *et al.* 2003) and NN Ser (Pigulski & Mischalska 2002) are good examples of deeply eclipsing systems.

Figure 4.3 shows a light curve of the eclipsing dwarf nova OY Car. The most notable features are the gradual increase in luminosity before eclipse caused by the appearance of the bright spot as it rotates into view (the orbital hump), the four abrupt changes in luminosity during eclipse and the eclipse minimum near conjunction of the white dwarf and secondary[3]. A slightly sharper decline after the peak of the orbital hump indicates that the secondary has started to obscure light from the accretion disc. The first abrupt decrease in luminosity marks the immersion, or ingress, of the white dwarf. This is followed by a brief, less rapid, decline indicating the continued occultation of the disc, then a second abrupt decrease in luminosity, signaling the ingress of the bright spot. The lightcurve slowly declines to minimum light, indicating further obscuration of the disc, before an abrupt increase in luminosity signals the emergence (or egress) of the white dwarf. Finally after a brief standstill, the duration of which varies from cycle to cycle depending on the location of the bright spot relative to the white dwarf, a second small increase in luminosity marks the emergence of the bright spot. The apparent change in

[3]Eclipse minimum is not coincident with conjunction of the white dwarf and secondary.

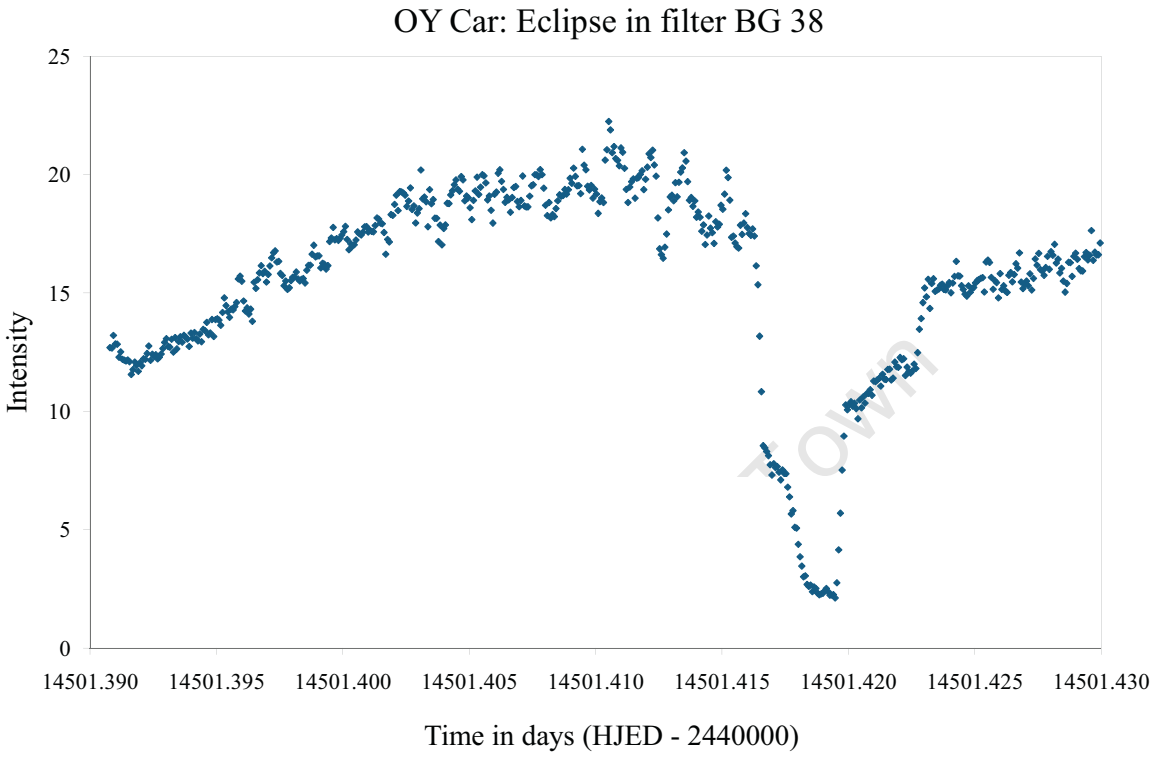

Figure 4.3: Example lightcurve showing a typical eclipsing CV binary (OY Car).

the luminosity of the bright spot from ingress to egress demonstrates that it is the source of the orbital hump. The approximately semi-sinusoidal shape of the hump arises from the effect of foreshortening of the bright spot[4]. The quasi-periodic flickering characteristic of CV lightcurves is not present during the eclipse of the white dwarf, and is greatest during orbital hump maximum, indicating the origin of the flickering is the bright spot.

The eclipse width, $\Delta\phi$, is defined as the phase interval of the orbital cycle between the half-flux points of the white-dwarf's ingress and egress (mid-ingress and mid-egress). The depth and width of eclipse depends on the mass ratio, q, and the inclination, i. The parameters (q, i) cannot be determined independently from the white dwarf eclipse: there are multiple (q, i) combinations which fit the same eclipse width. This is because the volume of the secondary is bounded by its Roche limit, therefore any increase in the mass ratio, for a fixed inclination, would result in an increase in depth and width of the eclipse. Similarly, an increase in inclination would require a decrease in the mass ratio

[4]The bright spot can be thought of as a planar shock front 'painted' onto the outer rim of the disc (Wood *et al.* 1986, 1989a, Warner 1995)

to maintain a fixed eclipse width. This relationship is shown graphically in figure 2.24 of Warner (1995) and can be described as:

$$\sin i \approx \frac{1 - [R_L/a]^2}{\cos^2 2\pi\phi_{mid}}$$

where $\pm\phi_{mid}$ are the phases of mid-ingress and mid-egress of the white dwarf (Warner 1995 and references therein).

The phase of eclipse minimum depends partly on when the secondary has completed ingress of the bright spot. Since the phase of bright spot ingress is variable, eclipse minimum shifts relative to the conjunction of the white-dwarf and secondary (mid-eclipse of the white dwarf). Hence eclipse minimum does not provide a good indicator for counting orbital cycles and the time of mid-eclipse of the white dwarf is used instead (see Section 5.2.5). Phase $\phi = 0$ in the orbital cycle is taken to be conjunction of the white dwarf and secondary (where phase $\phi = 1$ indicates the next conjunction). Measured times of conjunction can be used to determine an equation of time, known as the ephemeris, which defines the period and can be used as an approximate predictor for mid-eclipse (see end of Section 5.5.1).

In the next chapter, it will be shown how observations of eclipses, such as the one shown in Figure 4.3, can be used to test the prevailing theories which seek to explain SU UMa outbursts and superoutbursts.

Chapter 5

Monitoring Disc Radii over the Dwarf Novae Supercycle

5.1 Dwarf Nova Outburst Models

As discussed in Section 4.1.4, it is believed that an increase in viscosity (from low to high) in the accretion discs of dwarf novae causes their radii to expand during outburst until further expansion is halted by tidal interactions with the secondary. In between outbursts, during quiescence, low specific angular momentum gas from the L_1 point is added to the disc leading to an expected decrease in disc radius. Observational support for this scenario was first obtained when Smak (1971) extracted disc radius variations from observations of U Gem between outbursts. This sparked an interest in determining the variation in disc size for dwarf novae over their outburst cycles as a means of distinguishing between the mass-transfer-burst and disc-instability models, two competing models for the explanation of dwarf novae outbursts. The mass-transfer-burst model, originally proposed by Bath (1973), suggested a sudden increase in the mass loss rate from the secondary (or a 'burst' of mass transfer through the L_1 point) to explain the sudden increase in accretion rate through the disc during outburst. Both the disc instability and mass-transfer-burst models predict a decrease in accretion disc radius through quiescence (Livio & Verbunt 1988).

Eclipse observations through the rise and onset of outburst are critically needed to distinguish between the two models. This is because Livio & Verbunt (1988) showed that a sudden enhancement of mass transfer from the secondary should lead to an initial shrinking of the disc radius at the onset of outburst[1], followed by a subsequent expansion. They concluded that this was consistent with observations, but this was subsequently challenged by observations of U Gem (Smak 1984, 1989) which showed a significant increase of the disc radius at the very onset of an outburst.

[1]This is because the matter leaving the L_1 point has low specific angular momentum compared with the material at the outer edge of the disc.

The DI model was extended by Osaki (1989) to explain the superoutburst phenomenon of the SU UMa stars. One of the main features of the superoutburst behaviour which the model had to explain was the observed supercycle, which consists of a series of several successive short outbursts punctuated by a long superoutburst. Osaki's model built on theoretical results presented by Whitehurst (1988) and Vogt (1982) which showed that CVs with mass ratios less than $q \sim 0.25$ can become tidally unstable forming eccentric precessing accretion discs. This behaviour provided a natural explanation for the observed presence of the superhumps observed during superoutburst but did not explain what triggered a superoutburst, as opposed to a normal outburst, and what the possible relation between the two could be.

The superoutburst model, known as the Thermal and Tidal Instability (TTI) model, proposed by Osaki (1989) essentially combines the two kinds of disc instabilities, the thermal instability and the tidal instability, to explain the occurrence of the frequent normal outbursts and the less frequent superoutbursts. This model assumes that the mass transfer rate from the secondary is constant throughout the supercycle (and during the outburst). At the beginning of a superoutburst cycle, just after superoutburst, the disc is relatively compact. Mass transfer from the secondary causes an accumulation of mass in the outer regions of the disc until the surface density in these regions reaches the critical value for the thermal instability to cause a normal outburst. Osaki (1989) showed that only $\sim 30\%$ of the mass transferred from the secondary between normal outbursts is accreted onto the white dwarf; $\sim 70\%$ remains in the disc. Therefore the disc returns to quiescence after a normal outburst with a slightly larger radius than it had at the beginning of the supercycle. With each successive normal outburst the disc radius expands until it exceeds the critical radius at which the disc becomes tidally unstable. The tidal instability is caused by a 3:1 resonance, located at the critical radius[2], arising between the frequency of the material orbiting in the disc and the motion of the secondary star. This has been shown (Whitehurst 1988, Whitehurst & King 1991) to cause the disc to become eccentric and begin to precess in the inertial reference frame. The precessing disc greatly enhances the tidal torque exerted by the disc on the secondary and angular momentum is efficiently removed from the outer edge of the disc. This causes the disc to contract, pushing the density in the rim of the disc beyond the thermal instability threshold and so triggering a superoutburst. The superoutburst maximum is sustained until the disc radius shrinks enough for its eccentricity, and thus the tidal torque, to become insignificant. Then the outburst proceeds as for a normal outburst: the viscous

[2]This critical radius is less than the tidal truncation radius and is given by (Frank, King & Raine 1992, Pearson 2006): $r_3 = \frac{1}{3^{2/3}(1+q)^{1/3}}$ for the 3:1 tidal resonance.

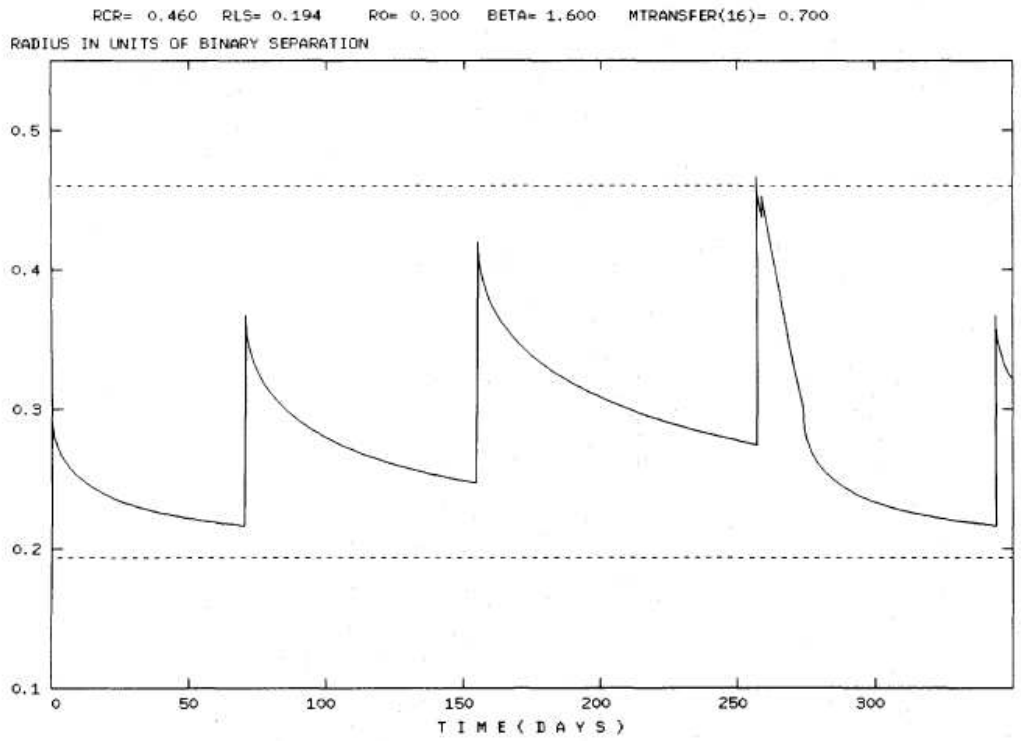

Figure 5.1: [Reproduced from Osaki (1989), Figure 4a] Evolution of the outer disc radius (R_d/a) over the supercycle for the Z Cha model. The lower dashed line represents the minimum disc radius as given by Lubow & Shu (1975) and the upper dashed line represents the tidal instability radius.

accretion of matter onto the white dwarf drains the disc until eventually it makes a downward thermal transition, returning to its quiescent state. This is the end of the superoutburst (and the supercycle). It is assumed that the disc returns to the original (minimum) radius after each superoutburst. This saw-tooth progression of the disc's radius throughout the supercycle is illustrated in Figure 5.1, reproduced from Osaki 1989 (figure 4a). This supercycle has been numerically calculated with model parameters (such as the disk viscosity in outburst and quiescent states, the minimum disk radius and mass transfer rate) chosen for Z Cha, but the overall distinctive trend remains true for all SU UMa stars over the supercycle.

The current alternative model which seeks to explain the superoutburst phenomenon, the Enhanced Mass Transfer (EMT) model, is a modified version of the mass-transfer-burst model and essentially proposes that a superoutburst is due to a sudden enhancement in the mass transfer rate at a normal outburst maximum. A comparison between the two competing models is made in the next section.

Comparison with Observations

The TTI model makes a few testable predictions, one being that the outer disc should expand during normal outburst, yet contract during superoutburst. Another is that the ~ 3.5 power of the disc radius, after each normal outburst, should increase linearly with time throughout the supercycle. Detailed measurements of U Gem (Smak 1984) and Z Cha (O'Donoghue 1986 and references therein), as well as less extensive measurements of other systems (Wood *et al.* 1989b, Wolf *et al.* 1993) show that the disc substantially increases during normal outburst, then steadily shrinks during quiescence. However Smak's (1984) and O'Donoghue's (1986) results (see also Zola 1989) have significant scatter and have not yet been used for quantitative testing of the disc instability model. The reason for their scatter is evident: the inter-outburst time scale is months and observations from different outburst cycles had to be combined to provide the published results.

In addition to the shrinking of Z Cha's disc during quiescence, O'Donoghue (1986) discovered what appeared to be an abrupt decrease in disc size just before the onset of outburst however this has still to be confirmed by further observations. O'Donoghue (1986) also showed that there was least scatter in the data when the disc radius was plotted as a function of 'fractional time' between outbursts. This suggests that the outburst is triggered in the disc when the disc's radius has dropped below a particular threshold (0.26-0.28 R_d/a as measured in the case of Z Cha) and that the disc radius shrinks at different rates in different outburst intervals.

The disc instability model was widely accepted as the model for dwarf novae eruptions until observations made in the 1990s started to question its validity. van Amerongen *et al.* (1990) found that, in observations made of Z Cha, the luminosity of the bright spot increased between two outbursts. This could be explained by O'Donoghue's (1986) observation that the disc radius decreased between outbursts. Moreover the brightnesses of the white dwarf and accretion disc did not increase. This is in disagreement with the disc instability model which predicts a systematic increase of the disc brightness between outbursts. Similar results (van Amerongen *et al.* 1987) were previously found for other dwarf novae such as VW Hyi, SS Cyg and U Gem.

Smak (1991) presented an excellent synopsis of the merits and shortfalls of the EMT and TTI models. In it, Smak summarises the predictions that are made by each model, the most relevant for our purposes being:

- The EMT model predicts that the radius of the disc *expands* as a result of a superoutburst and then slowly *decreases* during the supercycle while,
- The TTI model predicts that the radius of the disc *shrinks* as a result of a superout-

burst and then slowly *increases* during the supercycle[3] .

Smak (1991) compares these models with observations by reproducing the disc radius plots of Z Cha compiled by O'Donoghue (1986) and grouping the observations into (normal) cycle counts within the supercycle (refer to figures 4 and 5 in Smak (1991)). The TTI model predicts that, for a given phase in a normal outburst cycle, observations made during the first outburst within a supercycle should yield measurements of a smaller disc radius than observations made during the second outburst of the supercycle (and similarly for the second versus third outbursts within the supercycle). However Smak (1991) found that during the first half of the normal cycle there was no difference in disc radius between the second and third outbursts and, during the second half of the cycle, where the disc radius is supposed to decrease most rapidly, the disc is larger during the first outburst than during the second. Thus, Smak (1991) tentatively concluded that observational evidence seems to support the EMT model and contradict the TTI model. However further disc determinations for Z Cha and similar objects, OY Car being a prime candidate, are necessary to strengthen that conclusion.

It is crucial to note that, for both the TTI and the EMT models, superhumps are believed to be caused by tidal resonance acting on a disc that has expanded beyond the r_3 critical radius which then becomes eccentric and precesses about its orbital axis. The initiator of the *superoutbursts*, however, is the point of contention[4]. In the case of the TTI model it is due to the initiation of the 3:1 tidal instability during a normal outburst which maintains the disc viscosity at the high state for an extended period. In the case of the EMT model, the cause of superoutburst is the response of a highly viscous disc (in normal outburst) to an enhancement in mass transfer from the secondary. One of the responses of the disc to the sudden enhancement of mass transfer is to expand beyond r_3 (Schreiber *et al.* 2005 and references within).

Observations supporting both models continued to accumulate during the last decade: Wolf *et al.* (1993) found an exponential decline in the disc radius of the eclipsing dwarf nova IP Peg between outbursts (supporting the TTI model), similar to what is seen in observations of U Gem (Smak 1984). Cheng *et al.* (1992) found that the disc accretion rate in OY Car (estimated from the measured flux of the disc) *decreased* following superoutburst, in contradiction to the TTI model, though they stressed the need for further observations of OY Car, sampling the entire quiescent state, to confirm their finding.

[3]Note: As previously mentioned, *both* models predict a contraction of the disc during quiescence in the normal outburst cycle.

[4]Although more recent work by Smak (2009, 2010) questions the validity of all tidal resonance models, and thus the explanation for superhumps employed by both the TTI and EMT models. However, a review of the substantial literature on the topic of superhump models, and Smak's contentious critisisms in particular, is beyond the scope of this work.

Since then Smak (2000), summarising the shortfalls of the TTI model, included three more objections to the TTI model, the two of relevance to the nature of the superoutburst trigger being: first, contrary to the TTI model, wider outbursts are brighter than narrower outbursts and second, the TTI model fails to account for observations which clearly show that mass transfer from the secondary increases during outburst.

On the theoretical side, Schreiber *et al.* (2005) maintain that the strong sensitivity of the EMT model to small changes in the mass transfer rate can be used to explain the variations in the outburst cycle (frequency and duration of normal outbursts in a supercycle) observed between different systems and the variations in light curves seen within a single system.

Thus the growing sentiment (Smak 2000, 2004a, 2004b, Hameury *et al.* 2000, Buat-Ménard *et al.* 2001, Hameury 2002, Hameury & Lasota 2005) over the last few years has been that the TTI model is insufficient and a complete picture of the dwarf nova superoutburst cycle will require a hybrid of the two models: something approximating the TTI model combined with irradiation-induced enhanced mass transfer (Smak 2004a, Smak 2004b) which, perhaps, also includes other heating effects such as those caused by tidal dissipation and the impact of the stream on the disc. However Osaki & Meyer (2003, 2004) vigorously dispute the necessity of this, claiming to show that the evidence 'for increased mass transfer in outbursts of cataclysmic variables is inconclusive, partially contradictory and in all cases can be explained otherwise, in fact supporting the TTI model' .

The most recent observational work (Borges & Baptista 2005, Hameury & Lasota 2005, Schreiber & Lasota 2007, Collins & Wheatley 2010 and references therein) testing the validity of the TTI model has focused on the predictions of accretion disc brightness/accretion rates, outburst frequency and duration and the onset of the superhump phenomenon made by the model. Since Smak (1991) there has been no recent observations made to probe the variations in disc radii over dwarf novae supercycles. Yet there is still a need for such observations to be made to help further examine this aspect of the theory. This is the motivation for the investigation presented here.

Testing the Theory: Bright Spot Location as an Estimate of Disc Radius

Ritter (1980) first showed that it is possible to determine the size of the disc by analysing the light curves of cataclysmic binaries which undergo "double eclipses" or eclipses of both the bright spot and central object (as illustrated in Figure 4.3). The method makes the assumption that the disc radius is equal to the distance of the bright spot from the cen-

tre of the disc and only requires straightforward geometrical interpretations of the eclipse curves. Ritter showed that the disc radius could be expressed as a weakly varying function of the mass ratio. This means the disc radius can be determined without the mass ratio being known exactly. Hence, locating the position of the bright spot provides a method for determining disc size photometrically, with relatively small observational effort, as opposed to the usual spectroscopic method which requires the radial and projected rotation velocity of the bright spot to be known (Ritter 1980).

The goal of the project, therefore, is to obtain eclipse light curves of two dwarf novae for the purposes of measuring their accretion disc radii, and defining their variation during quiescence as accurately as possible. The sampling should, if possible, span 2 or 3 quiescent intervals, sampling each sufficiently frequently to define adequately the variation of disc radius with time.

5.2 Observations and Reductions

5.2.1 Targets

Z Cha and OY Car

Z Cha and OY Car are both dwarf novae which periodically undergo superoutbursts in addition to their usual outbursts and therefore are classified as SU UMa stars. Z Cha and OY Car are two of a small number (~ 30) of known dwarf novae in which the secondary eclipses the white dwarf, accretion disc and bright spot.

OY Car and Z Cha were two of the first dwarf novae to be discovered and as such are well studied systems (Wood *et al.* 1986, 1989). The detailed structure of their eclipses and their short orbital periods, have allowed the times of mid-eclipse to be measured accurately and hence the binary parameters of the systems have been tightly constrained and are given in Table 5.1. The mass ratio, q, quiescent magnitudes and orbital inclination, i, quoted have been obtained from the Ritter & Kolb catalog (2003). The orbital periods are taken from the sinusoidal ephemerides calculated by Baptista *et al.* (2002) for Z Cha and Greenhill *et al.* (2006) for OY Car.

The primary goal of observing these targets is to improve the measurements of the disc radius of Z Cha and define, for the first time, the variation of disc radius versus normal outburst and superoutburst phase for OY Car.

Table 5.1: Targets

	Z Cha	OY Car
Magnitude	17.3	15.5
RA (2000)	08 07 28.2	10 06 22.4
Dec (2000)	-76 32 01.1	-70 14 05.1
q	0.149	0.102
i	81.8°	83.3°
P	$0^d.074499297$	$0^d.0631209126$

5.2.2 Observations

Altogether 13 weeks were spent observing the targets during the course of this project. High speed differential photometry was performed on OY Car and Z Cha with the UCT CCD photometer mounted on the 0.75m telescope. The key features of the UCT CCD photometer have been described in Section 1.1. OY Car and Z Cha were observed in a BG38 filter (∼350-650nm) and also in white light. Observations were made in the BG38 filter to the minimise light contribution from the secondary[5]. OY Car and Z Cha were observed in December 2005; January, February, March, April, September and October 2006; January/February 2007; and January, February, March and May 2008. The observations of OY Car and Z Cha covered a total of 82 eclipses, of which 68 were suitable for the final data reductions and are shown in Tables 5.2-5.4[6]. Exposure times ranged from 5s to 30s.

5.2.3 Light Curves

Data reductions were performed using the CCD program `reduce`, created and developed by Darragh O'Donoghue, which enabled flat field correction, bias subtraction and cosmic ray removal. Standard differential PSF photometry was performed on the resulting cleaned frames using an adaptation of the CCD photometry package `DoPHOT` (Schechter, Mateo & Saha 1993). The data were left as uncalibrated instrumental magnitudes, although the quiescent/outburst state of the systems could easily be judged from the dif-

[5] Although Wood *et al.* (1986) showed that, in the case of Z Cha, the secondary only contributes ∼ 4% of the total light at 4800 $\AA$ during eclipse and so can be neglected.

[6] The remaining light curves had data gaps during the eclipses either due to instrument failure (particularly for the December 2005 and early January 2006 runs) or bad weather

Table 5.2: Observations of Z Cha. 'Date' refers to the approximate time of mid-eclipse for the run.

Mon/Year	Date (HJD) 2450000 +	Run	Filter	Exposure (s)	*Cycle	Comments
12/05	3711.478	102	None	30	180496	
01/06	3745.362	302	None	5	180951	Seeing > 3" towards end of run
01/06	3761.336	602	BG38	6	181165	Seeing > 4" towards end of run
01/06	3761.402	603	BG38	6	181166	Thin cloud
01/06	3762.404	701	None	15	181180	
01/06	3763.352	801	None	25	181192	Good seeing
01/06	3764.291	901	None	6	181205/6	
01/06	3765.303	1001	BG38	6	181219/20	Good seeing
02/06	3788.310	101	None	6	181527	Excellent seeing. In outburst.
02/06	3789.263	201	None	6	181541	Excellent seeing, good data
02/06	3794.269	501	BG38	6	181607/8	Excellent seeing at start
03/06	3818.255	301	BG38	6	181929/30	Good seeing
03/06	3820.238	501	BG38	5	181956	Excellent seeing, good data
03/06	3821.302	601	BG38	6	181970	
04/06	3830.235	101	BG38	6	182090	
04/06	3831.225	201	BG38	6	182103	Good seeing
04/06	3832.233	301	None	6	182117	
10/06	4031.520	501	None	6	184792	
02/07	4133.329	202	None	6	186159	Bright moon.
02/07	4134.304	301	None	6	186171	Bright moon. In outburst.
02/07	4135.277	401	BG38	6	186184	Bright moon. In outburst.
02/07	4136.309	501	None	6	186198	Bright moon. In outburst.
02/07	4137.277	601	None	6	186211	Bright moon. Dropping out of outburst.

*The ephemeris used to determine the cycle numbers is that given by Baptista *et al.* (2002).

Table 5.3: 2006-07 observations of OY Car. 'Date' refers to the approximate time of mid-eclipse for the run.

Mon/Year	Date (HJD) 2450000 +	Run	Filter	Exposure (s)	*Cycle	Comments
01/06	3763.467	802	BG38	6	126912	Good seeing
01/06	3765.490	1002	BG38	6	126944	
02/06	3789.383	202	None	5	127323	Excellent seeing
02/06	3790.417	302	None	6	127339	
02/06	3790.494	303	BG38	6	127340	
02/06	3794.387	502	BG38	6	127402	Humidity $> 80\%$, seeing ~ 3"
03/06	3816.409	102	BG38	4	127765	
03/06	3817.321	201	BG38	6	127766	
03/06	3817.414	202	None	6	127767	
03/06	3818.354	302	BG38	6	127782	
03/06	3818.427	304	BG38	6	127783	
03/06	3819.363	401	None	6	127788	Excellent seeing, good data
03/06	3819.418	402	BG38	6	127799	Good seeing
03/06	3820.326	502	BG38	6	127814	Excellent seeing
04/06	3830.285	102	BG38	6	127971	
04/06	3830.342	103	None	6	127972	
04/06	3830.400	104	BG38	6	127973/4	
04/06	3831.327	202	None	6	127988	
04/06	3831.399	203	BG38	6	127989	
04/06	3832.287	302	None	6	128003	
04/06	3832.360	303	BG38	6	128004	
01/07	4132.418	102	None	6	132758/9	Bright moon. Seeing ~ 3"
02/07	4133.416	202	None	6	132773	Bright moon.
02/07	4134.401	302	None	6	132789	Bright moon.
02/07	4135.437	402	BG38	6	132805	Bright moon.
02/07	4135.498	403	BG38	6	132806	Bright moon.
02/07	4135.550	404	None	6	132807	Bright moon.
02/07	4136.403	502	None	6	132821	Bright moon.
02/07	4136.474	503	BG38	6	132822	Bright moon.
02/07	4137.371	602	None	6	132836	Bright moon.
02/07	4137.432	603	BG38	6	132837	Bright moon.

*The ephemeris used to determine the cycle numbers is that determined by the author and given in Section 5.5.2.

Table 5.4: 2008 observations of OY Car.

Mon/Year	Date (HJD) 2450000 +	Run	Filter	Exposure (s)	*Cycle	Comments
01/08	4490.435	202	BG38	6	138429	
01/08	4491.382	302	None	6	138444	Thin cirrus, seeing ∼3”
01/08	4494.412	403	BG38	6	138492	Good seeing
01/08	4495.485	502	None	6	138509	Excellent seeing, good data
01/08	4498.388	803	BG38	6	138555/6	Excellent seeing, good data
01/08	4499.398	902	None	6	138571/2	
01/08	4501.418	112	BG38	6	138603	
01/08	4502.428	122	None	7	138619/20	
02/08	4524.394	102	None	6	138967	
02/08	4525.53	202	None	6	138985	Excellent seeing, good data
03/08	4527.361	402	BG38	6	139014/15	
03/08	4529.513	602	None	6	139048	
05/08	4588.272	101	None	6	139979	
05/08	4593.332	301	None	6	140059	

*The ephemeris used to determine the cycle numbers is that determined by the author and given in Section 5.5.2.

ference in mean brightness with respect to the comparison star(s). The brevity of eclipse - the feature of interest in this analysis - means that biased magnitude-difference between the comparison and target stars due to colour-dependent extinction can be considered negligible.

The corresponding light curves for Z Cha and OY Car are shown in Figures 5.2-5.3 and 5.6-5.8 respectively. Figures 5.4-5.5 and 5.9-5.10 show particular light curves selected to highlight features of interest in the data set and discussed further below. The time base of each data set is Heliocentric Julian Date (HJD) − 2450000 and the coordinate is intensity (relative to the comparison stars within the respective fields[7]).

In general, the observations taken using the BG38 filter produced light curves of comparable SNR quality to those taken in white light (compare consecutive cycles 128003-

[7]Note that Figures 5.2-5.3 and 5.6-5.7 did not have their comparison stars adjusted to the same baseline. Consequently the light curves are not on the same relative scale. The vertical offsets in these figures (including Figure 5.8) are arbitrary.

128004, 132821-132822 and 132836-132837 in Figures 5.6 and 5.7). However, at least in OY Car's case, during periods of high variability in the bright spot's luminosity it appears that the BG38 light curves' SNR is more flickering limited (compare the top and bottom of Figure 5.8) than those made from white light observations.

Z Cha

Figure 5.4 (top) shows a typical light curve of Z Cha. The contact features, which mark the eclipse of the white dwarf at the centre of the disc followed by the eclipse of the bright spot at the edge, are clearly visible. The gradual increase in brightness between end of white dwarf egress and the beginning of bright spot egress (usually a flat standstill) evident in cycle 181165 indicates a brighter than usual disc. Figure 5.5 shows the eclipse profile of Z Cha observed towards the end of outburst. The light curve intensities have been normalised with respect to the cycle 181608's average intensity. The cycles 181527, 181541 and 181608 show the progression of the eclipse profile as Z Cha rapidly drops out of outburst: from a smooth, disc dominated profile to a profile that begins to recover some of the typical quiescent features, namely the distinct eclipse of the white dwarf and the egress of the bright spot.

The bottom of Figure 5.4 shows an example of the more unusual light curves encountered in the data set; profiles which make determination of contact times more difficult. Cycle 184792 indicates the difficulty in sometimes judging the end of white dwarf ingress and the beginning of bright spot ingress[8].

OY Car

Figures 5.6, 5.7 and 5.9 show typical light curves for OY Car. In contrast to Z Cha, OY Car shows a much clearer standstill between white dwarf and bright spot ingress, as well as a much longer ingress of the bright spot. Using the phase plots to obtain a coordinate position for the average bright spot phase positions, it was found that, on average the angular position of the bright spot lies at $\theta = 35.2°$ for OY Car and at $\theta = 27.5°$ for Z Cha. This is consistent with previous estimations of the bright spot position in Z Cha (Cook and Warner 1984, Wood *et al.* 1986) and OY Car (Cook 1985b, Wood *et al.* 1989b).

Cycle 127767 (lower panel of Figure 5.9) shows a gradual, almost linear ingress of the bright spot. This indicates a relatively extended bright spot. This is thought to be due to a longer cooling time for the impact gas, downstream in the disc flow producing a bright spot

[8]Note that the differences between the features of the top and bottom plots in Figure 5.4 are note due to the choice of filter. These profile shapes can be seen in observations taken in white light or using the BG38 filter.

elongated along the rim of the disc (Smak 1971, Warner 1995). In contrast, the ingresses of all of the eclipses of the bright spot in Z Cha (sharp initial decline, followed by a more gradual decline) suggest a more compact spot. Both cycles 128003 and 127767 (Figure 5.9) show brightness modulations between white dwarf and bright spot egress. These are present in most of the light curves, some of greater amplitude, and suggest origin in the disc or the white dwarf boundary layer, and not in the bright spot as it is still in eclipse at the time. Hence the bright spot is not the only source of flickering. This is consistent with previous analyses of flickering in eclipse curves (Horne & Stiening 1985, Bruch 2000) which have identified the central region of the disc and/or boundary layer as an origin. Cycle 127402 (top panel of Figure 5.10) shows, on top of the characteristic flickering, even more distinct brightness modulations outside of eclipse. These semi-regular brightenings occur when the bright spot has passed out of the line of sight, indicating that they originate in the disc, or the white dwarf boundary layer, independent of mass transfer through the bright spot. These may be identified as *quasi-periodic oscillations*, or QPOs. Rarely seen in the naked light curve (usually found through Fourier analysis), QPOS are believed originate in the disc, though a definitive explanation of the mechanism of their generation has yet to be proved (Hellier 2001).

Based on observations of Z Cha, Cook & Warner (1984) suggest two types of structure for the bright spot. These have been derived from the two kinds of eclipse profiles observed. The first type, Type 1, have flat standstills between primary egress and bright spot egress, followed by an abrupt bright spot egress. Cycle 181165 (top light curve in Figure 5.4) is an example of a Type 1 profile in Z Cha. These arise from a small, compact bright spot situated near the edge of the disc. Type 2 eclipses have relatively slow bright spot egresses with a very short duration between the end of primary eclipse and the onset of the bright spot egress. OY Car's cycle 128004 (Figure 5.10) is an example of a Type 2 eclipse. These correspond to a bright spot extended along the stream trajectory caused by part of the stream overflowing the edge of the disc. Very few Type 2 eclipses could be identified in the data, with only two examples for OY Car and one for Z Cha. Thus no correlation between eclipse types and times of outburst could be found. However, in the case of Z Cha, a similar distinction can be made for the ingress of the bright spot; profiles where the duration of the standstill between the end of white dwarf ingress and the beginning of bright spot ingress is long and well defined followed by a sharp bright spot ingress contrast with profiles where virtually no standstill between component ingresses exist and the bright spot ingress is long and well rounded (cycles 181165 and 184792 in Figure 5.4 are typical examples of each). Many examples of each exist throughout the data obtained for Z Cha, suggesting that further classification of eclipse types could be made.

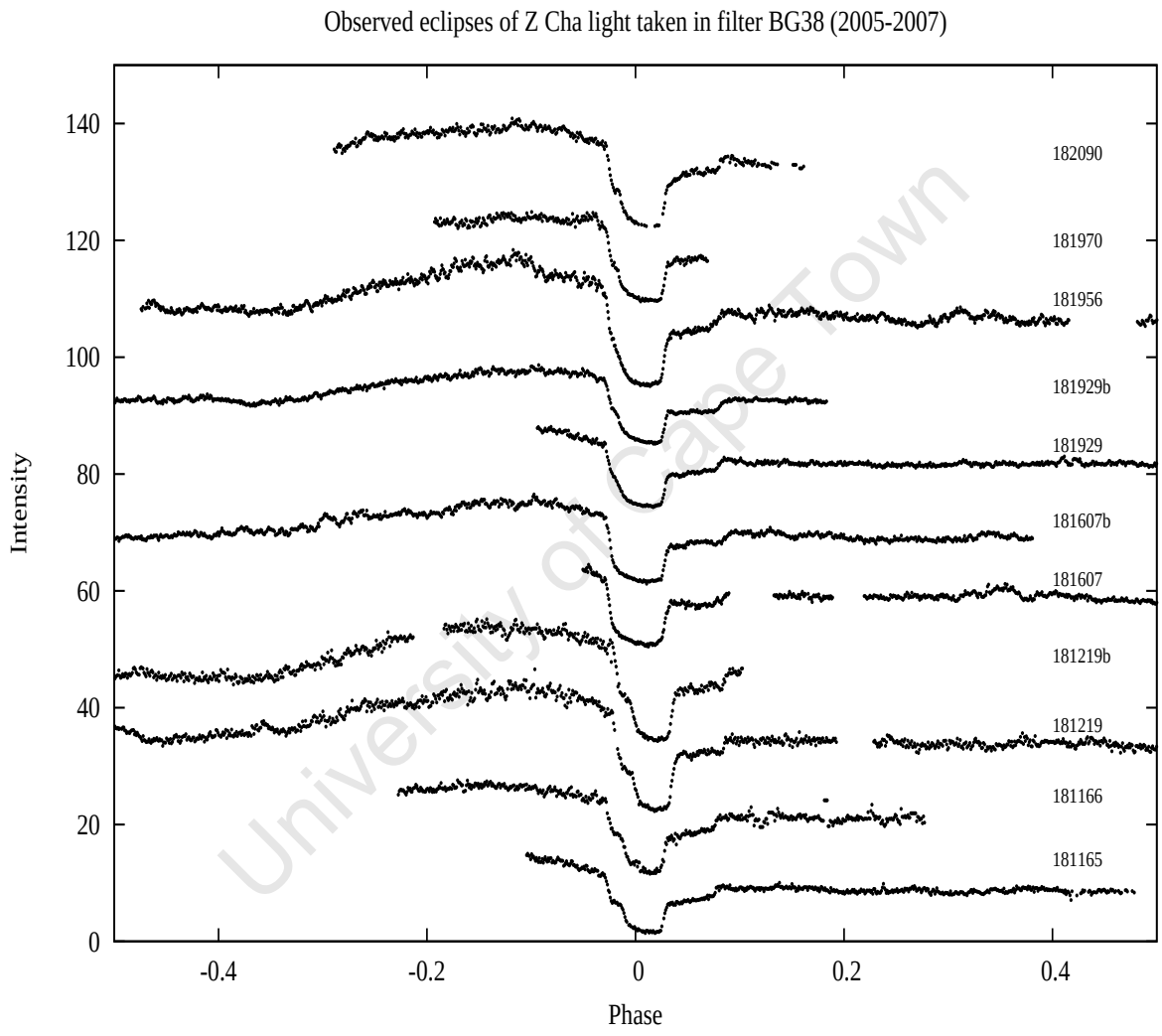

Figure 5.2: The eclipses of Z Cha observed in filter BG38 over the period December 2005 to February 2007. Cycle numbers were determined using the Baptista *et al.* (2002) ephemeris. Note that the comparison stars in this figure were not adjusted to the same baseline. Consequently the light curves are not on the same relative scale. The vertical offsets are arbitrary.

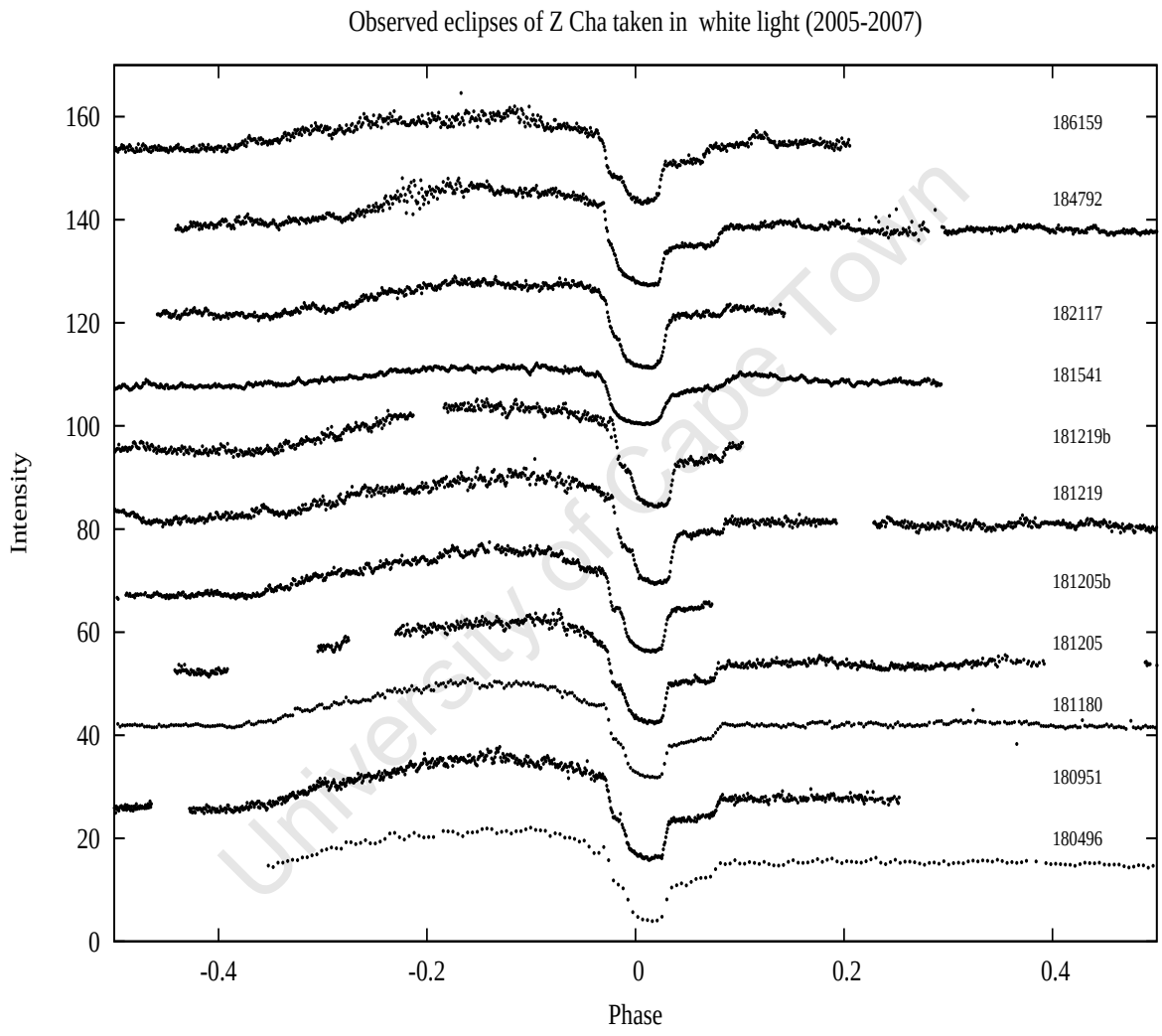

Figure 5.3: The eclipses of Z Cha observed in white light (no filter) over the period December 2005 to February 2007. Cycle numbers have been determined using the Baptista *et al.* (2002) ephemeris. Note that the comparison stars in this figure were not adjusted to the same baseline. Consequently the light curves are not on the same relative scale. The vertical offsets are arbitrary.

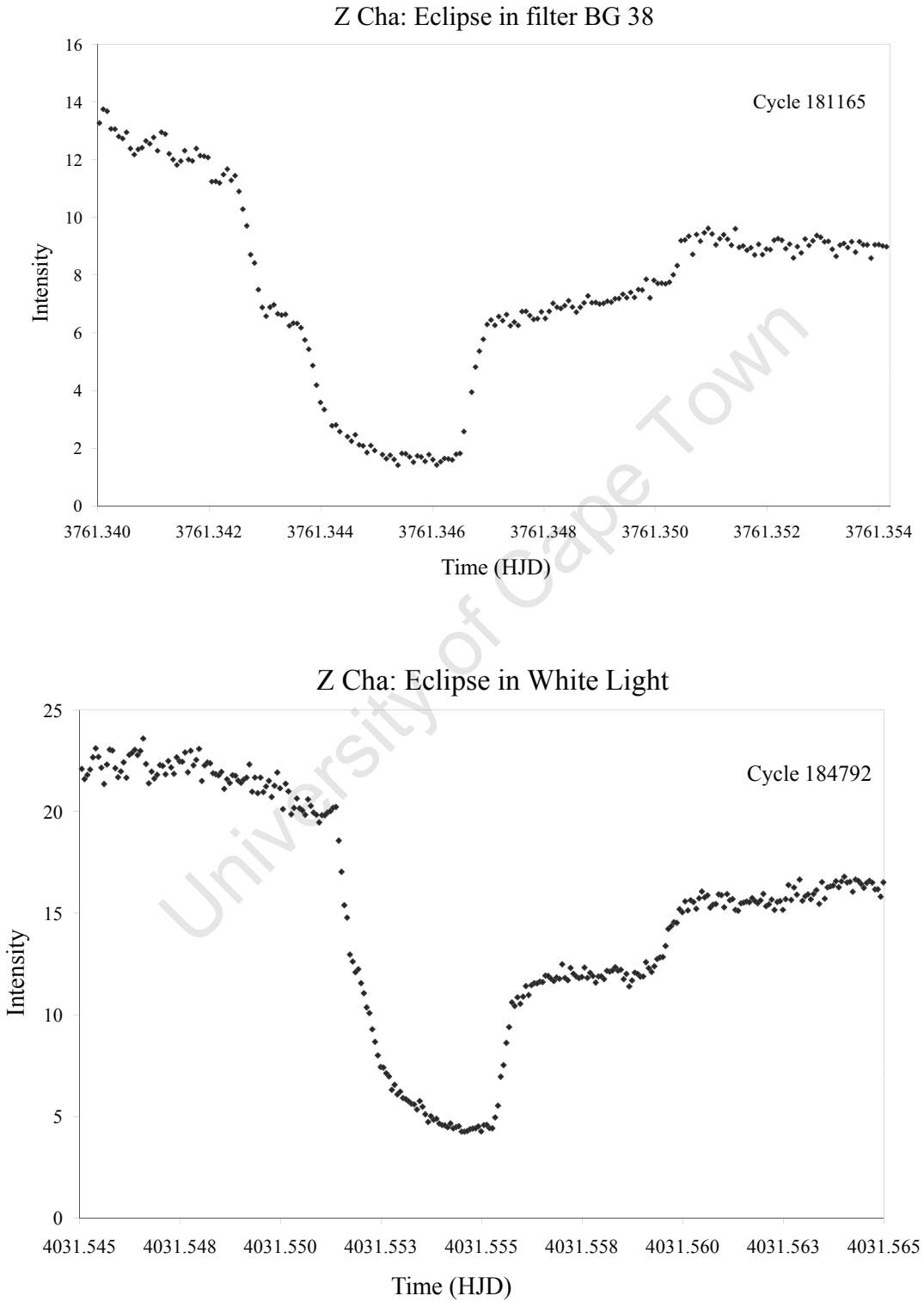

Figure 5.4: (Top) A typical light curve example of eclipsing dwarf nova Z Cha. (Bottom) A light curve of Z Cha's showing virtually no standstill between white dwarf ingress and bright spot ingress. The ordinate is in days, HJD-2450000.

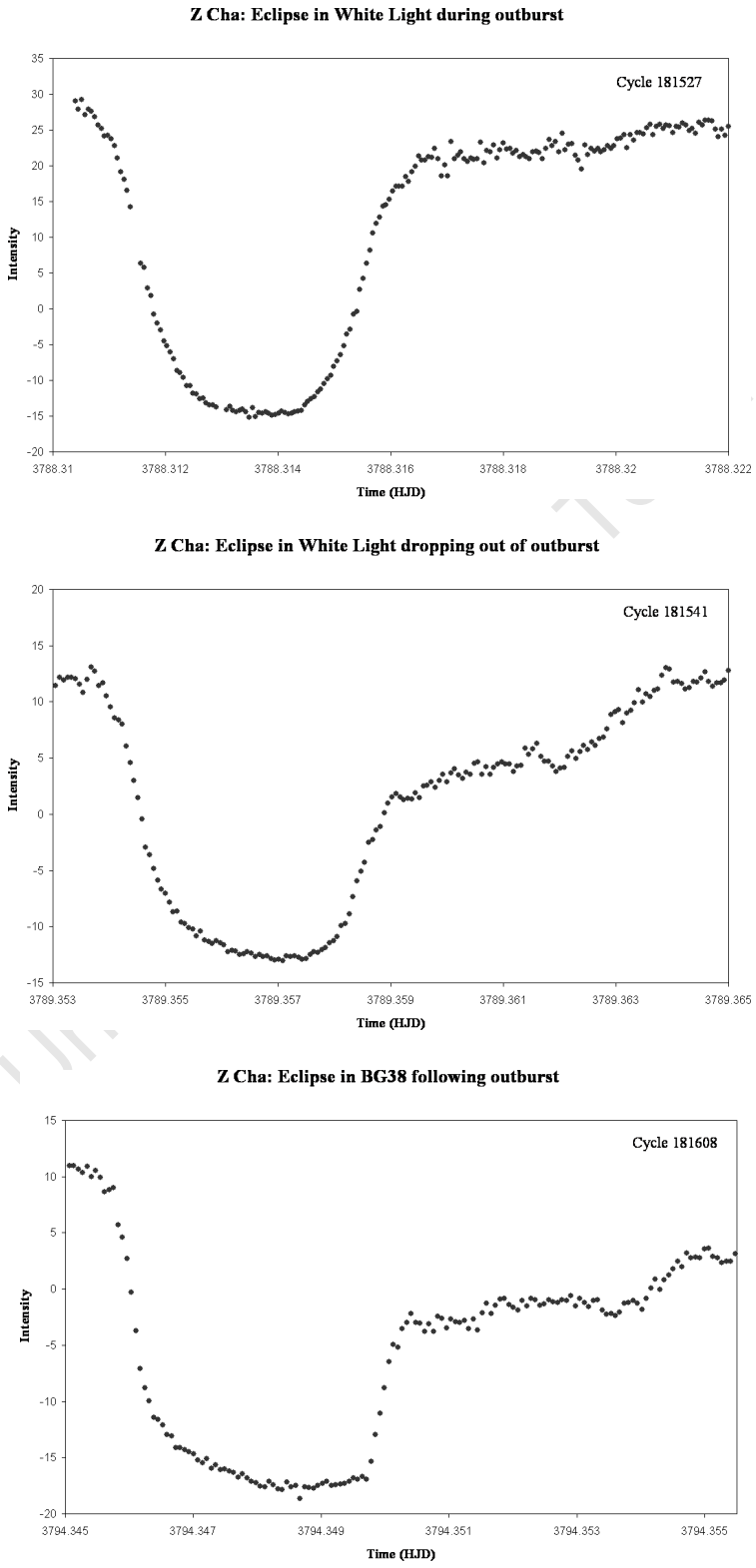

Figure 5.5: (Top to bottom) Z Cha caught dropping out of (normal) outburst. The ordinate is in days, HJD-2450000. From to bottom, the Z Cha was observed to be at 14.2, 14.7 and 15V-magnitudes having dropped from a peak of ∼11.7V-magnitudes on 2453786.50JD (V-magnitude data courtesy of the AAVSO's online Light Curve Generator).

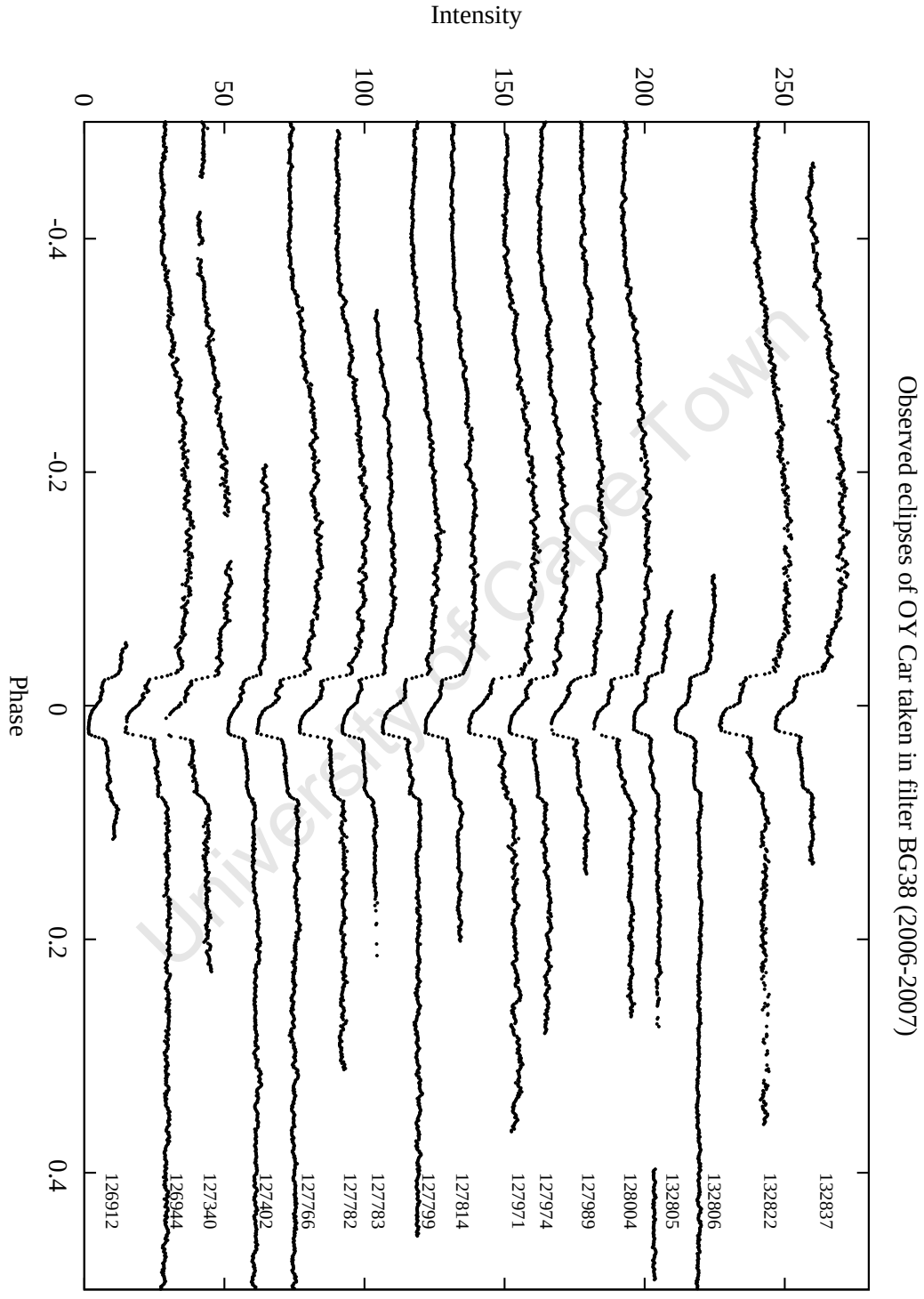

Figure 5.6: The eclipses of OY Car observed in filter BG38 over the period December 2005 to February 2007. Cycle numbers have been determined using the ephemeris determined in Section 5.5.2. Note that the comparison stars in this figure were not adjusted to the same baseline. Consequently the light curves are not on the same relative scale. The vertical offsets are arbitrary.

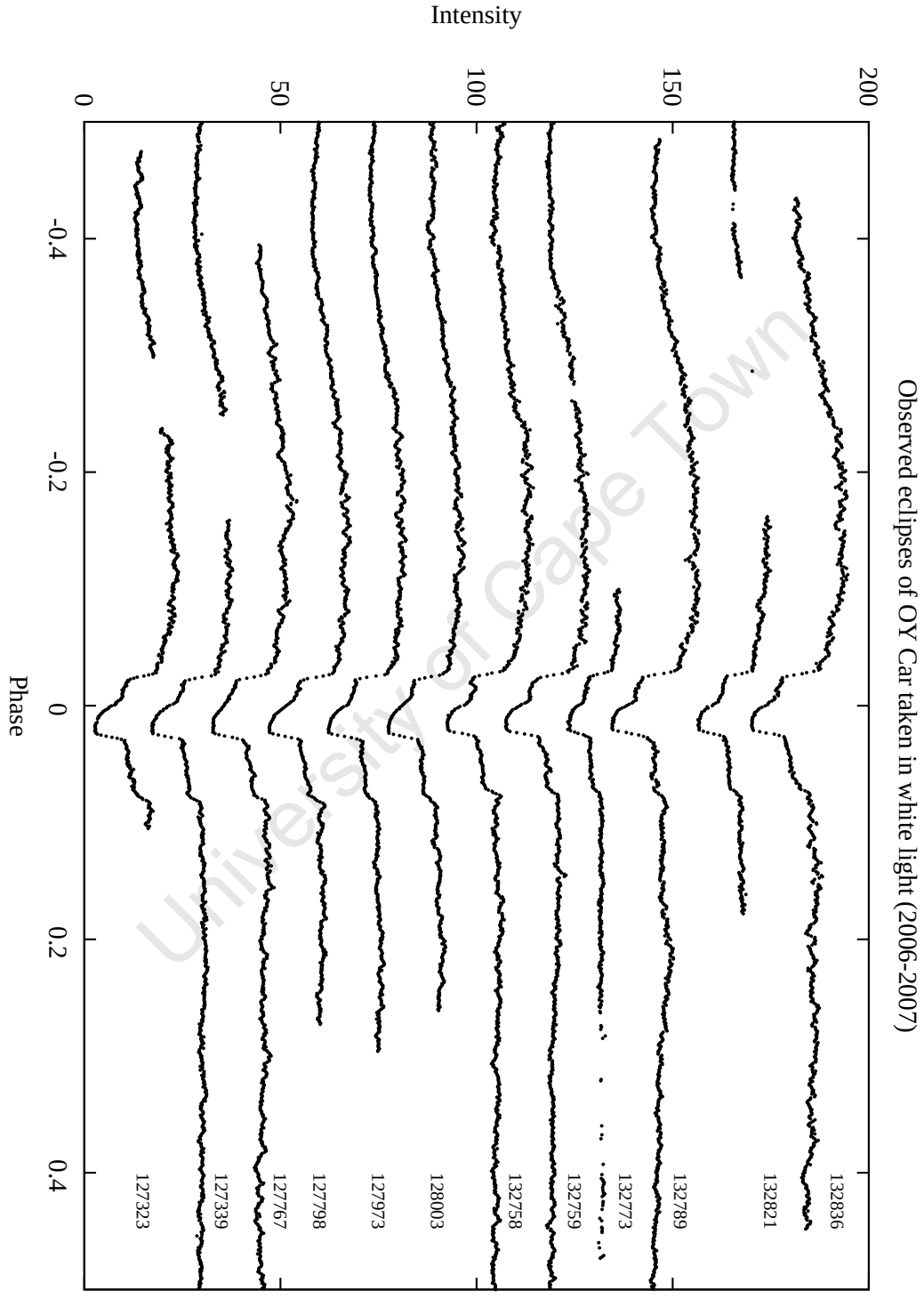

Figure 5.7: The eclipses of OY Car observed in white light (no filter) over the period December 2005 to February 2007. Cycle numbers have been determined using the ephemeris determined in Section 5.5.2. Note that the comparison stars in this figure were not adjusted to the same baseline. Consequently the light curves are not on the same relative scale. The vertical offsets are arbitrary.

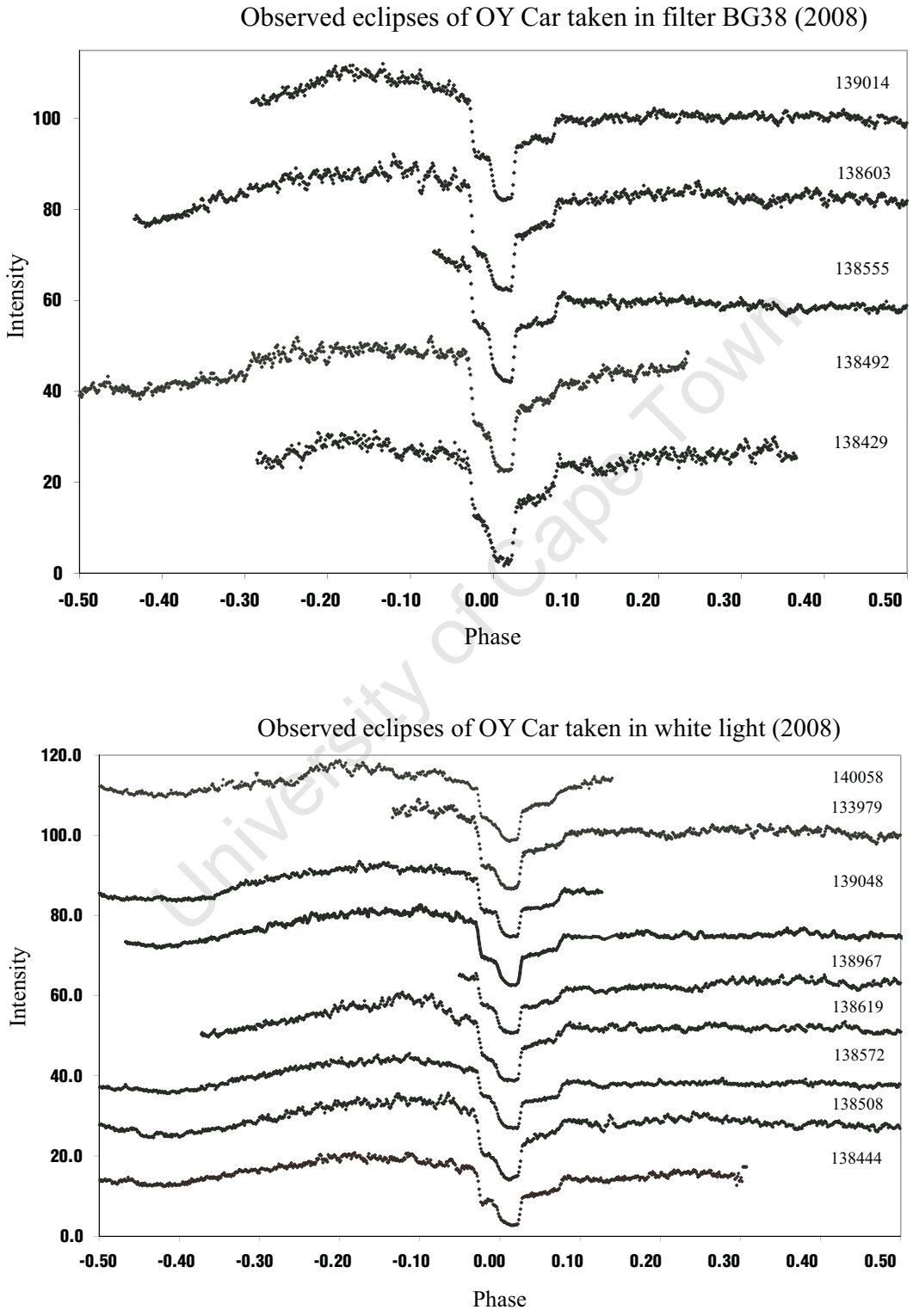

Figure 5.8: The eclipses of OY Car observed during the 2008 observing season in filter BG38 (top) and white light (bottom). Cycle numbers have been determined using the ephemeris determined in Section 5.5.2. The vertical offsets are arbitrary.

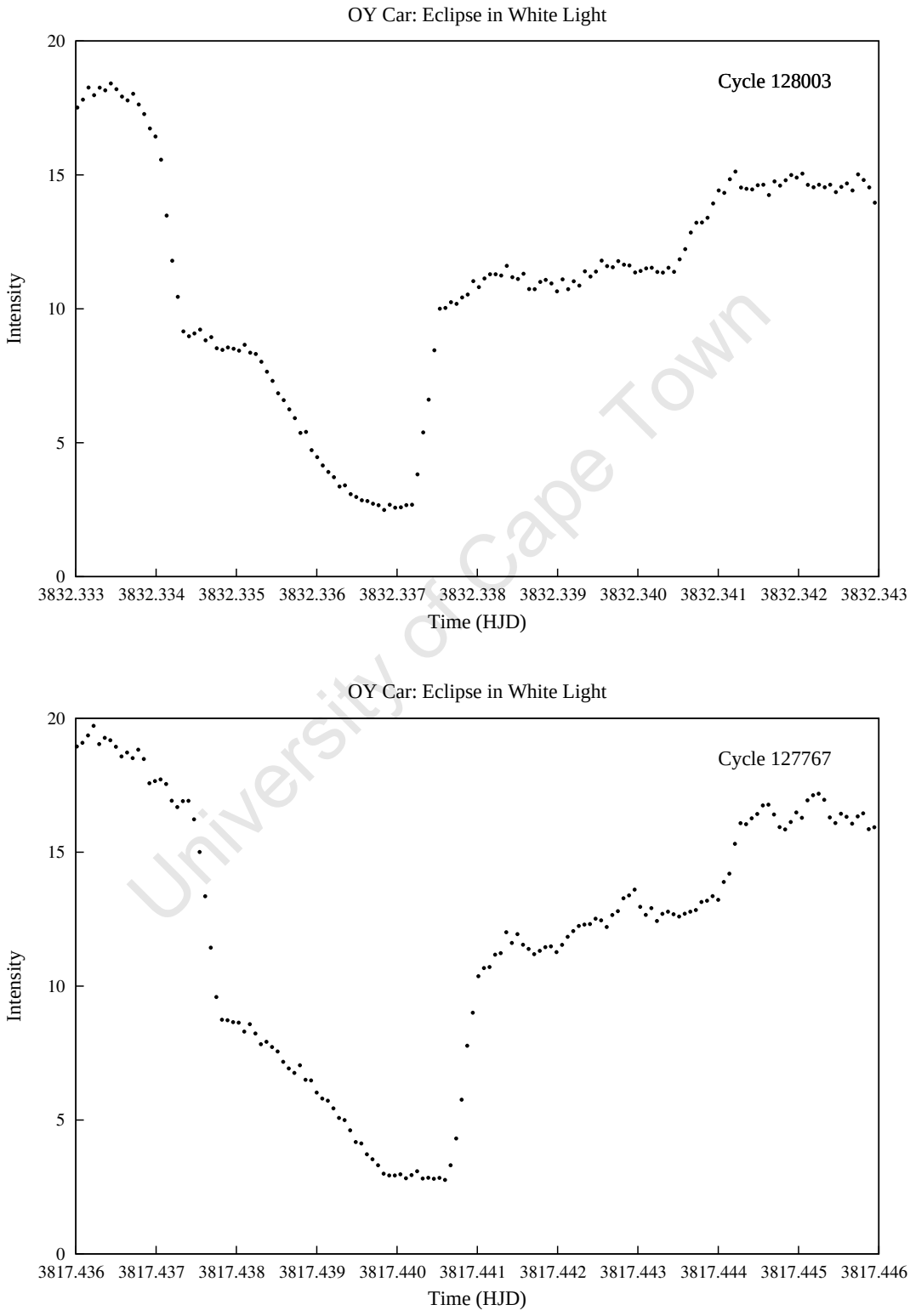

Figure 5.9: (Top and bottom) Typical lightcurve examples of the eclipsing dwarf nova OY Car. The ordinate is in days, HJD-2450000.

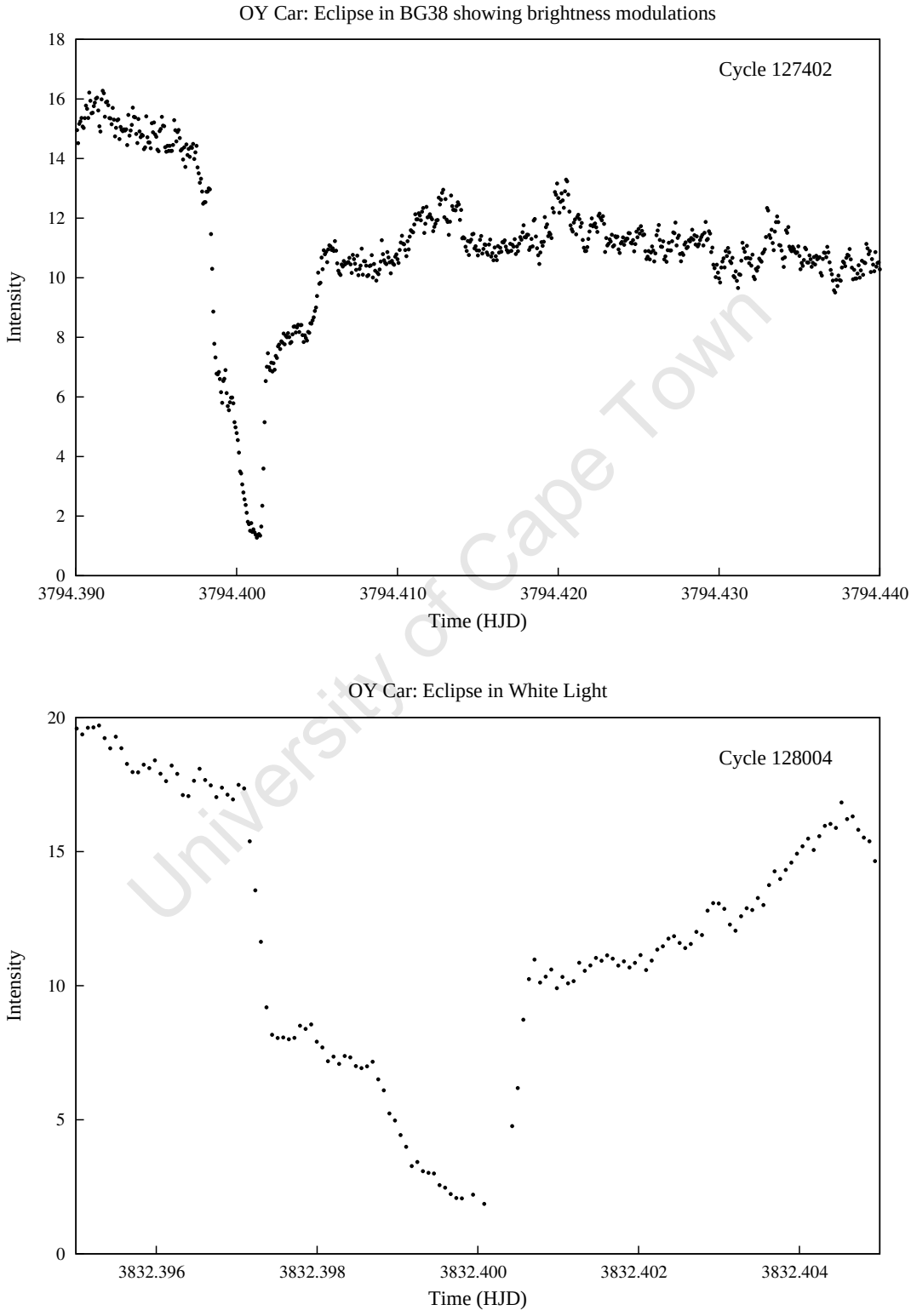

Figure 5.10: (Top) Eclipse of OY Car showing semi-regular, long-period, large amplitude flickering that appear to originate in the disc. (Bottom) Eclipse of OY Car showing an example of a type 2 eclipse profile as defined by Cook and Warner (1984). The ordinate is in days, HJD-2450000.

5.2.4 Eclipse Timings

Wood, Irwin & Pringle (1985) suggest using the gradient of the light curve to identify the times of the bright spot and white dwarf eclipse events. However this technique can on by used with reasonable confidence on high signal-to-noise, phase-folded light curves; the signal-to-noise ratio of *individual* light curves is too poor for this application. From trial estimations, the author has concluded that other 'objective' means of obtaining contact times, such as piece-wise regression fitting, does not yield as accurate results as estimations fitted by eye. Thus, the contact points of eclipse events were determined visually from the light curves as described below.

In the case of Z Cha, the contact times were estimated in Universal Time (UT), then corrected to the solar system's barycentre to obtain times in Barycentric Julian Ephemeris Date (BJED). For OY Car the times were corrected to Heliocentric Julian Ephemeris Date (HJED). The differing timescales are due to the fact that the most recent ephemerides for Z Cha and OY Car were calculated in HJED and BJED respectively (Baptista *et al.* 2002, Greenhill *et al.* 2006), and so these timescales were maintained for the sake of consistency with the published ephemerides. While heliocentric corrections account for light time effects caused by the earth's motion around the Sun, barycentric corrections take into account Jupiter's gravitational effect on the Sun's motion around the Solar System's barycentre. The latter effect contributes a difference in timings of up to ~ 0.5s over Jupiter's orbit. This can be considered negligible over the baseline (3 yr) of OY Car's observations. For the purpose of determining new ephemerides, the times were converted to Ephemeris times as it is a uniform timescale, as compared to UTC which varies on the order of a second on an annual basis. In the case of the author's observations, a correction of 65s was added to the timings to correct UT to the uniform ephemeris time scale.

Z Cha's cycle 180951 is shown in Figure 5.11, indicating where the points of contact denoting a rapid change in intensity were typically taken to be. The time of primary mid-ingress was determined using the definition of Cook and Warner (1984), namely the time at which "the intensity had fallen by half the total intensity change of primary ingress". The times of primary egress, bright spot ingress and bright spot egress all have similar definitions (see below and Wood *et al.* 1986, 1989b). That is:

$$T_{\mathrm{WDi}} = T\left(\frac{I_1 + I_2}{2}\right) \ , \ T_{\mathrm{WDe}} = T\left(\frac{I_5 + I_6}{2}\right)$$

for the white dwarf and

$$T_{\rm BSi} = T\left(\frac{I_3 + I_4}{2}\right)\ ,\ T_{\rm BSe} = T\left(\frac{I_7 + I_8}{2}\right)$$

for the bright spot where $\rm WD_i$, $\rm WD_e$ denote the white dwarf's ingress and egress respectively and $\rm BS_i$, $\rm BS_e$ denote the bright spot's ingress and egress respectively. The mid-ingress/egress times were measured in this way because it was deemed easier to estimate the average intensity close to one of the rapid intensity changes than to determine exactly at what *point in time* the change took place (associated with the start/end of ingress/egress).

The times of mid-eclipse of the white dwarf were taken to be the mean of their respective mid-ingress and mid-egress times and are listed in Tables 5.5-5.7.

Location of the contact points could be estimated to within $1/20^{th}$ of the full intensity change. This translated to an error in the mid-ingress/egress times (the approximate locations of fastest intensity change) of $\lesssim 1/4$ of the integration time. With the exception of three light curves in the collection (Z Cha cycles 180496, 181180 and 181192), all observations had integration times of 5-6s and were of similar data quality. This gives a typical measurement error of 1-2s in the bright spot and white dwarf mid-ingress/egress times.

The orbital phases of mid-ingress and mid-egress times of the white dwarf and bright spot for a each run were calculated relative to the mid-eclipse time, $\rm T_{\mathit{mid}}$, of the white dwarf for that particular run. This was done to eliminate any variability in the bright spot times that might arise from short term variability in the phase of mid-eclipse relative to the calculated ephemeris; eclipsing CV ephemerides show significant intrinsic timing jitter (Warner 1995).

The phases of eclipse for each component are given by:

$$\phi_{\rm WDi} = \frac{T_{\rm WDi} - T_{mid}}{P}\ ,\ \phi_{\rm WDe} = \frac{T_{\rm WDe} - T_{mid}}{P}$$

and

$$\phi_{\rm BSi} = \frac{T_{\rm BSi} - T_{mid}}{P}\ ,\ \phi_{\rm BSe} = \frac{T_{\rm BSe} - T_{mid}}{P}$$

for the white dwarf and bright spot respectively, where P is the period of the ephemeris chosen as the best fit to the mid-eclipse times[9]. These phases are listed in Tables 5.8 to 5.9. Thus the phase of mid-eclipse is 0 and the mid-ingress and mid-egress phases for the

[9]The error in this determined period can be considered a negligible contribution to the phase error in comparison to the observational error.

white dwarf are symmetrised about phase 0 (hence only the white dwarf's mid-ingress, $\phi_{\rm WDi} = -\phi_{\rm WDe}$, is given in the tables).

The times of mid-eclipse were collated with previously published timings to determine new ephemerides for each of the targets.

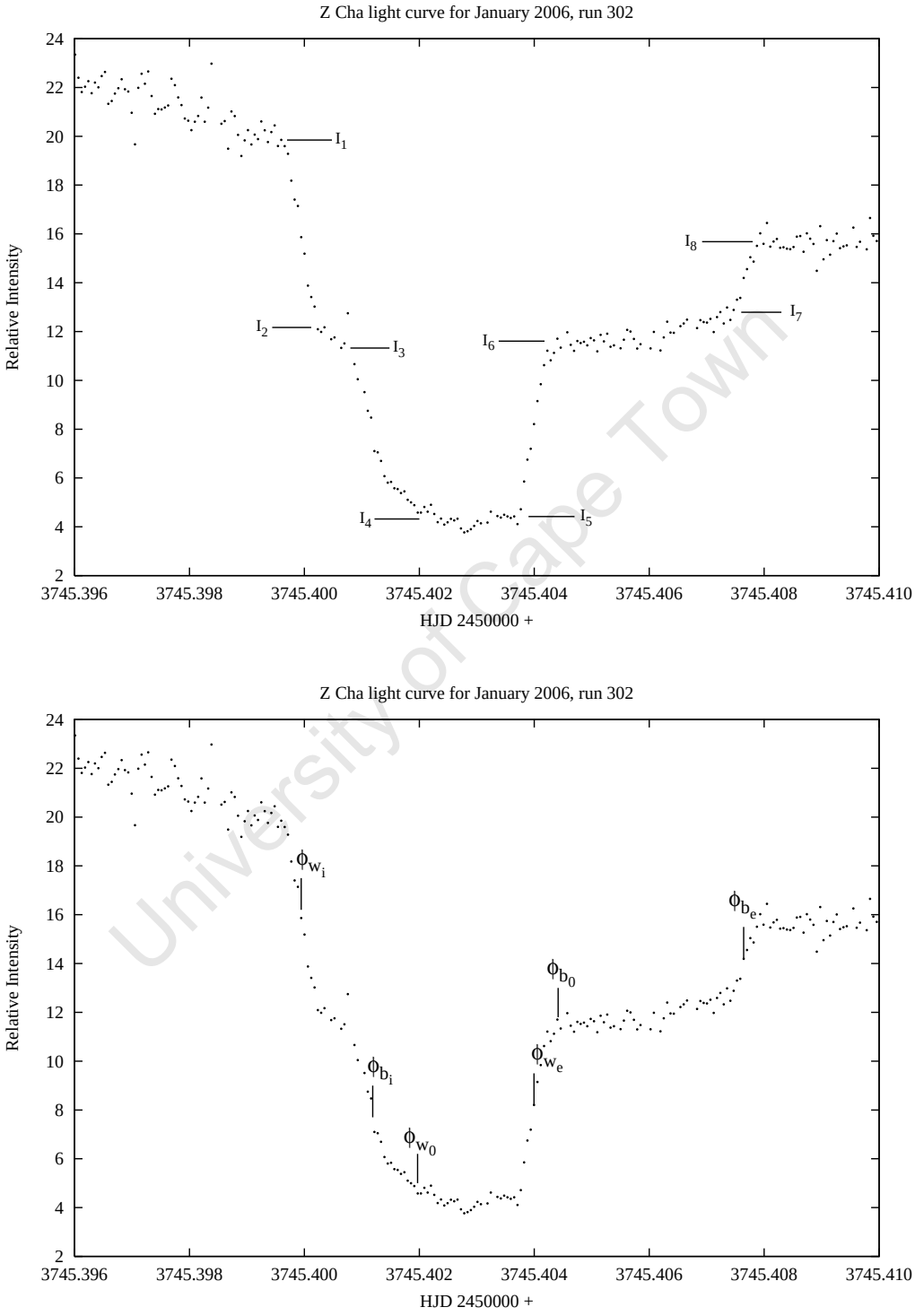

Figure 5.11: (Top) An example light curve of Z Cha indicating where the intensities of the contact points were estimated to be. (Bottom) The same lightcurve indicating the phases of the mid-ingress, mid-egress and mid-eclipse for the bright spot and white dwarf, respectively, yielded by the intensities shown in the top figure.

5.2.5 Revision of the Ephemerides

Z Cha

The ephemeris

$$JD_{mid} = JD_o + PE + sE^2$$

gives the time of mid eclipse, JD_{mid}, predicted for an eclipsing object during a particular cycle (E) where JD_o is the time of mid-eclipse of cycle 0, E is the integer number of cycles that have elapsed since JD_o, P is the orbital period and s is the quadratic coefficient. The cycle numbers were calculated using the approximation

$$E = int\left(\frac{JD_{mid} - JD_o}{P}\right)$$

because the coefficients of higher order terms are sufficiently small not to change the value of the integer E.

The ephemeris calculated by Baptista *et al.* (2002) for Z Cha has been updated here using the observed times of mid-eclipse determined in the previous section and listed in Table 5.5. Baptista *et al.* (2002) used optical timings from Cook and Warner (1984), Cook (1985a), Wood *et al.* (1986), van Amerongen (1990) and Robinson's (1995) X-ray timings to obtain the following linear and sinusoidal ephemerides for Z Cha:

Linear ephemeris	
$BJDD = T_0 + P_0E$	
$T_0 = 2440264.68070(\pm4)$ d	$P_0 = 0.0744993048(\pm2)$ d
$\sigma_L = 3.27 \times 10^{-3}$ cycles	
Sinusoidal ephemeris	
$BJDD = T_0 + P_0E + A\cos[2\pi(E-B)/C]$	
$T_0 = 2440264.6817(\pm1)$ d	$B = (120 \pm 4) \times 10^3$ cycles
$P_0 = 0.074499297(\pm2)$ d	$C = (136 \pm 7) \times 10^3$ cycles
$A = (7.2 \pm 1.0) \times 10^{-4}$ d	$\sigma_S = 1.09 \times 10^{-3}$ cycles

where E is the cycle number and σ_L, σ_S are the uncertainties in the fits.

The eclipse times presented in Table 5.5 were combined with the archival optical timings used by Baptista *et al.* (2002) (hereafter referred to simply as Baptista) and Baptista's own timings to produce a total of 146 timings. These times were converted to Barycentric Julian Ephemeris Dates (BJED) in order to combine with those used by Baptista to calculate their ephemeris[10]. The times of eclipse predicted for each cycle by the linear

[10]Previous ephemerides were calculated using Terrestrial Dynamical Time (TDT). The difference between the two time

ephemeris obtained by Baptista were subtracted from these observed times to produce the set of observed minus calculated (O-C) differences plotted in Figure 5.12 (top). The linear plus sinusoidal ephemeris derived by Baptista is plotted as the dashed line on top of the O-C data set. The residuals with respect to Baptista's fit are plotted in the lower panel.

Figure 5.12 shows that Baptista's sinusoidal ephemeris is no longer a good predictor of the time of eclipse. Baptista's ephemeris predicts that the rate of decline in orbital period should be decreasing in preparation for the next cyclical increase in period, while the timings presented here show that the orbital period is continuing to decrease. This suggests that the variations seen in the orbital period are either best described with a sinusoidal function of a different period and amplitude or they are not strictly sinusoidal.

Hence a new ephemeris was computed using the fortran program, `ephem.f`, developed by Dr Darragh O'Donoghue which employs the method of least squares to fit a function to the data (refer to Appendix A for further details).

Two fits were made to the O-C data, a cubic function of the form $BJED = T_0 + P_0E + cE^2 + dE^3$ and a sinusoidal function of the form $BJED = T_0 + P_0E + Acos(E + \phi)$ where $\phi = -2\pi B/C$ according to Baptista's notation. The sinusoidal function fit is shown in Figure 5.13. The first plot shows the linear component subtracted from the O-C timings with the higher order sinusoidal term plotted with the residuals, and the second plot shows the O-C timings with the full ephemeris removed. Table 5.10 gives the parameters obtained for the fitted sinusoid as well as the sigma of the residuals.

The fit obtained suggests an orbital variation of amplitude $A = 1.77$ min, cyclic on a time scale of $\sim$ 39 years, significantly longer than the $\sim$ 28 year period calculated by Baptista. Dai *et al.* (2009) calculated a new ephemeris for Z Cha using 187 times available from the archives, 37 of which were derived from poor quality photographic data and were subsequently discarded from the later analysis. They also determined that a sinusoidal ephemeris provided the best fit to the eclipse timings, but instead found the sinusoidal variation to have an amplitude $A = 1.58$ min, cyclic on a time scale of $\sim$ 34 years. However, Dai *et al.* (2009) were the sole contributers of the three eclipse timings in their data set which were post Robinson *et al.* (1995) and which had comparatively large errors in them. As a result, the sigma of the residuals to their fit is an order of magnitude larger than for the fit derived here and, as a consequence, the author has more confidence in the ephemeris presented in Table 5.10 being a better description of the data.

The sinusoidal term was chosen as a better fit than the cubic term (not shown here)

scales has been taken to be negligible.

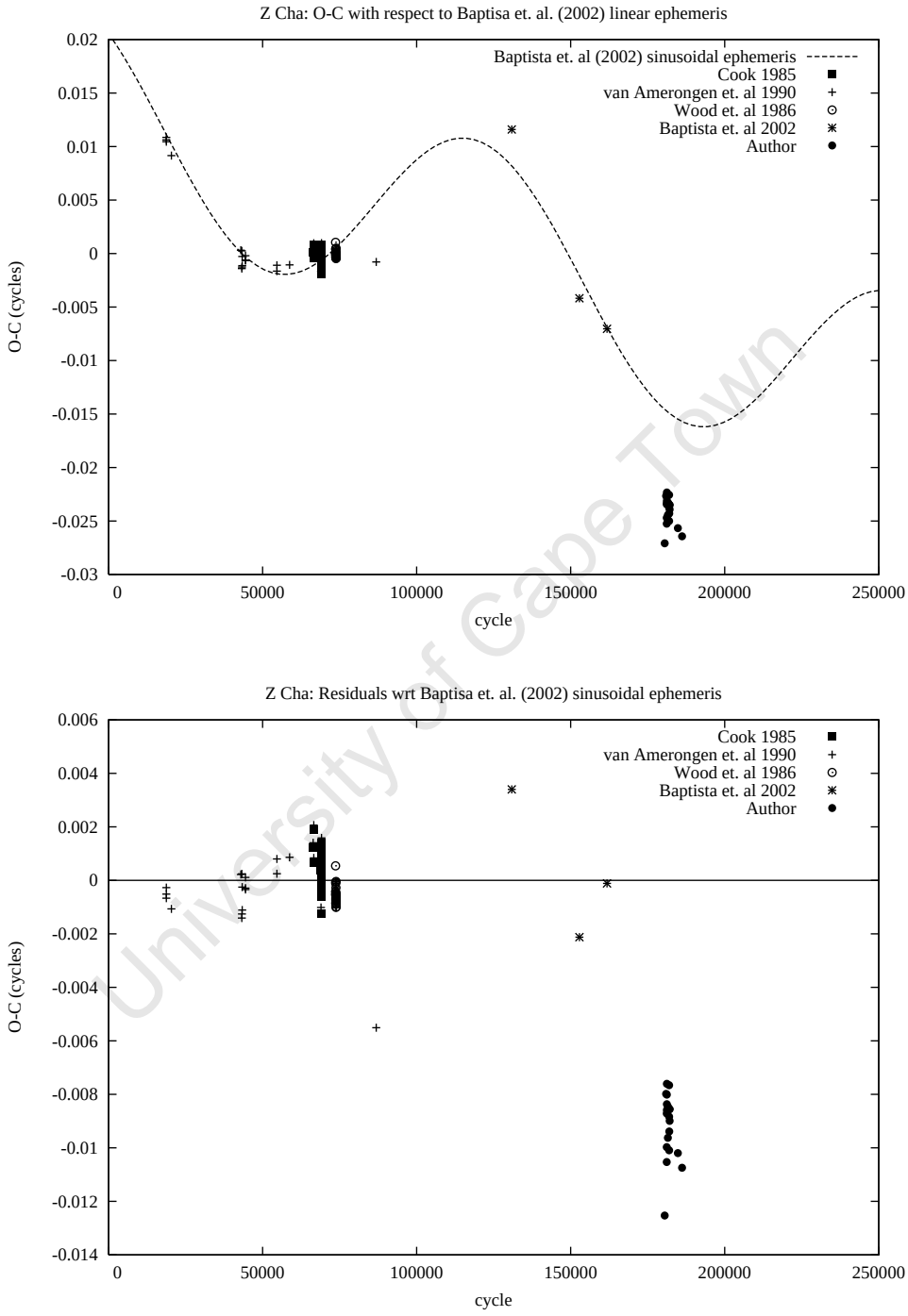

Figure 5.12: (Top) O-C plot compiled using optical timings from Cook and Warner (1984), Cook (1985a), Wood *et al.* (1986), van Amerongen (1990), Baptista *et al.* (2002) and those obtained in this thesis with respect to Baptista's linear ephemeris. The sinusoidal ephemeris derived in Baptista *et al.* (2002) is plotted as the dashed line. (Bottom) O-C residuals with respect to Baptista's sinusoidal fit.

on the grounds that it minimised the sigma of the residuals (by an order of magnitude). However, it should be noted that the fits are visually comparable. In Baptista *et al.* (2002) the significance of adding additional terms to the linear ephemeris was estimated using the F-test. Tests for statistical significance were not included here as they are best applied in cases where the data is well represented by the model (taking into account statistical error). This is not the case here. It is anticipated that this new calculated ephemeris will not be a good fit to data obtained, say, 10 000 cycles in the future from the set of observations presented here. Thus this ephemeris was calculated to serve more as a convenient empirical representation of the behaviour rather than as a representative physical model. If Z Cha's ephemeris is indeed a sinusoidal movement with a period of $30 - 40$ years, then the data available in the literature has yet to span more than one cycle and thus provide adequate sampling of the ephemeris. All we may say here is that, if the orbital period changes seen in Z Cha are cyclical, then the variations are of greater amplitude and much longer period than previously anticipated.

Cyclical period changes have been observed in other eclipsing CV systems (Warner 1995 and references therein, Rubenstein, Patterson & Africano 1991, Baptista *et al.* 2000, 2002). At a cyclical period of ~ 39 years, the apparent cyclical variability of Z Cha's orbital period is on a slightly longer timescale than previously observed (from 4 years in EX Dra to 30 years in UX UMa). Explanations for the cause of cyclical variation have included the presence of a third body, angular momentum exchange in the binary or the presence of a solar-type magnetic activity cycle in the secondary. Explanations involving angular momentum exchange in the binary have been discarded as these require disc masses well in excess of what has been observed. For a third body to be present in the Z Cha system, the orbital period variation would have to be shown to be strictly periodic i.e. observed for more than one complete cycle. This has yet to be established.

The idea that variations in the orbital cycles or CVs are due to the presence of a solar-type magnetic activity cycle in the secondary, proposed by Applegate & Patterson (1987) and elaborated by Richman *et al.* (1994), is the most popular current explanation for the cyclical modulations. This model suggests that the secondary's magnetic activity cycle causes changes in the secondary Roche lobe's volume radius. As the secondary fills its Roche lobe, this results in changes in the orbital separation and hence the orbital period.

Whether the energy budget available from the secondary is sufficient to support the momentum transfer mechanism which underlies Applegate's model is still contested (Lanza 2006, Yuan & Qian 2007, Dai *et al.* 2009). One of the ways in which the model can be tested is to use the fact that changes in the secondary's Roche lobe leads to a change in the mass transfer rate. This in turn modulates the luminosity of the bright spot which

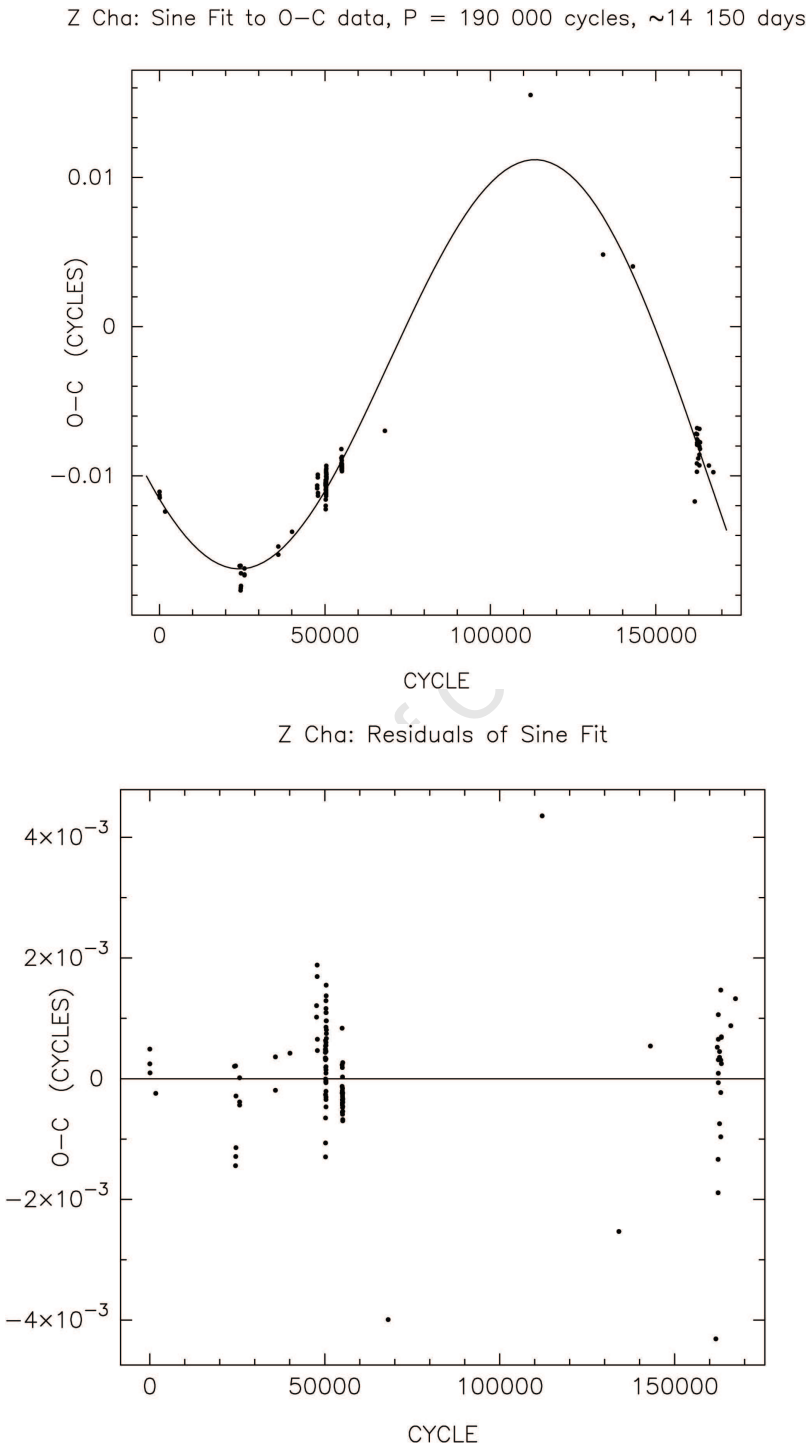

Figure 5.13: (Top) O-C plot compiled using optical timings from Cook and Warner (1984), Cook (1985a), Wood *et al.* (1986), van Amerongen (1990), Baptista *et al.* (2002) and those obtained in this thesis with respect to the linear part of the sinusoidal ephemeris given in Table 5.10. The sinusoidal component of the ephemeris is plotted as the solid line. (Bottom) O-C residuals with respect to the sinusoidal fit derived here.

can be detected in the total luminosity of the system in quiescence. Ak *et al.* (2001) observed brightness modulations in the quiescent magnitude of Z Cha on a timescale of 14.6 years. Baptista suggested that a simple test of the Richman *et al.* (1994) model would be to determine if the maximum of the variation in quiescent magnitude coincides with the minimum of the orbital period variation. Baptista's calculated period of orbital modulation, $\sim$ 28 years, might have substantiated this and thereby confirm Ak *et al.*'s conclusion that fully convective secondary stars also possess magnetic fields. However the data presented here indicates that, if Z Cha does indeed undergo brightness modulations on a timescale of 14.6 years, then it is unlikely they will be found to correlate with any cyclical variation in orbital period which may be present.

OY Car

In the same manner as for Z Cha, a new ephemeris was determined for OY Car, updating the ephemeris calculated by Greenhill *et al.* (2006). The ephemeris was calculated using the mid-eclipse times determined by Wood *et al.* (1989), Pratt *et al.* (1999), Greenhill *et al.* (2006) and combined with the observations reported here, amounting to 89 timings in total. Quadratic, cubic and sinusoidal terms were separately fitted to the O-C residuals of the least squares fit of a linear ephemeris. The linear-plus-sinusoidal fit yielded the smallest sigma of the total residuals. However the difference between the sigmas of total residuals for the different fits is small and, as in the case of Z Cha, the cubic also provides a good fit to OY Car's data. The cubic and sinusoidal ephemeris fits are shown in Figures 5.14 and 5.15 respectively. The corresponding ephemerides are given in Table 5.11 and are quoted in HJED to be consistent with previously published ephemerides.

The sinusoidal fit yields a cyclic change in orbital period with an amplitude of $\sim$ 31 seconds and a period of $\sim$ 23 years, compared to Greenhill *et al.*'s (2006) sinusoidal ephemeris which has an amplitude of $\sim$ 46 seconds and period $\sim$ 35 years (with an orbital period $P_0 = 0.0631209126d$). Whether or not a sinusoid is the appropriate physical interpretation for the data, the new timings presented here indicate that OY Car's orbital period is continuing to decrease, but at a rate reduced from that measured by Greenhill *et al.*'s (2006). Measurements appropriately spanning the next 50 000 cycles will determine whether the orbital period change is in fact cyclic – and therefore possibly related to cycles of magnetic activity within the secondary – or even sinusioidally periodic, indicating the prescence of a third body, or due to some mechanism for angular momentum loss not considered to date. Whichever scenario may prove to be the case, OY Car and Z Cha serve as examples in exercising caution before attributing fits of small-scale long-term

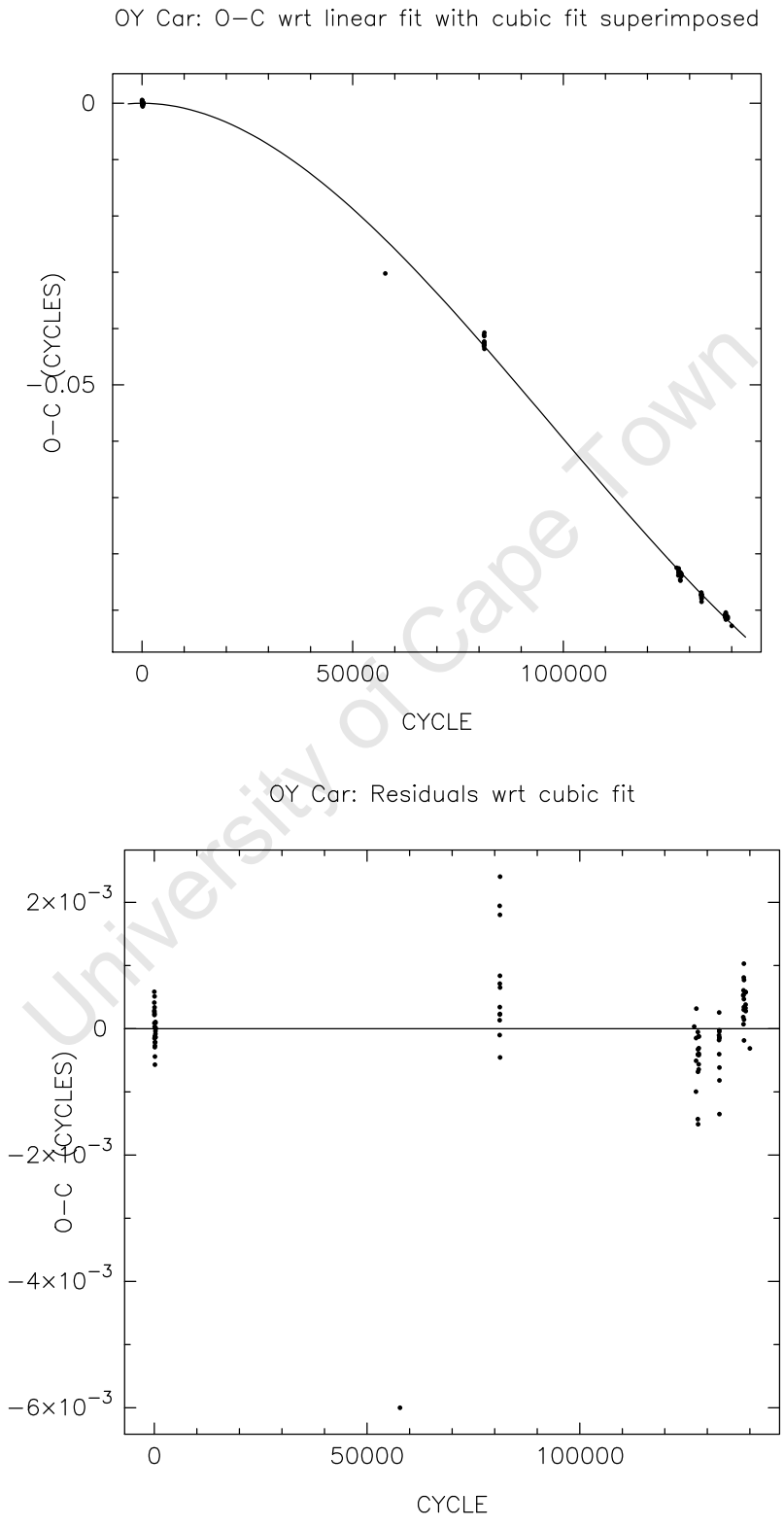

Figure 5.14: (Top) O-C plot compiled using optical timings from Wood *et al.* (1989), Pratt *et al.* (1999), Greenhill *et al.* (2006), and those obtained in this thesis, calculated with respect to a linear fit to the timings. A cubic fit is superimposed on the results, with the coefficients given in Table 5.11. (Bottom) Residuals with respect to the cubic fit.

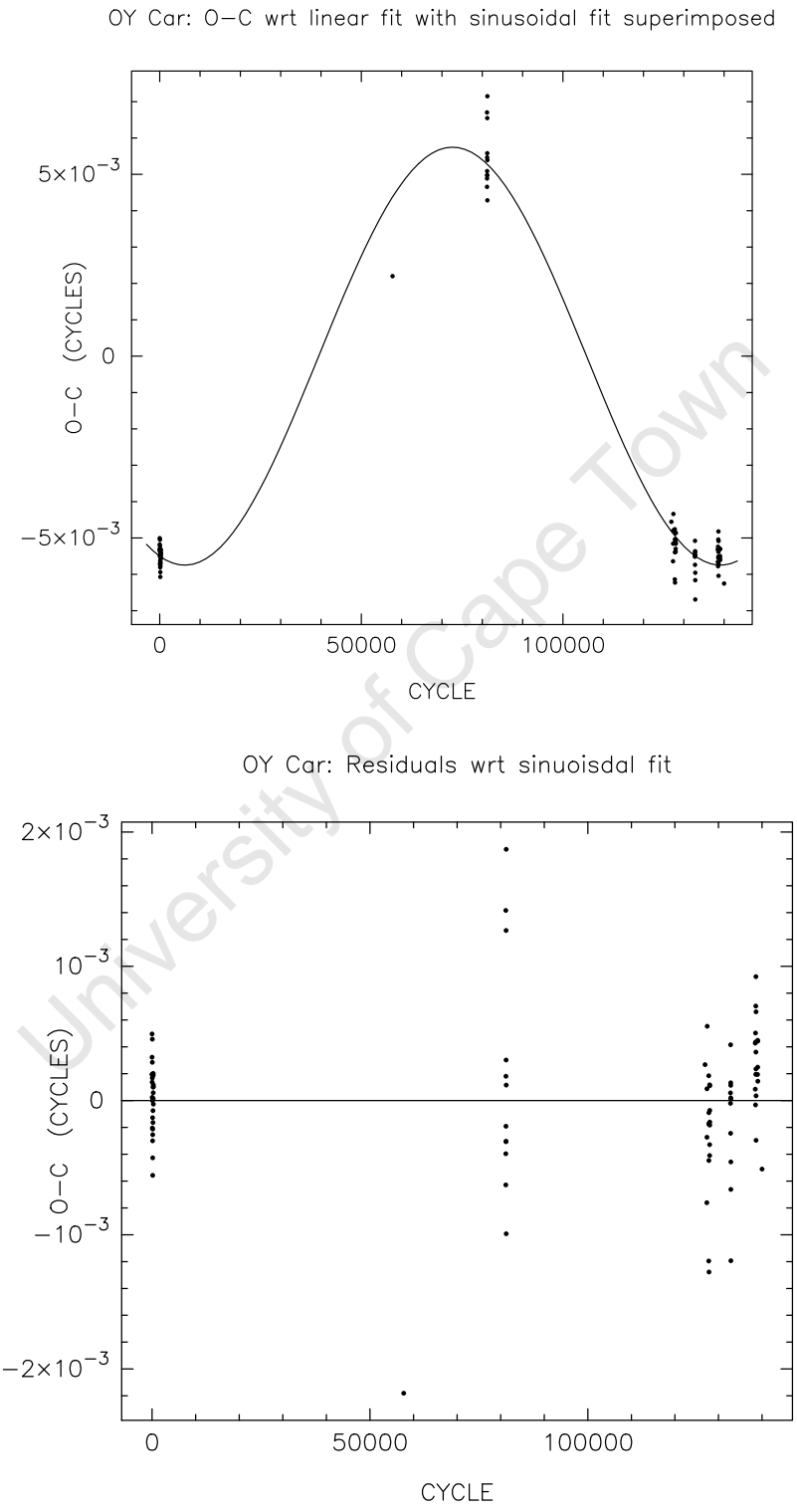

Figure 5.15: (Top) O-C plot compiled using optical timings from Wood *et al.* (1989), Pratt *et al.* (1999), Greenhill *et al.* (2006), and those obtained in this thesis, calculated with respect to a linear fit to the timings. A sinusoidal fit is superimposed on the results with the coefficients given in Table 5.11. (Bottom) Residuals with respect to the sinusoidal fit.

variations in limited data sets to a particular physical model.

Table 5.5: Z Cha: Times of mid-eclipse (BJED), symmetrised phases of half-flux of the central object and corresponding eclipse width.

Cycle	Mid-eclipse (BJED)	$\phi_{\mathrm{WDi/-e}}$	$\Delta\phi$
180496	2453711.504448	-0.0278	0.0559
180951	2453745.401962	-0.0272	0.0544
181165	2453761.344702	-0.0268	0.0536
181166	2453761.419125	-0.0268	0.0536
181180	2453762.462238	-0.0268	0.0536
181205	2453764.324803	-0.0266	0.0533
181206	2453764.399278	-0.0272	0.0544
181219	2453765.368027	-0.0311	0.0621
181220	2453765.442565	-0.0315	0.0631
181541	2453789.356419	-0.0275	0.0550
181607	2453794.273452	-0.0268	0.0536
181608	2453794.347956	-0.0268	0.0536
181929	2453818.262289	-0.0275	0.0550
181930	2453818.336625	-0.0263	0.0527
181956	2453820.273694	-0.0266	0.0531
181970	2453821.316631	-0.0261	0.0522
182090	2453830.256608	-0.0261	0.0522
182104	2453831.299565	-0.0266	0.0531
182117	2453832.268088	-0.0270	0.0541
184792	2454031.553567	-0.0266	0.0531
186159	2454133.393674	-0.0260	0.0521
Mean		**-0.0272**	**0.0545**
Std dev		**0.0014**	**0.0029**
Wood *et al.* 86		-0.0268/0.0266	0.0534
Std dev		0.0006	0.0012

Table 5.6: OY Car: Times of mid-eclipse (HJED), symmetrised phases of half-flux of the central object and corresponding eclipse width for the observing seasons 2006-2007.

Cycle	Mid-eclipse (HJED)	$\phi_{\mathrm{WDi/-e}}$	$\Delta\phi$
126912	2453763.471546	-0.0257	0.0513
126944	2453765.491442	-0.0252	0.0504
126945	2453765.554559	-0.0243	0.0486
127323	2453789.414260	-0.0260	0.0521
127339	2453790.424248	-0.0253	0.0506
127341	2453790.550549	-0.0266	0.0532
127402	2453794.400895	-0.0253	0.0506
127766	2453817.376893	-0.0253	0.0506
127767	2453817.440021	-0.0254	0.0509
127782	2453818.386790	-0.0253	0.0506
127783	2453818.449888	-0.0254	0.0508
127798	2453819.396708	-0.0249	0.0499
127799	2453819.459851	-0.0256	0.0512
127814	2453820.406595	-0.0250	0.0501
127971	2453830.316631	-0.0256	0.0512
127972	2453830.379757	-0.0256	0.0512
127973	2453830.442901	-0.0253	0.0506
127988	2453831.389697	-0.0259	0.0517
127989	2453831.452834	-0.0253	0.0506
128003	2453832.336515	-0.0259	0.0517
128004	2453832.399636	-0.0256	0.0512
132758	2454132.476420	-0.0256	0.0512
132759	2454132.539525	-0.0253	0.0506
132773	2454133.423237	-0.0257	0.0515
132789	2454134.433138	-0.0259	0.0517
132805	2454135.443095	-0.0253	0.0506
132806	2454135.506193	-0.0261	0.0523
132807	2454135.569292	-0.0257	0.0513
132821	2454136.452948	-0.0259	0.0517
132822	2454136.516133	-0.0259	0.0517
132836	2454137.399851	-0.0254	0.0509
132837	2454137.462979	-0.0253	0.0506

Continued in Table 5.7....

Table 5.7: OY Car: Times of mid-eclipse (HJED), symmetrised phases of half-flux of the central object and corresponding eclipse width for the observing season 2008.

Cycle	Mid-eclipse (HJED)	$\phi_{\mathrm{WDi/-e}}$	$\Delta\phi$
138429	2454490.435087	-0.0256	0.0513
138444	2454491.381880	-0.0258	0.0517
138492	2454494.411705	-0.0258	0.0517
138508	2454495.421610	-0.0264	0.0528
138509	2454495.484765	-0.0255	0.0510
138555	2454498.388307	-0.0256	0.0513
138556	2454498.451460	-0.0253	0.0505
138571	2454499.398252	-0.0256	0.0512
138572	2454499.461365	-0.0254	0.0507
138603	2454501.418122	-0.0259	0.0517
138619	2454502.428035	-0.0254	0.0507
138620	2454502.491135	-0.0258	0.0517
138967	2454524.394121	-0.0259	0.0517
138985	2454525.530313	-0.0256	0.0512
139014	2454527.360819	-0.0256	0.0512
139015	2454527.423921	-0.0256	0.0512
139048	2454529.513180	-0.0256	0.0512
139979	2454588.272436	-0.0256	0.0511
140059	2454593.332097	-0.0256	0.0512
Mean		**-0.0256**	**0.0511**
Std dev		**0.0004**	**0.0007**
Wood *et al.* 89		-0.0252/0.0253	0.0506
Std dev		-0.0004/0.0003	0.0004

Table 5.8: Bright spot mid-ingress, mid-egress and mid-eclipse phases relative to mid-eclipse for Z Cha

Cycle	$\phi_{\rm BSi}$	$\phi_{\rm BSe}$	$\phi_{\rm BS0}$
180496	-0.0047	0.0749	0.0351
180497	-0.0069	-	-
180951	-0.0109	0.0758	0.0325
181165	-0.0099	0.0805	0.0353
181166	-0.0095	0.0763	0.0334
181180	-0.0082	0.0769	0.0343
181192	-0.0090	0.0778	0.0344
181205	-0.0103	0.0746	0.0322
181206	-0.0110	0.0628	0.0259
181219	-0.0073	0.0775	0.0351
181220	-0.0099	0.0819	0.0360
181541	-	0.0873	-
181607	-	0.0820	-
181608	-	0.0861	-
181929	-0.0093	0.0783	0.0345
181930	-0.0149	0.0876	0.0364
181956	-	0.0783	-
181970	-0.0075	-	-
182090	-0.0131	0.0797	0.0333
182104	-0.0121	0.0789	0.0334
182117	-0.0131	0.0850	0.0360
184792	-0.0158	0.0811	0.0326
186159	-0.0064	0.0817	0.0377
Mean	**-0.0100**	**0.0793**	**0.0340**
Std dev	**0.0029**	**0.0054**	**0.0026**
Wood *et al.* 86	-0.0121	0.0787	-
Std dev	0.0010	0.0014	-

Table 5.9: Bright spot mid-ingress, mid-egress and mid-eclipse phases relative to mid-eclipse OY Car

Cycle	ϕ_{BS_i}	ϕ_{BS_e}	ϕ_{B0}	Cycle	ϕ_{BS_i}	ϕ_{BS_e}	ϕ_{B0}
126912	0.0002	0.0822	0.0412	138429	-0.0008	0.0745	0.0368
126944	-0.0004	0.0798	0.0397	138444	-0.0017	0.0764	0.0374
126945	0.0016	0.0791	0.0403	138492	-0.0017	0.0753	0.0368
127323	0.0006	0.0787	0.0396	138508	-0.0063	0.0764	0.0351
127339	0.0011	0.0787	0.0399	138509	-0.0035	0.0789	0.0377
127402	0.0011	0.0770	0.0391	138555	-0.0019	0.0767	0.0374
127766	-0.0016	0.0765	0.0375	138556	-0.0016	0.0760	0.0372
127767	-0.0031	0.0772	0.0371	138571	-0.0025	0.0773	0.0374
127782	0.0016	0.0792	0.0404	138572	-0.0030	0.0765	0.0368
127783	0.0021	0.0777	0.0399	138603	-0.0027	0.0748	0.0361
127798	0.0015	0.0801	0.0408	138619	-0.0033	0.0770	0.0368
127799	-0.0003	0.0767	0.0382	138620	-0.0016	0.0765	0.0375
127814	0.0008	0.0800	0.0404	138967	-0.0017	0.0759	0.0371
127971	-0.0008	0.0832	0.0412	138985	-0.0003	0.0778	0.0388
127973	0.0000	0.0792	0.0396	139014	-0.0003	0.0740	0.0369
127988	0.0011	0.0781	0.0396	139015	-0.0003	0.0745	0.0371
127989	0.0006	0.0803	0.0404	139048	-0.0003	0.0740	0.0369
128003	0.0006	0.0798	0.0402	139979	-0.0019	0.0795	0.0388
128004	0.0019	0.0773	0.0396	140059	0.0014	0.0701	0.0358
132758	0.0025	0.0751	0.0388				
132759	0.0017	0.0748	0.0382	**Mean**	**-0.0001**	**-0.0770**	**0.0385**
132773	0.0023	0.0750	0.0386	**Std dev**	**0.0020**	**0.0025**	**0.0016**
132789	0.0032	0.0789	0.0410	Wood *et al.* 89	-0.0005	0.0756	-
132805	0.0011	0.0748	0.0380	Std dev	0.0014	0.0025	-
132806	0.0025	0.0740	0.0382				
132807	0.0029	0.0773	0.0401				
132821	0.0017	0.0754	0.0385				
132836	0.0021	0.0741	0.0381				
132837	0.0018	0.0733	0.0375				

Table 5.10: Calculated ephemeris for Z Cha

Sinusoidal ephemeris	
$BJDD = T_0 + P_0E + A\cos[(2\pi E/C) + \phi)]$	
$T_0 = 2441660.501444(\pm 4)$ d	$A = (1.250 \pm 0.03) \times 10^{-3}$ d
$P_0 = 0.0744992826(\pm 3)$ d	$\phi = -1.91379 \pm 0.01778$
$\sigma = 6.9 \times 10^{-5}$ d	$C = 190x10^3$ cycles

Table 5.11: Calculated ephemerides for OY Car

Cubic ephemeris	
$HJED = T_0 + P_0E + AE^2 + BE^3]$	
$T_0 = 2445752.670872(\pm 11)$ d	$A = (-5.709 \pm 0.49) \times 10^{-13}$ d
$P_0 = 0.063120949(\pm 2.6)$ d	$B = (1.951 \pm 0.23) \times 10^{-18}$
$\sigma = 5.7 \times 10^{-5}$ d	
Sinusoidal ephemeris	
$HJED = T_0 + P_0E + A\cos[(2\pi E/C) + \phi]$	
$T_0 = 2445752.671225(\pm 10)$ d	$A = (3.628 \pm 0.14) \times 10^{-4}$ d
$P_0 = 0.06312090817(\pm 6.3)$ d	$\phi = -0.86107 \pm 0.03975$
$\sigma = 3.5 \times 10^{-5}$ d	$C = 132.84x10^3$ cycles

5.3 Modeling of Non-Spherical Binary Stars using the Roche model

The Roche model, introduced in Section 4.1.1, is named after the mathematician and astronomer Edourd Roche. It was developed as a solution to the restricted three body problem where a third infinitesimal mass moves in the gravitational field of two other massive bodies. Roche found that, for a range of potentials, Φ, experienced by the third body, a range of corresponding three dimensional surfaces could be constructed around the two point masses which represent the surfaces in space where the motion of the third particle, for a given *fixed energy*, would be zero relative to the two masses (Mireles James 2006). These zero-velocity surfaces[11] represent surfaces of constant gravitational potential. This has important consequences for describing the geometry of such systems as "the surface of a star is an equipotential surface, a description of these surfaces provides a means of quantifying the shapes of stellar surfaces in a binary system" (Hilditch 2001, p. 250). Unlike gravitational perturbation theory, the Roche model allows extension to systems with extreme tidal distortions (non-spherical).

The classic introductory text on Roche lobe geometry, Kopal's (1959) "Close Binary Systems", makes the simplest set of assumptions and so is most successfully used for systems where the components can be considered as point masses and their orbits circular[12]. The Roche model also assumes the absence of any other force such as radiation pressure or stellar wind (Darling 2007). The relevant sections of Kopal's work on Roche lobe geometry and the Roche model are summarised.

When modeling binary systems one must take into consideration the fact that axial rotation and tidal interactions cause the shape of the binary components to depart from a sphere. For simplicity we would like to consider a theory of equipotentials where second order and higher powers of axial rotation and tidal pull are negligible. This applies to centrally condensed systems which have such high densities that they can be approximated as point masses.[13]

A further simplifying assumption is that there exists in the system an equilibrium theory of tides. This supposes that the stars can adjust to the effects of rotational and tidal distortions relatively quickly in comparison with the period of the orbit. The stars must adjust adiabatically so that mass exchange is *not* proceeding at a rate such that

[11] So called zero-velocity because they are equilibrium surfaces under the influence of the two masses and therefore cannot expand or shrink (Kopal 1959).

[12] Later techniques developed by Lucy (1968) and Rucinski (1973) allowed analysis of systems which are clearly non-spherical and where mutual interactions (such as the reflection effect) cannot be ignored (Hilditch 2001).

[13] This is not such a bad approximation as most stars are centrally condensed, with some $85\% - 95\%$ of the total mass contained within the inner 50% of its radius for zero age main-sequence stars (Kippenhahn and Weigert 1991).

the stars cannot maintain hydrostatic equilibrium (and are thus changing on a dynamical timescale). In systems where these assumptions hold, we can assume that within the system "level surfaces of constant density coincide with those of constant potential", the boundary of zero density being the special case (Kopal 1959).

Kopal's formulation takes the centre of gravity of mass m as the origin of the system, giving the coordinates of the centre of gravity for the binary as: $\left(\frac{m'R}{m+m'}, 0, 0\right)$ where R is the orbital separation, $m = m_2$ and $m' = m_1$. The angular velocity is taken to be Keplerian i.e: $\omega^2 = G(m + m')/R^3$. In rectangular coordinates, the x-axis lies along the line of centres and the z-axis lies along the axis of rotation.

With these assumptions, the resulting potential at an arbitrary point $P(x, y, z)$, is the sum of three terms: the potential arising from the distorted mass component m, the disturbing potential of mass m' and the potential arising from the centrifugal force[14]. In spherical components this potential is Ω (Kopal 1959, p. 127):

$$\Omega = \frac{1}{r} + q\left\{\frac{1}{r'} - \lambda r\right\} + \frac{q+1}{2}r^2\left(1 - \nu^2\right) \tag{5.1}$$

where Ω is the potential of an arbitrary point at distance $r' = \sqrt{1 - 2\lambda r + r^2}$ from m' and r from m, $\lambda = \cos\phi \sin\theta$ and $\nu = \cos\theta$ (as given by spherical polar coordinates). Setting $\Omega = constant$ defines surfaces of constant potential. These are the Roche potentials.

The analysis of the equation for Ω is simplified by noting that if Ω is large then r or r' (distances of an arbitrary point from m and m' respectively) must be small, due to the $1/r$ and $1/r'$ dependence of the gravitational potential. Therefore, close to the centre of each star, the surfaces differ little from spheres. As Ω becomes smaller, the equipotentials become tear-drop shaped, elongated in the direction of the centre of mass (along the line of centres). A critical equipotential surface lies where each star's respective equipotential unite at a single point on the x-axis. This equipotential forms a two-lobed figure of eight, each lobe centred on a component star (see Figure 4.1). The intersection (or 'saddle-point') is known as the inner Lagrange point, usually desnoted by L_1, and occurs at a certain critical value for $\Omega = \Omega_1$. Ω_1 is known as the Roche limit; the limit at which matter remains gravitationally bound to its parent star. The lobes, defined by Ω_1, are known as the Roche lobes. Any star filling its Roche limit is called a contact component. As can be seen from equation (5.1) the mass ratio q determines the geometry of the system. Hence mass loss from the secondary and the resulting angular momentum

[14] Added because we have changed to the rotating reference frame. This is equivalent to the potential felt at the surface of a star since the axial rotation of the star and orbital motion are locked.

exchange can be well described using Roche geometry.

Equation (5.1) gives $r(\lambda, \nu)$ for known values of Ω and q. Analytical solutions to this equation are not easy to derive. Approximate solutions can be found involving Legendre polynomials and an expansion of r_0 where the first approximation $r_0 = 1/(\Omega - q)$ is defined as the Roche equipotential for large Ω (approximately a sphere of radius r_0). This approximation assumes that r is small compared to unity (i.e. the orbital separation[15], R).

For application to cataclysmic variables, we want to look at contact configurations i.e. to determine Ω where the critical equipotentials make contact at L_1. This can be solved for by noting that L_1 is characterised by the vanishing of gravity due to all forces:

$$\frac{\partial}{\partial x}\Omega = \frac{\partial}{\partial y}\Omega = 0$$

Kopal (1959) lists Ω_1 and x_1 for a range of mass ratios. These have provided approximate initial values for computational solutions which use the Roche model to specify equipotential surfaces. The `roche` program described in the next section is an example of such a computational model.

5.4 The `roche` program

The Roche model was first used as the basis for calculating a theoretical light curve binary system for the contact binary W UMa by Lucy (1968a, 1968b). W UMa consists of two Roche lobe filling components and Lucy's analysis introduced the now well-established concept of convective envelopes. As both stars filled their Roche lobes, a range of stellar surfaces were mapped. Light curve synthesis models following this work became more generalised until Hill & Hutchings (1970) presented general numerical codes which offered complete accounts for reflection effect and gravitational distortion. Analysis of cataclysmic variables essentially requires the mapping of one equipotential surface, the Roche lobe surrounding the primary and the secondary star.

The `roche` program, written and developed by Darragh O'Donoghue of the SAAO, is based on the light curve synthesis work of Horne (1985) and provides a computational solution to the problem of modeling eclipsing, semi-detached binaries. Specifically, `roche` is a light-curve synthesis program which models the Roche geometry of a particular system and computes the corresponding light curve of light emitted from the primary Roche lobe

[15]Note that R is Kopal's notation for the orbital separation. In the remainder of this chapter the orbital separation is denoted by the modern conventional notation, a.

and eclipsed by the contact secondary. It was most recently employed to model eclipses of the white dwarf primary of the CV SDSS J015543.40 +002807.2, (O'Donoghue *et al.* 2006). The task of light curve synthesis is to calculate the total flux emitted by the white dwarf along the line of sight at a particular phase in the orbit. In cylindrical coordinates, this is a summation over all visible surface elements:

$$F = \sum_j I_j \left(\cos\gamma\right) \cos\gamma \Delta S_j$$

where ΔS_j is the area of each surface element at position (ρ, ϑ, x) on the white dwarf, $\cos\gamma$ is the angle between the local surface normal and the line of sight and I_j are the specific intensities emitted in direction γ (Hilditch 2001).

The `roche` program takes as input parameters the mass ratio q, the inclination i, the white dwarf radius r_{wd} and the orbital phase ϕ. The program accepts further options relating to the representation of the white dwarf such as setting up a grid of θ and ϕ elements over the surface of the white dwarf, incorporating a flux distribution and creating polar accretions spots. To synthesise light curves for SU UMa stars such as OY Car and Z Cha, an accurate surface flux distribution for the accretion disc would be needed, as well as an appropriate distribution to describe the bright spot and its orbital modulation. However only the location of the bright spot is of interest here, not the accurate representation of the total flux of the system. Therefore eclipse mapping and subsequent modeling of the accretion disc has been left out of the present analysis.

5.4.1 Modelling the Accretion Stream

To model the trajectory of the incomming accretion stream `roche` first uses the given input parameters to determine Ω, the position of L_1, and the shape of the secondary Roche lobe. `roche` then uses single particle trajectories to determine the position and motion of the accretion stream. One might expect a hydrodynamical approach to be a better representation, due to the high densities present in the stream and "...since the mean free path in the flow regions is many orders of magnitude smaller than the orbital separation" (Flannery 1975) . However it has been found (Lubow & Shu 1975) that particle stream trajectories can well describe the motion of the gas stream because the effects of finite gas pressure can be ignored to a large extent throughout a large part of the flow. The concern regarding the mean free path becomes relevant only if the ballistic trajectories of the particles try to cross one another (Lubow & Shu 1975) but, because of the high densities present in the stream, in reality such particles would be swept along by the general stream motion (Warner & Peters 1972). Therefore we can assume that

the mean motion of the stream can be approximated by a single particle trajectory where hydrodynamic considerations are negligible.

The algorithm used by `roche` to compute the stream's trajectory is that developed by Warner & Peters (1972) and corrected by Flannery (1975). The algorithm was used to provided a set of computations calculating the size and location of the bright spot as a function of mass ratio. The computations were made for the simplest model of mass transfer in semi-detached systems and makes the following assumptions:

(i) That due to the balance of all forces at L_1, the stream material is "evaporated" with thermal velocities through L_1.

(ii) That 'the dimensions of the stream will be determined by the forces that dominate single particle trajectories' (Warner & Peters 1972), as opposed to hydrodynamics.

(iii) That the travel time from L_1 to the bright spot is short, ($\sim 10^3$s) so that the stream's thermal velocity distribution cannot depart significantly from its original distribution at L_1.

The trajectory is calculated according to the two-dimensional restricted[16] three-body problem. A corotating coordinate system is used where the primary is located at (1,0) and the secondary is at (0,0). In these coordinates the equations of motion are (Warner & Peters 1972):

$$\ddot{x} = 2\dot{y} - \frac{\mu x}{r_2^3} + \frac{(1-\mu)(1-x)}{r_1^3} + x + \mu - 1$$

$$\ddot{y} = -2\dot{x} - \frac{\mu y}{r_2^3} + \frac{(1-\mu)y}{r_1^3} + y$$

where $\mu = M_2/(M_1 + M_2)$, r_1 and r_2 are the distances to the primary and secondary respectively. Warner and Peters integrated these equations using a sixth order Runga-Kutta integration scheme. The specific angular momentum of the particle, j_t calculated at each iteration, was used to calculate the radius at which the particle would be orbiting the primary if it occupied a Keplerian orbit with the same angular momentum. Flannery corrected the Warner and Peters formulation by noting that they had neglected the fact that, in the corotating reference frame, particles at L_1 have an initial angular momentum.

The `roche` program uses the motion of a single particle to map out the mean motion of the stream. The particle is given an initial velocity equal to its mean thermal velocity

[16] The two stars are considered to be so centrally condensed that the effects of departures from sphericity can be ignored and the stream of particles have negligible mass.

at L_1 and the path of the stream is mapped using a fourth order Runga-Kutta integration scheme. The path of the particle is checked using a quantity known as the Jacobi energy, which is conserved along the trajectory in the corotating reference frame:

$$E_J = \dot{x}^2 + \dot{y}^2 - 2\Omega\,(x, y)$$

After integration the final Jacobi energy is compared to its initial value to ensure that the values do not differ by more than 0.0001.

The `roche` trajectory subroutine returns the position and velocity components for particles at each point along the trajectory. The mapping of the stream was chosen to be well defined such that the spatial resolution was at least double that of the temporal resolution i.e. for each step in phase in the orbital cycle, (a single step being equivalent to the average integration time used during the observations divided by the orbital period) at least two discrete points marked the path of the stream in phase space.

We now turn to measuring the accretion disc radii using the phases listed in Tables 5.8-5.9.

5.4.2 Using `roche` to Locate the Bright Spot

As described in Section 4.1, detecting disc radii variations in OY Car and Z Cha is the focus of the present investigation. The problem of determining the radius of an accretion disc is effectively reduced to the problem of locating the position of the bright spot, which is assumed to be at the edge of the accretion disc. The position of the bright spot is best determined in the *phase* plane where the phases of mid-egress *vs.* mid-ingress of the bright spot for each cycle are plotted. Plotting this position for different eclipses reveals any change in the bright spot position over time. Plots of the bright spot positions in the *orbital* plane will also show if there are significant variations in the position of the bright spot (and hence the disc radius). However, as pointed out by Wood *et al.* (1989a), even for a stationary bright spot, random errors in the measurements of the phases of mid-ingress and mid-egress of the bright spot, ϕ_{BS_i} and ϕ_{BS_e}, produces an elongation of the bright spot positions along the stream trajectory when mapped in the orbital plane. Therefore evidence for intrinsic disc variations must be obtained from examining the ingress-egress phase diagrams.

Just as plotting phases of mid-egress *vs.* mid-ingress reveals the position of the bright spot in the phase plane, plotting phases of mid-egress *vs.* mid-ingress for points along the theoretical stream trajectory reveals the path of the particle stream in the same plane. Making the assumption that the stream trajectory passes through the bright spot

(Lubow & Shu 1975, Pringle 1977) provides the means to determine the location of the bright spot in physical coordinates: any variation in the bright spot position is expected to occur along the stream, thus identifying bright spot positions with points along the stream in phase space, allows an approximate mapping of the bright spot positions to (xyz) Cartesian coordinate space. All that is required to define the path of the stream in phase space is to determine the phases of ingress and egress for all the points along the trajectory.

Determining when a point along the trajectory is eclipsed can be achieved using the same techniques employed by `roche` for determining whether or not any particular point in the primary Roche lobe is visible at a particular phase angle.

There are a number of techniques to determine whether or not a surface element is eclipsed. One procedure employed by Wilson & Devinney (1971) is to define the shape of the eclipsing object projected onto the sky at a particular phase angle. The centre of the eclipsing star is used as the origin of the coordinate system. "The projected distance onto the sky of the surface element on the eclipsed star is compared with the shape of the eclipser at that phase" (Hilditch 2001). If the projected distance is less than the radial size of the eclipser, then the surface element is not visible at that phase angle.

The technique used in the `roche` program is that of Mochnacki & Doughty (1972a, 1972b). Here the normalised potential, Φ, is sampled at discrete points along the line of sight. If any of these values are greater than the value of Φ which defines the Roche lobe of the eclipsing star (the secondary) then the line of sight must be intersecting the surface of the eclipsing star and therefore that surface element on the central, primary star, is not visible. This ray-tracing technique is what was used here to determine whether a particular point along the stream trajectory (instead of a surface element on the white dwarf) was eclipsed.

To determine which points along the trajectory were eclipsed at a given phase, a `roche` subroutine previously used to determine which surface elements on the surface of the white dwarf were eclipsed was modified to take the points along the trajectory as inputs instead. The ray tracing technique used by this subroutine is described below.

The system is parameterised by the phase angle, ϕ and the inclination, i. For each point of interest, along the trajectory (x_0, y_0, z_0), parallel lines of sight (s) are drawn from (x_0, y_0, z_0) to the observer at infinity. $s = (x, y, z)$ where

$$x = x_0 + s\hat{\imath}$$

$$y = y_0 + s\hat{j}$$

$$z = z_0 + s\hat{k}$$

and $\hat{\imath}$, $\hat{\jmath}$ and $\hat{\mathrm{k}}$ are the unit vectors along the line of sight:

$$\hat{\imath} \longrightarrow \sin i \cos \phi$$
$$\hat{j} \longrightarrow \sin i \sin \phi$$
$$\hat{k} \longrightarrow \cos i$$

The algorithm begins at the point along the line of sight which is closest to the surface of the secondary. This is calculated by making the centre of the secondary (1, 0, 0) so that the perpendicular distance from the point (x, y, z) on s to the centre of the secondary is given by:

$$d^2 = ((x_0 + s\hat{\imath}) - 1)^2 + \left(y_0 + s\hat{j}\right)^2 + \left(z_0 + s\hat{k}\right)^2$$

The initial point (x_0, y_0, z_0) is found by minimising this function, i.e. $\frac{d(d^2)}{ds} = 0$. Then $\frac{d\Omega}{ds} \cdot s$ is calculated to obtain the variation of Ω along s where

$$\frac{d\Omega}{ds} = \left(\frac{\partial \Omega}{\partial x}, \frac{\partial \Omega}{\partial y}, \frac{\partial \Omega}{\partial z}\right)$$

`roche` determines if the point (x_0, y_0, z_0) is eclipsed by progressing along the line of sight, s, in the direction of decreasing Ω until a minimum value for Ω is found. If the minimum is less than Ω_1 then the line of sight passes through the secondary and (x_0, y_0, z_0) on the stream is eclipsed.

Ultimately one can obtain a table of values showing, for each point along the trajectory, the phases of ingress and egress.

5.5 Eclipse Timing Analysis

Figures 5.16 and 5.17 show the ingress-egress phase diagrams for OY Car and Z Cha. The ingress-egress phases for the white dwarf are plotted to indicate its relative position.

The measurement errors in the *individual* bright spot phase positions are indicated by the error bars on the *mean* bright spot positions in Figures 5.16 and 5.17 (top). The white dwarf phase positions lie on the line $\phi_{\mathrm{WDi}} = -\phi_{\mathrm{WDe}}$. This is an artifact of the interaction of a varying eclipse width and the fact that, during the phasing of the JD timings, the white dwarf ingress/egress times are forced to be symmetrical about $\phi = 0$. Therefore any changes in the mid-ingress and/or mid-egress position (and, consequently, the eclipse width), relative to some average reference position, results in the movement of the white dwarf phase position along the $\phi_{\mathrm{WDi}} = -\phi_{\mathrm{WDe}}$ line. It should be noted that

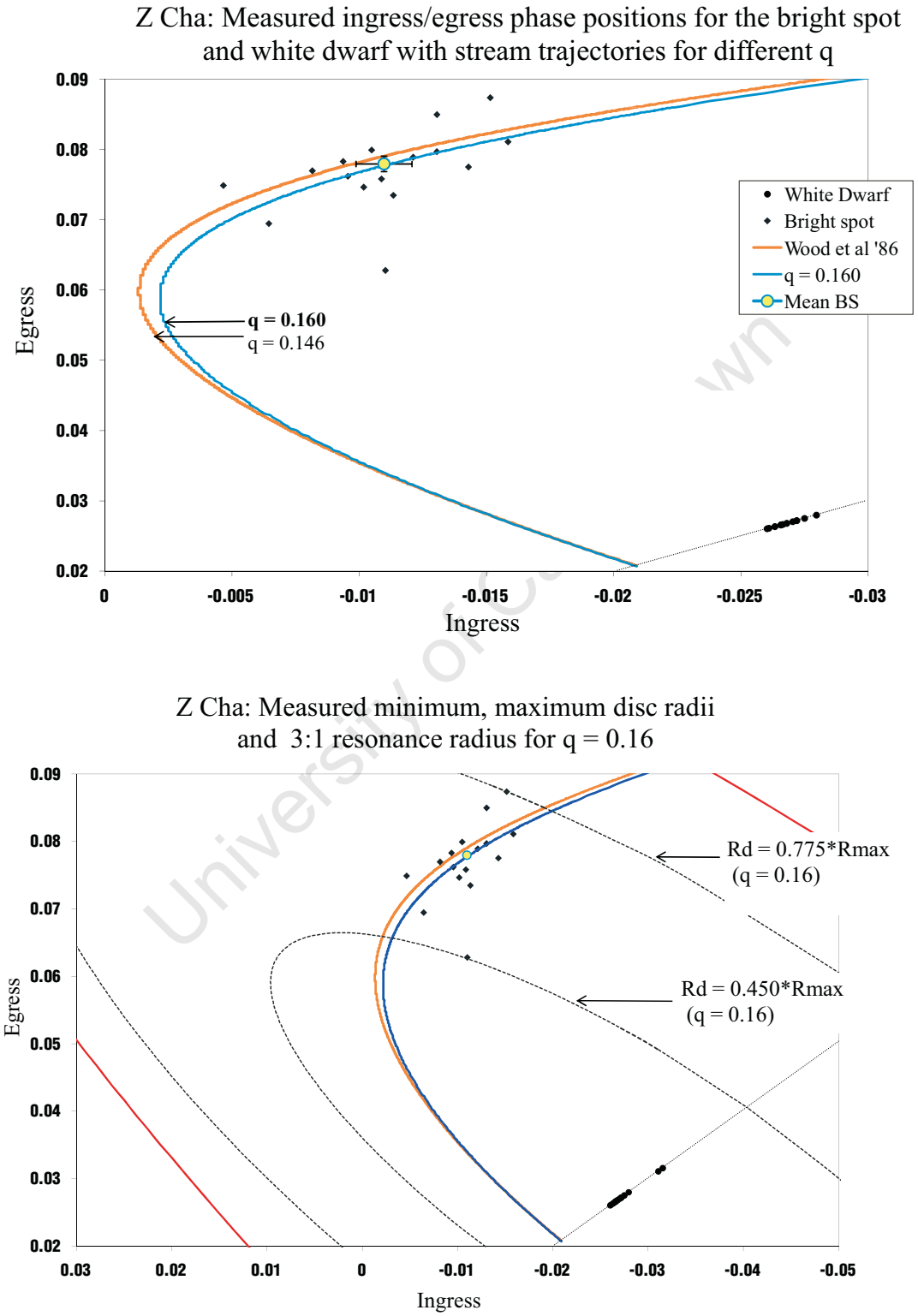

Figure 5.16: Phase diagrams plotting egress *vs.* ingress of the measured bright spot and white dwarf phase positions for Z Cha. The yellow circle indicates the bright spot's average position. Phase positions for stream trajectories (corresponding to different mass ratios, top) and different radii of the disc (bottom) have been included. The red line (bottom) indicates the phase position for the 3:1 resonance radius, r_3. $R_{\max} = \frac{R_{d(max)}}{a}$ is the tidal truncation radius as defined in Section 4.1.3. Note the error bars in the top plot indicate the estimated error in the *individual* timings, an not in the mean. See text for further details.

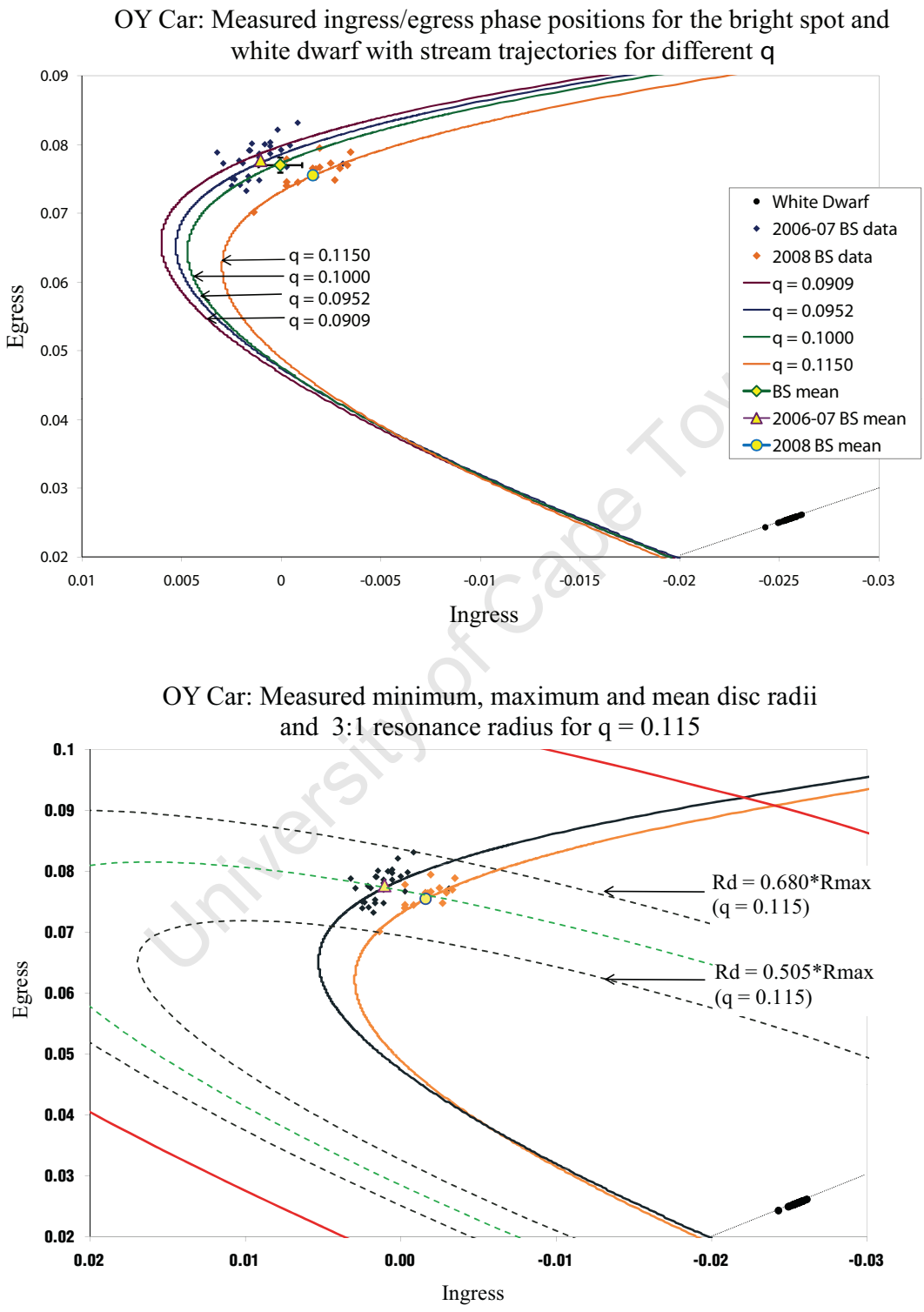

Figure 5.17: Phase diagrams plotting egress *vs.* ingress of the measured bright spot and white dwarf phase positions for OY Car. Phase positions for stream trajectories (corresponding to different mass ratios, top) and different disc radii (bottom) have been included. The red line (bottom) indicates the phase position for the 3:1 resonance radius, r_3. Note the error bars in the top plot indicates the estimated error in the *individual* timings, an not in the mean. See text for details.

there was no correlation found between the scatter in the bright spot phase positions and this symmetric movement of the white dwarf in phase.

As discussed in the the previous section, a fundamental assumption in our approach is that the locus of the mass-transfer stream passes through the light centre of the bright spot for all eclipses. The stream trajectory in phase space is solely prescribed by the mass ratio and inclination (q, i), thus these parameters can be constrained by enforcing the condition that the gas stream passes through the bright spot position in phase space (hereafter referred to as the 'stream-constraint'). The top plots of Figures 5.16 and 5.17 show the stream trajectories determined by `roche` (see section 5.4) for a range of (q, i) combinations. This has led to revised estimates of (q, i) for OY Car and Z Cha, summarised in Table 5.12 with associated uncertainties. These can be compared to the most popularly used published estimates (quoted in Table 5.1); for Z Cha (q, i)=$(0.149 \pm 0.003, 81.8 \mp 0.2)$ (Wood *et al.*, 1986) and OY Car (q, i)=$(0.102 \pm 0.003, 83.3 \mp 0.2)$ (Wood *et al.*, 1989a). The mass ratio most strongly determines the trajectory of the stream and, conversely, the uncertainty in the bright spot position is the greatest source of uncertainty in q. The uncertainties in q given in the tables are determined from the measurement uncertainty in the bright spot timings, although this should be considered a significant underestimation[17]; Figures 5.16 and 5.17 clearly show that the greatest source of uncertainty in q is the inherent scatter in the bright spot positions (see Sections 5.5.1 and 5.5.2 for further details of this discussion). The uncertainties in inclination are quoted as associated with the quoted uncertainties in q. It should be noted that an additional source of uncertainty in (q, i) stems from the observed range in the white dwarfs' eclipse width, $\Delta\phi$. For a range of $\Delta\phi$, there is a range of (q, i) parameters which still satisfy the 'stream-constraint'. This is not commented on in the literature, most likely because the range in q which this characteristic prescribes is negligible in comparison to the measurement uncertainty. The range in i, however, is comparable to the measurement uncertainty. As shall be seen in Section 6.2.4 in the next chapter, this additional source of uncertainty originating from the range in $\Delta\phi$ becomes important in both the determination of q and i when there are very few bright spot timings available to define clearly a choice of q.

The disc radius for each eclipse was determined visually by plotting a series of disc radii in phase space and identifying the nearest disc radius to the bright spot phase position for that eclipse. The minimum and maximum measured disc radius positions found for each object are plotted as the black dashed lines in the bottom plots of Figures 5.16 and 5.17. The red lines indicate the 3:1 resonance radius at which, theory predicts, the disc becomes

[17]However an accurate mass ratio is not necessary to determine a *relative* change in the position of the bright spot (Cook 1985a).

Table 5.12: OY Car and Z Cha: Binary parameters

	Z Cha	OY Car
q	0.160 ± 0.008	0.115 ± 0.003
i	$81.4 \pm 0.1°$	$82.7 \pm 0.3°$
R_d/a	0.3149 ± 0.0024	0.3130 ± 0.0036

tidally unstable at the onset of superoutburst. The disc radii were plotted as fractions of the tidal truncation radius, $R_{\max} = \frac{R_d(max)}{a}$ (see Section 4.1.3). The measurements are accurate to within $0.0025 * R_{\max}$, significantly smaller than the error introduced by the estimated error in the timings. Tables 5.13 and 5.14 give the resulting disc radii for OY Car and Z Cha along with the approximate error (estimated from the average error in the bright spot positions). The means of the disc radius measurements are also quoted in Table 5.12.

For each cycle, the dates of the nearest preceding and following outbursts, and *superoutbursts*, were identified from archival data obtained from the Variable Star Section of the Royal Astronomical Society of New Zealand (RASNZ) and the American Association of Variable Star Observers (AAVSO). Thus, for each star, two sets of plots were created to determine any correlation between disc size and outburst times. One set consisted of a plot of disc radius *vs.* time since last outburst, disc radius *vs.* time before next outburst and disc radius *vs.* fractional time between outbursts, where no distinction is made between the type of outburst. The other set plotted disc radius *vs.* time since last superoutburst, disc radius *vs.* time before next superoutburst and disc radius *vs.* fractional time between superoutbursts. Note that in the rest of this chapter the term 'normal cycle' (or 'normal outburst cycle') refers to the short outburst cycles where the intervals are commenced and terminated with either kind of outburst: a superoutburst or a normal outburst. The term 'supercycle' refers to the long outburst cycles which are commenced and terminated only by superoutbursts and within which normal outburst cycles occur.

The OY Car and Z Cha data sourced from the RASNZ and AAVSO archives, for the period of observation presented in this work, are plotted and shown in Appendix D as example of the coverage supplied by these archives of amateur data. The identification of normal outbursts was not easy, and the coverage of the author's period of observation

displayed was better than the relatively poor coverage of the periods of observation in the literature. Superoutbursts, by their nature, were far easier to identify and the author is confident that all superoutbursts occuring during the relevant periods were found. Consequently, it should be noted that, in Figures 5.18-5.19 and 5.22-5.23, where normal outburst could not be confidently identified or were suspected to be missed, the relevant data points are not included in the plots. This applies to a total of four data points from the Cook and Warner (1984) series (Z Cha) and three data points from my own set (OY Car). Criteria for how dates of normal and superoutburst were selected are discussed in Appendix D.

5.5.1 Z Cha

Mass ratio determination

The scatter in the bright spot phase positions perpendicular to the direction of the stream trajectory (refer to Figure 5.16) is most likely due to downstream (off-stream) movement of the bright spot along the rim of the disc. However, the small number of data points available for Z Cha does not allow for a stream trajectory corresponding to a maximal estimate of the mass ratio to be confidently identified. Thus a mass ratio/inclination parameter pair (corresponding to the average eclipse width given in Table 5.5) was chosen so that the prescribed stream trajectory simply passed through the mean bright spot position. This trajectory corresponds to the blue curve in Figure 5.16. The orange curve is the trajectory determined by the (q, i) pair chosen by Wood *et al.* (1986) to fit their measurements.

Variation of Disc Radius with Outburst

Figures 5.18 and 5.19 show the measured disc radius positions obtained from Figure 5.16 and given in Table 5.13. These have been combined with the disc radius positions published previously by Cook and Warner (1984), Wood *et al.* (1986) and O'Donoghue (1986).

Figures 5.18 (top), 5.18 (bottom) and 5.19 show disc radius versus time since last outburst, time before next outburst and fractional time between outburst respectively, essentially reproducing the plots presented in O'Donoghue (1986) (with the omission of Cook's data[18]). The error bars represent the errors in disc radius measurements arising

[18]Cook (1985a) also obtained disc radius measurements for Z Cha from a number of optical measurements using a mass ratio $1/q = 5$. However, when the bright spot phases were plotted in a phase diagram along with the stream trajectories shown here, the scatter in the bright spot egress measurements was considered too large to yield any useful results. Therefore

Table 5.13: Disc radius measurements for Z Cha

$q = 0.160$		
Date BJED - 2450000 (mid-eclipse)	Cycle	R_d/a
3711.504	180496	0.2850
3745.402	180951	0.3085
3761.345	181165	0.3308
3761.419	181166	0.3060
3762.462	181180	0.3060
3764.325	181205	0.2998
3764.399	181206	0.2243
3765.368	181219	0.2949
3765.443	181220	0.3296
3818.262	181929	0.3184
3818.337	181930	0.3816
3830.257	182090	0.3370
3831.300	182104	0.3308
3832.268	182117	0.3655
4031.554	184792	0.3569
4133.394	186159	0.2627
	Mean	0.3149
	Std dev	0.0388
	∼Error	0.0024

Table 5.14: Disc radius measurements for OY Car. The dates with asterisks indicate measurements made from SALT observations presented in the next chapter.

$q = 0.115$					
Date HJED - 2450000 (mid-eclipse)	Cycle	R_d/a	Date HJED - 2450000 (mid-eclipse)	Cycle	R_d/a
3763.472	126912	0.3437	4490.435	138429	0.2994
3765.491	126944	0.3332	4491.382	138444	0.3150
3765.555	126945	0.3228	4494.412	138492	0.3072
3789.414	127323	0.3228	4495.485	138509	0.3359
3790.424	127339	0.3202	4498.388	138555	0.3176
3794.401	127402	0.3098	4498.451	138556	0.3124
3817.377	127766	0.3150	4499.398	138571	0.3228
3817.440	127767	0.3254	4499.461	138572	0.3189
3818.387	127782	0.3228	4501.418	138603	0.3072
3818.450	127783	0.3124	4502.428	138619	0.3241
3819.397	127798	0.3280	4502.491	138620	0.3150
3819.460	127799	0.3124	4524.394	138967	0.3085
3820.407	127814	0.3293	4525.530	138985	0.3189
3830.317	127971	0.3541	4527.361	139014	0.2942
3830.443	127973	0.3267	4527.424	139015	0.2968
3831.390	127988	0.3176	4529.513	139048	0.2942
3831.453	127989	0.3319	4588.272	139979	0.3359
3832.337	128003	0.3280	4593.332	140059	0.2630
3832.400	128004	0.3085			
4132.476	132758	0.2942	4584.313*	139916	0.3150
4132.540	132759	0.2942	4584.376*	139917	0.3385
4133.423	132773	0.2929			
4134.433	132789	0.2919		Mean	0.3130
4135.443	132805	0.2955		Std dev	0.0176
4135.506	132806	0.2864		$\sim$ Error	0.0039
4135.569	132807	0.3072			
4136.453	132821	0.2981			
4137.400	132836	0.2890			
4137.463	132837	0.2838			

from the errors in the times of eclipse contacts.

The measurements compiled from the literature cover six outburst[19] intervals, where the outburst is either a superoutburst or a normal outburst, while the measurements derived here cover an additional four. Where mass ratios used in the literature differed significantly from the value determined here, the average shift needed to calibrate previous disc radius measurements with those determined here was estimated. This shift is indicated in Figures 5.18 to 5.21 by error bars. Hence the error bars indicated on O'Donoghue's (1986, referred to as 'DOD 1986' in the plots), and Wood *et al.*'s (1986) data points indicate that their measurements should be shifted downwards by the corresponding amount for comparison with the author's measurements (Cook & Warner's data points - referred to as 'C&W 1984' in the plots - corresponding to $1/q = 6$, required a negligible movement).

The results in Figure 5.18 (top) are broadly consistent with a steady decline in the size of the disc of ~ 0.001 units of orbital separation per day after outburst, though with some added scatter. The small disc radius, however, observed at ~ 40 and ~ 75 days are due to the fact that the observations were less than 20 days before the next outburst. This indicates that analysing the measurements following outburst does not give the least scatter due to the large variability in outburst intervals. The results presented in Figure 5.18 (bottom) tentatively confirm the result of O'Donoghue (1986) that the disc seems to undergo an abrupt decrease in size just before outburst.

As was noted in O'Donoghue (1986), the trend with the least scatter is seen in the plot showing disc radius versus fractional time between outbursts (Figure 5.19). This suggests that the conditions necessary for outburst are a function of inter-dependent physical parameters as opposed to simply a function of time. The TTI model would suggest that the variable outburst intervals is an indication that the disc shrinks at different rates.

O'Donoghue did not find any significant differences between the disc radius following a superoutburst and those following a normal outburst. This is illustrated in Figure 5.20, where 5.19 has been reproduced differentiating between observations made following a superoutburst and those preceding one. The data label 'Next outburst superoutburst' indicates data points which were taken in the normal cycle leading up to a superoutburst. The data label 'Previous outburst superoutburst' indicates the data points that were taken in the normal cycle immediately following a superoutburst and the data label 'Between normal outbursts' indicates data points that were taken during normal cycles where the

Cook's findings were left out of this analysis.

[19] Unless otherwise specified, the reader should take "outburst" to refer to both superoutbursts and normal outbursts. Distinction is only made in the text when one type of outburst is examined.

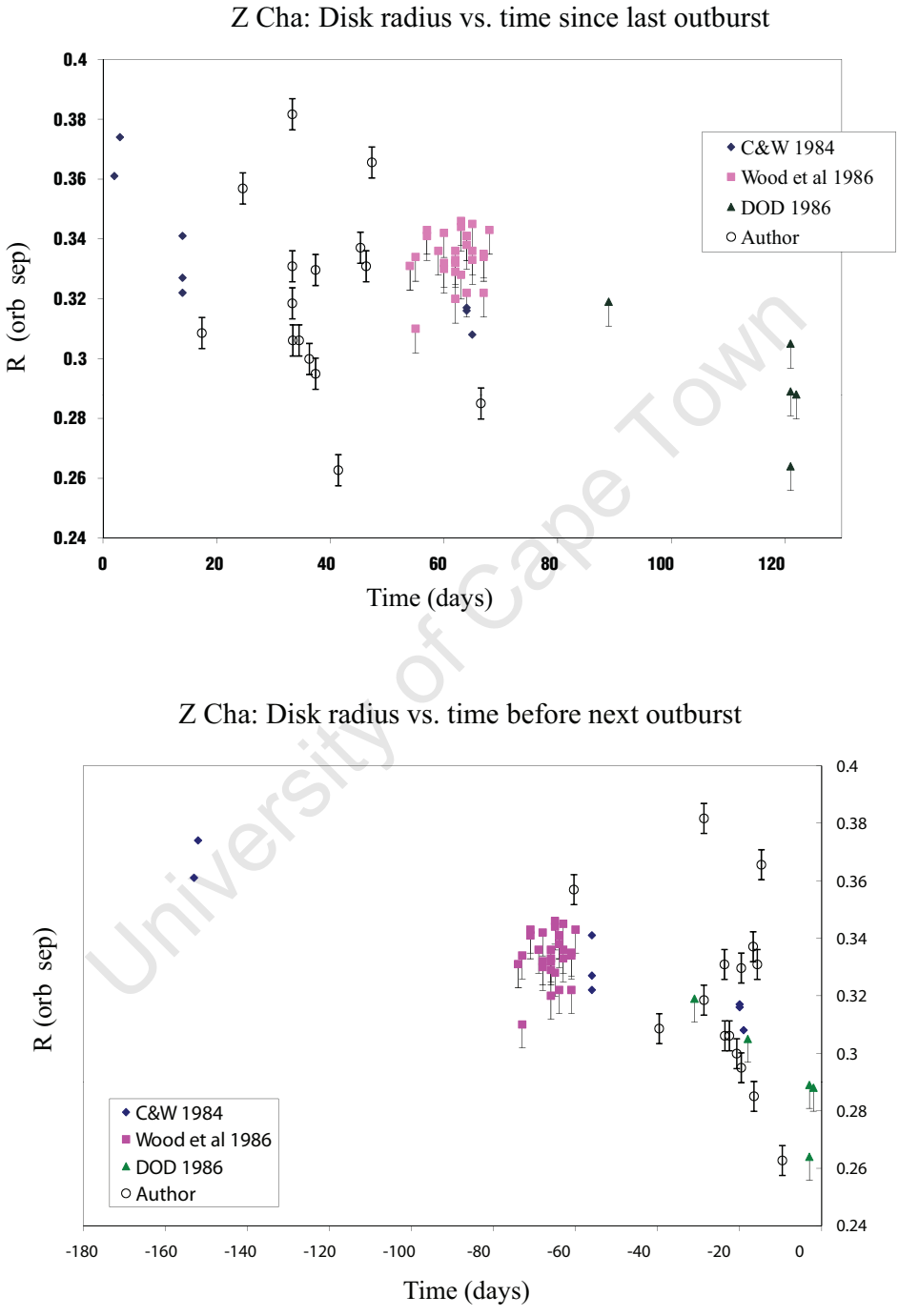

Figure 5.18: Disc radius measurements for Z Cha: (Top) Disc radius *vs.* time (days) since last outburst and (bottom) Disc radius *vs.* time before next outburst.

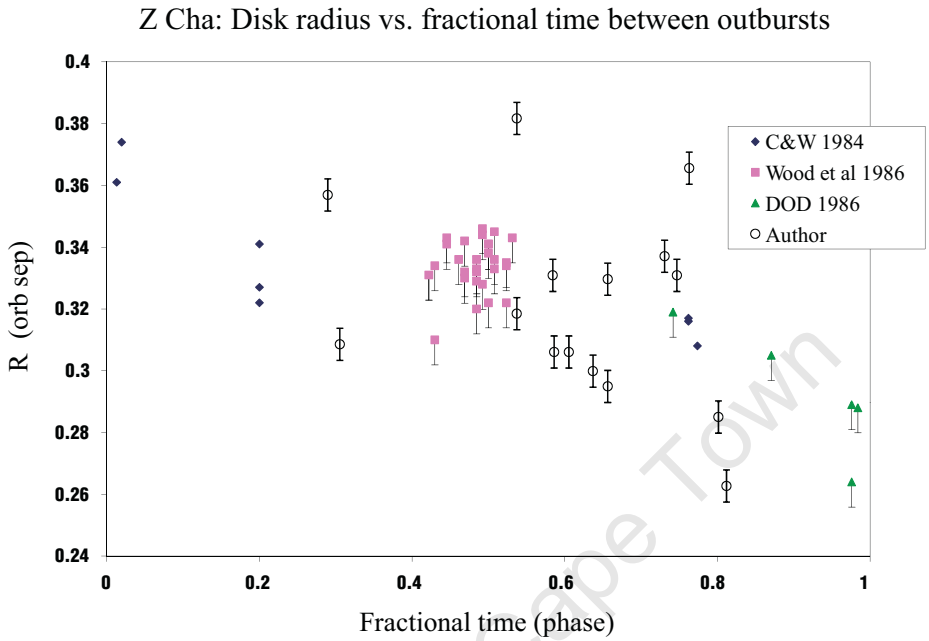

Figure 5.19: Disc radius measurements for Z Cha: Disc radius *vs.* phase in the outburst cycle (fractional time between outbursts).

previous outburst and the next outburst are normal outbursts. It is expected that the disc radius measured in the normal cycle preceding a superoutburst should be systematically larger than the disc radius measured during the normal cycle immediately following a superoutburst (Osaki 1989, Smak 1991). There is no sign of this in Figure 5.20 but more observations are needed at the beginning and end of a superoutburst cycle before any difference between the disc radius over the cycle preceding a superoutburst and over the cycle following superoutburst can be conclusively ruled out.

It should be noted that a large scatter in the data is expected when analysing disc radii collected over a number of normal outburst cycles from Osaki's theory (1989) as, for any given phase in the normal cycle, the radii will depend on the phase in the *supercycle* at which the observations were made[20]. However, some of the scatter in the plots is due to inherent orbital cycle-to-cycle variability. Comparing the results from Table 5.13 with those in Wood *et al.* (1986) there appears to be short term – $\leqslant$10 orbital cycles – disc variability (significant above the estimate of uncertainty) of typically $\sim$ 0.01. **Where consecutive cycles could be identified, there is an average *cycle-to-cycle vari-***

[20]For Z Cha this can be as much as $\sim$0.12 immediately following outburst, near phase 0, and $\sim$0.04 immediately preceding outburst near phase 1 (Osaki 1989).

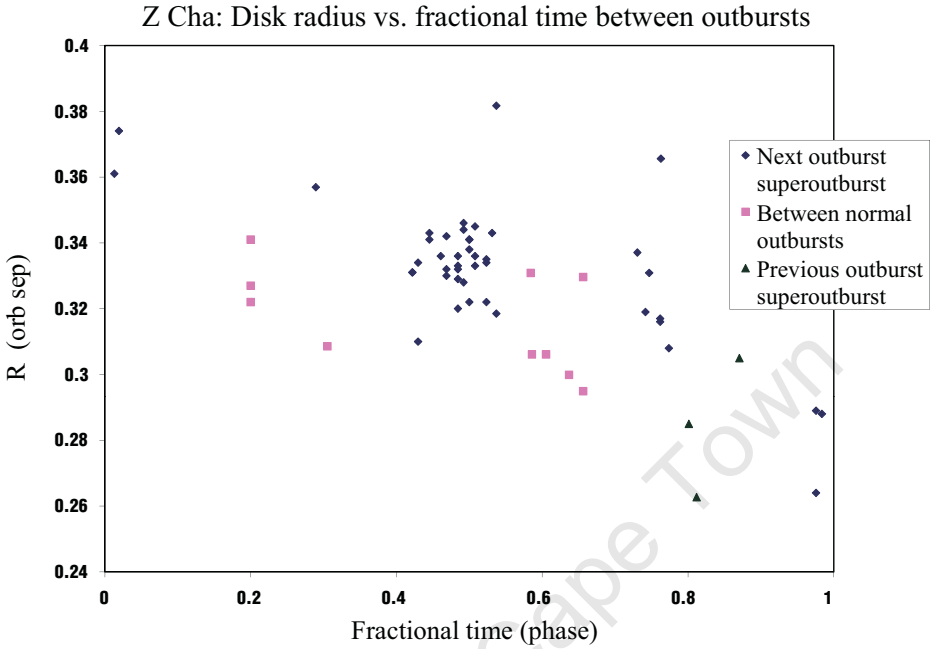

Figure 5.20: Disc radius measurements for Z Cha: Disc radius *vs.* phase in the outburst cycle (fractional time between outbursts). Measurements are differentiated according to where they lie in the superoutburst cycle.

ability of **∼0.028** (refer to Table 5.13 and Figure 5.18). **This is comparable to the expected overall trend in variability over the latter half of a normal outburst cycle**.

Figure 5.21 shows plots of the disc radius measurements correlated with times of superoutburst. The top plot shows disc radius versus time since last superoutburst. The bottom plot shows disc radius versus superoutburst phase with the minimum outer disk radius (black dashed), 3:1 resonance radius (red dashed) and the variation of disc radius (in black) expected for Z Cha by the TTI model (Osaki 1989) superimposed. It should be emphasised that the inclusion of the TTI calculations is **not** an attempt at model fitting. It is included to simply give a qualitative impression of the behaviour expected from the TTI model.

The author's data subset spanning one supercycle suggests an increase in R_d over the cycle (top of Figure 5.21). The set of published measurements was compiled at different phases from a number of different supercycles. This introduces the possibility that the decline in R_d seen over the supercycle in the published data is due to the selection effect of observing R_d at different phases in the *normal* outburst cycle. Only the data presented by

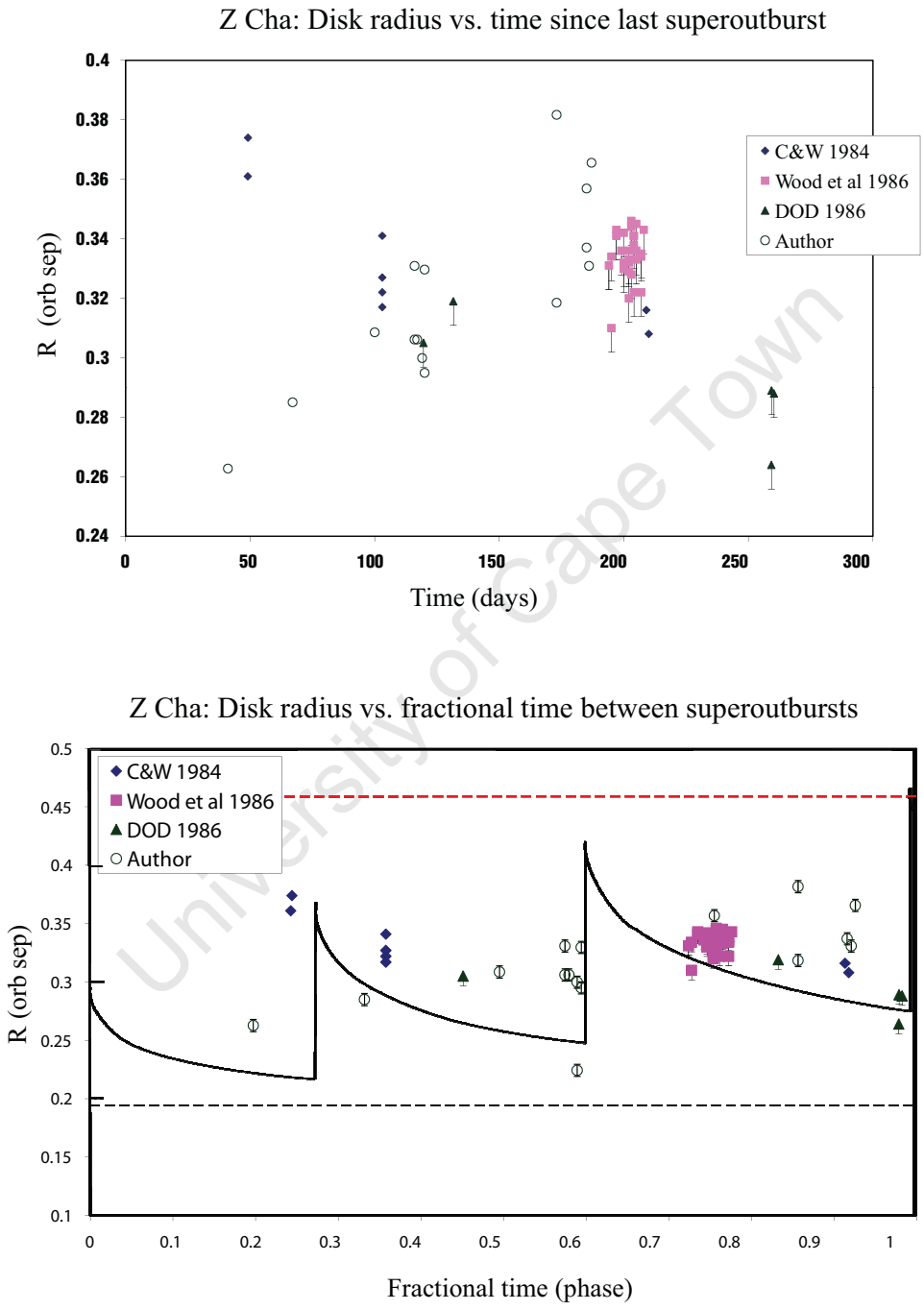

Figure 5.21: Disc radius measurements for Z Cha: (Top) Disc radius *vs.* time (days) since last *superoutburst* and (bottom) disc radius *vs.* fractional time before next *superoutburst*.

O'Donoghue have a few measurements which fall within the same supercycle, and so can be used for equal comparison. These three measurements tentatively suggest a declining disc radius late in the supercycle (phase $0.8 - 1$). Combined with the measurements made here during the same period, a large range in the disc radius possible just before superoutburst is evident (over and above typical cycle-to-cycle variation). A discussion comparing the results given in this section to the predicted supercycle variability given by Osaki (1989, bottom of Figure 5.21) is given in Section 5.6.

5.5.2 OY Car

Mass ratio determination

Figure 5.17 shows an interesting feature of the bright spot positions; the comparatively large number of timings reveals a clear systematic jump in the average bright spot position from the 2006-2007 observing seasons to the 2008 season. There is also significantly smaller scatter in the bright spot positions across the direction of the incoming stream within the 2008 data set. The mean positions of the 2006-2007 data sets, the 2008 data set and all the data are plotted as the yellow triangle, the circle and the diamond symbols respectively. The bottom plot superimposes the phase position of the radius of the disc which passes through the mean of all the bright spot positions (green dashed). What is observed is a change in the mean bright spot position, from 2006-07 to 2008, 'up-stream', along the rim of the disc. Making the argument that the 2006-2007 observations are that of a bright spot translated downstream along the rim of the disc, the 2008 data set indicates the real location of the mass-transfer stream. The justification for this reasoning is that the disc gas is highly supersonic so movement of the bright spot up-stream, towards the line of centres and away from the incoming stream, is implausible.

Thus the trajectory which most closely identifies with the 2008 bright spot positions, and specified by the mass ratio $q = 0.115$ ($1/q = 8.69$) and $i = 82.7°$, (plotted as the blue curve in Figure 5.17), was chosen as the most reliable indicator for the trajectory of the mass transfer stream. This is the largest mass ratio thus far proposed for OY Car.

Variation of Disc Radius with Outburst

The disc radius measurements determined for OY Car, and given in Table 5.14, are plotted versus time since previous outburst, time preceding the next outburst and the fractional time between outbursts in Figure 5.22 (top and bottom) and Figure 5.23 respectively. Again, no distinction is made between the type of outburst in these plots. The uncertainty in these disc radius measurements, arising from the uncertainty in the timings, was

determined in the same manner as for Z Cha and is indicated in the plots as error bars.

The disc radius measurements determined here have been combined with previous disc radius measurements published by Cook (1985b, hereafter Cook85b) and Wood *et al.* (1989a, hereafter Wood89). The radius measurements made by Cook85b were determined using a mass ratio $1/q = 11.0$ while Wood89's were determined using a mass ratio $1/q = 9.8$. Again, this introduces systematic differences between the three sets of observations. The magnitude of these differences is indicated by half error bars in the plots: Cook85's data should be shifted by 0.0155 upwards (in units of orbital separation) to adjust his disc radius measurements from $1/q = 11.0$ to $1/q = 8.69$. Wood89's data points should be shifted upwards by 0.0065 to adjust their disc radius measurements from $1/q = 9.8$ to $1/q = 8.69$.

Figure 5.22 shows very little variation in the size of the disc either following or leading up to outburst. This is in contrast to the data compiled for Z Cha (refer to Figure 5.18). In addition, the intrinsic cycle-to-cycle variation is smaller for OY Car than for Z Cha. Neglecting outliers in Figure 5.23 there could be a slight decrease in the disc radius by ~ 0.03 over the latter half of the cycle (the abscissa is from phase 0.3 to 0.9; there are no measurements immediately preceding or following outburst). The possibilities cannot be ruled out of a sudden drop in disc size occurring *immediately* before outburst (as seen in Z Cha between phase 0.9 and 1, Figure 5.19) or the presence of an 'enlarged' disc radius, comparable in magnitude to Z Cha's maximum observed radius, *immediately* following outburst.

Figures 5.24 (top and bottom) and 5.25 show the combined data sets plotted versus time since previous superoutburst, time preceding the next superoutburst and the fractional time between superoutbursts respectively. The small scatter in disc radius noted for the normal outburst cycle (Figures 5.22-5.23) applies equally, of course, to the supercycle (Figures 5.24-5.25). Comparing the top and bottom plots in Figure 5.24 we can see the variability in the length of the superoutburst cycle, varying from $\sim 250-400$ days; Cook's measurements were made ~ 250 days after superoutburst and ~ 140 before the next while Wood *et al.*'s were made ~ 220 days after superoutburst and just ~ 30 days before the next. Again, Figure 5.25 shows disc radius versus superoutburst phase with the minimum outer disk radius (black dashed) and 3:1 resonance radius (red dashed) superimposed. The solid black line is the same as that in Figure 5.21, i.e. the disc radius variation expected for Z Cha by the TTI model, as corresponding calculations have not been published for OY Car. The difference between the expected behaviour for the two systems is mainly determined by the difference in the observed mass transfer rates. In Osaki's model, the (stable) mass transfer rate affects the frequency and duration of the normal outbursts

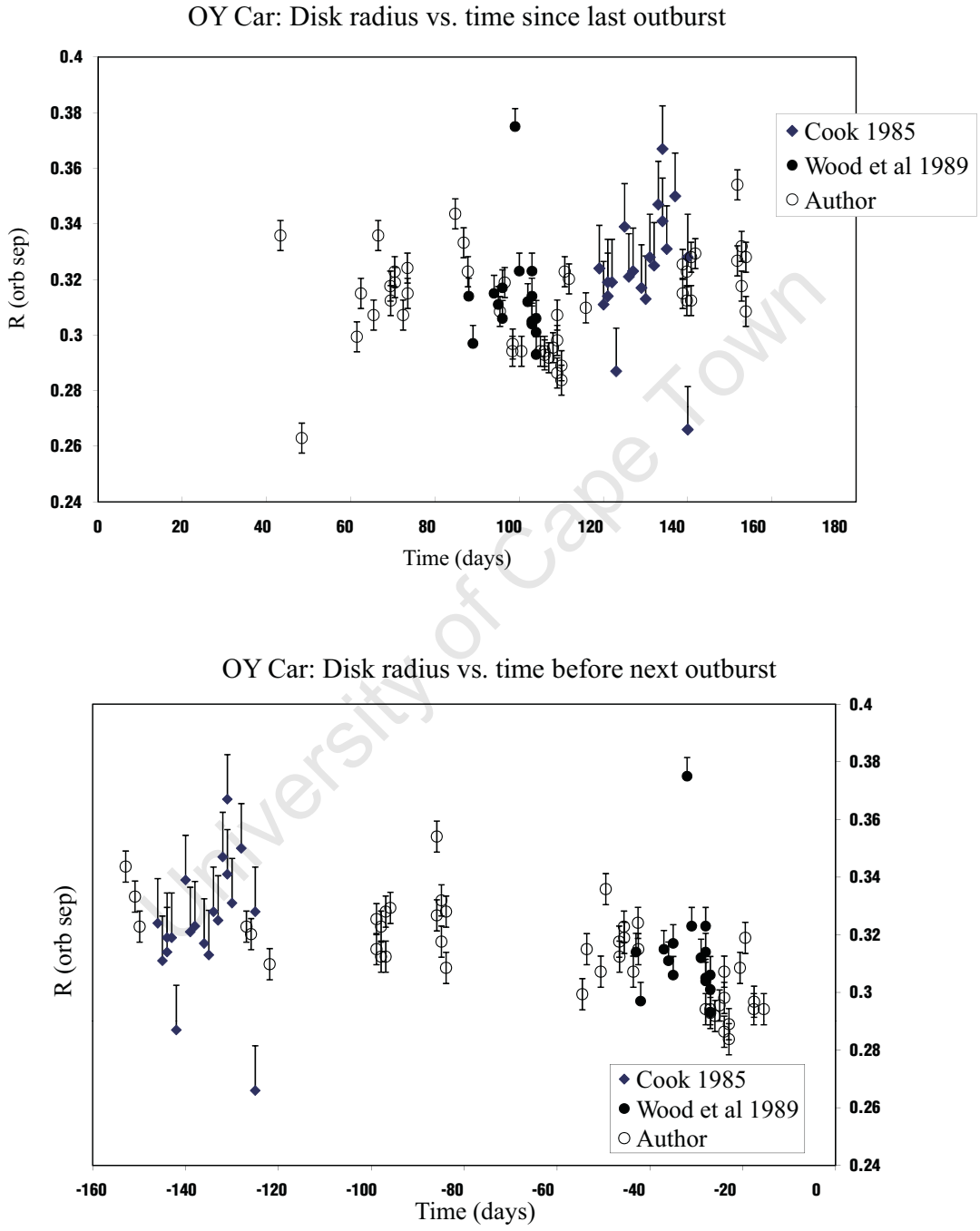

Figure 5.22: Disc radius measurements for OY Car: (Top) Disc radius *vs.* time (days) since last outburst and (bottom) Disc radius *vs.* time before next outburst.

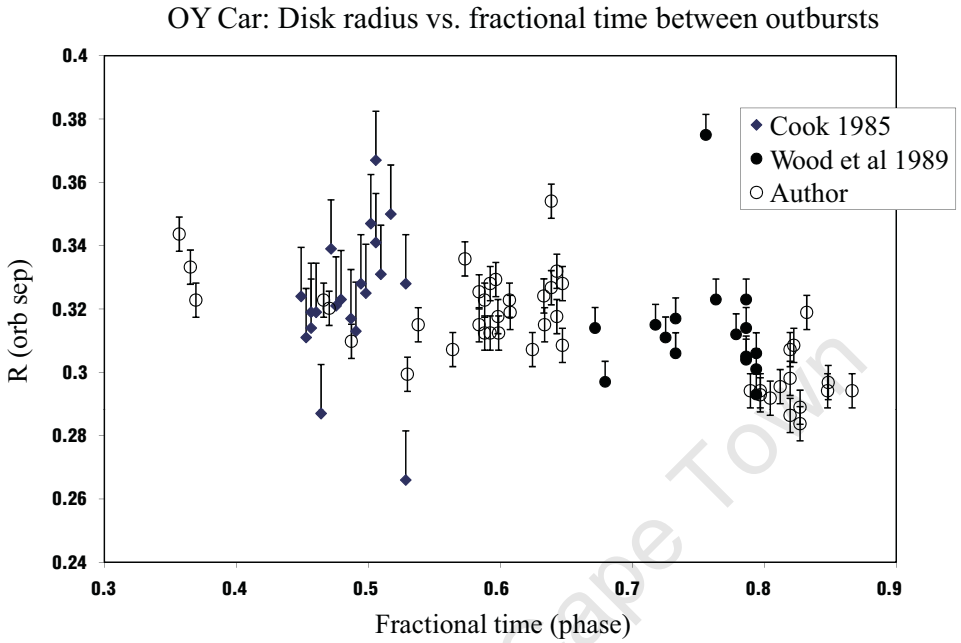

Figure 5.23: Disc radius measurements for OY Car: Disc radius *vs.* phase in the outburst cycle (fractional time between outbursts).

within the supercycle. With estimates of OY Car's mass transfer rate, $\dot{M} \sim 2 \times 10^{15}\mathrm{gs}^{-1}$ close to the estimate used for Z Cha, $\dot{M} \sim 7 \times 10^{15}\mathrm{gs}^{-1}$ (Mineshige & Wood 1989[21]), Z Cha's disc radius calculations serve as a good approximation of what can also be expected for OY Car. Therefore, just as in Z Cha's case, the expected trend is not included here as a model fit but simply as an aid to comparison with disc radius measurements. As can be seen, OY Car clearly does not follow the expected trend.

Finally, Figure 5.26 shows the disc radius measurements determined in the present work plotted versus time in days. This subset was selected for graphical display as it represents the most homogeneous and continuous subsets of the available measurements. The red lines indicate dates of superoutburst maxima and the brown dashed lines indicate dates of normal outburst maxima. The difference in the disc radius measurements obtained for the first two superoutburst intervals are statistically significant[22]. What is demonstrated in

[21]The mass transfer rates were determined from model fitting of OY Car's and Z Cha's disc brightness profiles and are consistent with estimates derived from measurements of the bright spots' luminosities (Wood 1986).

[22]A histogram of the OY Car disk radius measurements was plotted for each data set. A gaussian with a mean equal to the mean of the data set and a standard deviation equal to the estimated measurement error was superimposed on each data set. It was found that the standard deviation one data set did not overlap to within $\pm 2\sigma$ deviations of the other data. In addition, considering the reasonable assumption that the data were not sampled from normal distributions, the

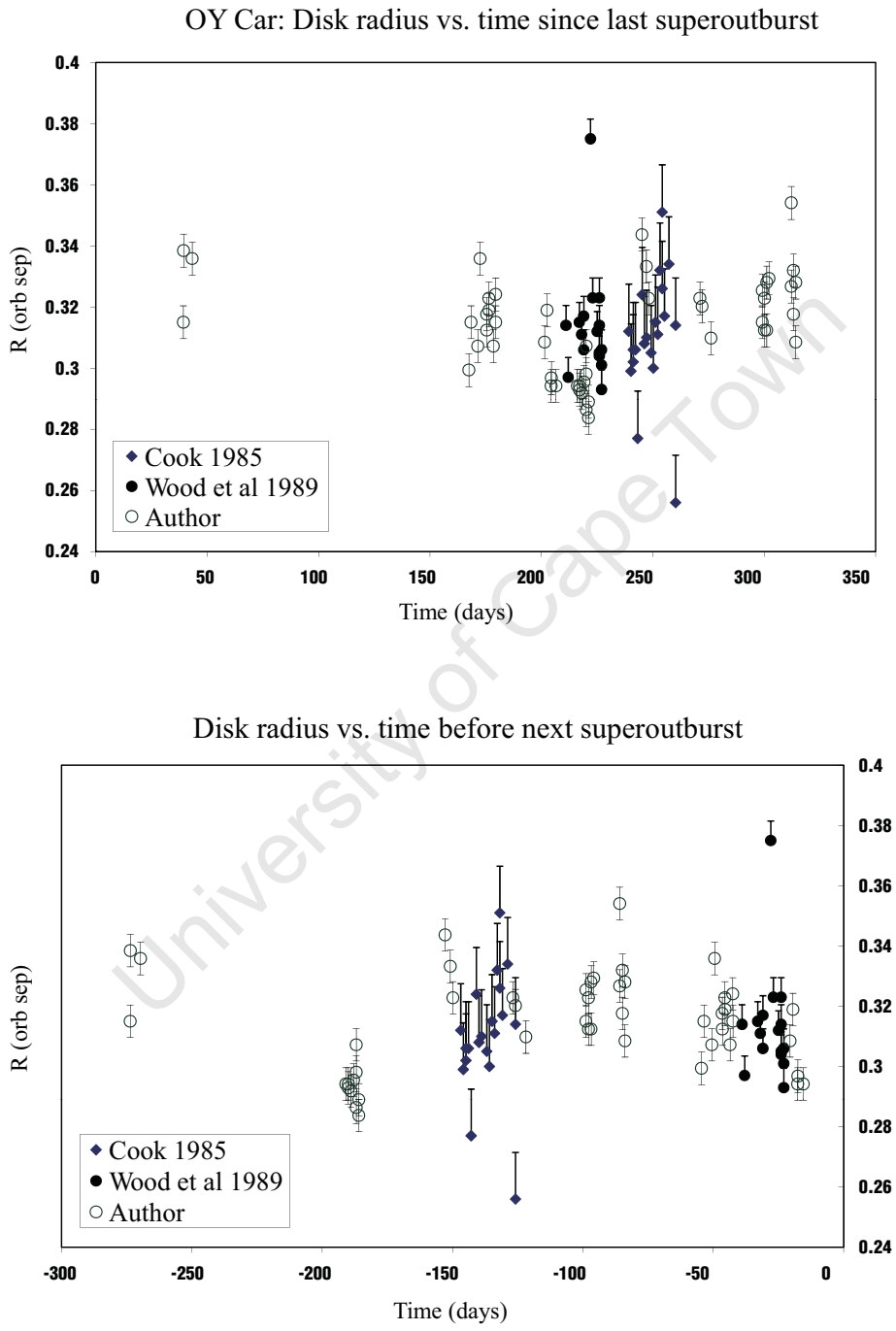

Figure 5.24: Disc radius measurements for OY Car: (Top) Disc radius *vs.* time (days) since last *superoutburst* and (bottom) Disc radius *vs.* time before next *superoutburst*.

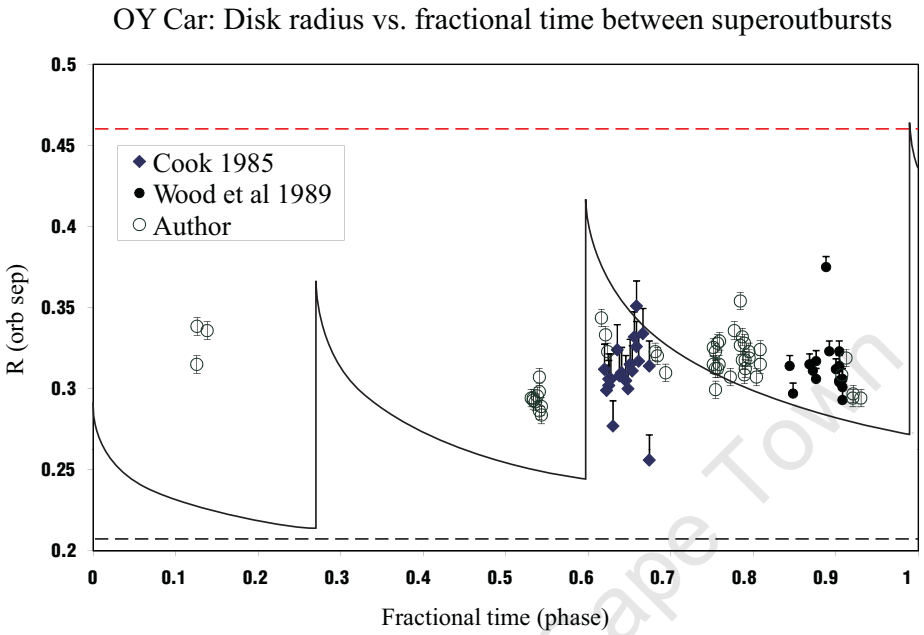

Figure 5.25: Disc radius measurements for OY Car: Disc radius *vs.* phase in the *supercycle* (fractional time between superoutbursts).

Figure 5.26 is the variability in i) the length of the supercycle (comparing supercycle three with the previous two), ii) the length of the normal outburst cycle within the supercycles and iii) the disc radius on orbital timescales, the magnitude of which is comparable to the variability *between* supercycles.

5.6 Summary, Discussion and Conclusions

5.6.1 Summary

This chapter has presented analysis of the eclipse structure of 25 eclipse lightcurves for Z Cha and 49 lightcurves for OY Car. These eclipses have been used, together with previous data in the literature, to define systems parameters more accurately and further investigate possible correlations between the disc radius and the normal and superoutburst cycles.

Kolmogorov-Smirnov (K-S) 2-sample test was also applied to the data set. The test found that the cumulative distributions of the two data sets were did not overlap, giving a P-value of 0.0. This gives the strongest evidence that the null-hypothesis – that the disc radii measurements from the first two supercycles were drawn from the same population distribution – should be rejected and thus the differences between the two sets are statistically significant.

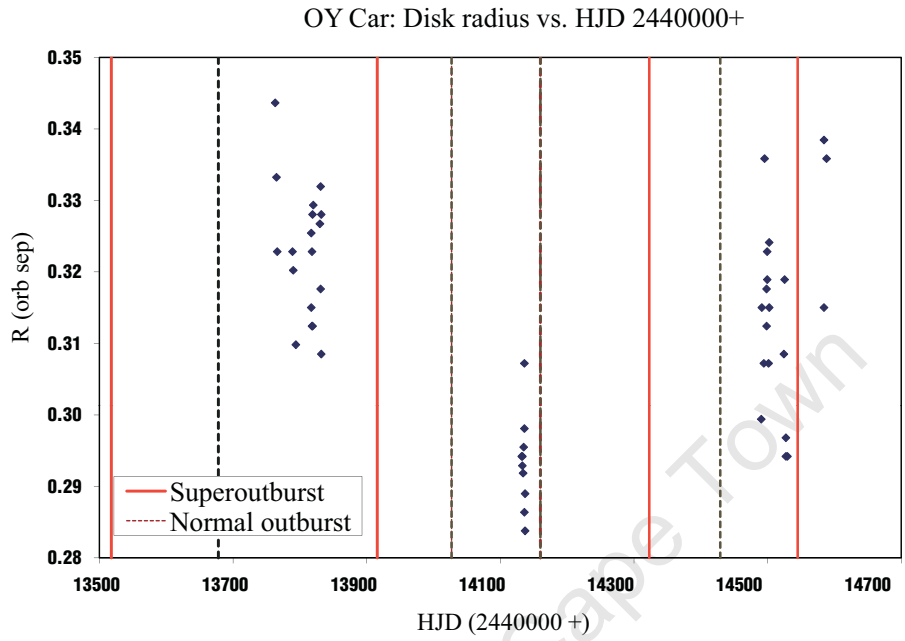

Figure 5.26: Disc radius measurements for OY Car given in Table 5.14 and plotted versus HJD-2440000.

The results presented here have shown that:

(i) A mass ratio of $q = 0.16$ ($1/q = 6.25$) was determined for Z Cha, with a corresponding inclination of $i = 81.4$. The mass ratio previously used in the literature (Wood86) which came closest to this value ($1/q = 6.71$) was found to fall just outside of the margin of uncertainty, though this should not be treated as statistically significant.

(ii) Z Cha's eclipse times are continuing to decrease with respect to the previously calculated (Baptista 2002) linear trend. A new sinusoidal ephemeris has been calculated to fit the author's plus published eclipse times:

$$24401660.501444 + 0.0744992826E + (1.23 \times 10^{-3}) \cos[(2\pi E/190000) - 1.91379]$$

Continued monitoring of Z Cha is necessary to confirm whether the orbital modulation is truly varying sinusoidally. Nevertheless, the eclipse timings presented here have shown that Z Cha's brightness modulations (observed by Ak *et al.* 2001) do not correlate with variations in the orbital cycle, further weakening support for the suggestion that the Applegate mechanism is responsible for the modulation of Z Cha's period.

(iii) Z Cha's disc radius was found to decrease from ~ 0.38 to $\sim 0.28 - 0.26$ over the normal outburst cycle. The intrinsic scatter present in the plots makes it difficult to determine what would be the best function fit to the behaviour, but the data collected here supports a sudden rapid decline in radius immediately preceding outburst.

(iv) It is unclear whether Z Cha's disc radius increases or decreases over the supercycle. The new data presented here may support an increasing disc radius while the data compiled from the literature indicates a decreasing disc radius. More studies are required, critically sampling the disc radius over the same supercycle, in order to settle the issue.

(v) A mass ratio of $q = 0.115$ $(1/q = 8.69)$ was determined for OY Car, with a corresponding inclination of $i = 82.7°$. The mass ratio previously used in the literature (Wood89b) which came closest to this value $(1/q = 9.8)$ was found to fall outside of the margin of uncertainty and thus the author's result represents the largest mass ratio so far proposed.

(vi) A new sinusoidal ephemeris has been determined for OY Car:

$$2445752.671225 + 0.06312090817E + (3.628 \times 10^{-4}) \cos[(2\pi E/132840) - 0.86107]$$

confirming that OY Car's period is also continuing to decrease. Again, as in the case of Z Cha, a cubic ephemeris also provides a reasonable fit to the data and only continued eclipse timing will reveal whether the changes in period are truly cyclic.

(vii) The position of OY Car's bright spot was found to translate along the rim of the disc from one observing season to the next.

(viii) There does not seem to be any significant correlation between OY Car's disc radius and phase either during the normal outburst cycle or the superoutburst cycle. To establish the result beyond any doubt, more observations are required **immediately** preceding and following normal and/or superoutburst. While straightforward, this test is difficult to implement as it requires observations framing a few days around the highly unpredictable onset of normal and/or superoutburst.

(ix) The cycle-to-cycle disc radius variability in both systems studied here was found to be comparable to the variability over the normal and/or superoutburst cycle. A complete treatment of the origin of dwarf nova outbursts and, in particular, the SU UMa superoutburst cycle, depends on understanding the underlying causes of this.

5.6.2 Discussion

The average radial and angular positions of the bright spot determined here for Z Cha and OY Car are consistent with previous estimations of the location of the bright spot in these systems. The morphology of the light curves show that Z Cha appears to have a bright spot with a compact structure, in contrast to OY Car's bright spot which is typically extended along the rim of the disc. This suggests that the mass transfer stream penetrates deeper into the disc in OY Car than in Z Cha, thereby releasing kinetic energy at greater depths, locally heating the rim of the disc and producing an extended bulge for a bright spot.

Measurements of the bright spot assume a small, symmetric, compact spot centrally located with respect to the stream trajectory. Evidence of an intermittent extended-rim feature in OY Car suggests the possibility of an accompanying elliptical or asymmetric compact region. In these cases the assumption of a symmetric compact region incorrectly places the light centre of the bright spot in azimuth (off-stream) and radius (Smak 1996). This may provide an explanation for some of OY Car's cycle-to-cycle scatter although a correlation between the morphology of the light curves (i.e. the identification of the presence or absence of extended rim features) and the position of the bright spot in phase space was difficult to establish from simple inspection.

The changing shape of the bright spot in OY Car can not explain, however, the clear systematic change in azimuth observed from the 2006-07 data sets to the 2008 set; there is no change in the morphology of the mean bright spot eclipse between these two periods. Here, a real offstream-onstream translation is observed. Interestingly, this shift appears to be independent of disc radius variability but may still indicate a fundamental change in the conditions in the outer rim of the disc. The differences between previously published mass ratios for OY Car and the value determined here are most likely due to this variation in the downstream location of the bright spot's light centre seen here. A similar, lower amplitude, effect could also be occurring in Z Cha which would explain the small discrepancy between Z Cha's published mass ratios and the value determined here.

Z Cha's disc radius measurements confirm the decline over the normal cycle already identified by O'Donoghue (1986), although the intrinsic scatter in the data almost disguises the trend. The author's data showing an increase in R_d over the supercycle does not support the EMT model (which supports a general decrease in disc radius, Smak 1991) and contradicts previously published data (Cook & Warner 1984, Wood *et al.* 1986, O'Donoghue 1986) which, together, show a decline in the disc radius following superoutburst, similar to what is seen over the normal outburst cycle.

There is intrinsic scatter in the disc radius measurements for both objects. From the TTI model, we can expect a large scatter in the collated measurements midway through the supercycle as, although the superoutburst cycle length should be more regular than the normal cycle, there is some variability in the number and duration of the normal outbursts within an superoutburst cycle. However, this does not explain the large differences in the disc radius observed at the end of Z Cha's supercycle. According to the TTI model, only a radius close to the range of minima should be observed so late in the supercycle. Moreover, the cycle-to-cycle variability is comparable to variability from one normal outburst to another over the supercycle. This suggests that the saw-tooth pattern predicted by the TTI model is not compatible with observations.

OY Car has no identifiable secular trend over either the normal outburst cycle or the superoutburst cycle. The former contrasts with the other extensively studied CVs within the SU UMa class – Z Cha and IP Peg (Wood 1989b) – which show clear trends in normal cycle disc radius development supporting DI model predictions. The latter, like Z Cha, poses problems for both the EMT and TTI supercycle models. In addition, the variability in the length of the OY Car superoutburst cycle needs to be explained by the TTI model which predicts a regular supercycle period which can be estimated from the basic binary parameters and is thought to be insensitive to the size of the disc at the beginning of the supercycle (Osaki 1989).

5.6.3 Conclusions

This work has put two different accretion theories competing to explain the mechanism of superoutbursts in SU UMa stars to a simple test. Both have failed to explain the two very different normal and supercycle behaviours revealed by observations of a pair of near-identical systems.

Where the TTI model fails, the EMT model's sensitivity to mass transfer variations *may* best explain some of the variation observed in the light curves – supercycle length, disc radius, magnitude variations – from one outburst to another and within a single system (Schreiber *et al.*, 2004, 2005). At present the TTI model lacks a mechanism which naturally explains these observed features. However, neither model can explain the range of Z Cha's disc radii seen from cycle-to-cycle or so late in the supercycle. In puzzling contrast, OY Car's virtually 'deadpan' behaviour over the normal and supercycle also defies explanation by both models. In either case, the lack of a distinctive long-term decreasing or increasing trend (an increasing 'saw-tooth' trend, in the case of the TTI model) is problematic for both models. The *difference* in supercycle behaviour observed

between these two systems which are similar in the binary characteristics relevant to both models – estimated mass transfer rate, mass ratio and inclination – poses an even deeper puzzle for the two theories. Moreover, it is worth emphasising again that there has been **not one single observed supercycle feature** found in this work in favour of either of the models.

Thus this study supplies no evidence supporting either the TTI model or the EMT model as providing the essential physics governing the behaviour of the accretion disc over the supercycle.

Chapter 6

Examining the Central Object in an Eclipsing Dwarf Nova

6.1 White Dwarf and Boundary Layer Models

Deeply eclipsing cataclysmic variables (CVs) offer a unique opportunity to constrain binary system parameters from analysis of their lightcurves alone. As was demonstrated in Section 5.2.5, in the cases of double eclipses, measurements of the eclipse width, bright spot and white dwarf positions allow estimates of the size of accretion disc and determination of the mass ratio-inclination (q, i) parameter pair (refer to Section 4.1). This, combined with photometric measurements of white dwarf radii in eclipsing systems and a theoretical mass-radius relationship, have the potential to be the most accurate means of determining white dwarf masses in dwarf novae (Wood & Horne 1990).

The white dwarf radius ($R_{\rm WD}$), and consequently the white dwarf mass ($M_{\rm WD}$), can be derived either from direct measurements of the eclipse contact times (Wood *et al.* 1986, 1989a; Wood 1986) or from eclipse profile fitting using a physical model of the binary system (Wood & Horne 1990, Robinson *et al.* 1995, Feline *et al.* 2004, Littlefair *et al.* 2007, 2008). However, whichever method is used, the derived value of $R_{\rm WD}$, and hence $M_{\rm WD}$, has been shown to depend, critically, on what model is used to describe the shape of the central object's surface brightness distribution (Wlodarczyk 1986, Wood 1987, Wood & Horne 1990, Baptista *et al.* 2000).

The small variety of models which have been proposed to describe the central source include: 1. a white dwarf with *or* 2. without its lower hemisphere occulted by the disc; 3. a white dwarf totally covered by an optically thick boundary layer; 4. a white dwarf with an optically thick, equatorial boundary layer extended in latitude along the sides. Of the few cases in the literature where differing models for the central sources[1] in eclipsing CVs

[1]Note that in the rest of this chapter, where previously the term 'white dwarf' was used to refer to the primary binary component, this is replaced with 'central object' or 'central source'. This is because, for the purposes of this investigation, the nature of the primary's brightness distribution is no longer assumed to be that of a simple, bare white dwarf.

are discussed (Cook & Warner 1984, Cook 1985, Smak 1986, Wood 1987, Horne 1990, Silber *et al.* 1994, Robinson *et al.* 1995, Baptista *et al.* 2000), only Wood (1987), Wood & Horne (1990) and Robinson *et al.* (1995) have fitted a selection of model profiles to eclipse lightcurves. None have been able to identify, confidently, a particular model as a unique representation for any one of the individual central sources in the dwarf novae examined. This is most likely due to the difficulty of discerning the more subtle features of an eclipse profile which are necessary to distinguish between the models and, as a result, no similar recent attempt to clarify the situation has been made.

Testing the Models: Light Curve Derivatives as a Map of the Brightness Distribution

Wood (1987) and Wood & Horne (1990, hereafter referred to as WH90), were the first to generate, numerically, eclipse profiles for different models of the surface brightness distribution of the central object in eclipsing CVs. For the rest of this discussion, please refer to the model light curves of ingress, given in WH90 (figure 2 in WH90) and reproduced in Figure 6.1, for ease of reference.

The three classes identified by WH90 are distinguished as: models with no boundary layers (Class 1), those with opaque boundary layers (Class 2) and those with optically thin boundary layers (Class 3). These are further subdivided according to the shape of the brightness distributions, as shown in Figure 6.1 and detailed in the caption. In classes 2 and 3, the white dwarf's photosphere is assumed to be dark in comparison to the boundary layers and gravity darkening is ignored in all of the models.

In WH90's investigation, it is not the model light curves which are examined and compared to the data, but their derivatives. This is because the eclipse light curve can be seen as a running integration of the observable brightness of the system and so its derivative is in fact a one dimensional map of the brightness distribution. In addition, the derivatives of the light curves reveal features which, in principle, make the models easier to distinguish than from inspection of their light curves.

Derivatives of the ingresses of the model light curves presented in Figure 6.1 are given in Figure 6.2, reproduced from WH90's figure 3. The models of the surface brightness distributions assume azimuthal symmetry so the egresses are inverted mirror images of the ingresses seen in the derivative profiles.

What is immediately obvious from the profiles is that the derivatives provide two readily identifiable features which allow discrimination between models, specifically:

(i) whether or not the (ingress/egress) derivative profile is single or double peaked and,

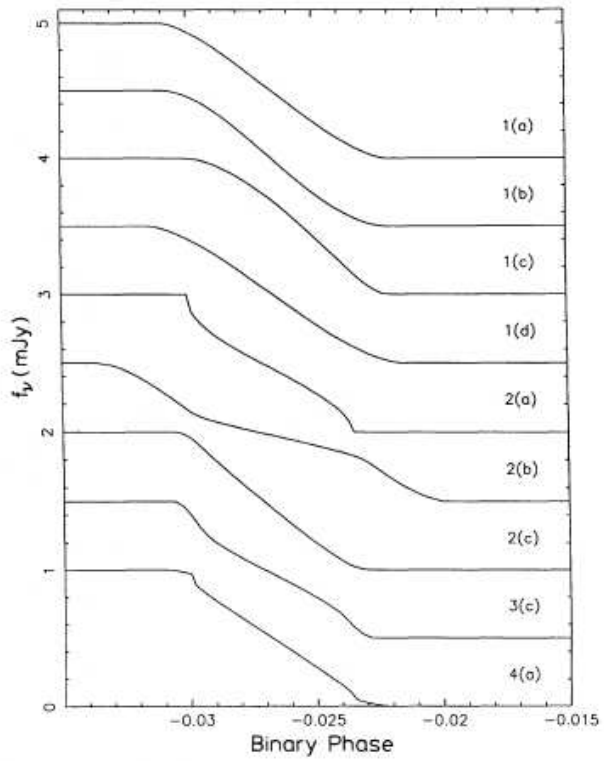

Figure 2. Model light curves of ingress, normalized to 1 mJy, for $q = 0.15$, $\Delta\phi = 0.0534$ and $R_{wd} = 0.0195a$. Each light curve is offset by 0.5 mJy from the next. 1(a) A white dwarf with limb darkening $u = 0$. 1(b) A white dwarf with limb darkening $u = 1$. 1(c) A white dwarf with limb darkening $u = 0$, with its lower hemisphere totally occulted by the disc. 1(d) A white dwarf with polar radius, $0.0195a$, whose outer layers follow the shape of a self-gravitating object rotating near break-up velocity. 2(a) An optically and geometrically thin equatorial boundary layer. 2(b) An optically thick boundary layer extended radially in the orbital plane to a radius of $2R_{wd}$. 2(c) An optically thick boundary layer extended in latitude up and down the sides of the white dwarf to a height $H = 0.175R_{wd}$. 3(c) An optically thin boundary layer extended in latitude up and down the sides of the white dwarf to a height $H = 0.175R_{wd}$. 4(a) Model 1(a) plus 2(a) with equal total intensities.

Figure 6.1: Model light curves of ingress for different surface brightness distribution models as reproduced from WH90, figure 2.

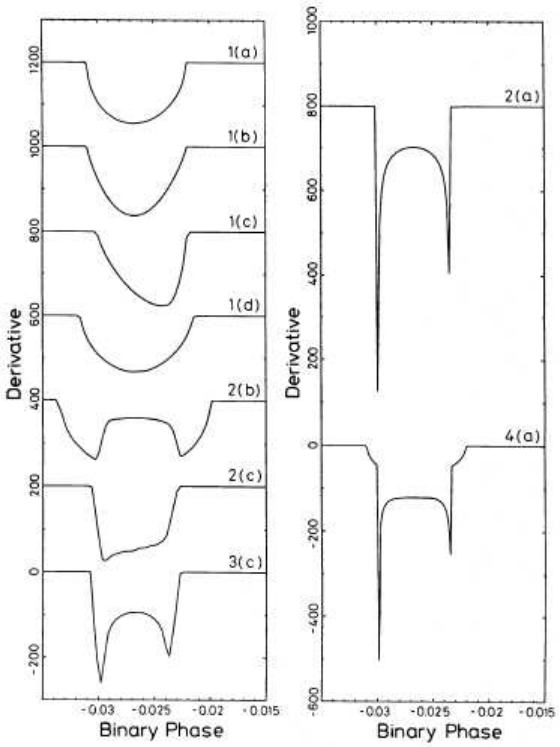

Figure 3. Derivatives of model light curves during ingress, for $q = 0.15$, $\Delta\phi = 0.0534$ and $R_{wd} = 0.0195a$. Each derivative is offset by $400/2\pi$ mJy/rad^{-1} from the next, except 2(a) and 4(a) which are offset by $800/2\pi$ mJy/rad^{-1}. 1(a) A white dwarf with limb darkening $u = 0$. 1(b) A white dwarf with limb darkening $u = 1$. 1(c) A white dwarf with limb darkening $u = 0$, with its lower hemisphere totally occulted by the disc. 1(d) A white dwarf with polar radius, $0.0195a$, whose outer layers follow the shape of a self-gravitating object rotating at break-up velocity. 2(a) An optically and geometrically thin equatorial boundary layer. 2(b) An optically thick boundary layer extended radially in the orbital plane to a radius of $2R_{wd}$. 2(c) An optically thick boundary layer extended in latitude up and down the sides of the white dwarf to a height $H = 0.175R_{wd}$. 3(c) An optically thin boundary layer extended in latitude up and down the sides of the white dwarf to a height $H = 0.175R_{wd}$. 4(a) Model 1(a) plus 2(a) with equal total intensities. Models 2(a) and 4(a) are plotted separately so that the shapes of all the derivatives can be seen more easily.

Figure 6.2: Model derivative profiles of ingress for different surface brightness distribution models as reproduced from WH90, figure 3.

(ii) the symmetry of the (ingress/egress) profile about the time of mid ingress/egress.

These broadly discriminating features[2], along with particular models of interest, are discussed in more detail in Section 6.7.

It is clear from Figure 6.2 that the derivative profiles need to be of sufficient quality so as to be able to discern adequately the discriminating features i) and ii) listed above, as well as to test the assumption of symmetry between the ingress and egress of the light curves.

The SALT First Science paper (O'Donoghue *et al.* 2006) demonstrated the unique capability for SALT, equipped with its imaging camera SALTICAM, to resolve eclipse features that may only be detectable for a few seconds during an eclipse. In the same manner as the SALT First Science paper, the goal of this investigation, presented here and in the next section, is to obtain white light observations of a suitable dwarf nova candidate taken at very high speed (250-500 ms), operating in SALTICAM's slotmode. This would allow unprecedented resolution of the central source's eclipse and, hence, the luminosity profile of its surface boundary. Binning of the observations should yield light curves of sufficient quality for individual analysis.

Most analyses of eclipsing CVs, particularly eclipsing dwarf novae, have followed the approach of Wood, Irwin & Pringle (1985) and Wood *et al* (1986): Araujo-Betancor *et al* (2003), Baptista *et al.* (1994, 1998, 2000, 2004, 2007), Borges *et al* (2008), Feline *et al* (2004a, 2004b), Horne *et al* (1991), Steeghs *et al* (2003) and Wood *et al* (1989a, 1989b, 1990) have all applied the technique of measuring phases of contact and half-flux of the central object from the derivatives of the eclipse curves.

While the derivatives of model light curves clearly provide a unique probe into the nature of candidate surface brightness distributions, the common treatment of the data used to obtain the derivative profiles in all of the investigations cited above has the effect of amplifying the noise in the data while concealing the subtle differences expected between the model derivative profiles (this shall be demonstrated in Section 6.3). The noise amplification characteristic renders cycle-to-cycle analysis of the light curves nearly impossible, necessitating the averaging of many cycles in order to form a mean light curve of sufficient signal-to-noise for analysis. This averaging further mitigates the possibility of detecting subtle features in the derivative profile (as such features are smeared in the averaging process) and assumes, without justification, that the observed brightness distribution is unchanging from eclipse to eclipse.

In this investigation, following WH90, it is the derivative of the light curves which

[2]The specific features of the different model derivatives are discussed by Wood & Horne in WH90, section 2.1, and will not be repeated here, therefore please refer to WH90 for a detailed discussion of Figure 6.2.

will be examined and qualitatively compared to the model profiles. However, in order to exploit the high signal-to-noise (SNR) data as fully as possible, a variety of traditional smoothing and differentiation techniques will be investigated and these results compared with the results of using a regularisation technique, most commonly used in 2-dimensional image processing, with the aim of finding the best treatment of the data.

6.2 Observations and Reductions

6.2.1 Target

The CV target proposed for observation is OY Car. OY Car has already been introduced in Chapter 5 as a low mass-ratio, SU UMa system. Wood & Horne (1990) analysed the observations presented in Wood *et al* (1989a, hereafter WH89) in an attempt to discern the nature of OY Car's central brightness distribution and came to the tentative conclusion that the central object's brightness distribution matches that of a spherically symmetric bare white dwarf *or* with a radially extended boundary layer. However, there is evidence that their analysis of the data was compromised both by its treatment and the fact that the low SNR did not allow cycle-to-cycle analysis of the data. Cycle-to-cycle analysis is necessary for OY Car – and probably most CVs – as the central object's flux is known to fluctuate by as much as $\sim 10\%$ from one cycle to another (WH89). Thus high speed photometry of this object on a 10m-class telescope could accurately discern, for the first time, the central brightness distribution of this well studied system[3].

6.2.2 Observations

Observations of OY Car were made using a clear filter with SALTICAM operating in slotmode. Slotmode is a mode of high speed observing where a 20 arcsec x 8 arcmin slot mask is placed over the imaging CCDs along the frame transfer boundary. Operation of the CCDs is similar to standard frame transfer devices except that only 144 rows are vertically moved instead of 2048. This minimises smearing due to vertical clocking of the rows of the CCD (0.2 ms/row). Further details are available in O'Donoghue *et al.* (2006).

Usually just two stars are imaged within the slot: the target star and a comparison star (where the comparison star is expected to be constant with time and so may be used as a comparison for performing differential photometry of the target star). After the imaging strip on the CCD is exposed for the length of the integration time, the charge counts are shunted one slot-width down the columns of the CCD so that the slit again exposes a blank strip of pixels for the next exposure. This continues throughout the length of

[3]Z Cha would also have been an ideal target but it lies outside of the accessible declination range of SALT.

the observation run with the slit images being continuously shunted down the length of the CCD until they are read out at the end by the readout amplifier. This mode of observation allows for very fast read-out – and therefore integration times – so exposure times as short as 0.15 seconds can be achieved without deadtime.

Altogether, during the 2008 and 2009 observing seasons, SALT spent 12 nights observing OY Car. These yielded 15 light curves, 13 of which were useful. Observations from the archives added a further 7 light curves to the set. Due to the addition of the archival data from two other observing campaigns, there are 3 different comparison stars in the final set presented here. Table 6.1 details these sets of observations. Integration times vary from $0.1 - 2s$ (where $\approx 0.049s$ of overhead should be added to the times given) depending on seeing and sky brightness conditions.

6.2.3 SALT Data Reduction and Photometry

Reduction of SALT image frames was performed using the data reduction routine `SALTSLOT`. `SALTSLOT` is the 'slotmode' data reduction package which forms part of `SALTRED`, the SALT data reduction package provided by the suite of SALT pipeline software, `PySALT`, and coded by Dr S. M. Crawford of the SAAO. `SALTSLOT` implements gain correction of the images, correction of pixel bias and cross-talk between the amplifiers (Crawford 2008). At present, there is no provision for flat-field correction but no large scale gradients have been found in the flat-fields measured to date. For the observations presented here, the effect of vignetting across the slot has been minimised by ensuring that the centroids of the target and comparison stars fall on the identical rows of the same CCD readout amplifier. Cosmic ray removal was effected using the `SALTCRCLEAN` routine provided by `SALTRED`.

Differential photometry of the target was obtained using a reduction package created by Dr O'Donoghue, `scamphot`. `scamphot` operates using virtually identical routines to that of the `reduce` package described in Chapter 5, but customised to deal with SALTICAM image files. PSF photometry was used for OY Car. After reduction, the instrumental magnitudes were converted to relative intensities which were corrected to the same baseline using the comparison stars. The data were then binned to $\simeq$1.1 secs (0.0002 in phase). The resulting light curves are shown in Figures 6.3 to 6.5 and have been separated according to comparison stars where applicable.

Table 6.1: SALT observations of OY Car: The asterisks denote observations for which different comparison stars were used compared to the rest of the set. Observations with the same number of asterisks (including zero) used the same comparison stars.

Day/Mon/Year-2000	Date (HJD) 2450000 +	Exposure (s)	Cycle	Comments
10/03/07	4170.366	0.2	133358	Excellent conditions
30/03/07 *	4190.312	0.2	133674	Bright moon, some cirrus
31/03/07 *	4191.323	0.2	133690	Excellent conditions
12/04/07	4203.315	0.5	133880	
14/04/07	4205.272	0.1	133911	Some cirrus
19/02/08 **	4516.395	0.2	138840	
19/02/08 **	4516.458	0.2	138841	
04/04/08	4561.274	1.0	139551	Declining from outburst
05/04/08	4562.284	1.0	139567	Declining from outburst
23/04/08	4580.335	1.0	139853	
27/04/08	4584.313	1.0	139916	
27/04/08	4584.376	1.0	139917	
14/05/08	4601.229	1.0	140184	Some cirrus
10/06/08	4628.245	1.0	140612	Some cirrus
29/03/09	4920.369	1.0	145240	
30/03/09 (1st)	4921.377	1.0	145256	
30/03/09 (2nd)	4921.415	1.0	145257	
31/03/09 (1st)	4922.389	1.0	145272	
31/03/09 (2nd)	4922.413	1.0	145273	
04/04/09	4926.429	1.0	145336	

6.2.4 Light Curves

In the rest of this analysis, the light curves presented in this section shall be referred to by their date designations. Where more than one light curve was obtained on a particular night, the light curves will be differentiated by the suffix qualifier (1st) or (2nd). The light curves have been phased in the same manner as the light curves presented in Chapter 5: each cycle was phased relative to the mid-eclipse times for that cycle using the same ephemeris as that used in Section 5.2.5 to phase the data and listed in Table 5.11[4].

Following the method of Wood, Pringle & Irwin (1985), WH89 obtained $(\phi_{\rm WDi}, \phi_{\rm WDe})$ (as defined in Section 5.2.4) for each of their light curves of OY Car using the derivative profiles. For each derivative profile, the contact times – defined as being the points at near ingress/egress of the central object which deviated from zero – were flagged. The profile outside of these contact times was then fitted with a spline. This spline was subtracted from the full profile with the intention of removing the contribution of the bright spot and accretion disc from the derivative. The remaining derivative curve between the flagged contact times was then integrated to obtain the white dwarf profile. Times of mid-ingress/egress were determined from this integrated curve.

As demonstrated in Section 5.2.4, this technique is not used here as, for profiles not dominated by the disc eclipse, the variation of the light from the bright spot and the disc can be taken to be linear during the comparatively short duration of ingress/egress of the central object. This is the case for the quiescent light curves of OY Car. Moreover, the bright spot makes no contribution at all to the egress of the central object as it is completely hidden during the event (making the egress of the eclipse more favourable for analysis than ingress, as shall be seen in the next section). Thus the phases of the half-flux points determined from the light curves, $(\phi_{\rm WDi}, \phi_{\rm WDe})$, can be assumed to be identical to the phases of half flux (for ingress and egress respectively) of the central object itself. The linear variation of the bright spot and disc over the ingress/egress intervals of the central object would then add a small vertical offset to the ingress/egress humps in the derivative profiles. This may affect the measurement of the contact times, $(\phi_1, \phi_2, \phi_3, \phi_4)$, noticeable as ingress/egress widths which are slightly larger than those previously found in the literature[5], but avoids the possible corruption of the shape of the ingresses/egresses by subtraction of fitted functions. Since the vertical offsets will not affect the overall shapes of the central object's ingress/egress derivatives, the accurate measurement of contact

[4]Note that, due to the domination of the disc profile in light in and declining from outburst, only the quiescent light curves in Table 6.1 were subjected to the analysis presented in Section 6.6.

[5]As they are taken to be the points near the start/end of ingress/egress for which the derivative profile significantly deviates from zero.

times is of secondary concern in this work.

The phase results presented in Chapter 5 indicated that intrinsic cycle-to-cycle variation produces an over-estimate of the observational error if the standard deviation is used as the estimate. Accordingly, and in the same manner as Section 5.2.4, the errors associated with the timings presented in this chapter have been estimated by propagating the estimated errors in relative intensity due to noise in the region of interest in the light curve (e.g. immediately preceding/following points of contact). For the binned SALTICAM observations presented here, this translates to errors in the bright spot and central object mid-ingress/egress timings of less than 1 second, or $\lesssim 0.00022$ in phase.

The light curves taken on the dates 30/03/07, 31/03/07 and 19/02/08 used different comparison stars to the rest of the curves (refer to Figure 6.3, calendar dates are given as (year-2000)). The same vertical scale factor was used for all curves having the same comparison stars. The general features of OY Car's light curves have already been discussed in Chapter 5. This section summarises the particular features of interest noted in the light curves presented here:

- Examination of the region of the light curves (Figures 6.3-6.5) immediately preceding egress (at $\phi \sim 0.015$) show that in a few cases (30/03/07, 12/04/07, 14/04/07, 19/02/08 (1st eclipse) and 14/05/08) the flux does not reach minimum with the accretion disc starting to emerge just before egress of the central region. Instead, the flux continues to decrease right into the start of egress (refer to Figures 6.3 to 6.5). This indicates that there is some extended bright feature still undergoing eclipse. In the case of 12/04/07, the eclipse of this feature continues right the way through the egress of the central region (the same rate of brightness decay is observable immediately following egress). This suggests an extended region of brightness present, elongated along the rim of the disc, downstream of the bright spot. The fact that this decrease continues right through disc egress shows that it is brighter, in optical light, than the innermost parts of the disc. A systematic change in the phase characteristics due to the presence of this bright feature could not be identified.

- ΔL_e is defined here as the measure of the change in intensity during egress of the central source. There is a clear variance in ΔL_e present. There is no correlation between the variations in minimum light at $\phi \sim 0.015$ and ΔL_e which suggests that the variations in ΔL_e are due to brightness variations within the central region (either the central object itself or the very inner disc) and not to the outer regions of the disc. This shows that the brightness of the central region from cycle-to-cycle can not be considered constant for analysis.

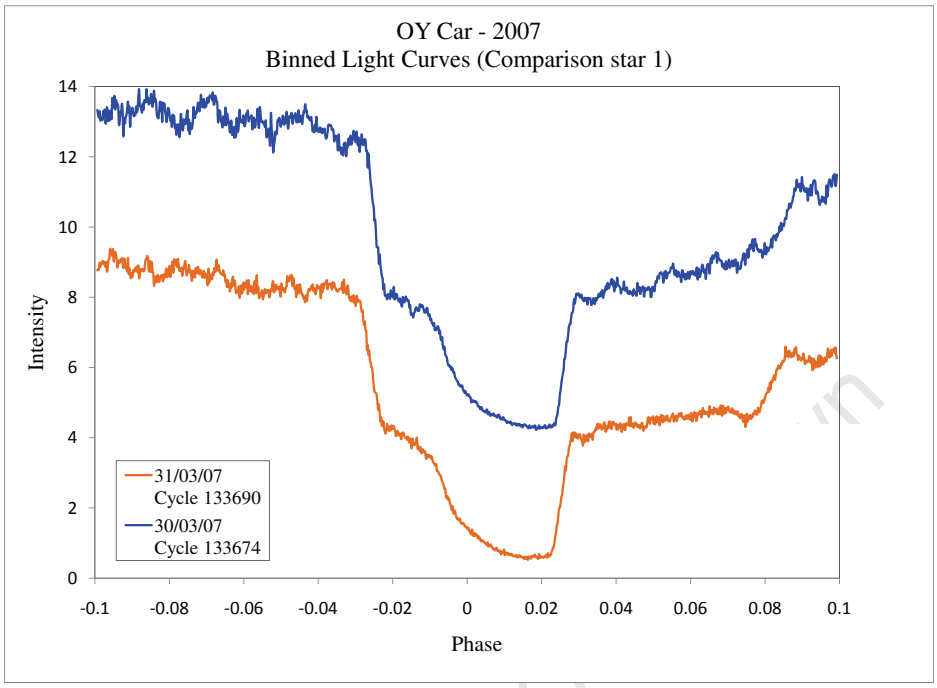

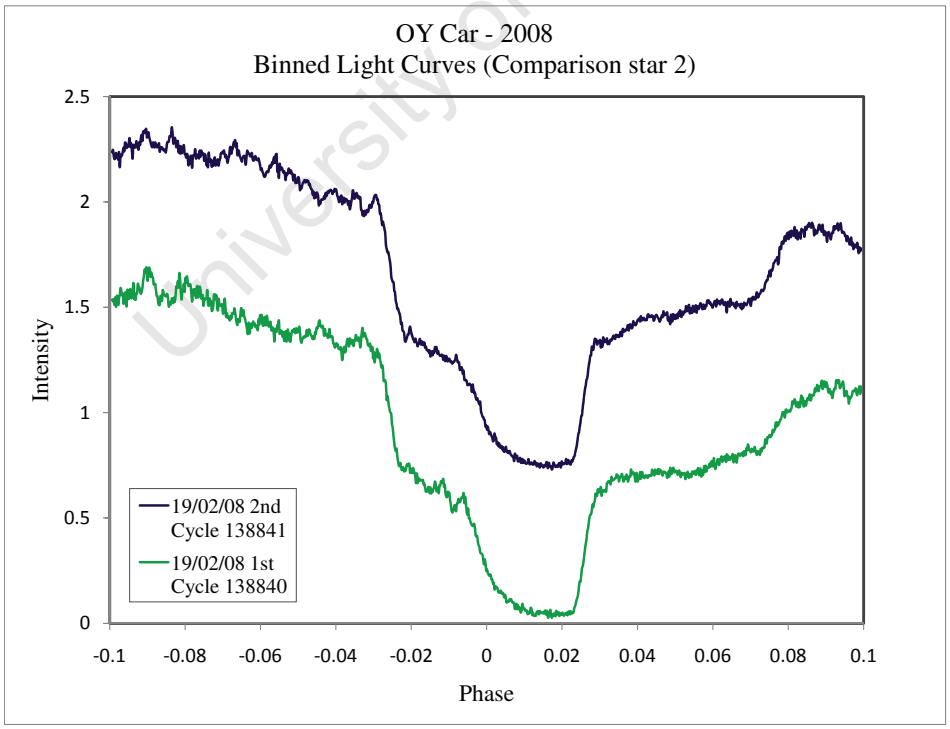

Figure 6.3: OY Car light curves for 2007 and 2008, taken in white light and binned to 1 second intervals. The observations have been separated according to the comparison stars used for different runs (all curves within the same plot use the same comparison star).

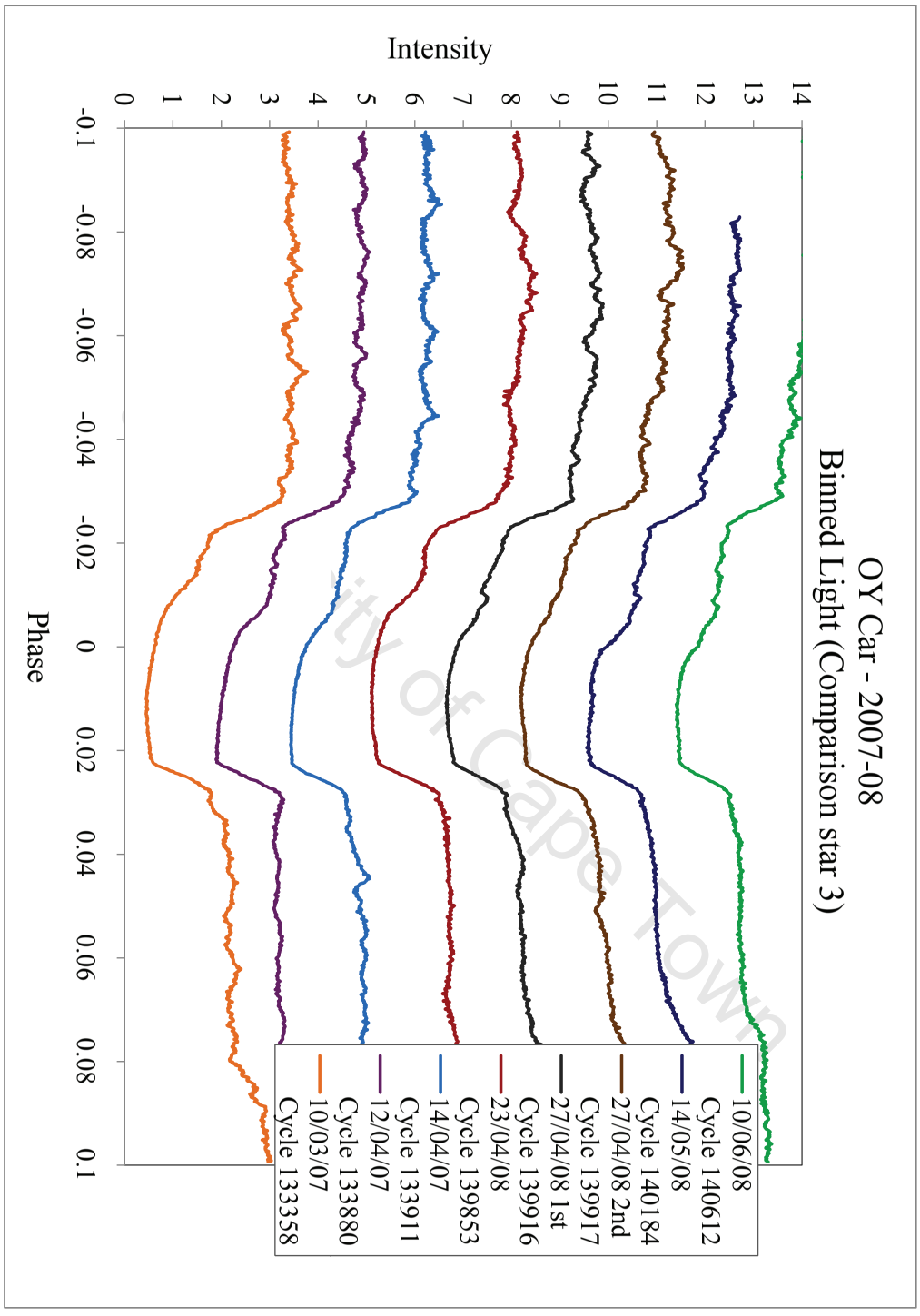

Figure 6.4: OY Car light curves for 2007-2008, taken in white light and binned to 1 second intervals. The observations have been separated according to the comparison stars used for different runs (all curves within the same plot use the same comparison star).

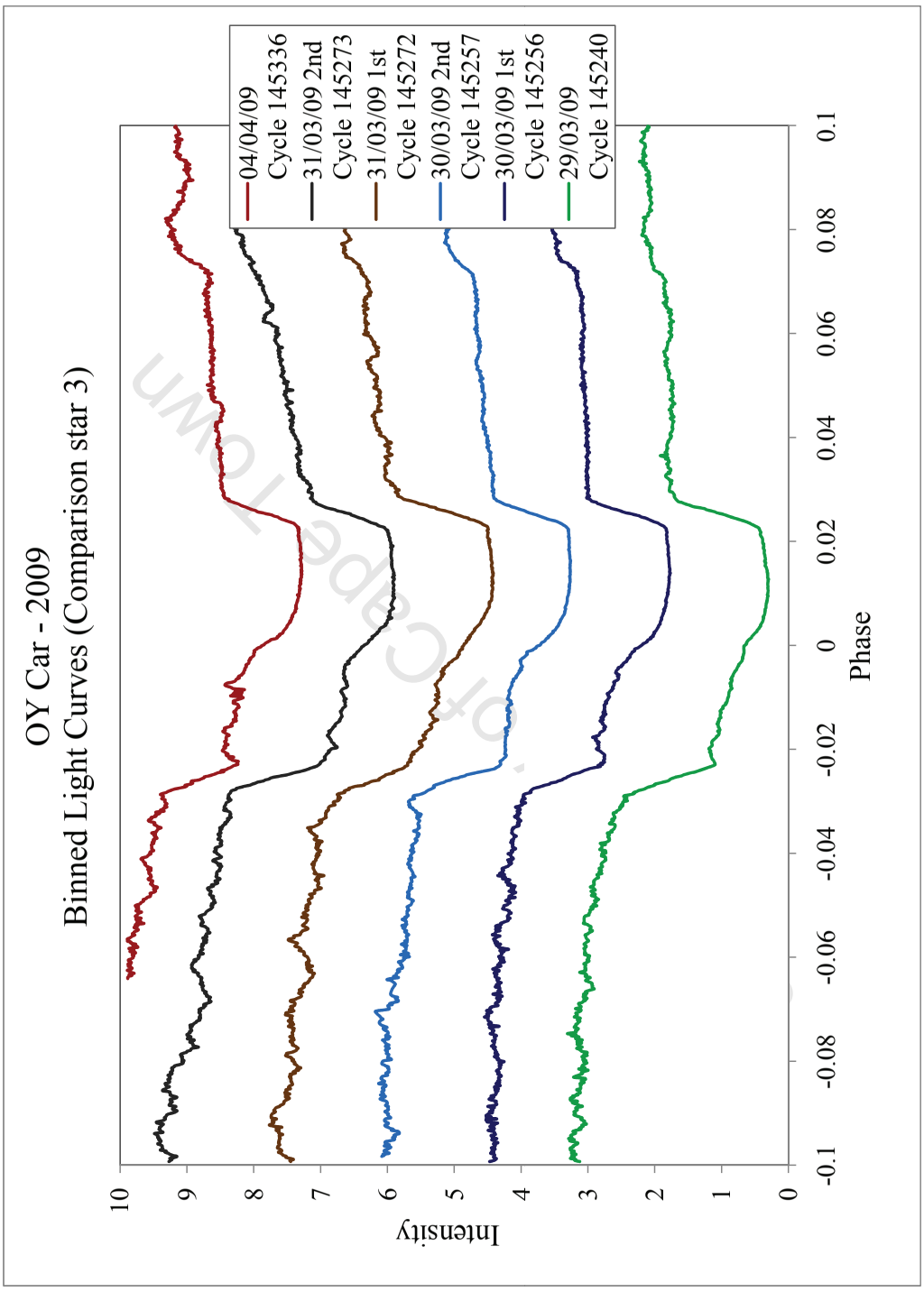

Figure 6.5: OY Car light curves for 2009, taken in white light and binned to 1 second intervals. The observations have been separated according to the comparison stars used for different runs (all curves within the same plot use the same comparison star).

Table 6.2: OY Car: Times of mid-eclipse (HJED), symmetrised phases of half-flux of the central object and corresponding eclipse width. The asterisks denote observations for which different comparison stars were used compared to the rest of the set. Observations with the same number of asterisks (including zero) used the same comparison stars. The † tagged observations at the end of the table indicate observations that were taken while OY Car was declining from outburst.

Date	Cycle	Mid-eclipse (HJED)	$\phi_{\mathrm{WDi/-e}}$	$\Delta\phi$
10/03/07	133358	2454170.36603940	-0.02477	0.04953
30/03/07 *	133674	2454190.31275111	-0.02547	0.05094
31/03/07 *	133690	2454191.32268977	-0.02554	0.05108
12/04/07	133880	2454203.31596340	-0.02556	0.05112
14/04/07	133911	2454205.27240654	-0.02575	0.05150
19/02/08 ** (1st)	138840	2454516.39534999	-0.02629	0.05258
19/02/08 ** (2nd)	138841	2454516.45848340	-0.02559	0.05118
23/04/08	139853	2454580.33689051	-0.02534	0.05068
27/04/08 (1st)	139916	2454584.31347800	-0.02534	0.05069
27/04/08 (2nd)	139917	2454584.37659267	-0.02602	0.05204
14/05/08	140184	2454601.22993630	-0.02544	0.05088
10/06/08	140612	2454628.24570311	-0.02578	0.05156
29/03/09	145240	2454920.36924190	-0.02554	0.05108
30/03/09 (1st)	145256	2454921.37761815	-0.02559	0.05118
30/03/09 (2nd)	145257	2454921.41527435	-0.02544	0.05089
31/03/09 (1st)	145272	2454922.38905158	-0.02607	0.05214
31/03/09 (2nd)	145273	2454922.41317395	-0.02530	0.05060
04/04/09	145336	2454926.42904442	-0.02578	0.05156
04/04/08†	139551	2454561.27438411	-	-
05/04/08†	139567	2454562.28431864	-0.02688	0.05377
Mean			**-0.02560**	**0.05132**
std dev			**0.00044**	**0.00089**
Wood 89			-0.0252/0.0253	0.0506
std dev			0.0004/0.0003	0.0004

- Interestingly, 12/04/07 also presents the largest disparity in luminosity between ingress and egress where $\Delta L_i \sim= 1.16$ (the change in intensity during ingress of the central source) increases to $\Delta L_e \sim= 1.49$ and the duration of ingress, $\Delta_{wi} = 0.005$ increases to $\Delta_{we} = 0.0074$ for duration of egress[6]. This shows that, not only is the brightness of the central region variable, but it can vary on a timescale comparable to the *duration of eclipse* of the central object. WH89 also noted variations in the flux of the central region from the eclipse ingress and egress (a standard deviation of $\sim 10\%$ of the average) 'most certainly due to the white dwarf'. The present study reaches the same conclusion; the variations are due to the central object. This could be due to an increase in brightness of a thin accreting boundary layer.

Table 6.2 gives the mid-eclipse times and cycle numbers for the light curves shown in Figures 6.3 to 6.5. The phases of mid-ingress/-mid-egress, $(\phi_{\mathrm{WDi}/-\mathrm{e}}) \equiv (\phi_{\mathrm{WDi}}, -\phi_{\mathrm{WDe}})$, are given along with the corresponding eclipse widths $\Delta\phi$, derived in the same manner as that described in Chapter 5. In addition, WH89's phase results - the data set used for OY Car's central object's analysis by WH90 - are included for comparison.

The larger scatter in the timings presented in Table 6.2, compared with those of WH89, is due to the fact that their timings were not symmetrised about mid-eclipse. Symmetrising them would commute the scatter in the mid-eclipse timings - taken to be largely due to the chosen ephemeris not fully describing the eclipse cycle - to the mid-ingress and mid-egress timings, thereby increasing their scatter. This however will not increase the scatter in the eclipse widths as the process is simply a horizontal offset in the mid-ingress and mid-egress times (uncorrelated between cycles). WH89 use the standard deviation of their phase timings as an estimation of the measurement error, though, in the case of the eclipse widths, this should be seen as an underestimation. If the standard deviation in the mid-ingress/egress timings can be taken as the estimated error in their measurements then simple propagation of errors should yield errors in the eclipse widths of greater magnitude than those of the constituent mid-ingress/egress times. At the end of the next section an estimate of WH89's error in the eclipse, ingress and egress widths are included in the summary of results.

In order to discriminate between the various profiles shown in Figure 6.2, the highest resolution of sharp discontinuities in the data and in their derivatives is needed. Accordingly, in sections 6.3 and 6.4, we turn our attention to an investigation of various techniques of differentiating noisy, one-dimensional data sets.

[6]Since, in this case, the egress of the central region is superimposed on top of the continued occultation of the rim feature, this value of ΔL_e - the largest in the set for the third comparison star - is in fact an underestimation of the total brightness of the central region observable at egress.

6.3 Smoothing and Differentiation of Noisy Data: Common Methods

Differentiation yields a measure of the rate of change in a function or data set and, hence, is very sensitive to rapid variations. Therefore, depending on the method of differentiation, the derivative profile of a data set can be strongly affected by the presence of noise. Slowly varying features inherent in the data can be heavily corrupted by the amplification of noise that is a consequence of differentiation, rendering the result all but useless for detecting weak features in a low signal-to-noise data set.

There are two common approaches to addressing this problem. The first is to smooth the data set using a simple form of low-pass filter before differentiating the set using straightforward finite differences. This is the approach taken by WH90 after Wood, Irwin & Pringle (1985) and will be shown to be less than adequate for the purpose of the investigation. The second approach is to try to fit a smooth function to the data, usually a form of least-squares polynomial fitting and then to obtain the derivative of the final fit using the coefficients of the polynomials. The results of both these approaches are examined and compared in the rest of this section.

6.3.1 Smoothing using Moving Averages

The simplest form of low-pass filter is the 'boxcar' or moving averages method. This method runs through a data set replacing each data point with the average value of its neighbours. If the neighbouring data points include points 'ahead' of the current point to be replaced, the filter is said to be non-causal. A similar technique, and that used by WH90, replaces each point with the median of its neighbours. The larger the number of neighbouring points included in the averaging, the smoother the result will be, at the expense of averaging out sharp or subtle changes inherent in the data.

A more general form of moving averages is presented here, which allows fine tuning of the trade-off between the smoothness of the result and its sensitivity to local discontinuities. This form can be written as:

$$s_t = \alpha x_t + \left(\frac{1-\alpha}{N-1}\right) \sum_{j=1}^{\frac{N-1}{2}} (x_{t-j} + x_{t+j})$$

where s_t is the weighted average of the point, x_t, to be replaced, N is the filter width (assumed to be an odd number of data points) and α is the weighting parameter. $\alpha = 1/N$ reduces the form to a simple average of all $x_1 - x_N$.

WH90 first smoothed their OY Car data set using a median filter, 9 seconds in width, before differentiating and smoothing the results using a 3 second width 'boxcar' filter. This approach to filtering and smoothing the data was taken from the work of Wood, Irwin & Pringle (1985) and is unsuitable for discriminating between the derivatives of model eclipse curves for two reasons. Firstly, Wood, Irwin & Pringle (1985) were interested in isolating the eclipse of the central object from the rest of the eclipse curve and so the width of the median filter was selected to be small in comparison to the *full width* of ingress(/egress). The sharply discontinuous features present in the double peak profiles shown in Figure 6.2 are between $0.001 - 0.003$ of phase in width (compared to ~ 0.009 for the full ingress/egress)[7] therefore any double peaked features would have been smeared out by WH90's selection of median filter. Secondly, the 'box car' filter used to smooth the derivatives was selected to match the expected form of the ingress/egress derivative i.e a roughly constant value within ingress/egress (and zero elsewhere). This was done by Wood, Irwin & Pringle (1985) because one of the main aims of the investigation was to detect the times of contact as accurately as possible. However, the assumption of a flat ingress/egress derivative profile selects against the detection of inherent higher order features which may be present.

After smoothing, WH90 used a form of finite differencing to differentiate the data set. Differentiation of data sets using finite differencing is very sensitive to noise. Figures 6.6 and 6.7 shows a comparison of derivatives of a smoothed test function $y = |x - 1/2|$ with gaussian noise of standard deviations $\sigma = 0.01$ (Figure 6.6) and $\sigma = 0.05$ (Figure 6.7) added[8]. The noise-free test function is well suited for testing numerical differentiation as it has a discontinuous derivative at $x = 1/2$. The test functions were first smoothed (before differentiation) using the form of moving averages described above with $N = 3, \alpha = 0.2$ (green), $N = 9, \alpha = 1/N$ (blue) and a median filter of width 9 (orange)[9]. The resulting smoothed functions were differentiated using centred differences, with the derivative result of the median filter further smoothed using a 3-second width 'boxcar' filter following WH90 (data points at the filter boundaries have been ignored). The ideal (exact) derivative of the function (using centred differences) is shown in black.

As can be seen from the results, all three methods of smoothing are quite sensitive to

[7] Though these eclipse profiles were calculated for the dwarf nova Z Cha, the assumed scalability of eclipsing profiles means that we can assume that any 'higher order features' (i.e features seen over-and-above the simple bare-white-dwarf ingress/egress profile) will be of the same fraction of the ingress/egress widths for a given eclipse profile.

[8] The noise profiles added to the data are generated by randomly drawing the errors from gaussian profiles of standard deviations $\sigma = 0.01$ and $\sigma = 0.05$. The test function results presented here, and in the rest of this chapter, serve as typical samples of a test result population where the noise profiles were randomly generated for each case as described.

[9] WH90's observations were binned to 1 second intervals, so choosing a median filter of width 9 here is an appropriate demonstration of their process.

the amount of noise present. Whether WH90 used finite differencing or another method of numerical differentiation, it can be seen from the Figure 6.7 (top) that, in the presence of noise, using a median filter is not a good first smoothing treatment of the data. In Figure 6.6 the 9-point moving average offers the smoothest result but smears out the point of discontinuity in the derivative over the widest range. Nevertheless, all three smoothing techniques fail to mitigate the noise amplifying effects of finite-differencing in the high noise condition (note that Figure 6.7 has had to be plotted at double scale to compare the results to the exact solution): the derivatives are so heavily compromised by this differentiation procedure as to render them useless. Thus finite differencing is clearly not a good derivative technique, even in the best of noise conditions.

6.3.2 Smoothing using Least-Squares Polynomial Fitting

A second approach to the problem of smoothing and differentiating a noisy data set is to fit the data with a polynomial using least squares regression, and to use the fitting coefficients to obtain a derivative of the fitted function. Two implementations of this approach are discussed and compared below.

Savitzky-Golay filters

Savitzky-Golay smoothing is a form of moving average where polynomial regression is used to fit to running sets of m (an odd number) data points, a polynomial of degree $\leq m-1$. For a data set $x_i, y_i; i = 1, \ldots, n$, the polynomial is defined as:

$$Y = a_0 + a_1 z + a_2 z^2 + \cdots + a_k z^k$$

where $z = \frac{x-\overline{x}}{h}$, h is the separation interval between adjacent points and $\overline{x}$ is the central point within set m, so z takes the values $(1-m)/2 \ldots 0 \ldots (m-1)/2$ (Savitzky & Golay 1964). The coefficients $a_0, a_1 \ldots$ are determined by solving the normal equations:

$$\mathbf{a} = (\mathbf{J}^T\mathbf{J})^{-1}\mathbf{J}^T\mathbf{y}$$

where the ith row of $\mathbf{J}$ has the values $1, z_i, z_i^2, \ldots, z^k$. The coefficient of interest is $a_0 = \sum_{i=1}^{m} C_i y_i$ which is the smoothed value for the central point $z = 0$. The coefficients C_i are known as the convolution coefficients (Lohninger 1999, 2006). Savitzky and Golay (1964) published tables of convolution coefficients in their seminal paper "Smoothing and Differentiation of Data by Simplified Least Squares Procedures" and their technique has been widely favoured as it "tends to preserve features of the distribution such as relative

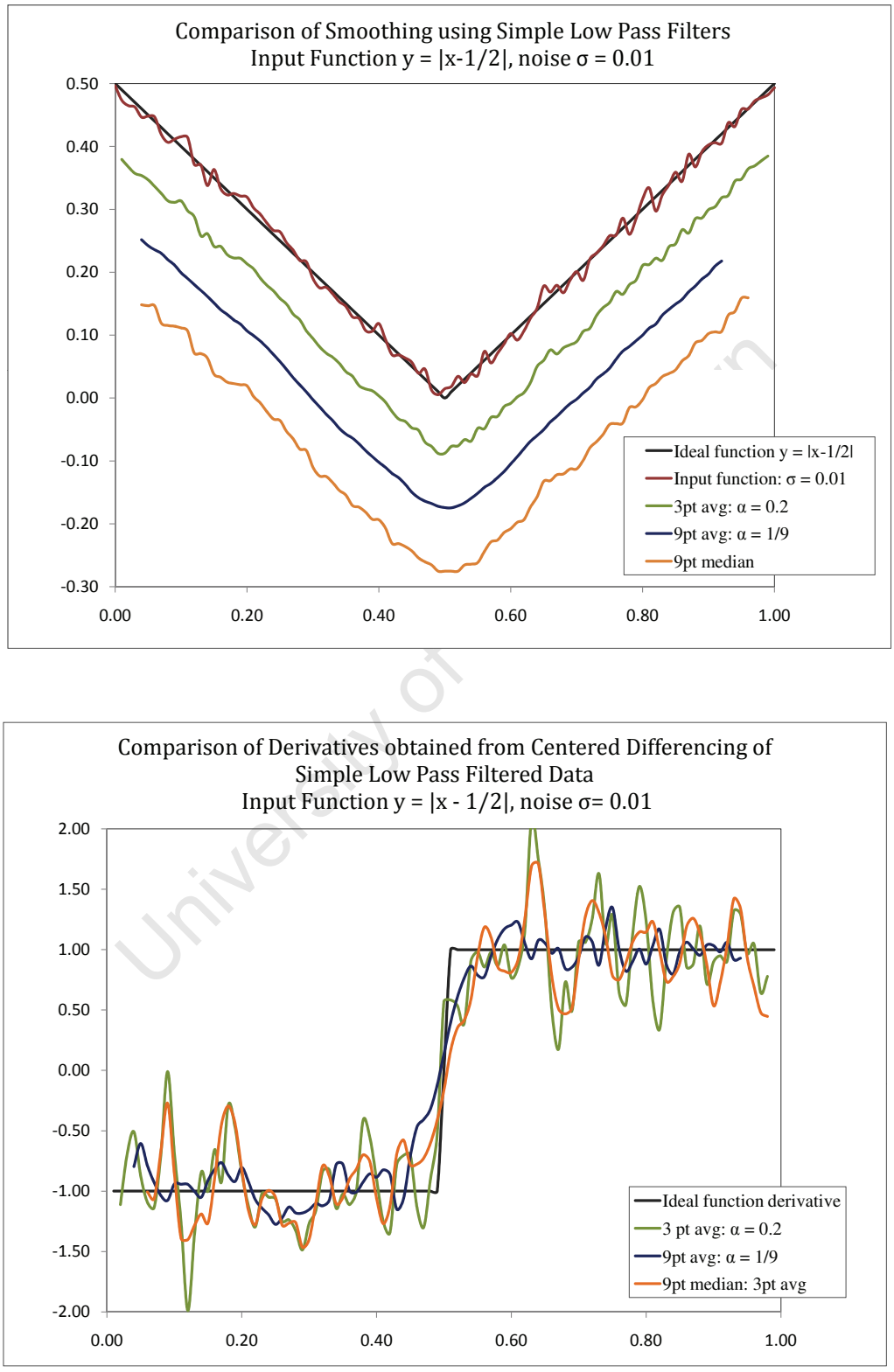

Figure 6.6: The test function $y = |x - \frac{1}{2}|$ with gaussian noise of $\sigma = 0.01$ added (top) and its derivatives (below) taken using finite differencing. See text for further details.

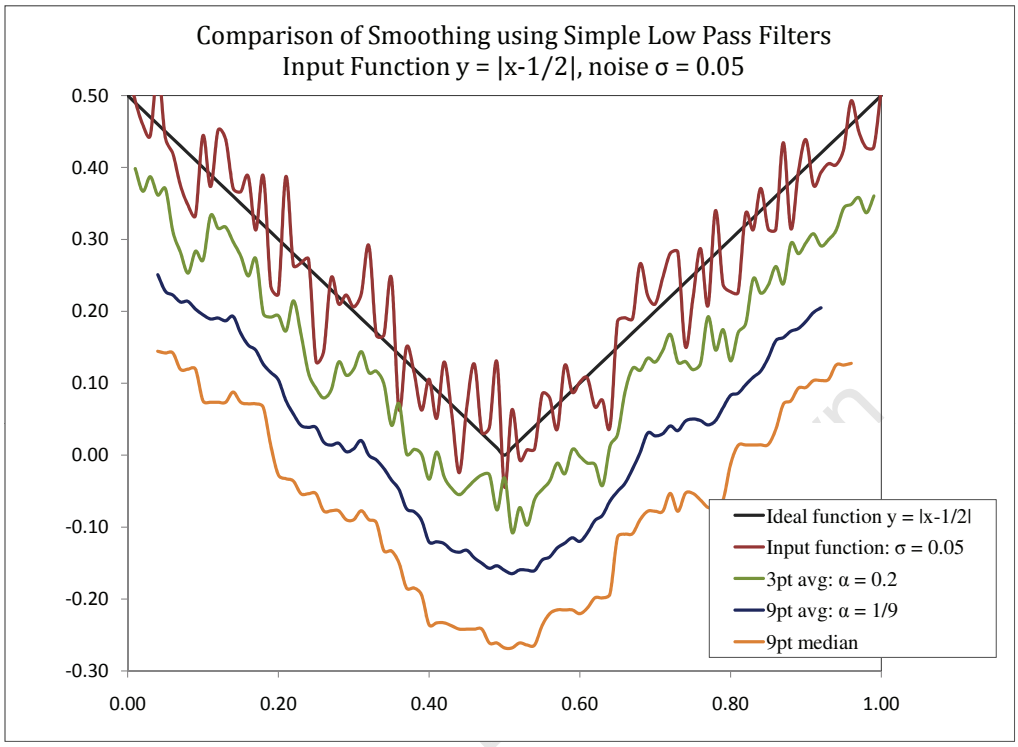

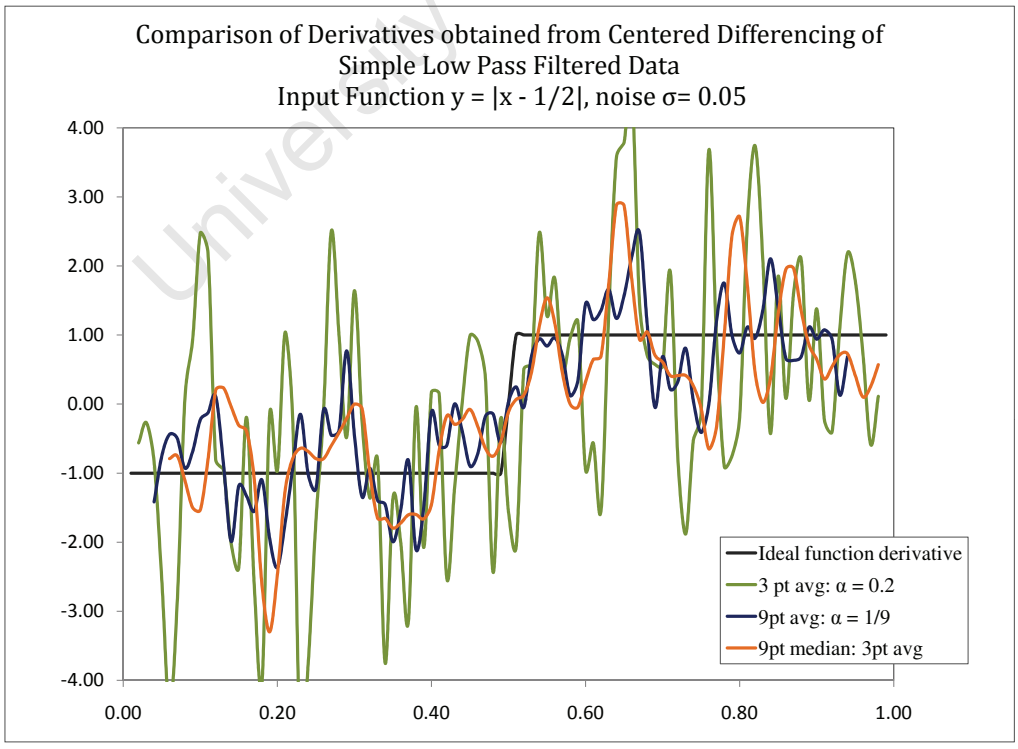

Figure 6.7: The test function $y = |x - \frac{1}{2}|$ with gaussian noise of $\sigma = 0.05$ added (top) and its derivatives (below) taken using finite differencing. Note that the scale in the bottom plot has been doubled (with respect to the derivative plot scale in Figure 6.6) for clarity. See text for further details.

maxima, minima and width, which are usually flattened by other adjacent averaging techniques", like moving averages (Wikipedia 2009). Numerical derivatives are simply obtained by differentiating Y (Lohninger 2006).

Higher orders (k) of polynomials admit more rapid signal variations to the final result, while wider convolution function widths (m) increase signal to noise, with different (m, k) combinations producing different response functions. Here (Figures 6.8 and 6.9, see below) a quartic, fitted to a filter width of 7 points is applied to our test function and compared to the most commonly used form of polynomial regression smoothing: smoothing cubic splines.

Smoothing cubic splines

Cubic spline interpolation is a method of interpolating data by fitting piecewise polynomials to a set of coordinates or observations $(x_0, y_0), (x_1, y_1), ..., (x_n, y_n)$ which approximate the function $y(x)$. The polynomials are cubic functions which guarantee continuity in the first and second derivatives of the resulting interpolant at the nodes (observations) of the cubic segments. The cubic spline holds the important property that it is the minimiser to the squared norm of the function:

$$||y(x)||^2 = \int_{x_0}^{x_n} \{f''(x)\}^2 \, dx$$

In other words, of *all the possible functions* which can pass through the nodes $(x_0, y_0), (x_1, y_1), ..., (x_n, y_n)$, the cubic spline is the function which *minimises the total curvature* (as the squared norm is an approximation of the total curvature of $y(x)$) (Pollock 1993).

If one relaxes the strict criterion that the spline function should pass through all of the data points, then the resulting fit is known as a smoothing spline. If we take the ordinates to be $y(x_i) = f(x_i) + \varepsilon_i$ where $\varepsilon_i; i = 0, ..., n$ form a sequence of independently distributed random variables and $V(\varepsilon) = \sigma_i^2$, then we can attempt to extract $f(x_i)$ by finding the spline function $S(x)$ which minimises the value of

$$L = \lambda \sum_{i=0}^{n} \left(\frac{y_i - S_i}{\sigma_i} \right)^2 + (1 - \lambda) \sum_{i=0}^{n-1} \int_{x_i+1}^{x_i} \{S_i''(x)\}^2 \, dx$$

where $S_i = S(x_i)$ are defined piecewise and $\lambda \in [0, 1]$ is the parameter which weights the relative importance of the first term, the data fidelity term, and the second, smoothing term (Gans 1992).

The result of a cubic spline fit to our test function, $y = |x - \frac{1}{2}|$, and its derivative, are shown in Figures 6.8 and 6.9, along with the results of the Savitzky-Golay (SG) 7-point quartic filter. The cubic spline fit and its derivative were obtained using Python's scipy.interpolate package, with the best result produced using smoothing parameter $s = 0.01$ for the gaussian noise of $\sigma = 0.01$ and $s = 0.026$ for gaussian noise of $\sigma = 0.05$.

Polynomial regression performs reasonably (Figure 6.8) for smooth, low noise, slowly varying data but, as can be seen from Figure 6.9, does not perform so well for noisy data with discontinuities. The SG filter provides a noisy derivative of the data with gaussian noise of $\sigma = 0.01$ added as input, which improves somewhat when the filter width is increased (not shown). However the SG derivative completely breaks down when the input noise is increased (see bottom of Figure 6.9, note that the vertical scale has been doubled). The smoothing cubic spline filter produces a far smoother derivative for both test inputs however, the amount of smoothing necessary to produce a derivative uncorrupted by noise when the noise input is increased to $\sigma = 0.05$, greatly smoothes out the discontinuity.

Therefore what is required is a differentiation technique that does not 1) over-smooth discontinuities (important for discerning contact times and higher order peaks in the ingress/egress shape) and 2) does not fail under relatively poor SNR conditions. Both of these requirements are satisfied by the technique of smoothing and differentiation of data described in the next section, namely "Total Variation Regularisation".

6.4 Smoothing and Differentiation of Noisy 1D Functions using Regularisation Techniques

6.4.1 Total Variation Regularisation (TVR)

Total variation regularisation (TVR) is an extension to Tikhonov regularisation, the most commonly used technique for regularising the solutions to a particular class of ill-posed problems, integral equations. Tikhonov regularisation involves regularising the solution which minimises the least squares residual $||\mathbf{Au} - \mathbf{f}||^2$ – where $\mathbf{A}$ is a matrix operator, $\mathbf{u}$ is the fitting function to fit to $\mathbf{f}$, the data – by including the regularisation term, $||\mathbf{\Gamma u}||^2$ for some suitably chosen Tikhonov matrix[10], Γ as part of the minimisation functional (Nguyen 2006, Siltanen 2009). However, while yielding smooth solutions, Tikhonov regu-

[10]Chosen to be the identity operator if smoothing of the data is the desired result. When this is the case, the problem becomes the minimisation of the H^1 norm in u and is hence also known as H^1 denoising.

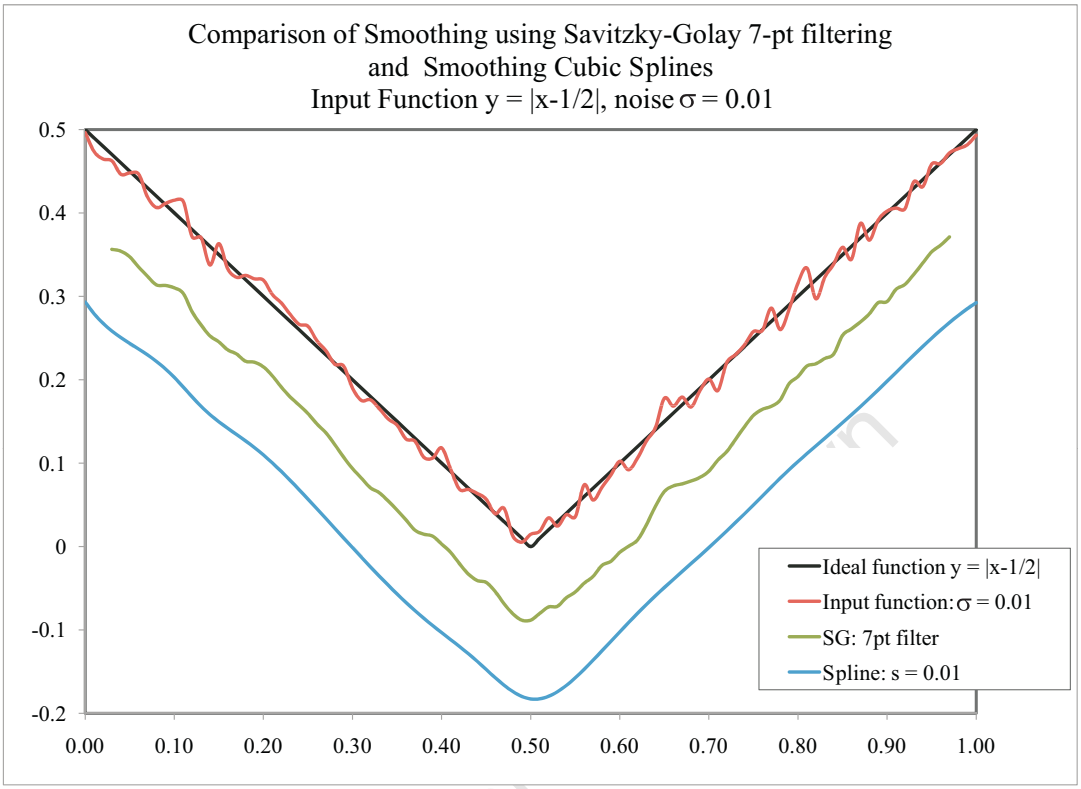

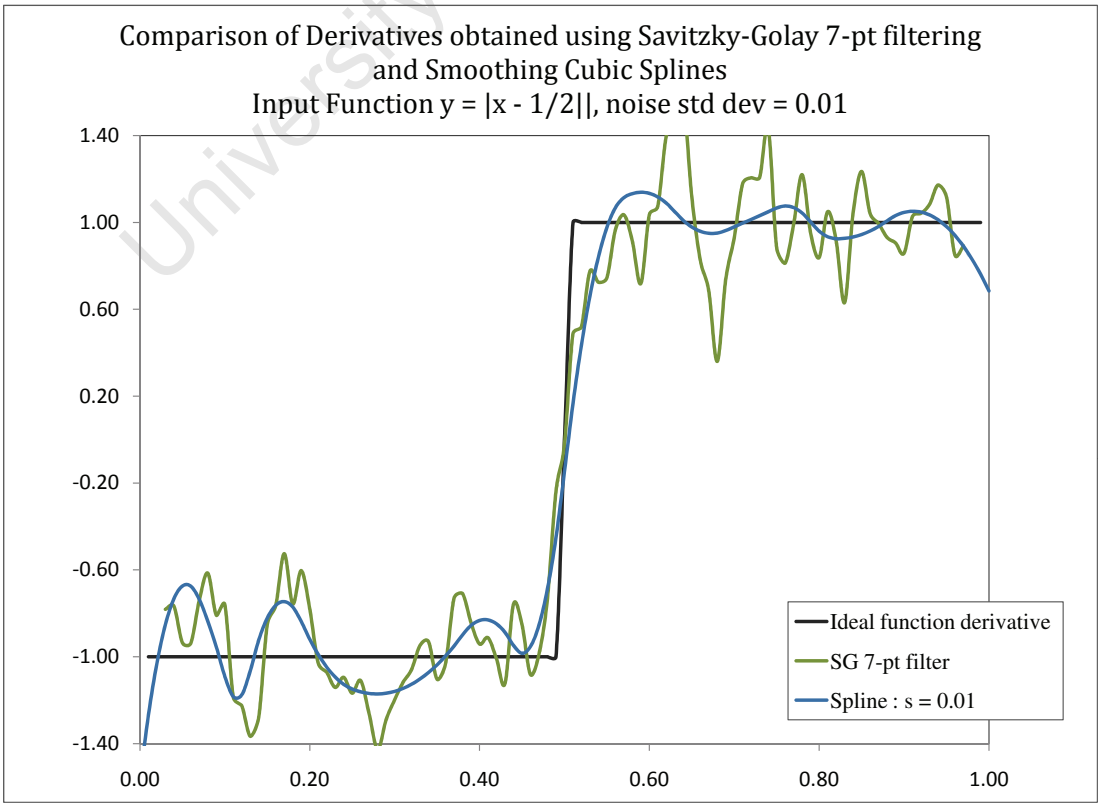

Figure 6.8: The test function $y = |x - \frac{1}{2}|$ with gaussian noise of $\sigma = 0.01$ added (top) and its derivatives (below) taken using polynomial regression. See text for further details.

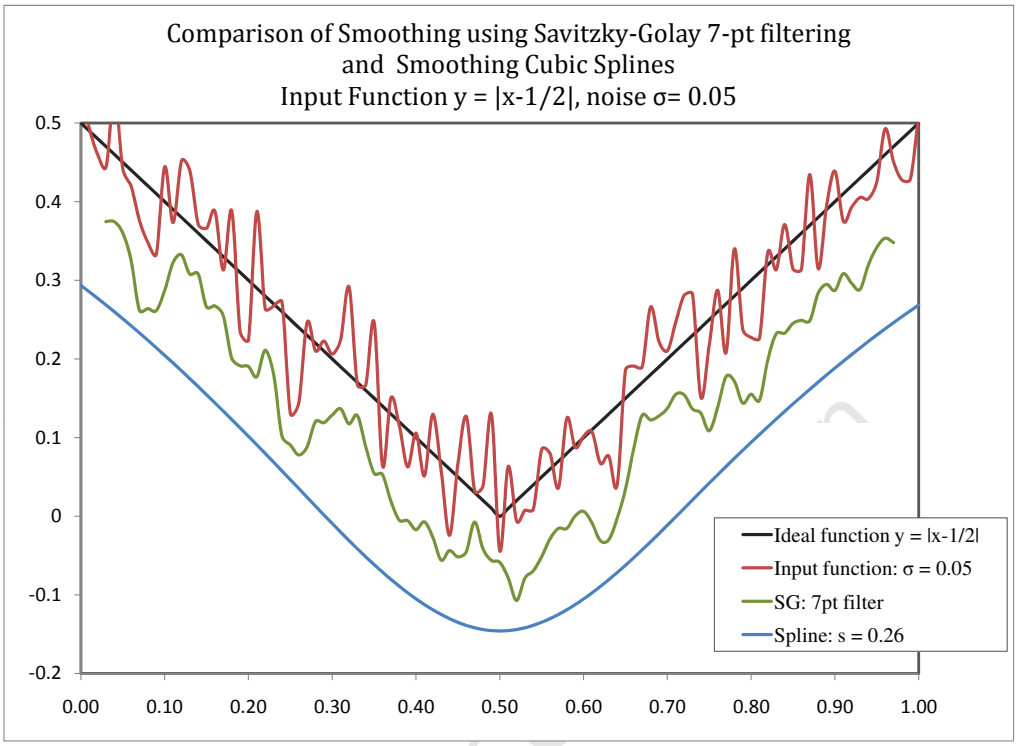

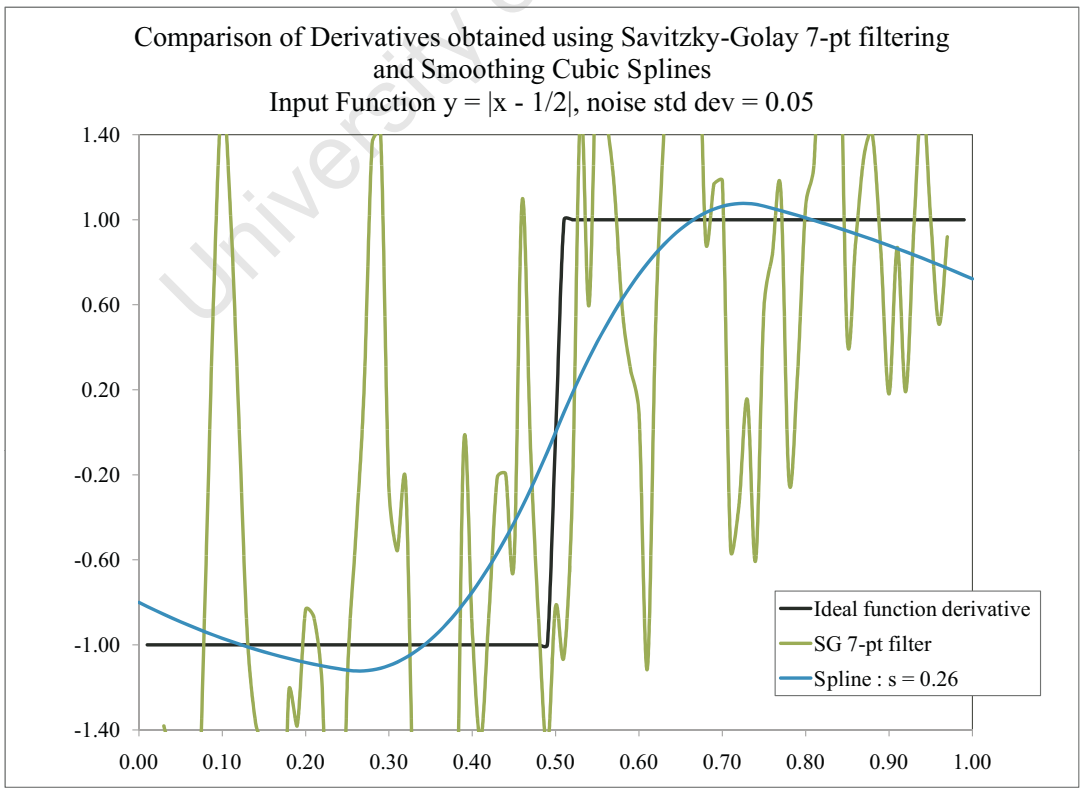

Figure 6.9: The test function $y = |x - \frac{1}{2}|$ with gaussian noise of $\sigma = 0.05$ added (top) and its derivatives (below) taken using polynomial regression. See text for further details.

larisation assumes the input data to be continuous, therefore enforcing smoothness of the result.

TVR, first presented by Rudin *et al* (1992), hereafter ROF, and since well extended and developed (Blomgren *et al.* 1997, Chan & Mulet 1999, Chambolle 2003, 2004, Caselles *et al.* 2007, Zach *et al.* 2007, Edoh & Roop 2009), replaces the Tikhonov term with the 'TV' (total variation) norm in the minimisation functional. TV-norms are essentially L^1 norms of derivatives and, while still regularising the solution, the resulting functional does not assume a continuous input. As such, TVR is used as an 'edge-preserving' technique for denoising data, popularly used in modern image processing (Li & Santosa 1996, Chambolle & Lions 1997, Osher, Solé & Vese 2003, Chambolle 2004, Chan & Esedoglu 2005).

For one-dimensional data sets, TVR involves reconstructing a function, $u(x)$, defined on the interval $x \in [0, L]$, from noisy data, f, by minimising a functional of the form:

$$\begin{aligned} F(u) &= \alpha TV(u) + g(u, f) \\ &= \int_0^L \alpha|\nabla u| + \frac{1}{2}|Au - f|^2 dx \end{aligned} \tag{6.1}$$

where A is an invertible linear operator, the first term is the total variation in u and the second is a data fidelity term. α is the smoothing or 'regularisation' parameter which weighs the cost of the smoothness of the fitted function, $u^\dagger$, against how faithfully it matches the data.

Finding the minimiser, u_0, to equation 6.1 is equivalent to finding the stationary solution to the partial differential equation obtained from the Euler-Lagrange equation:

$$u_t = \alpha \nabla \cdot \frac{\nabla u}{|\nabla u|} - A^* (Au - f) \tag{6.2}$$

Numerically, the solution to equation 6.2 can be arrived at iteratively using a few methods such as the time marching method presented by Rudin *et al* (1992) or the technique of gradient descent. The method used in this investigation, and which delivers the fastest convergence, is the lagged diffusity method employed by Vogel & Oman (1996). This can be expressed by solving the discrete form of equation 6.2 where the equation is "lagging" in the nonlinear term:

$$0 = \alpha \nabla \cdot \frac{\nabla u_{n+1}}{\nabla |u_n|} - A^* (Au_{n+1} - f) \tag{6.3}$$

which makes equation 6.2 linear in u_{n+1}.

[†]If A is the identity operator.

In the next section the numerical implementation of equation 6.3 is discussed and used to differentiate noisy, one-dimensional, test functions.

6.4.2 Differentiation using TVR

Chartrand (2005, 2007 and references therein) proposed applying TVR as a technique to regularise the process of differentiation without enforcing smoothing of the result. This is done by making A in equation 6.3 the antidifferentiation operator so that u becomes the derivative of Au, the smoothed function of f. The results are robust, minimal-noise solutions which reproduce discontinuities very well.

6.4.3 Numerical Implementation

The Algorithm

The method of numerical implementation is that described in Chartrand (2005). Replacing $\nabla|u_n|$ in equation 6.3 with $\sqrt{((u')^2+\eta)}$ (where u' is the derivative in u) for some small $\eta > 0$ avoids division by zero.

The discrete implementation of the algorithm was coded in the free matrix computation software `Octave`. The program structure is shown in Figure 6.10 and can be summarised as the following algorithm, as briefly described in Chartrand (2005):

$n = 0$
$\mathbf{u}_0$: / initial guess
begin loop
$\mathbf{L}_n := L(u_n) = \Delta\mathbf{x}\mathbf{D}^T\mathbf{E}_n\mathbf{D}$ / the 'diffusion' operator
$\mathbf{g}_n := \mathbf{K}^T(\mathbf{K}\mathbf{u}_n - \mathbf{f}) + \alpha\mathbf{L}_n\mathbf{u}_n$ / the gradient
$\mathbf{H} := \mathbf{K}^T\mathbf{K} + \alpha\mathbf{L}_n$ / the approximation to the Hessian
$\mathbf{s}_n := -\mathbf{H}^{-1}\mathbf{g}$ / quasi-Newton step
$\mathbf{u}_{n+1} := \mathbf{u}_n + \mathbf{s}_n$ / update approximate solution
$[\mathbf{u}_{n+1} - \mathbf{u}_n := \epsilon)]$ / exit condition
$n := n + 1$
end loop

where $\mathbf{f}$ is the vector containing the data values (relative intensities in this case) and $\mathbf{u}_0$ is the initial first estimate for the derivative of $\mathbf{f}$, $\mathbf{u}$. $\mathbf{E}_n$ is the diagonal matrix whose i^{th} entry is $\sqrt{((u_n(x_{i+1}) - u_n(x_i))^2 + \eta)}$, $\mathbf{D}$ and $\mathbf{D}^T$ are the matrix forms of the differential operator and its transpose respectively and $\mathbf{K}$ and $\mathbf{K}^T$ are the antidifferentiation operator and its transpose respectively.

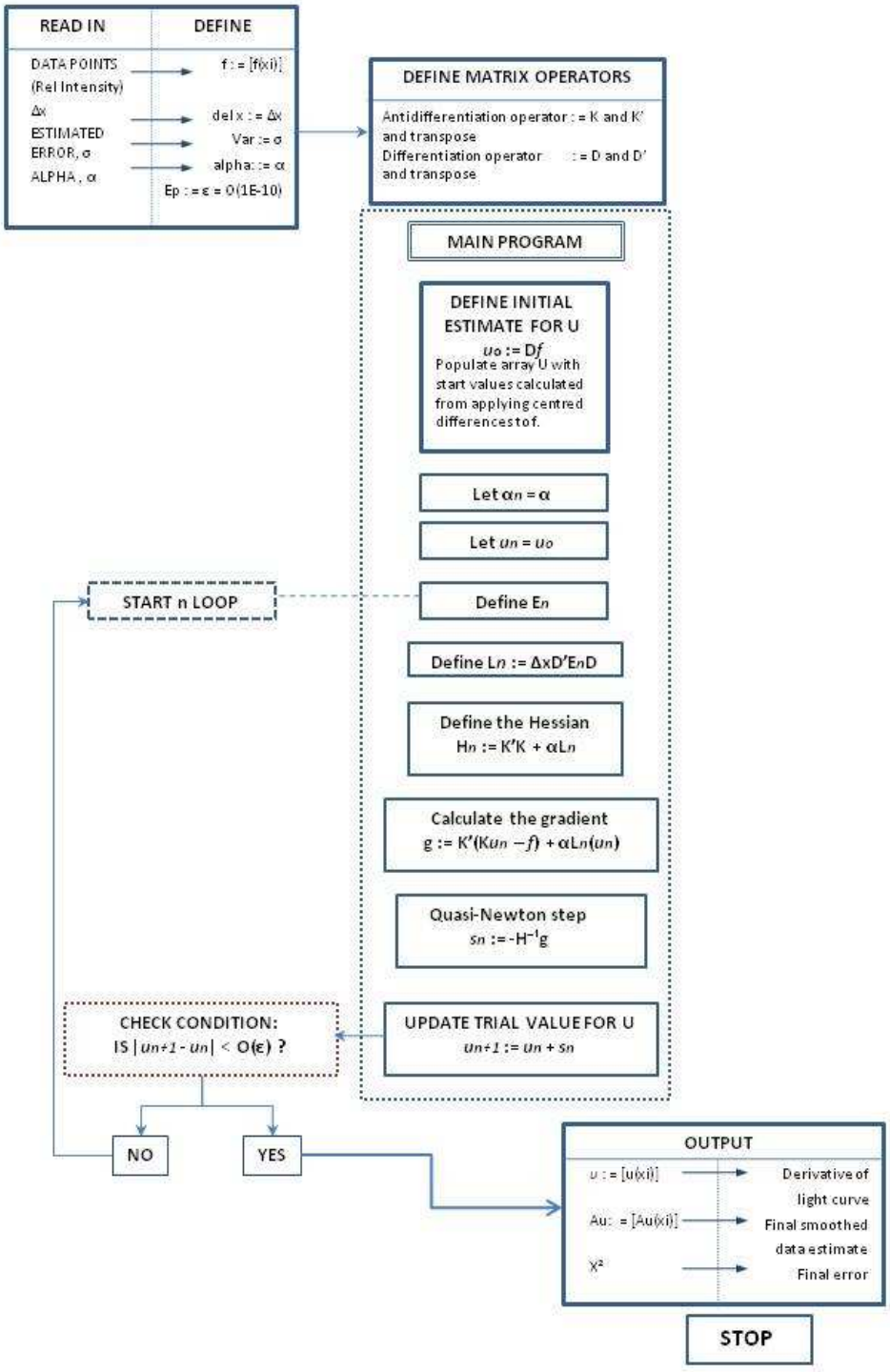

Figure 6.10: Flow diagram showing the author's program structure of the TV regularised differentiation algorithm.

The data is assumed to be defined on a uniform grid of n points. The derivatives are computed halfway between grid points using forward differences in order to deal with the end point conditions ($\mathbf{D}, \mathbf{D}^T, \mathbf{K}$ and $\mathbf{K}^T$ are of dimension $n+1$). Therefore $\mathbf{D}$ is given by the matrix:

$$\mathbf{D} = \begin{bmatrix} \frac{-1}{\Delta x} & \frac{1}{\Delta x} & 0 & 0 & 0 & \cdots & 0 \\ 0 & \frac{-1}{\Delta x} & \frac{1}{\Delta x} & 0 & 0 & \cdots & 0 \\ 0 & 0 & \frac{-1}{\Delta x} & \frac{1}{\Delta x} & 0 & \cdots & 0 \\ \vdots & \vdots & \vdots & \vdots & \ddots & \vdots & \vdots \\ 0 & 0 & \cdots & 0 & \frac{-1}{\Delta x} & \frac{1}{\Delta x} & 0 \\ 0 & 0 & 0 & \cdots & 0 & \frac{-1}{\Delta x} & \frac{1}{\Delta x} \end{bmatrix}$$

The initial estimate for $\mathbf{u}$ is given by $\mathbf{u}_0 = \mathbf{Df}$.

Similarly, the anti differentiation matrix is calculated using the trapezoidal rule and is given by the triangular matrix:

$$\mathbf{K} = \begin{bmatrix} \Delta\frac{x}{2} & 0 & 0 & 0 & 0 & \cdots & 0 \\ \Delta\frac{x}{2} & \Delta x & 0 & 0 & 0 & \cdots & 0 \\ \Delta\frac{x}{2} & \Delta x & \Delta x & 0 & 0 & \cdots & 0 \\ \vdots & \vdots & \vdots & \vdots & \ddots & \vdots & \vdots \\ \Delta\frac{x}{2} & \Delta x & \Delta x & \cdots & \Delta x & \Delta x & 0 \\ \Delta\frac{x}{2} & \Delta x & \Delta x & \cdots & \Delta x & \Delta x & \Delta\frac{x}{2} \end{bmatrix}$$

At the end of every new update of $\mathbf{u}_n$, a terminating condition checks whether $\mathbf{u}_n$ has 'evolved to stationarity' i.e. whether all the values within the array $|\mathbf{u}_{i+1} - \mathbf{u}_i|$ are less than some small minimising value (here chosen to be $\epsilon \sim O(E-10)$).

The smoothing parameter α is chosen so that the χ^2 criterion is satisfied, namely that

$$\chi^2 = \Sigma_i^N \left(\frac{f_i - Au_i}{\sigma} \right)^2 \sim N$$

where N is the total number of data points and σ is the estimated error for the data points, f_i. This insures that the anti-derivative $\mathbf{Au}$ is the simplest smoothed estimate of f which just falls within the estimated noise for the observations. The result is thus intended to bias towards smoothness unless there is clear evidence in the data (above the selected noise limit) to suggest the contrary.

Testing and Results

The results of differentiating the standard test function, $y = |x - \frac{1}{2}|$, using ROF's TVR are shown in Figure 6.11. The top panel shows the results when gaussian noise of $\sigma = 0.01$ is added to the test function, the bottom panel shows the results for $\sigma = 0.05$. The ideal (exact) derivative is given in black, the TVR derivative in blue (top panel) and blue and green dashes (bottom panel).

As can be seen by inspection of Figure 6.11 (the blue curve at the top and the dashed green curve at the bottom of the figure), compared to the traditional differentiation techniques discussed in the previous sections (Figures 6.6-6.9), TVR produces excellent results, even in the high noise case. The discontinuity in the derivative is reproduced remarkably well and the regularisation process provides a noise-free result which closely describes the magnitude and shape of the gradient of the original function. These characteristics - correct location of discontinuities, correct description of the shape of the derivative - are repeatable for low noise data sets. The magnitude of the gradient, however, is not perfectly accurate, an artifact of TVR in the presence of noise referred to as 'contrast loss' (Chartrand 2005). But, as the focus of this work is to describe the overall *shape* of the derivative of a time-series data set, a slight loss of contrast is of no significant consequence in the present application.

However, another artifact of TVR which is of significance to this work, reveals itself in the regularisation of a more heavily noise-compromised, discontinuous data set. This can be seen as the blue curve at the bottom of Figure 6.11 and is well-known as the *staircase* effect. The effect is the presence of false 'steps' in the regularised result and is due to the fact that the simplest function which minimises total variation along a slope is a step-wise, monotonic function. The effect is not repeatedly seen in the regularisation of purely discontinuous data sets but only when the noise profile happens to be such that a continuous solution, i.e a smoothly varying or 'ramp' gradient, could also be admitted as a solution. This is illustrated in the bottom panel of 6.11; 'ROF TV norm regularisation I, II' are the solutions for the same input function with different instances of the noise profile (but the same standard deviation). 'I' gives a good approximation to the ideal derivative but 'II' suffers from the staircase effect because the input noise profile happened to be such that a ramp would have provided a good fit. Hence the kind of data subject to staircasing are in fact the more realistic data sets which contain gradual ramps[11]. This can be seen in the TVR differentiated observations of OY Car taken on 10/03/07 and

[11] Note that this is only the case in the presence of noise. Noiseless functions with gradual gradients still produce close to exact solutions under TVR.

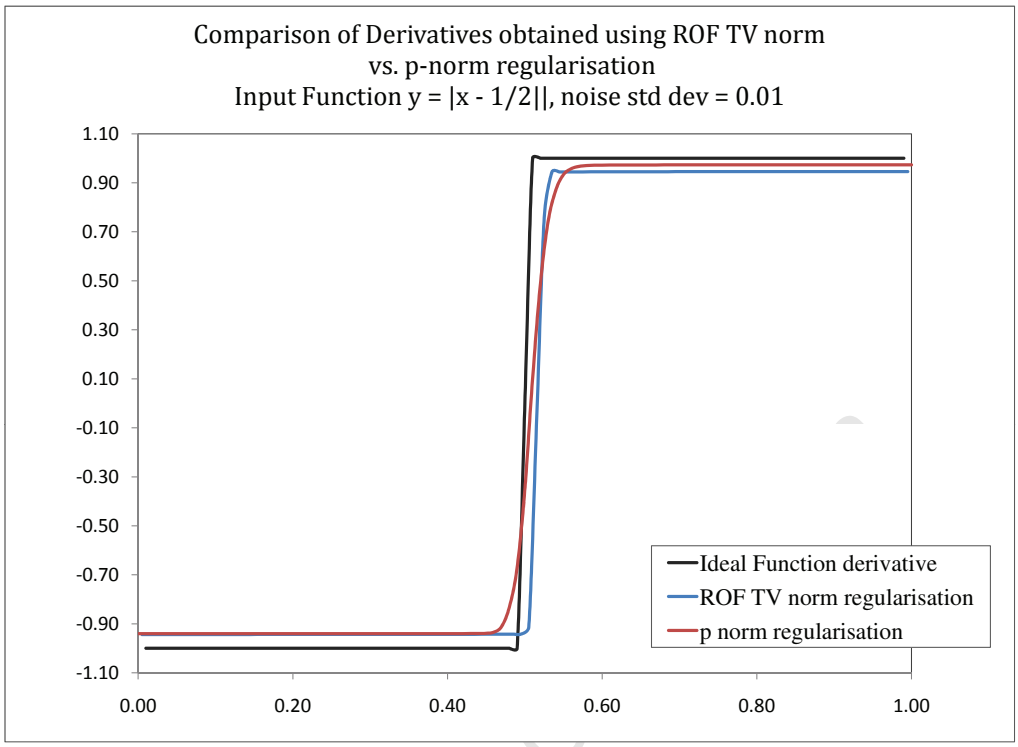

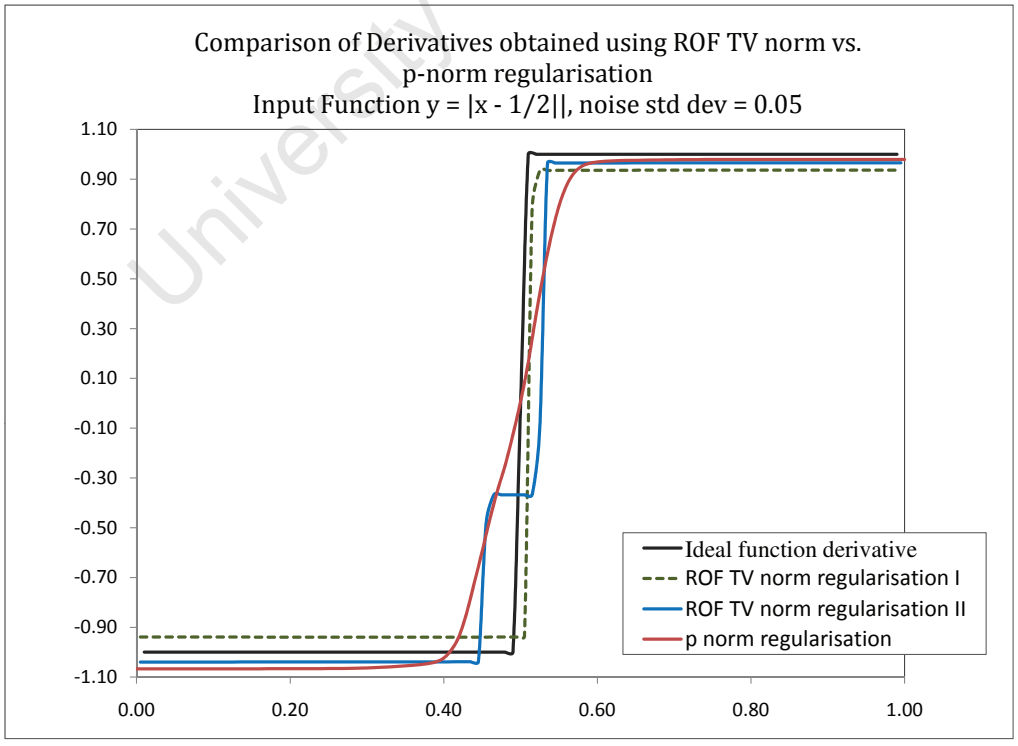

Figure 6.11: The derivatives of the test function $y = |x - \frac{1}{2}|$ with gaussian noise of $\sigma = 0.01$ (top) and $= 0.05$ added taken using regularisation techniques (see text for further details).

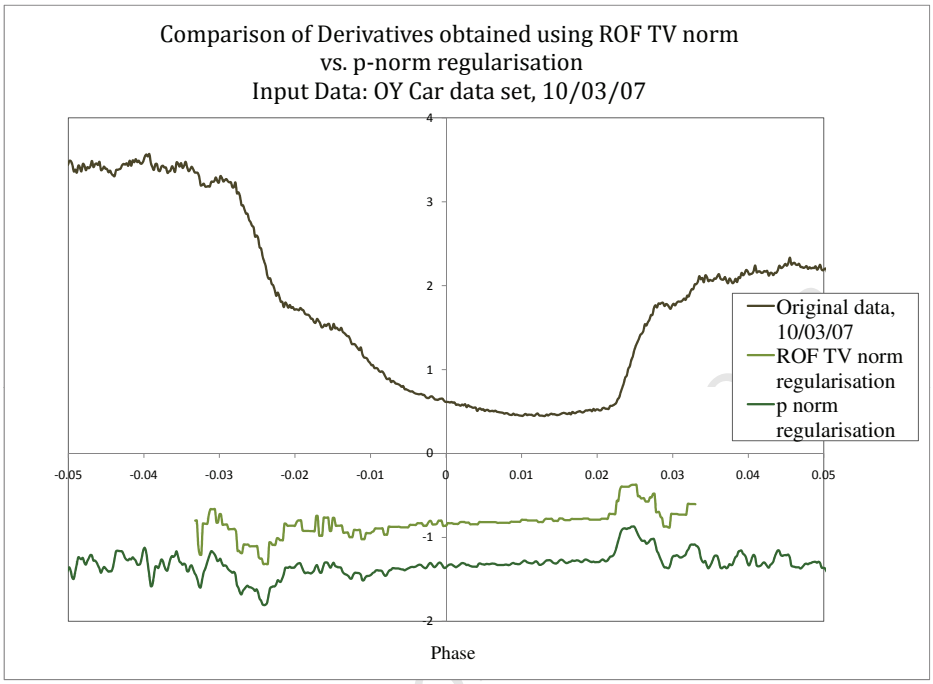

Figure 6.12: Results of differentiating a light curve of OY Car (taken 10/03/07) using regularisation techniques. The light green curve at the bottom of the figure shows the result of ROF's TV-norm regularisation, the dark green curve shows the results of p-norm regularisation.

shown in Figure 6.12 (the derivatives shown in the figure have been scaled up for clarity).

The ROF TV-norm derivative solution is shown as the light green curve in the figure. The derivative has a distinctly quantised appearance as a result of the staircasing effect due to TVR forcing step-wise solutions to the ramp-regions of the light curve. This is less than desirable but a well-known effect in image-processing where regularisation is used to smooth images with gradual tonal gradients and many authors in the field have investigated analytic methods of dealing with the problem (Blomgren, Chan & Mulet 1997, Chambolle & Lions 1997 and references therein, Marquina & Osher 2000, Osher *et al* 2005, Chan & Esedoglu 2005, Chan *et al.* 2005, Elo 2009 and references therein).

The most common and popular approach is to combine Tikhonov and TV regularisation in order to retain the ramp-preserving features of Tikhonov's technique and the edge-preserving features of TVR. Chambolle & Lions (1997) proposed higher order models such as including both TV and H^1 norms in the minimisation functional. A parameter determines where each term dominates according to whether $|\nabla u|$ is greater or less than

some threshold value demarcating edges from ramps.

A much simpler approach is to generalise the ROF model to the problem of minimising the functional:

$$F(u) = \int_0^L \alpha\Phi(|\nabla u|) + \frac{1}{2}|Au - f|^2 dx \tag{6.4}$$

where Φ is a smooth function. Setting $\Phi(s) = s$ corresponds to TVR, $\Phi(s) = s^2$ corresponds to Tikhonov regularisation. Blomgren, Chan & Mulet (1999) proposed setting:

$$\Phi(|\nabla u|) = \frac{1}{p}|\nabla u|^p \tag{6.5}$$

so that the Euler-Lagrange equation 6.2 becomes:

$$\begin{aligned} u_t &= \alpha\nabla \cdot \left(\Phi'\left(|\nabla u|\right)\frac{\nabla u}{|\nabla u|}\right) - A^*\left(Au - f\right) \\ &= \alpha\nabla \cdot \left(\frac{\nabla u}{|\nabla u|^{2-p}}\right) - A^*\left(Au - f\right) \end{aligned} \tag{6.6}$$

where $1 < p < 2$. Replacing $|\nabla u|$ with $\Phi(|\nabla u|) = \frac{1}{p}|\nabla u|^p$ in the minimisation functional is the staircase reduction technique implemented in this work and hereafter the resulting regularisation will be called 'p-norm regularisation'.

The results of differentiation using p-norm regularisation (or PNR) of our test functions are shown as the red curves in Figure 6.11. For the low noise condition there is very little difference between p-norm and ROF's TV norm regularisation, though one can see that some of the sharpness of the discontinuity has been smoothed. For the high noise condition, PNR again produces a similar result to the TVR solution (the blue curve at the bottom of Figure 6.11) but smooths out the staircase artifacts[12].

While this does not improve the resolution of the discontinuity, it does do something vitally important for the focus of this investigation: it provides the smoothest solution permitted by the noise. This is important in light of the distinguishing features of derivative profiles for different model light curves discussed in Section 6.1. Many of the models exhibit double peaked profiles where these 'higher order' features are detectable right near the beginning of ingress/egress. This makes it absolutely essential that any derivative method employed does not add false features near or during these discontinuities. Instead, the smoothest solution should rather be assumed as the default in the current case; exact discontinuities are rarely present in the variations of natural phenomena.

[12]The p-norm regularised result presented in Figure 6.11 is the solution to the same noise profile as that used for 'ROF TV regularisation II'.

For PNR, there are two parameter sets, (α, p), which satisfy the χ^2 criterion, since both α and p affect the regularisation of the solution. The first set corresponds to $p \sim 1$ and so produces results similar to TVR. The second set, which is used in the p-norm regularised results presented in this investigation, satisfies the χ^2 criterion for $1 > p \lesssim 2$. These two parameter sets allow the investigator to 'tune' the regularisation process according to the features of interest in the data set; sharp features such as the detection of contact times or gradual features such as the shape of the ingress or egress. The results of differentiating OY Car's 10/03/07 light curve using PNR is shown in Figure 6.12 as the dark green curve.

A more sophisticated p-norm treatment, also proposed by Blomgren, Chan & Mulet (1999), would be to have $p(|\nabla u|)$ sensitive to the behaviour of $|\nabla u|$ so that equation 6.4 reduces to TVR near edges and H^1 regularisation in gradual-gradient regions. This implementation is beyond the scope of this investigation; the specification of p using the χ^2 criterion is sufficient for our aims.

In the next section the estimation of noise in the data set will be discussed for the purpose of determining σ in the χ^2 criterion. It shall also be demonstrated that PNR produces reasonably noise-free results. Finally, the results of PNR differentiation of the light curves presented in Chapter 6 will be given.

6.5 Differentiating Light Curves using 'p-norm' Regularisation

6.5.1 Noise Estimation for the χ^2 Criterion: 'bright' vs. 'faint' Objects

Determining a p-norm regularised fit to the data according to the χ^2 criterion assumes that the noise inherent in the data has a mean of zero and a standard deviation of σ. The question then becomes how to estimate σ for the data sets.

A minimum estimate for the noise present can be determined from estimates of instrumental noise, photon noise in the target, comparison stars and sky, and errors in magnitude estimations made by the data reduction software. For faint objects the noise present in the data dominates the variability (the data are noise-limited) so, in those cases, the χ^2 criterion is sufficient as a fitting criterion.

However, for OY Car, the $\chi^2 \sim N$ did not produce an optimal derivative when the value for σ was chosen to be the minimum noise estimate.

This is illustrated in 6.13 which shows the results of p-norm regularised derivatives for three light curves using three different estimates for σ in each case. '1 sigma', '2 sigma' and '3 sigma' refer to σ_{min}, $2\sigma_{min}$ and $3\sigma_{min}$ where σ_{min} is the minimum noise estimated

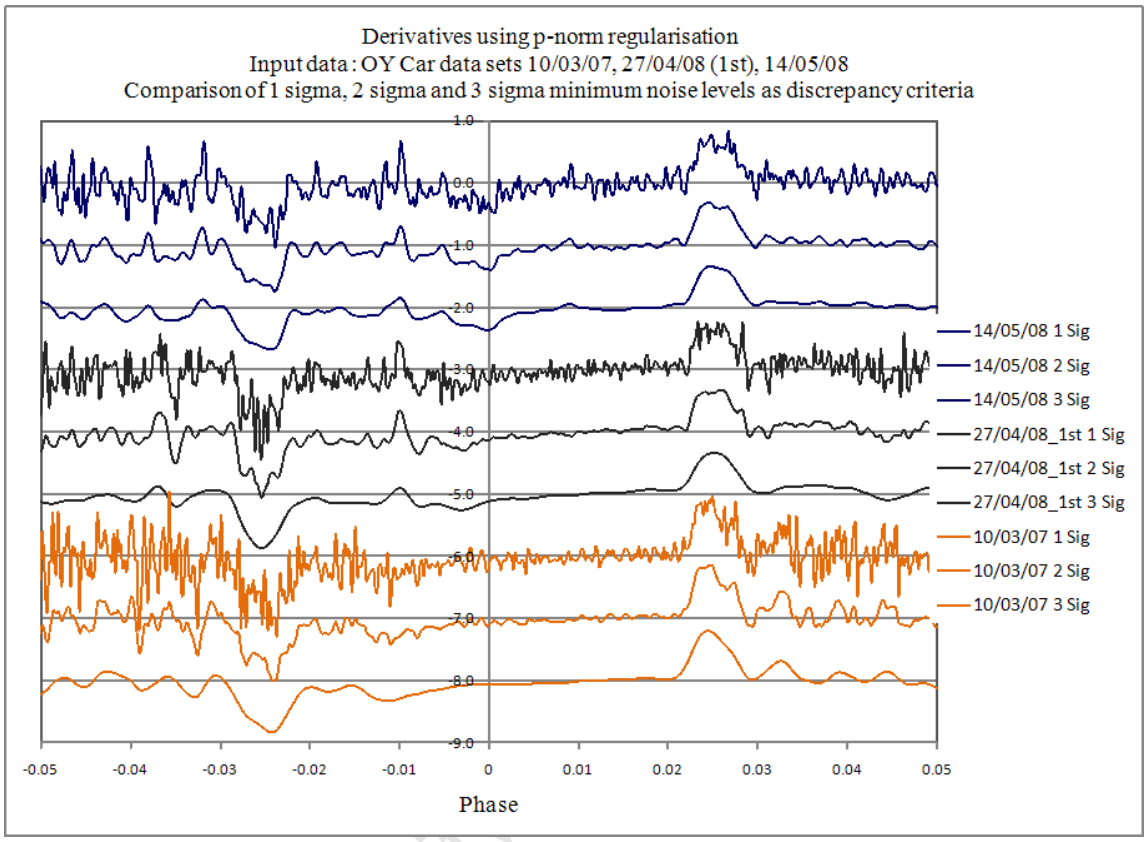

Figure 6.13: Comparison of p-norm regularised derivatives determined for three data sets using three different estimations for σ (see text).

to be present in the data as discussed above. As can be seen, choosing $\sigma = \sigma_{min}$ produces a very noisy result and $\sigma = 3\sigma_{min}$ seems to oversmooth features.

Hence $\sigma = 2\sigma_{min}$ was chosen as a first estimate and worked reasonably well for a few of the data sets, but not all of them. A couple of the derivative results with this estimation for σ seemed to be oversmoothed while still more were compromised by noise. The reason for this is because, for OY Car, a relatively bright object with good signal-to-noise, the dominant source of variability in the light curves is not random noise, as described above, but inherent flickering in the system; the data sets are flickering limited. Thus the regularisation algorithm also has to act as a filter of rapid fluctuations in the signal and can do so by choosing σ such that it includes an estimate of the amplitude of the flickering.

Estimates for flickering amplitudes were made from inspection of the light curves. As will be discussed in the next section, the central object's egress is of greatest interest to

this work because the prime sources of the system's variability (and therefore flickering 'noise') – the bright spot and the accretion disc – are eclipsed during this interval, thereby offering us the 'cleanest' view of the central object. Thus, estimations for σ were chosen to optimise the resolution of the egress features by choosing values between $\sigma_{e,min}$ and $\sigma_{e,max}$, the estimated noise immediately preceding and following egress respectively[13] .

The derivative curves obtained for OY Car, obtained according to the fitting criteria as discussed above, are presented in the next section.

6.6 Results

Figures 6.14, 6.15 and 6.16 show the results of differentiating the light curves (plotted in Section 6.2.4) obtained for OY Car in 2007, 2008 and 2009 respectively. As mentioned in Section 6.2.4, the light curves taken on the dates 30/03/07, 31/03/07 and 19/02/08 used different comparison stars to the rest of the observations and these are indicated with superscripts in the figures' keys (derivative curves with the same superscripts having the same comparison star). A vertical scale factor was chosen for derivatives with the same comparison star so that the peaks of all the derivatives span one unit on the vertical axis for ease of comparison.

From inspection of the results presented in the figures, the following inferences can be made:

- There are clear variations between the derivative profiles.
- Of the 18 curves, 10 could be said to have the 'cleanest' egresses: 31/03/07, 12/04/07, 23/04/08, 27/04/08 (2nd eclipse), 14/05/08, 10/06/08, 29/03/09, 30/03/09 (both eclipses) and 04/04/09 with 23/04/08, 14/05/08, 10/06/08 and 04/04/09 providing the least noisy curves.
- 30/03/07, 31/03/07, 23/04/08 have the cleanest ingresses (via inspection of noise present either side of ingress) and, of these, 31/03/07 and 23/04/08 have the closest (though not strong) resemblance to their egresses.
- General symmetry between ingress and egress was assessed by examining the results of choosing σ to estimate the flickering around *ingress*. Some of the curves display symmetry between their ingresses and egresses (identified in Table 6.3) while more

[13]Note that ingress and egress intervals for a few light curves were experimentally selected and regularised separately for differing estimations of noise appropriate to their respective (ingress or egress) neighbourhoods. The results obtained were not significantly different from those presented in the next section (where estimations for σ, based on the egress' neighbourhoods, were used to regularise the full eclipse).

than half of the profiles change (in some cases, quite dramatically) from ingress to egress.

- The curve with the closest apparent symmetry between ingress and egress is that of 10/03/07 although the profile presents a unique ingress/egress shape (which bears no resemblance to any of WH90's proposed models, as will be discussed in the next section).

In order to draw firm conclusions from the comparison of the derivatives, one must be confident that the observed differences in the profiles are a consequence of the observations and not due to either some noise-dependant artifact present during the regularisation process or the noise[14] estimates chosen for each profile. The tests described in 6.4.3 demonstrated that PNR offers almost exact, repeatable results in very high signal-to-noise data (SNR $\approx 100:1$) but slightly differing results in greater noise conditions (SNR $\approx 20:1$). OY Car, with an average SNR $\approx 40:1$ at minimum light, could fall into the latter category. A test of the regularisation process's robustness to noise, and the noise estimates, needs to demonstrate that any observed differences between the derivatives can be confidently attributed to changes in the central object's brightness profile.

Robustness to noise

In a similar manner to the tests conducted in Section 6.4.3 for the relatively high noise conditions, the PNR algorithm can be tested for sensitivity to the kind of real-world noise present in the data by comparing the results of inputing a model light curve with a variety of realistic noise profiles added. If the regularisation process is reasonably insensitive to noise, then the resulting derivatives should barely differ in shape.

As shall be seen in the next section, two of the egresses of the derivative profiles obtained and presented in Figures 6.14 to 6.14, 10/06/08 and 31/03/09 (1st), match two of the theoretical model profiles presented by WH90. Thus their regularised light curve profiles (i.e., the anti-derivatives) can be regarded and used as test model light curves. To these two test light curves, noise profiles extracted from other data sets were added. The noise profiles added to the model light curves were obtained from the following observations: 10/03/07, 12/04/07, 14/04/07, 23/04/07, 27/04/08 (1st and 2nd), 14/05/08 and 10/06/08 (the latter included for the 31/03/09 model). The noise profiles were obtained from these observations by subtracting the p-norm regularised light curves from the original data sets. For example, one such result is shown in Figure 6.17; the p-norm regularised curve (in black) is plotted on top of the binned observations (red). The noise profile resulting

[14] Where noise is defined here to be determined by the intrinsic flickering of the bright spot and disc components.

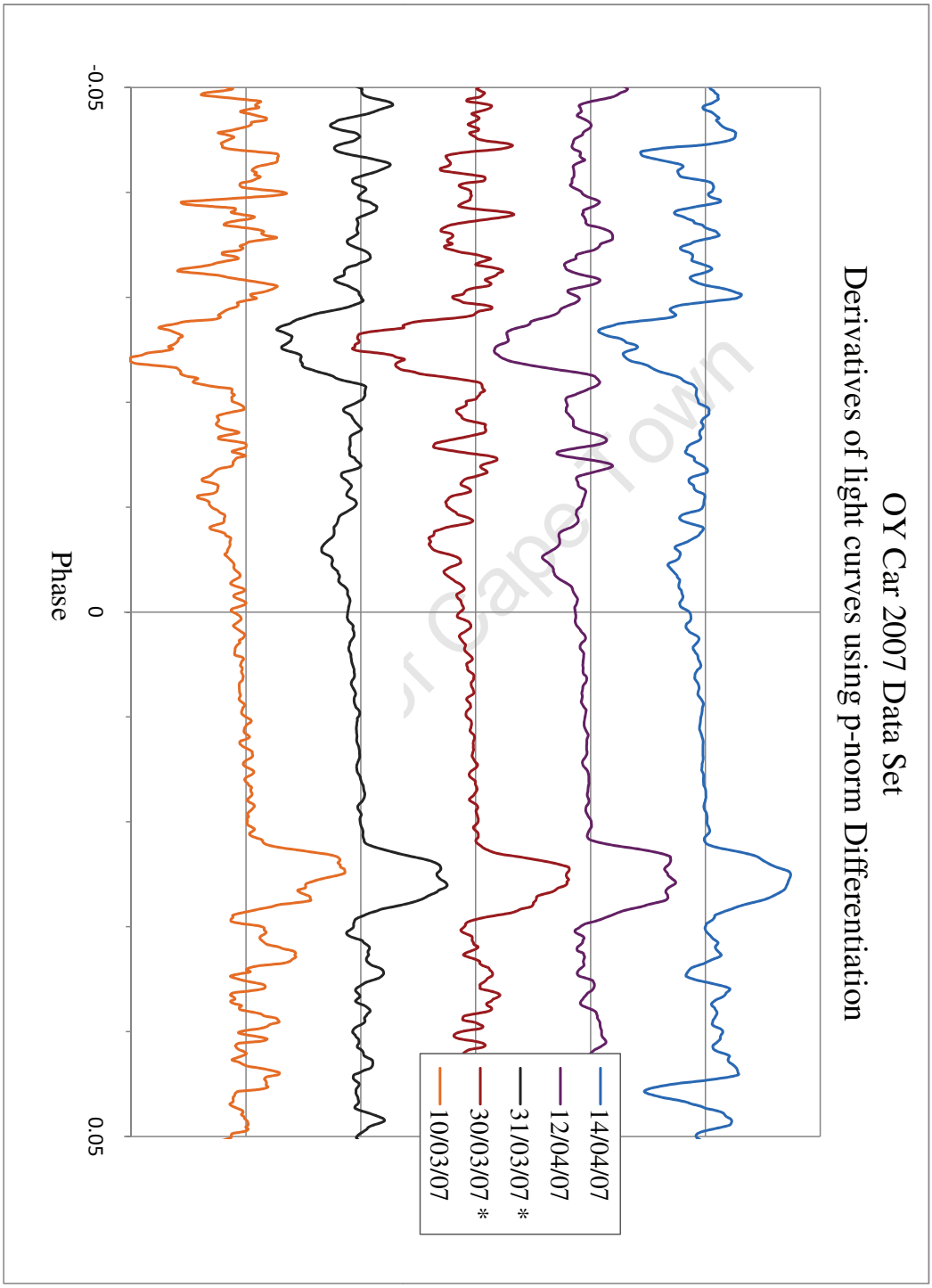

Figure 6.14: Derivative profiles of all of the OY Car light curves obtained in 2007. The asterisks denote observations which were differentially photometrised with respect to a different comparison star to the rest in the set (though the derivatives were scaled appropriately for ease of comparison).

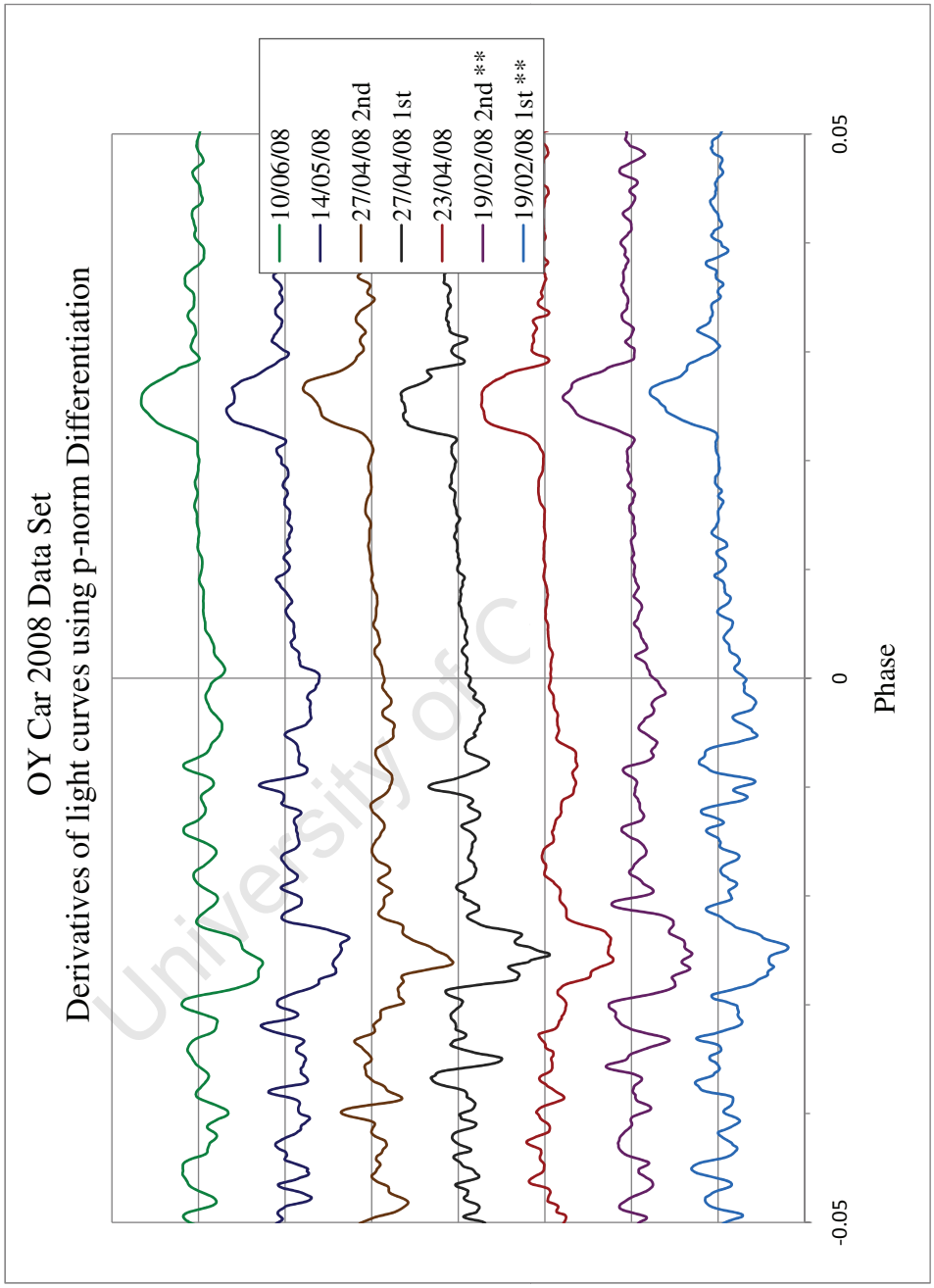

Figure 6.15: Derivative profiles of all of the OY Car light curves obtained in 2008. The double asterisks denote observations which were differentially photometrised with respect to a different comparison star to the rest in the set (though the derivatives were scaled so appropriately for ease of comparison).

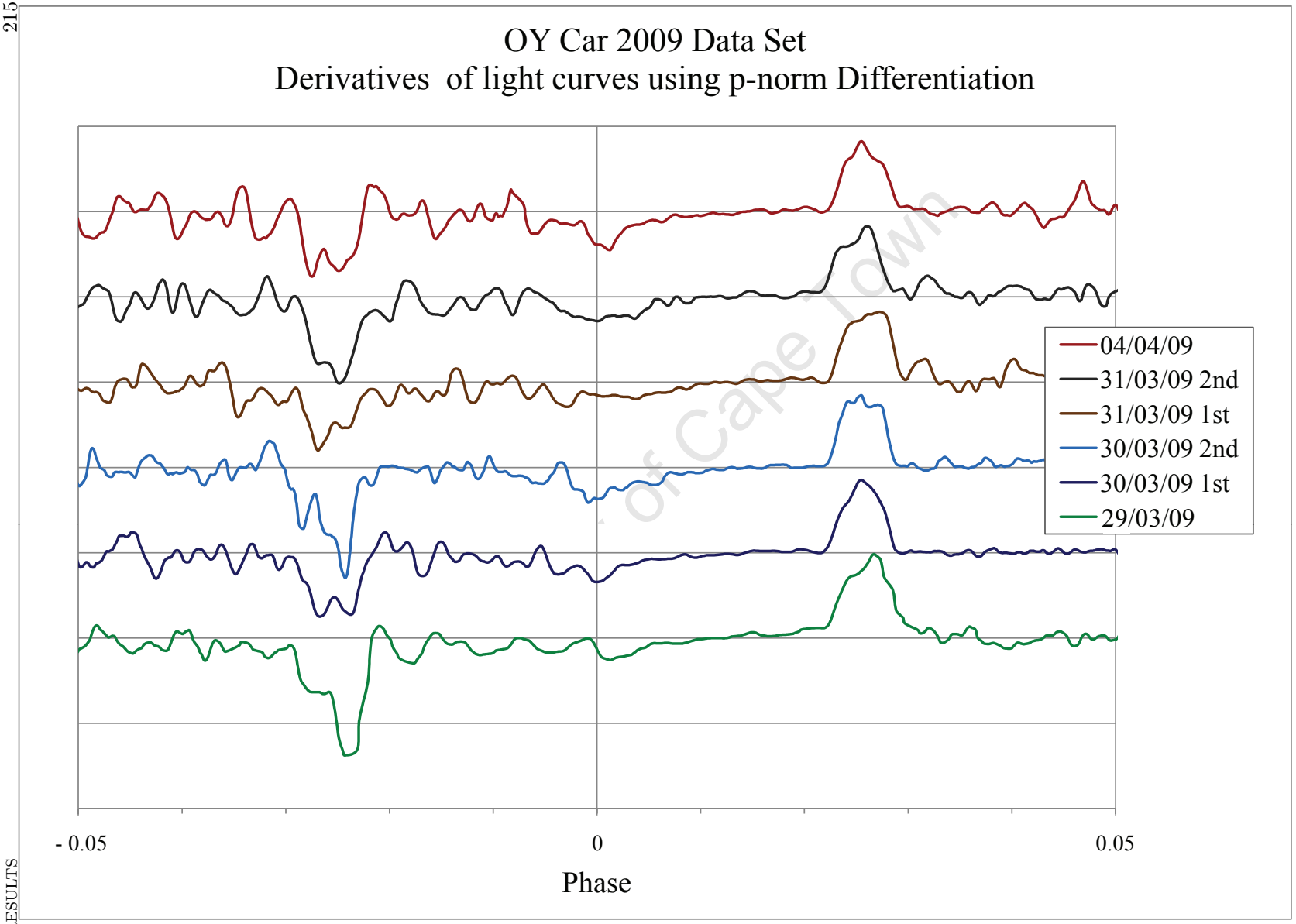

Figure 6.16: Derivative profiles of all of the OY Car light curves obtained in 2009.

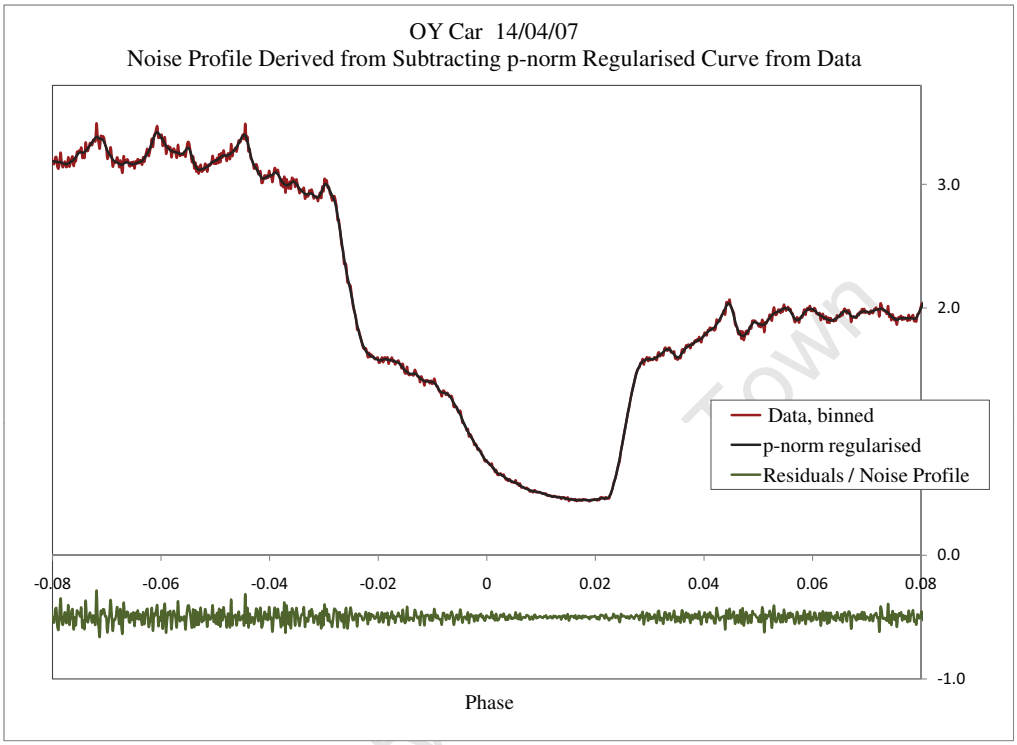

Figure 6.17: Binned observations of OY Car taken on 14/04/07 (red) with its p-norm regularised curve superimposed (black). The noise profile obtained from subtracting the two is plotted below (green), scaled up by a factor of 2.

from subtracting the two is plotted below (green), scaled up by a factor of two for clarity. The regularisation algorithm was then tested for robustness to noise according to the following procedure:

- For each of the two model light curves, a set of test curves was generated by adding the noise profiles to the model light curve.
- Each test curve was fed into the PNR routine where the σ (for the χ^2 fitting criterion) for each curve was the same σ used to regularise the original data sets from which the noise profiles were derived. The results are plotted in Figure 6.18.

At the top of each plot in Figure 6.18 is the original derivative which provided the model light curve (its antiderivative). The curves below give the PNR derivative results for each test curve. In other words, the curve second to the top of the 31/03/09 plot gives

the PNR derivative result for the model light curve obtained from the 31/03/09 data set which has had the noise profile derived from the 10/06/08 data set added to it. The next curve down gives the PNR derivative result for the 31/03/09 model light curve which has had the noise profile derived from the 14/05/08 data set added to it and so on.

If the PNR routine is sensitive to the noise profile, then we would expect the profiles in Figure 6.18 to differ significantly from each other and from the model derivative. As can be seen, this is not the case. Thus we can be confident that the observed differences in the derivatives results plotted in Figures 6.14 to 6.16 are real and inherent to the brightness profile of the central object.

Notice that, in both plots in Figure 6.18, for the test light curves with 14/05/08's noise profile, the derivatives do not resemble the model derivative but, instead, appear oversmoothed. This is an indication that, in the regularisation of the 14/05/08, σ was over estimated[15]. This, plus inspection of the noise profile shown in Figure 6.17 demonstrates how the χ^2 criterion is used in PNR to provide a good fit to the data. As can be seen from Figure 6.17, even though a single value for σ was chosen for all the data points, we do not have a flat noise profile removed in the fitting process. The criterion only specifies that the *total* σ normalised square of the residuals $\simeq N$. PNR preferentially regularises the noisiest sections of the data set (i.e sections with the largest total variation), so most of the error budget is spent on those sections of the data. However, if the error budget is *too* large then sections of the data set with low total variation will be oversmoothed.

This a useful feature of PNR; when little is known about the noise distribution, other than it is variable/none-flat, such tests of first approximations to the noise with model data sets can check whether the estimated σs have been too aggressive. In addition, the noise profiles obtained from the first fitting approximation reveal the distribution of the noise. A second round of fine-tuned fitting can then include a σ profile where the fitting criterion becomes $\chi^2 = \Sigma_i^N \left(\frac{f_i - Au_i}{\sigma_i}\right) \sim N$ where σ_i is the estimated error in each data point, f_i.

6.7 Qualitative Comparison of Derivative Results and Theoretical Models

A note on the figures discussed and presented in this section:

- For this discussion, please refer to WH90's, derivative profiles of model light curves (their figure 3), reproduced here in Figure 6.2. Note that the derivative profiles given in Figure 6.2 are of the ingress and should be inverted in both axes for comparison

[15]The 14/05/08 derivative shown in Figure 6.15 was corrected for this.

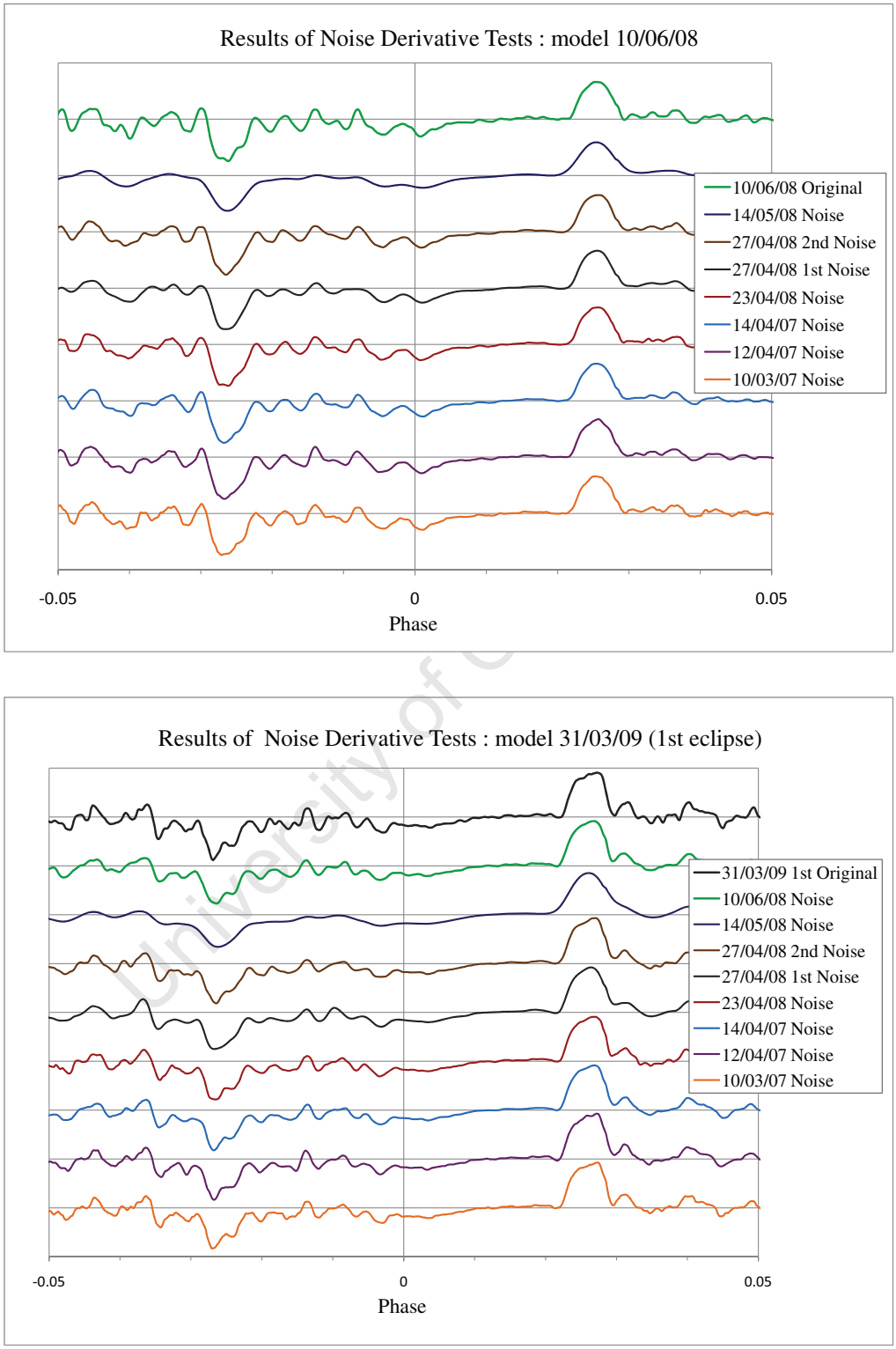

Figure 6.18: Results of testing the PNR routine's sensitivity to noise. The top plot shows results for the 10/06/08 model light curve (the antiderivative of the derivative shown at the top of the plot). The following curves are the PNR derivative results of the model light curve for a variety of noise profiles taken from other data sets (see text). The bottom plot shows similar results for the 31/03/09 (1st) model light curve.

with the egress results presented in Figures 6.14 to 6.16. Derivative curves of particular interest have been re-plotted here (Figures 6.19-6.21), inverted in both axes and, where appropriate, WH90's model derivative curves have been superimposed for comparison. These model egress derivatives are referred to as 'inverted' egresses in the rest of this discussion.

- WH90's models were calculated for the ingress of Z Cha where the difference in mass ratio (and far less sensitively, the white dwarf radius) affects the width of ingress/egress. The dashed lines on the images of the models superimposed in Figures 6.19 to 6.21 indicate the start and end of ingress. The ingresses have been scaled horizontally for the closest possible fit to the inverted egress derivatives from the OY Car data.

The rest of this chapter will be devoted to the qualitative analysis of the derivatives presented in Figures 6.14 to 6.16 to determine which, if any, of the theoretical models presented by WH90 describing the nature of the central object best explain the brightness distributions found here.

As mentioned in Section 6.1, there are broadly two classes of features to discriminate between the derivatives of the model light curves: firstly, whether the ingress/egress in the profile exhibits double or single peaks and secondly, if they are single peaked, what the symmetry is of the ingress/egress profile. In addition, further information for comparison to the models can be obtained from the phase information of the derivative curves: phase widths of ingress/egress, phases of contacts times and phases of mid-ingress/egress. The phase information will be discussed in the second half of the analysis. The first section shall focus on the shapes of the egresses in the derivative profiles.

Estimations for σ in the PNR routines were chosen so that the regularisation process was sensitive to preserving features in the egress as it was known *a priori* that this section of the light curve should deliver results least corrupted by inherent variability. This choice is what is responsible for the comparatively greater variability seen around ingress present in the derivative profiles given in Section 6.6. It should be noted that PNR trials were conducted where σ was chosen to best estimate the variability surrounding the ingress (and thus have the regularisation more sensitive to ingress features) but these did not reveal derivative profiles as well resolved as the egress profiles. Thus the most confidence is given to conclusions drawn from the egresses in the derivative profiles

6.7.1 Egress Derivative Profile Shapes: Comparison to Theoretical Models

In the derivative results presented here there are discernable, recurring egress shapes, although very few of them exactly resemble any of the models presented by WH90. The most common shapes obvious to the eye (Figures 6.14-6.16) are: (1) a 'table-top' shape (eg. 30/03/09 (2nd) and 12/04/07) and, (2), what appears to be the simple bare white dwarf shape (refer to models 1a) and 1b)) with a 'nipple-like' protrusion superimposed (e.g 14/05/08, 29/03/09, 04/04/09).

A few of those in the second category can plausibly be explained by fitting the model of a bare white dwarf with maximal limb darkening (WH90's model 1b)), with minimal flickering present during the egress causing small deviations from the exact profile. The egress of 19/02/08 (2nd), shown in Figure 6.19, is an example of this. However not all of the deviations from this simplest model can be easily explained to be the result of flickering (eg. egress profiles of 29/03/09, 30/03/09 (1st and 2nd) and 04/04/09). In these cases, the magnitude of the residual flickering immediately preceding and following egress are too small to account fully for the 'bumps' seen during the egresses which make them significantly different from each other and from the smooth, simple bare white dwarf profile. These robust profile shapes are repeated elsewhere in the data and so suggest that the majority of the deviations from model 1b) are due to real changes in the central object's, or its boundary layer's, brightness distribution.

Table 6.3 lists the eclipses and the WH90 theoretical model of the derivative profile with which they can be most closely classified according to shape. Where the profiles can be well approximated by the bare white dwarf model (WH90's model 1b)), as described above, they have been classified as such. Of the egress shapes which do not fall into this category, many look to be a convolution of WH90's model 1b) and 2c) a bare white dwarf with an optically thick, latitudinally extended boundary layer and these have been tentatively classified as '1b) * 2c) (?)'. One curve can be reasonably classified as fitting model 2c) and the rest, which do not comfortably fit into any of WH90's designations have simply been categorised as 'Other'. Where a symmetry between ingress and egress could be identified, this is indicated.

Of the 18 eclipses listed, there are 4 derivative curves that deserve further comment. The first two are that of 10/06/08 and 31/03/09 (1st) shown in Figure 6.20[16]. As can

[16]Please note that the egress derivative curves, presented and discussed in greater detail in this section, are shown with both axes inverted in order to compare them to the model derivative profiles of egress presented by WH90. Thus the plots have been headed 'Inverted Egress' (though, more accurately speaking, the egresses have been rotated 180 degrees about $\phi = 0$).

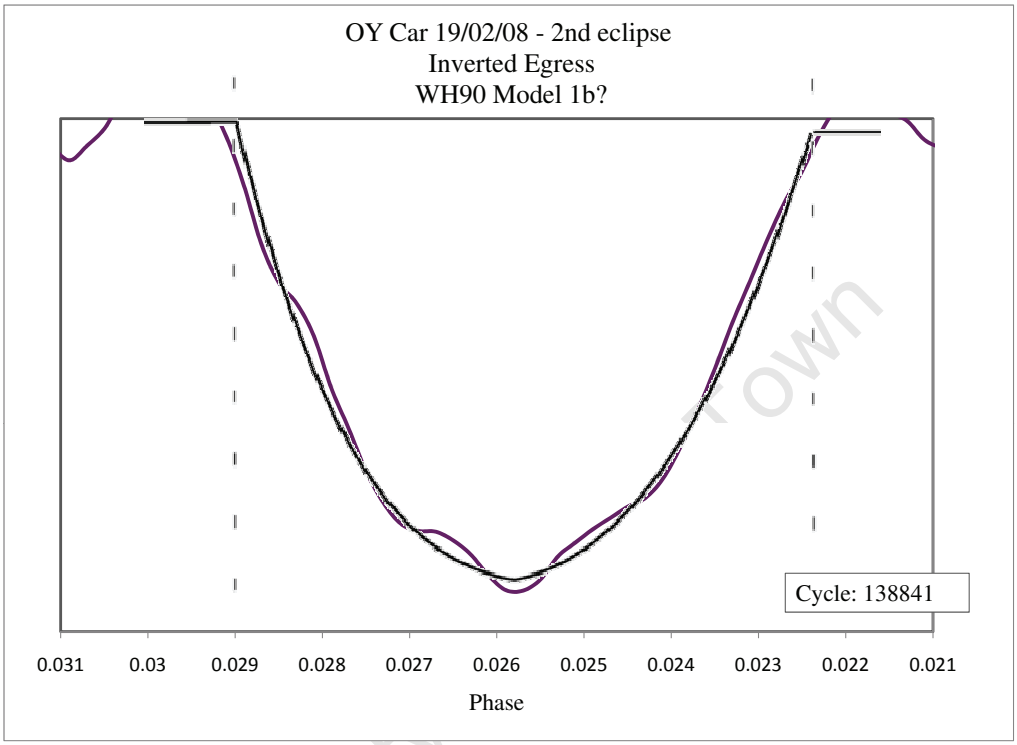

Figure 6.19: Inverted egress derivative of observation 19/02/08 (2nd) with WH90's model 1b) derivative superimposed.

be seen from the figure, the form of 10/06/08 is almost perfectly fitted by WH90's model derivative of a bare white dwarf with maximal limb darkening[17]. 31/03/09 (1st), by contrast, is closely approximated by WH90's model derivative of a bare white dwarf with an optically thick, latitudinally extended boundary layer.

The most curious of all the curves is that of 10/03/07 shown in Figure 6.21 (top). The ingress (dashed blue curve) has been rotated (inversion of both axes) and superimposed, while the egress (orange curve) is reproduced as shown in 6.14 (unrotated). This derivative profile is clearly double peaked and exhibits rough symmetry between its ingress and egress. However, the symmetry of this double peak is not described by any of WH90's models which offer double peaked derivative profiles. The curve does coincide with a period of high and rapid variability not seen elsewhere in the profiles with the exception

[17]Note that the vertical unit spanning the plot in the 10/06/08 plot is 0.8 whereas one unit = 1.0 in the rest of the plots given in this section. Thus, integrating the derivative, 10/06/08's total (egress) luminosity, ΔL_e, is the smallest of the set.

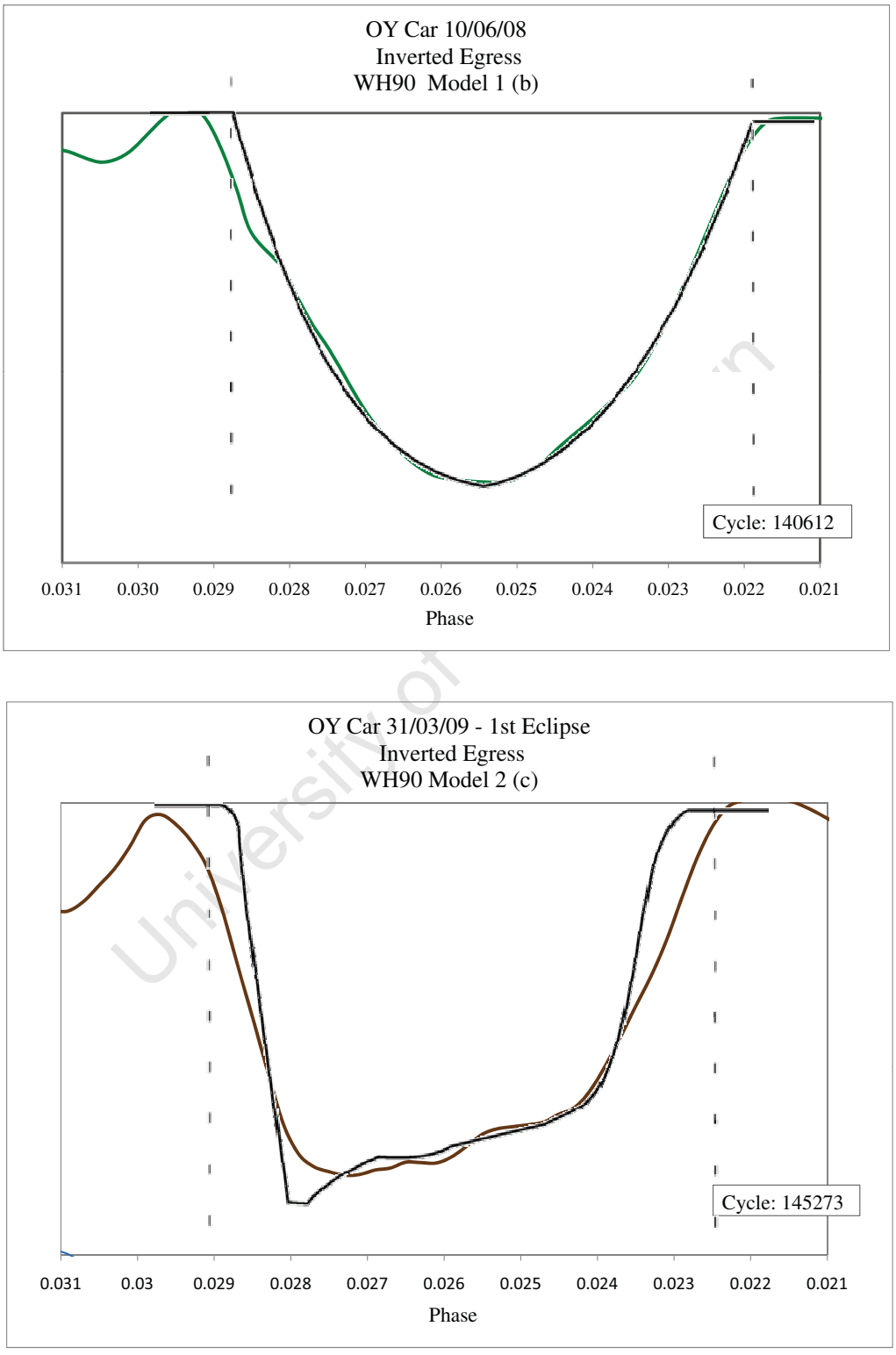

Figure 6.20: The two egress derivative profiles which most closely match WH90's model profiles. That of 10/06/08 (top) very closely matches the derivative profile of a bare white dwarf with maximal limb darkening (WH90's model 1b)) and the derivative of 31/03/09's (1st eclipse) egress most closely matches that of a bare white dwarf with an optically thick, latitudinally extended boundary layer (WH90's model 2c)).

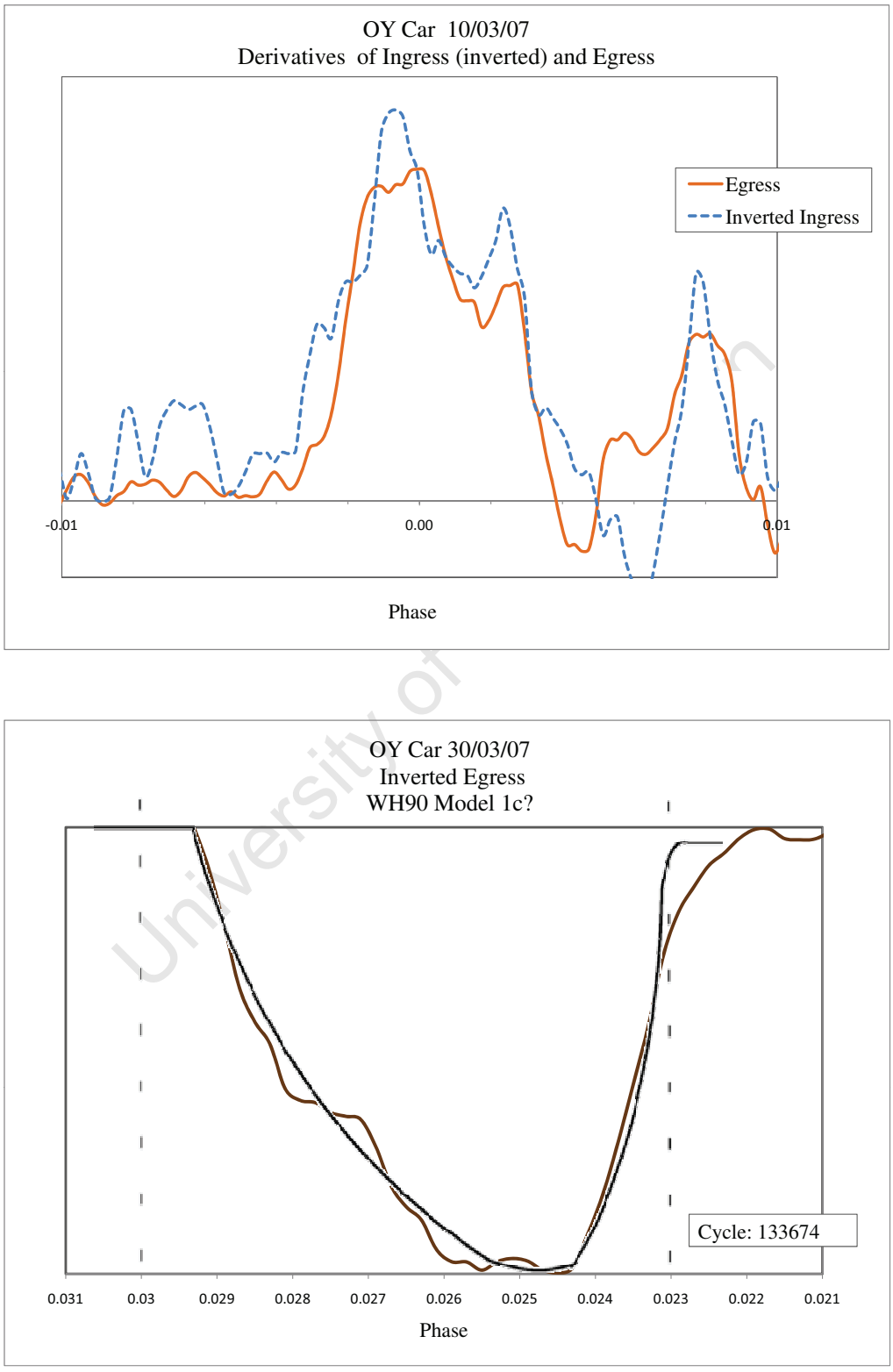

Figure 6.21: Top: The peculiar derivative profile of 10/03/07 shows the usual inverted egress with the ingress superimposed and both shifted in phase so that their respective symmetrised half-flux points are at $\phi = 0$. Bottom: The derivative of 30/03/07's egress with the model egress derivative profile for a white dwarf with minimal limb darkening and lower hemisphere occulted by an opaque disc, (WH90's model 1 c)), superimposed (bottom).

Table 6.3: Categorisations of OY Car's egress derivative profiles according to WH90's models

Date	Cycle	Model	Comments
10/03/07	133358	Other	Double peaked, symmetric
30/03/07 *	133674	Other	Egress similar to 10/03/07
31/03/07 *	133690	1b)	Symmetric
12/04/07	133880	Other	Egress similar to 30/03/09 (2nd)
14/04/07	133911	1 b) * 2 c) (?)	
19/02/08 (1st) **	138840	1b)	Symmetric
19/02/08 (2nd) **	138841	1b)	
23/04/08	139853	1b)	Symmetric
27/04/08 (1st)	139916	1b)	Symmetric
27/04/08 (2nd)	139917	1 b) * 2 c) (?)	
14/05/08	140184	Other	Symmetric
10/06/08	140612	1b)	Near perfect fit, symmetric
29/03/09	145240	1 b) * 2 c) (?)	
30/03/09 (1st)	145256	Other	
30/03/09 (2nd)	145257	Other	Egress similar to 12/04/07
31/03/09 (1st)	145272	2 c)	
31/03/09 (2nd)	145273	1 b) * 2 c) (?)	
04/04/09	145336	1 b) (?)	

of an observation taken later that month, that of 30/03/07. The (rotated) egress of this derivative curve is also shown in Figure 6.21 (bottom). The profile has been tentatively fitted with WH90's derivative curve for a white dwarf with minimal limb darkening and the lower hemisphere occulted by an opaque disc (model 1 c)). The derivative egress from 30/03/07 does bear some similarity to the egress of 10/03/07. Whether this similarity is due to a coincidence of noise or is indicative of a real, recurring and unexplained change in the central brightness distribution of these particularly highly variable curves is unclear.

WH90 concluded that their surface brightness models 1(a), 1(b) or 2(c), (the latter model having an equatorial belt extended over a large fraction of the white dwarf's surface), offered the best fits to OY Car's mean derivative profile. Here again, these models

Table 6.4: White dwarf radii for those WH90 SB distribution models which could be identified and fitted to the data.

Date/Profile	Model	R_{wd}/a	$\Delta\phi$	ϕ_i
10/06/08	1(a)	0.0155	0.0508	-0.0254
31/03/09 (1st)	2(c)	0.0160	0.0516	-0.0258

emerge as candidate fits to a select number of individual profiles. The modelling program `roche`, (refer to Section 5.2.5), is able to generate model light curves for basic parameter inputs. Thus, model light curve derivatives were generated by using `roche` and the PNR derivative technique to fit, by eye, the egress derivatives of 10/06/08 and 31/03/09 (1st). A bare white dwarf, model 1(a), was fitted to 10/06/08 (`roche` does not accommodate deviations due to limb darkening) and a dark white dwarf with a latitudinally extended, bright equatorial belt, (model 2(c)) was fitted to 31/03/09 (1st); the resulting white dwarf radii are given in Table 6.4.

R_{wd} was the only free fitting parameter. The parameters (q, i) affect the contact times/position of ingress/egress. The (q, i) values established here (Section 5.2.5) actually provided a very good fit to the derivative profiles, with no need for tweaking of the parameters within their estimated uncertainties. Also given in the table are the eclipse widths and mid-ingress from the model fits. In addition to 10/06/08, the model parameters for model 1(a) also provides a reasonable fit to the egresses of 12/04/07, 14/05/08 and 23/04/08. The R_{wd} obtained for 1(a) is compared to WH90's derived values of R_{wd} later in this section.

As noted in the beginning of this section, while WH90's model of a spherically symmetric white dwarf, with or without maximal limb darkening, can be identified and fitted to some of the derivative profiles obtained here, the vast majority of the profiles do not match any of the models offered by WH90. A subset of these share the attribute of a 'bump' or 'protrusion', seemingly superimposed on a spherically symmetric white dwarf/boundary layer profile. For the profiles in this category, a new surface brightness (SB) profile is proposed as the best model; that of a spherically symmetric distribution with a surface bright spot matching a near-Gaussian brightness profile superimposed.

The best example candidates for a 'spotty' SB distribution include the egress derivative

profiles of 27/04/08 (2nd), 29/03/09 and 04/04/09. However, identification of a spot profile in egress alone is not sufficient to constrain a surface spot's parameters. Thus, the ingresses of candidate spot profiles were re-examined, bearing in mind that, unlike the cylindrically symmetrical models of WH90, the ingress and egress derivative profiles of a spot profile are not necessarily rotationally symmetric about $\phi = 0$.

Of the four best candidate 'spot' derivative profiles, only one revealed an ingress derivative which could be confidently identified above the flickering limit as intrinsically different from the WH90 model profiles and exhibiting a 'spot-like' feature: that of 31/03/09 (2nd). This derivative profile was fitted with two surface spot models, as shown in Table 6.5.

The two spot model profiles were fitted for two different white dwarf radii: $R_{wd}/a = 0.0182$ (model 1, corresponding to columns 1(i) and 1(e) in Table 6.5), as determined in WH89 and considered to be the most reliable in the literature, (Wheatley *et al.* 2006, and references therein) and $R_{wd}/a = 0.0155$ (model 2, corresponding to columns 1(i) and 1(e) in Table 6.5), the radius given in Table 6.4.

Model 2, with the smaller R_{wd}, clearly provides the better fit to the derivative profile. The position of the spot is constrained from simultaneously matching the ingress and egress derivative profiles, but only within a range of latitudes. The derivative profile is best fitted by a spot at a latitude position 20.0° above or below the equator on a *co-rotating* white dwarf. If we make the assumption that a surface spot cannot rotate retrogradely with-respect-to the binary, this limits the spot position to being at a latitude greater than $|20.0°|$. The inclination of the binary, $i < 90°$, and the large radius of the secondary in comparison to the white dwarf's, actually constrains the spot position to lie within the 'upper' hemisphere[18]. This is because the limb of the secondary cuts a straight, *diagonal* shadow across the white dwarf. Thus, for the *same phases* of ingress/egress, any bright element on the white dwarf's surface occulted by the upper length of the secondary's limb has to rotate further relative to the observer's sightline than a bright element at a lower latitude. Thus, identifying a spot position which provides a matching eclipse profile at a particular latitude on the surface for the *co-rotating* case (a lower latitude would imply retrograde spot motion), puts a lower limit on the spot's latitude. An upper limit on the spot's latitude is imposed by the upper limit of the secondary's shadow at mid-ingress/egress of the spot; this is equal to $\sim 50.0°$ above the equator in this case.

The ratio of the *total* relative luminosity of the spot is constrained from the relative size and shape of the spot feature to the larger white dwarf hump. However, the stark, visible differences between the two SB distributions demonstrates again the limitations of 2-dimensional information. The peak brightness and extent of the spot on the white

[18] Where the 'upper' hemisphere is defined as that which is most visible to the earth observer.

Spot Model 1		Spot Model 2	
i	e	i	e

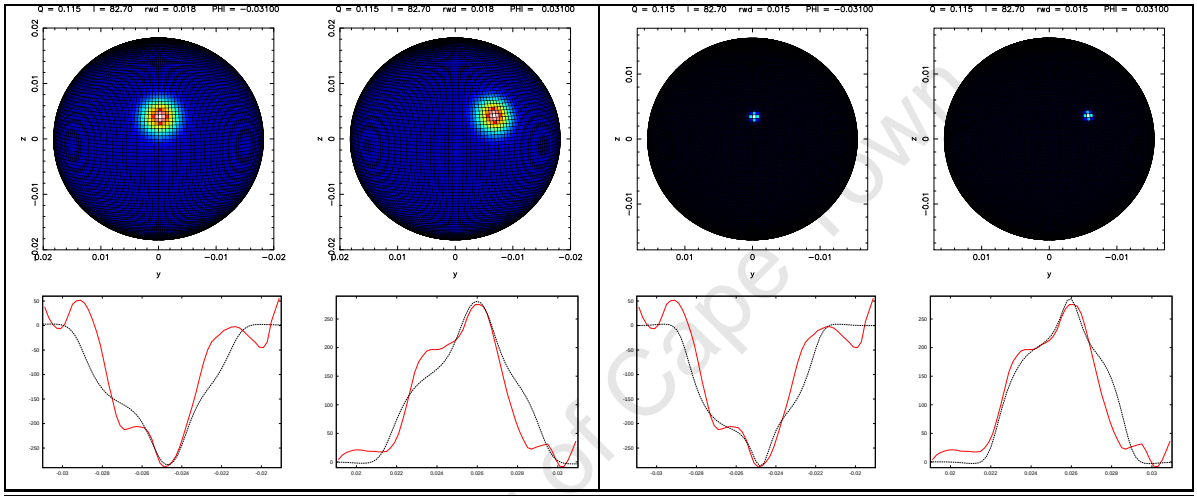

Spot parameters		
	Model 1	Model 2
R_{wd}/a	0.0182	0.0155
SB_p	~ 4.4	42.0
σ	10.0	2.2
(θ, ϕ)	$(20.0°, -12.0°)$	$(20.0°, -12.0°)$

Table 6.5: Top: Two model surface brightness distributions, as generated by `roche`, of a spherically symmetric white dwarf (no limb darkening) with a bright surface spot co-rotating with the binary. The spot is modeled by a simple Gaussian distribution. Columns 1_i and 2_i illustrate the observer's view of the white dwarf and spot just at the onset of ingress, columns 1_e and 2_e at the end of egress. Middle: Ingress (columns 1_i, 2_i) and egress (columns 1_e, 2_e) derivatives of 31/03/09 (1st)'s light curve (in red) with the spot model light curves generated by `roche` for the top surface brightness distributions superimposed (in black). Bottom: The spot parameters for each model; the peak relative brightness (x the white dwarf's surface brightness, SB_p), sigma (σ), and position angles ((θ, ϕ), θ degrees in latitude from the equator, ϕ degrees in longitude from the line of centres) on the surface of the white dwarf.

dwarf's surface is very sensitively determined by the white dwarf radius chosen. In the first model, the spot is relatively extended, with a peak brightness of ~ 4 times that of the white dwarf's surface brightness. In the second model, the white dwarf is virtually dark in comparison to the tiny spot, which has a peak brightness an order of magnitude larger than the spot of model 1. In addition, deviations of the fit from the derivative profiles are most likely due to non-Gaussianity of the spot's profile. Deviations from non-Gaussianity can not be confidently fitted with the resolution of the derivatives determined from the data here. Nonetheless, spot profiles with identical $(R_{wd}/a, \theta)$ parameters to those in Table 6.5 have provided reasonable fits to other derivative egresses: 27/04/08 (2nd), 19/02/08 (2nd), 29/03/09 and 04/04/09, albeit with varying peak spot brightnesses (and, thus, sigmas).

There are two estimates in the literature for OY Car's white dwarf radius R_{wd}; $R_{wd}/a = 0.0182$, obtained by WH89 by fitting the model of a spherically symmetric bare white dwarf to their derived contact times and $0.0144 \geqslant R_{wd}/a \leqslant 0.0163$, determined by WH90 from a parametric fit of a bare white dwarf eclipse, using five fitting parameters – (R_{wd}, $\Delta\phi$, ϕ_0, u) and the fraction of the white dwarf which was a bright accretion belt, x – to the mean light curve obtained in WH89 (the minimal value being for the minimal limb darkening, $u = 0$, case and the maximal value for $u = 1$). WH90 could not resolve the discrepancy between the parameter fitting results and the radius determined from the contact times. Wheatley & West (2002, 2003), in their X-ray analysis of OY Car, chose the radius obtained from the optical contact points (WH89) as the better estimate in order to motivate the polar regions of the white dwarf as the origin of their observed X-ray emission. This choice is based critically on the assertion that the bare white dwarf model is the best approximation to the optical eclipse profile and that WH89, WH90 "find no evidence for significant emission from the boundary layer or inner disc that could make the optical ingress/egress durations last longer that that of the white dwarf alone". The findings here contest both of these claims. The eclipse profile is found to be variable and, more often than not, not well described by a bare white dwarf. The deviations from a bare white dwarf profile equate to significant emission in the central object region; the fact that the *only* eclipse profile found in this work to match, almost perfectly, the bare white dwarf model also has the lowest (ingress/egress) flux found for the central object is an unlikely coincidence. Moreover, WH90 note that the parameter model required to fit the radius determined from the eclipse contacts requires a more gradual ingress/egress than can be fitted by maximal limb darkening. WH90 could not resolve whether the discrepancy was due to a systematic error in their eclipse contact measurement technique or a deficiency in the bare white dwarf model. Wheatley & West posit a bare white dwarf with a tem-

perature gradient decreasing towards the poles as a possible explanation. Considering the variable eclipse profile features found in this work: brightness distributions, total central object flux, ingress/egress widths, ingress/egress contact points (all contributing factors to the variable eclipse widths); the author proposes that the gradual ingress/egress profile found by WH90 is the result of averaging the brightness distribution of an inherently variable surface boundary layer. Hence, the radius of the underlying white dwarf should only be determined from the analysis of the individual, rare, eclipses where a bare white dwarf (in low flux state) can be confidently identified and fitted from the derivative profile.

The white dwarf radius determined here from such a profile $R_{wd}/a = 0.0155 \pm 0.00015$[19] can be compared to WH90's value, $R_{wd}/a = 0.0154 \pm 0.0004$, for a limb darkening value of $u = 0.5$. From the approximation to the Hamada-Salpeter mass-radius relation for cold, degenerate white dwarfs (Warner 1995), this gives an estimate for the white dwarf mass of $M_1 = 0.812 \pm 0.012 M\odot$, 30% larger than the mass obtained from the WH89 radius $R_{wd}/a = 0.0182$.

6.7.2 Phase Information

Phases of contact times were obtained from the derivative curves by measuring the points at which the derivatives deviate from zero, as stipulated by Wood, Horne *et al.* (1986). The mean values are given in Table 6.6 and compared with those obtained by WH89. As can be seen, there is no real significant difference between the two sets of results.

Examining the phase information derived from the light curves directly (refer to 6.2), estimates of $\phi_{i,e}$ obtained from the half flux points of the light curve indicate an average symmetrical shift from mean values of $\phi_i = -0.0253$, $\phi_e = 0.0252$ (WH89) to $\phi_i = -0.0256$, $\phi_e = 0.0255$. This translates to a small increase in $\Delta\phi$ to 0.0513 from WH89's results which gave $\Delta\phi = 0.0506$. More significant however, is the large, real, scatter within the eclipse width measurements, as indicated by the large standard deviation in $\Delta\phi$ given in Table 6.2. To illustrate the point, Figure 6.22 plots the egress widths reported in Table 6.6 against the eclipse widths given in Table 6.2[20]. At the centre of the plot the mean egress width is plotted against the mean eclipse width. The error bars correspond to the estimated errors in both measurements. The plot can be thought of as divided into quadrants by this 'mean' point. The mean of the egress and eclipse widths reported by WH89 for OY Car is, similarly, also plotted (labelled 'Wood 89 mean'). The categorisation of the phase measurements according to the models best describing the

[19] Where the uncertainty is the fitting error and has been estimated by eye.

[20] The egress width for each cycle was chosen in preference to the mean of the ingress and egress width in order to reduce the contribution of the bright spot to observed variability.

Table 6.6: OY Car: Mean phases of contact and central object ingress/egress widths derived from the derivative profiles and from model fitting (model 1(a) given in Table 6.4). For comparison, the same values as determined by WH89 are given.

Date	ϕ_1	ϕ_2	ϕ_5	ϕ_6	Δ_{wi}	Δ_{we}
Mean	**-0.02943**	**-0.02184**	**0.02171**	**0.02935**	**0.00759**	**0.00764**
std dev	**0.00055**	**0.00049**	**0.00044**	**0.00052**	**0.00085**	**0.00055**
Wood *et al* 89	-0.0290	-0.0213	0.0211	0.0290	0.0077	0.0079
std dev	0.0004	0.0005	0.0004	0.0003	0.0004	0.0003
Model 1(a) fit	-0.0290	-0.0218	0.0218	0.0289	0.0071	0.0071
Fitting error	0.0001	0.0001	0.0001	0.0001	0.00014	0.00014

corresponding (egress) derivative profiles (given in Table 6.3), are indicated to investigate the possibility that the scatter in eclipse widths is caused by a varying central brightness distribution. The points for the 10/06/08 and 31/01/09 (1st) observations are indicated.

The movement to a larger eclipse width from 10/06/08 to 31/01/09 (1st) seen in Figure 6.22 is consistent with the scenario of the central object transiting between two distinct SB distributions; while the egress/ingress width (assuming azimuthal symmetry) remains constant, the eclipse width increases as the brightness distribution changes from that of a bare white dwarf to that with a brightened latitudinally extended equatorial boundary layer [21].

In general, there is no strong correlation between model type and eclipse width. This makes the eclipse-width scatter more difficult to account for. Examination of a superposition of the light curves revealed that no single, consistent description can easily explain the observed $\Delta\phi$ variability. While some observations with $\Delta\phi$s significantly different from the mean are due to 'distortions' in the ingress/egress shape, some of them are due to peculiar light curve features - such as an uncharacteristically shortened ingress or egress

[21] Note that, while 31/01/09 (1st) has simply been labeled as model 2c) according to the shape of the egress derivative profile, this description of a brightening equatorial region describes a combination of models 1b) and 2c). This is because, while 31/01/09 (1st)'s eclipse width increases as expected, the ingress/egress widths do not decrease as if the bare-white dwarf's light contribution was 'switched off' and all that is left is the equatorial boundary layer, but remain the same as 10/06/08's.

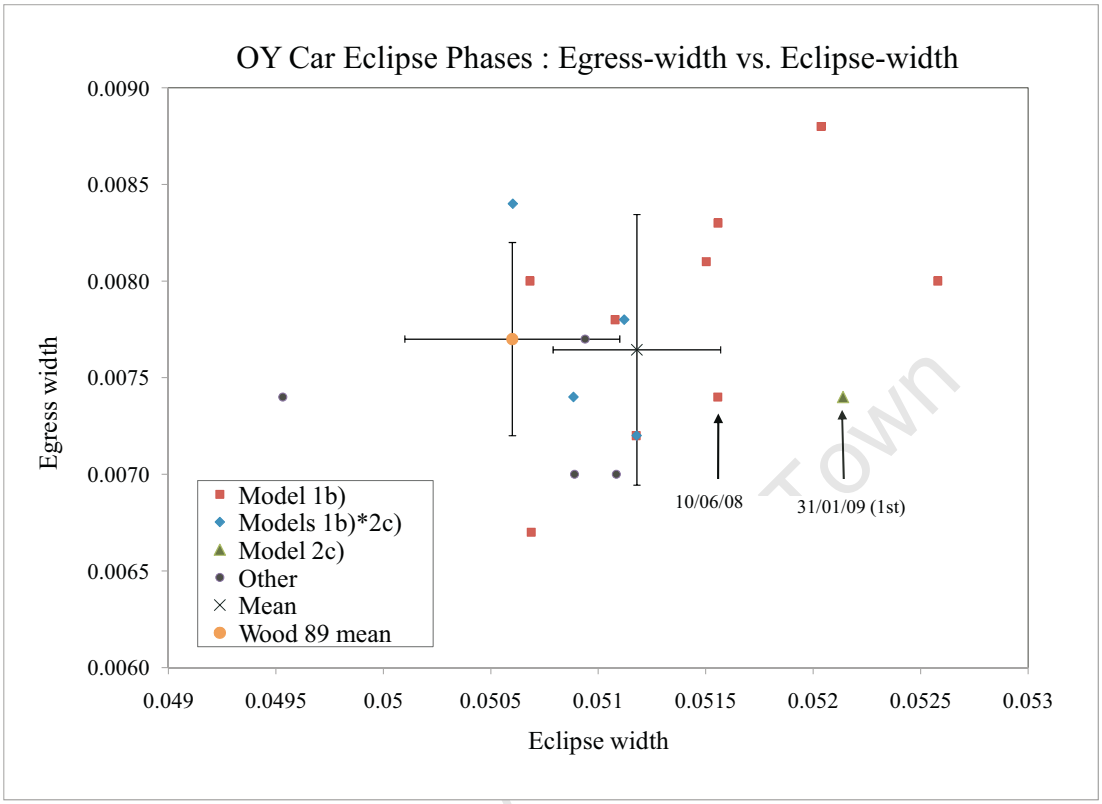

Figure 6.22: Egress widths, derived from phase timings in the derivative plots, plotted against eclipse widths, derived from phase timings in the light curves (see text for further details). The timings have been classified according to model type where the models have been categorised according to profile shapes (see Table 6.3).

- while others are due to a systematic shift in the ingress/egress shape towards or away from mid-eclipse.

The cause of the latter is a puzzle as the eclipse width is explicitly dependent on the binary parameters; (q, i) are taken to be fixed and the eclipse width is insensitive to changes in the central object's radius at such extreme mass ratios. Thus, excluding a change in the central object's brightness distribution, the only other variable is that of the secondary's radius, R_2. However, a change in R_2 of the order of $\Delta R/R_2 \sim 0.04$ is necessary to produce the observed range in $\Delta\phi$ (Ritter & Shröder 1979, Berriman 1984). This possibility is ruled out by Marsh & Pringle (1990), who showed that radius variations in the secondary of the order of 10^{-6} could not be supported by the energy budget of the secondary. Moreover, the possibility of the secondary's radius changing by the order of 10^{-2} as explanation is ruled out by the mass transfer rate's, $\dot{M}_2$ extreme sensitivity to

changes in R_2. Taking $\dot{M}_0$ to be the mass transfer rate when the secondary star's surface boundary just fills its Roche lobe, then the mass transfer rate due to a change in the secondary's radius, ΔR, causing a Roche lobe overfill can be described as:

$$\dot{M}_2 = \dot{M}_0 e^{\Delta R/H}$$

where $\Delta R = R_2 - R_0$, R_0 can be approximated as the Roche lobe volume radius, and H is the photospheric scale height (Osaki 1985). H/R is typically $\sim 3.2 \times 10^{-4}$ for lower main sequence secondaries, thus, for OY Car's M-dwarf companion, this gives $\dot{M}_2 \sim \dot{M}_0 e^{3.1\times10^3 \Delta R/R_2}$. Thus $\Delta R/R \sim 0.02$ would result in an incredible change in mass transfer rate, observable as a change in the system's brightness of the order of 50 magnitudes! (Warner 1995). Thus, global changes in the radius of the secondary can be excluded from consideration. However, it has been suggested (anonymous referee, private communication) that local, small-scale changes, in the form of star spots, could be responsible for the observed changes in the timing of the eclipse features. The rapidly-rotating lower-main sequence secondaries found in CVs are prescriptions for magnetically active photospheres and are thus likely hosts of solar-type starspot cycles. The work of Watson & Dhillon (2004) showed that, for a model pre-CV (detached) type system, reasonable star spot sizes with so-called Wilson depressions of ∼1000km can create delays in the onset of the central object eclipse of up to 3 seconds (for comparison, Sunspot depressions of up to 2500km have been previously observed, see Watson & Dhillon, 2004, and references therein). Scaling to OY Car's binary parameters, the author estimates that Wilson depressions of the order of 4000km would be required in order to account for the observed standard deviations in the eclipse width timings of ∼4.5 seconds. While we do not have typical spot depths for late-type stars – 4000km may be a reasonable depth for highly magnetic stars – one must take into account the effect of a dimpled atmosphere on mass transfer in the semi-detached case. The effect of starspots on mass transfer has been considered and well modelled, and their presence does have a significant effect on the total magnitude of the system. In fact, the presence of starspots has been invoked to explain the transition from high to low states in the case of the archetypal polar AM Her (Hessman *et al.* 2000, Kafka 2005). In the event that a star spot should pass the L_1 point, mass transfer would cease for the duration, with an immediate effect on the brightness, of the order of a few magnitudes (in the case of polars). The situation in a non-magnetic (accretion-disc-hosting) system is a little more complicated, but the effect on the disk of cessation of mass transfer, even for a short period, would be dramatic and obvious. The kind of brightness variability expected to accompany such changes is simply not observed here on the same timescale as the observed cycle-to-cycle changes in eclipse width.

The X-Ray work of Wheatley & West (2003) offers further insight into this problem. For their light curve, they found a central object eclipse with shorter ingress/egress durations and a shorter eclipse width than those given by WH89 for their mean optical light curve. While the ingress/egress and eclipse widths found here from the fitting of WH90's model 1(a) to light curve 10/06/08 for $R_{wd}/a = 0.0155$ (see Tables 6.4 and 6.6) are smaller than those derived by WH89, $\Delta_{wi/e} = 38 \pm 1$s and $\phi = 277 \pm 2$s are still significantly larger than the values determined by Wheatley & West: $\Delta_{wi/e} = 30 \pm 3s$ and $\Delta\phi = 262 \pm 1$s. Hence we may examine the inferences they make from this result. As they point out, a change in eclipse width requires some careful explanation, in this case "A narrower eclipse in X-rays implies that the secondary star must be narrower along our line of sight to X-Ray emissions than it is along our line of sight to the optical emission region... this situation can only arise if the X-ray emitting region is physically displaced vertically with respect to the centre of light in the optical.". They then go on to make the questionable assumption that the X-ray eclipse is centred on the optical eclipse which places the second and third optical contact times of both eclipses at coincidence. This neatly places the X-ray emitting region at the limit of the white dwarf's egress in the optical and Wheatley & West are able to posit that the X-ray emission originates from a polar cap. This argument all rests on their selection of $R_{wd}/a = 0.0182$ for reasons which, as discussed in the previous section, have not stood up to the analysis presented here. Choosing $R_{wd}/a = 0.0155$ does away with the neat coincidence of the X-ray/optical second and third contact times; the contact times move earlier and later respectively (Table 6.6). Moreover, the two eclipses need not be centred on the same mid-point, the location of the X-ray emitting region may be offset with-respect-to the line of centres in the optical. Nevertheless, the narrower X-ray eclipse width remains to be explained and Wheatley & West's argument throws an interesting perspective on the $\Delta\phi$ variability observed in the optical. Their X-ray source is vertically displaced with respect to the optical source and, if limited to the limbs of the white dwarf, may well emanate from an extended, oblate polar region. Such a surface brightness distribution – untested here – could also be the origin of variable optical emission sufficient enough to affect optical eclipse widths. As good SNR cycle-by-cycle X-ray eclipse curves are beyond the reach of current X-ray technology, as a next best alternative it would be interesting to see whether simultaneous X-ray and optical observations could reveal a correlation between the mean out-of-eclipse X-ray emission and optical eclipse width. For the moment however, the real observed changes in measured optical eclipse widths defy a simple, physical explanation.

6.8 Summary and Conclusions

To summarise the results of this chapter, the examination of 18 light curves obtained from high time resolution observations revealed that:

(i) OY Car's eclipse widths - in principle, strictly a function of the binary parameters - vary inexplicably on an orbital timescale.

(ii) Of the candidate surface brightness distribution models generated by WH90, no single model could be identified as representing the typical state of the central object in OY Car.

(iii) The central object's eclipse was found not only to be variable but changing on the time scale of the orbital cycle.

(iv) Where model distributions could be identified in the data, two distributions - one of a spherically symmetric bare white dwarf, one with a latitudinally extended equatorial boundary layer - could be fitted to individual cycles.

(v) A subset of the eclipse profiles revealed the eclipse of a localised bright region within the ingress/egress of the central object.

(vi) The constraint of this region's latitude relative to the equator of the white dwarf suggests a bright surface spot as the originator, as opposed to fast-moving blobs of bright material orbiting the white dwarf within the plane of the disc.

The possibility of a bright spot on the surface of the white dwarf offers an explanation for some, but not all, of the observed variability in the eclipse profile shape. The confident identification of a surface spot in eclipse ingress *and* egress is significant for the determination of the white dwarf radius as this identifies the white dwarf as being in near co-rotation with the binary. Thus the possibility of uncertainty introduced into radius estimates due to rapid rotation producing an oblate photosphere can be discounted. This would also make the mass determined for OY Car presented in this work the largest yet proposed. However, it may be that the spot features are ephemeral on a timescale shorter than the eclipse of the white dwarf, and thus, that identification of a bright spot in ingress and egress is not an indication of co-rotation. As high angular momentum material is continually deposited on the surface of the white dwarf, co-rotation is considered an unlikely scenario.

The aim of this study was to investigate the application of WH90's eclipse derivative analysis technique to high-time resolved data of a well-studied test case to determine

whether the technique offers, as the end result, a viable approach to the estimation of white dwarf masses in eclipsing CVs. The author concludes that the technique still presents the best method available for determining white dwarf masses from photometric data. However, due to the intrinsic variability of the white dwarf's boundary layer brightness profile on an orbital timescale, it is limited in application to bright targets which can produce high signal-to-noise derivative curves to be analysed on a cycle-to-cycle basis. Never-theless, a representive sample of CV-white dwarf masses is urgently needed to inform the current understanding of CV evolution. Thus, the author's findings begs a systematic, high-time-resolution, photometric survey of all known bright, double-eclipsing CVs. The survey would have to cover a few orbital cycles for each target in order to confidently distinguish the bare white dwarf profile shape from amongst the eclipse derivatives. This study, of some 30 objects, would provide the most accurate mass estimates for a CV sample. Such a survey would demand dedicated observing campaigns conducted using world-class, high-time resolution, optical instruments such as SALT but would be necessary to provide an invaluable contribution to the theory of CV evolution. As succinctly put in the concluding remarks of Sion (2006):

"We are still in the realm of speculation in many of the topics covered here....cooling curves and physical heating mechanisms of accretion-heated white dwarfs cannot be definitively interpreted unless white dwarf masses and accretion rates are pinned down with sufficient accuracy...we must advance to a more global picture of CV evolution and accretion physics by enlarging the observable sample. This requires a commitment on the part of observatory and mission directors to ensure that sufficient observing time is allocated to accelerate the accumulation of CV white dwarf properties beyond the present slow pace of one to two systems at a time. Only then will the wealth of information contained in CV white dwarfs be attainable."

Chapter 7

Summary and Future Outlook

Using the astrophysical setting of cataclysmic variable stars, the projects described in this thesis have illustrated the classical grooming of modern astronomical technology for marriage to demanding observational programs enabling key research questions to be tackled. Part I showed that studies (such as the dwarf novae disc-radius monitoring campaign conducted in Chapter 5) which require dedicated monitoring of variable systems to test long-term behavioural predictions, demand the kind of observing commitment that only a dedicated automaton can provide. Such observational programs are typical of the science drivers for the ongoing upgrade and conversion of small telescope operational processes, from manual to automatic, in observatories across the globe.

While some aspects of the observing process can use upgraded and converted equipment to accommodate more 'hands-off' observing modes, not all legacy technology can make the transition. The upgrade of the SAAO's 0.75m telescope, documented in Part I of this thesis, is an example: while the upgrade of the telescope's control system allowed successful implementation of a remote observing mode, the 15 year old camera earmarked for remote science imaging had a control system which could not meet the demands of remote observing. As concluded at the close of Part I, only the wholesale replacement of existing legacy CCD systems offers the most efficient route to competitive science.

The results from Part II of this thesis showed that the standard testbed for accretion theory still reveals challenges and surprises in the light of stringent testing. The small telescope work in Chapter 5 demonstrated the shortcomings of the two, currently, most popular SU UMa superoutburst theories which fail to explain accretion-disc-supercycle behaviour in two identical systems. However, only the accretions discs of OY Car – only 2 of 19 known (double) eclipsing SU UMa systems – have been monitored over their supercycles as presented here. Thus the extent of the true successes and failures of the EMT and TTI models to explain SU UMa accretion disc limit cycles is unknown. A coordinated systematic survey, the kind that a network of Northern and Southern Hemisphere auto-

mated telescopes could easily provide, is desperately needed to characterise the long-term accretion disc behaviour in eclipsing SU UMa systems. As has been demonstrated in this investigation, the test is simple and the results are likely to throw up an interesting variety of behaviours unique to particular systems, perhaps each with its own challenge to the existing models.

The 10m-class science offered unprecedented insights into the nature of accretion right at the boundary of a dwarf nova's white dwarf (Chapter 6). Follow up studies are needed to confirm the existence of a transient bright spot on OY Car's primary surface and whether surface bright spots can be found on white dwarfs in other dwarf novae. While highly speculative, the existence of white dwarf/boundary layer surface spots in dwarf novae offers a potential probe into the nature of accretion at the boundary and investigation of the possibility that very low-level magnetic fields are the mechanism for accretion in 'non-magnetic' CV systems.

Chapter 6's work also illuminated the fact that, as the demands of scientific enquiry push the boundaries of technological development, so they push the sophistication of data analysis techniques to exploit fully the quality of data which new technology produces. In the case of the work presented in Chapter 6, the TVR technique, adapted for the needs of the investigation, allows, for the first time, the realistic application of Wood & Pringle's (1985) pioneering derivative analysis technique to 1-dimensional time-series data. This technique can be applied to any astrophysical scenario where discrimination between synthesised light curves is a critical decider in choosing between competing models of surface brightness distributions and/or geometry. Such scenarios include:

- Investigating changes in accretion disc structure throughout dwarf novae outburst cycles and during outburst,
- Modelling the accretion geometry and brightness distribution of the accretion streams of polars,
- Eclipse timing analysis of X-Ray eclipses (where TVR can be adapted for Poisson noise distributions, Chartrand 2007),
- Eclipse mapping of starspots and the resolution of starspot distributions in chromospherically active stellar photospheres,
- Albedo mapping of satellite-hosting Solar-system objects (e.g. the Pluto-Charon system),
- Asteroid surface mapping from rotational light curves,
- Detection of exomoons or rings in exoplanet transit curves and,

- Selection of photospheric emission models of hot-Jupiters (where infrared measurements of hot-Jupiter eclipses by the James Webb Space Telescope could produce photometry of sufficient SNR and temporal resolution to exploit the derivative analysis technique, Rauscher *et al.* 2007).

Thus this potentially powerful technique for the analysis of 1-dimensional data sets may have lasting value far beyond the scope for which it was originally intended.

All of the science case scenarios listed above can be broadly defined as the study of compact objects. The study and resolution of compact objects fall under the remit of High Time Resolution Astrophysics (HTRA); astrophysics on the timescale of a second or less. In particular, the domain of HTRA has produced significant contributions to the study of highly variable, high energy systems and extreme environments as the research outputs of HTRA instruments in the 10m-telescope-class such as, FOCAS on Subaru, AcqCam on the Gemini telescopes and Ultracam on the VLT (Ryan 2006), has demonstrated. In 7 years of science, nearly 50% of the subscription rate for Ultracam was for the study of compact binaries (over half of which was dedicated to the study of CVs, Dhillon 2010). The reason for this, to quote Dhillon in his response to the question *'Why bother with compact objects?'* is that *'They are the end points of stellar evolution, providing a fossil record of the star formation history of our Galaxy. They are the cosmic laboratories, providing extreme conditions of gravity, density, pressure and temperature., pushing theories of fundamental physics to the limits of their predictive powers [and]... they are responsible for some of the most exotic inhabitants of our Universe'*. However, as in many of the science cases bulleted above, intricate geometries, faint compact systems and precise timing of rapid transient features cannot be resolved with even the best in 10m-class instrumentation currently available. It is this motivating factor which drives the forefront of ground-based HTRA instrumentation today, pushing HTRA into the era of ultra-high-time-resolution that the coming decade of 30m-class Extremely Large Telescopes (ELTs) will provide. ELTs currently under development, most notably the the Thirty Meter Telescope (TMT) and the European-Extremely Large Telescope (E-ELT), stand to make an enormous impact on the resolution of compact systems' features as, for faint point-like sources, the sensitivity dependence on telescope aperture renders a 30 m telescope a *hundred* times more sensitive than a 10m telescope (Silva *et al.* 2007). The full advantage of the high photon counts these large apertures will deliver can only be exploited with the advent of the fast detectors currently under development enabling photon time-tagging, high quantum efficiency, fast readout times and low readout and dark counts (Ryan 2006). The development of adaptive optics systems to operate in the optical waveband allows the near of removal atmospheric effects, enabling ground-based-instruments to achieve resolutions rivalling that of current

space telescopes (Ivanov *et al.* 2009). Together these new telescope technologies – IRIS on the TMT or the HTRI on the E-ELT – will allow the realisation of microsecond astronomy.

Figure 7.1: Current site layout of the LCOGT suite of telescopes at Sutherland. In the foreground lies the layout for the (initially two with the possible later addition of a third) 1.0m domes, on the right the layout for the aqawan (clamshell) enclosures which will each house two fully robotic 0.4m telescopes. The complete installation and testing of two 1.0m telescopes and four 0.4ms is scheduled for the end of 2011. Photo courtesy of Willie Koorts at the SAAO, local LCOGT project manager.

Turning to the future of small telescopes, during the last decade of the current Information Age progress in many fields has depended on exploiting the power of digital networks. So too in ground-based observational astronomy, where the demands of optical, time-domain research has been the driver of network-centric astronomy. The key features of network astronomy – a network of telescopes distributed globally, remotely-operated or automated observational procedures, real-time on-site data reduction, interoperability and flexible scheduling – enables maximum temporal coverage and rapid response to time-critical events. Examples of existing and growing telescope networks include the GCN (Gamma-ray bursts Coordinates Network, 2011), TALONS (The Telescope Alert Operations Network System, White *et al.* 2006a), RoboNET-II (Tsapras *et al.* 2009 and references therein) and SONG (Stellar Oscillations Network Group 2008). Thus, while the SAAO prepares for the substantial upgrades and replacements of their small telescope systems, private enterprise projects planned for implementation in 2011 usher in the frontline of automated observing at the Sutherland observing site: coordinated telescope networks in the form of an installation of a Las Cumbres Observatory Global Science Telescope (LCOGT) Network node. The LCOGT Network is a private initiative to create a global network of telescopes with nodes of 2 x 1.0m and 4-6 x 0.4m telescopes to complement the existing 2.0m LCOGT telescopes, (Faulkes Telescope South and Faulkes Telescope

North, located at Siding Spring Observatory, Australia and Mt. Haleakala on the Hawaiian island of Maui respectively). The SAAO's Sutherland site will host one of the three nodes located in the Southern Hemisphere and, with site planning already well underway, the site can be expected to host six new fully robotic telescopes by the end of 2011 (see Figure 7.1 for the planned site layout). This site will take part in a new concerted effort to surmount the challenges of time-domain astrophysics and further enrich knowledge in the fields of optical transients, exo-planets and binary-star systems (LCOGT 2011).

Collaborations between telescope network groups and network platform development teams – such as between eSTAR (e-Science Telescopes for Astronomical Research, Steele *et al.* 2004, Allan *et al.* 2002), RoboNET-II and LCOGT (Tsapras 2009), TALON and eSTAR (White *et al.* 2006b) – are ushering in the next level of network-centric astronomy: a metanetwork. As the term implies, a metanetwork is a network of networks of telescopes. A node in the metanetwork is comprised of a suite of telescopes and each node is interoperabily linked by a standard communication platform to enable the whole to work as a single instrument. This offers members of participating observatories the best possible in "observing flexibility, optimised observing performance and very high observing efficiency" (Solomos 2010). Each node need not represent a homogeneous ensemble (and thus such a metanetwork is also referred to as a Heterogeneous Telescope Network, Solomos 2010); the only requirement for each telescope within a node is a high degree of automation. Thus, existing observatory suites of small telescopes need not be left out of this next revolution in small-telescope science. For telescopes such as the 0.75m in Sutherland, steps towards remote operability may only be the beginning of realising the full-potential of these pack-ponies of astronomy.

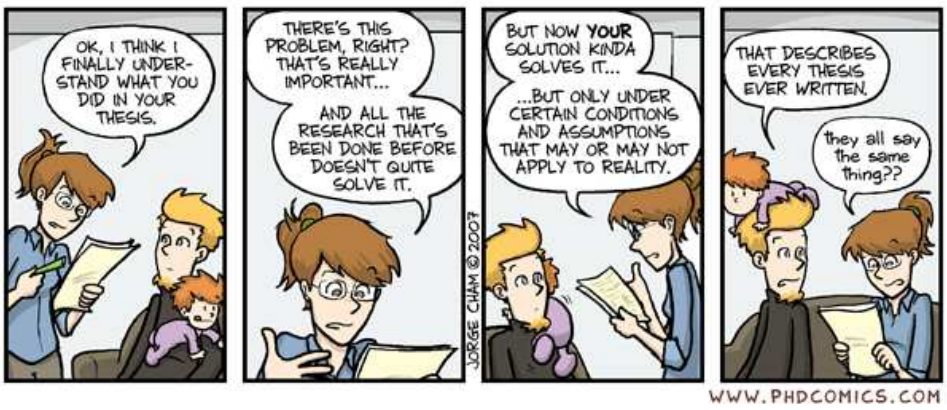

Figure 7.2: "Piled Higher and Deeper" by Jorge Cham www.phdcomics.com

Appendices

Appendix A

`Ephem.f` and Ephemeris Determination using Least Squares Fitting

Briefly, least squares function fitting is the technique of fitting a function

$$y = f(x) = a_0 + a_1\phi_1(x) + a_2\phi_2(x) + \cdots + a_I\phi_I(x)$$

to a set of data $(y_n),\ n = 1, \ldots, N$ at known points (x_n). This is parametric fitting as the form of the function is known before hand (Nikunen, 2001). The function need not be in the form of a polynomial but crucially the function must be linear in the parameters (a_k) even thought it may be nonlinear in the variables.

If we assume that the errors in y_n have a gaussian distribution then the best fit to the data can be determined by minimising the sum of the squared errors:

$$\chi_I^2 = \sum_n^N [y_n - f(x_n)]^2$$

with respect to the parameters. i.e:

$$\frac{\partial \chi_I^2}{\partial a_i} = 0; i = 0, 1, \ldots I$$

This results in a system of linear equations termed the 'normal' equations (Nikunen, 2001):

$$\mathbf{\Phi^T \Phi a} = \mathbf{\Phi^T y} \qquad (*)$$

where $\mathbf{a} = [a_1\ a_2\ \ldots\ a_m]^T$, $\mathbf{y} = [y_1\ y_2\ \ldots\ y_N]^T$ and

$$\mathbf{\Phi} = \begin{bmatrix} \phi_1(x_1) & \phi_2(x_1) & ... & \phi_M(x_1) \\ \phi_1(x_2) & \phi_2(x_2) & ... & \phi_M(x_2) \\ \vdots & \vdots & \vdots & \vdots \\ \phi_1(x_N) & \phi_2(x_N) & ... & \phi_M(x_N)S \end{bmatrix}$$

For example, if $f(x)$ is of the form

$$f(x) = a_0 + a_1 x + a_2 x^2 + a_3 x^3$$

then

$$\mathbf{\Phi} = \begin{bmatrix} x_1^0 & x_1^1 & x_1^2 & x_1^3 \\ x_2^0 & x_2^1 & x_2^2 & x_2^3 \\ \vdots & \vdots & \vdots & \vdots \\ x_N^0 & x_N^1 & x_N^2 & x_N^3 \end{bmatrix}$$

Equation $(*)$ can be solved for using Gaussian elimination but for high order matrices there are more computationally efficient techniques (refer to Gerhensfield 1999).

`Ephem.f`, programmed by Dr Darragh O' Donoghue, is the fortran routine used in this thesis to calculate a revised ephemeris for Z Cha. It fits an ephemeris of the form

$$T_0 + EP + E^2 s + E^3 t$$

to the observed minus calculated $(O - C)$ residuals obtained from the times of eclipse predicted by the previously determined ephemeris subtracted from the observed times of mid-eclipse.

In addition, `ephem.f` can add a sinusoidal component to the fit. Using the identity:

$$asinx + bcosx = \sqrt{a^2 + b^2} \cdot sin(x + \varphi)$$

where

$$\varphi = arcsin\left(\frac{b}{\sqrt{a^2 + b^2}}\right)$$

a sinusoidal term of the form

$$a\cos\left(2\pi\left(\frac{t - E_{Plong}}{P_{long}}\right)\right) + b\ sin\left(2\pi\left(\frac{t - E_{Plong}}{P_{long}}\right)\right)$$

can be fitted to the data where E_{Plong} is the phase relative to the epoch and P_{long} is the estimated period of variation over the whole data set.

Once $\mathbf{\Phi^T \Phi}$ is computed the matrix is factorised, inverted and multiplied by the matrix $\mathbf{\Phi^T y}$ to obtain the parameters, $\mathbf{a}$ of the fitted function.

Appendix B

Pointing Models

A pointing model is a software generated model of the telescope's movement used by the TCS to correct for imperfections in telescope manufacturing and construction. These are broadly classified as instrumental imperfections. The star coordinates obtained from a catalogue give an apparent right ascension, declination and an epoch to which the spatial coordinates are referenced. The coordinates take into account the observed changes in the star's position due to proper motion of the star, observed parallax, distortions created by annual aberration and the precession and nutation of the earth's axis. The coordinates are fed into the TCS which modifies the parameters according to hour angle, diurnal aberration and atmospheric refraction (which is mainly determined by the site's location above sea-level). This yields an apparent position. The apparent position must be further modified using telescope pointing corrections, combined as a pointing model, to compensate for instrumental imperfections to yield an instrumental place (Wallace 2005).

A pointing model can either be empirical or analytic, based on mechanical considerations. Empirical models create a map of the telescope's movement using observed pointing error data, then employ spherical harmonics and polynomials to correct the motion of the

Table B.1: The six geometrical terms for an Equatorial mount (reproduced from Wallace 2005). h and δ are hour angle and declination respectively

Term	**Description**	Δh	$\Delta\delta$
IH	h index error	IH	
ID	δ index error		ID
CH	collimation error	CH $\sec\delta$	
NP	h/δ perpendicularity	NP $\tan\delta$	
MA	polar axis left-right alignment	-MA $\cos h \tan\delta$	MA $\sin h$
ME	polar axis vertical alignment	ME $\sin h \tan\delta$	ME $\sin h$

telescope. Analytical mechanical models assume that the telescope's motion is governed by functions of its mechanical characteristics. Minimising these functions using observed pointing error data corrects the motion of the telescope. The pointing model program used by WinTCS is based on an analytical mechanical model of the telescope. The coefficients to be adjusted represent six telescope geometrical terms and three types of flexure (Wallace 2005). The table below gives the six geometrical terms and the corresponding corrections made to hour angle and declination.

IH and ID are zero point corrections made to the hour angle and declination indices. The collimation error describes how well aligned the optics are with respect to the tube, how close the tube is to making a right angle with the declination axis and how much East or West the centre of the CCD is displaced. NP describes the non-perpendicularity of the declination axis with respect to the polar axis. ME and MA describe how far off centre the telescope axis is with respect to the polar axis, left-right in the case of MA and up-down in the case of ME.

The three types of flexure that have to be corrected for is given in the table below, where phi is the site latitude. The most important term in our case is TF, tube flexure which is a droop in the telescope which increases the lower the telescope points. FO is most prevalent in telescopes which have fork or yoke mounts and DAF in cantilevered mounts.

Analytical mechanical models tend to be better than empirical ones because their coefficients address each of the main telescope imperfections. This yields a better fit to the true movement of the telescope, involving less terms and fewer observations to obtain the most accurate representation. A mechanical model is more likely to be better behaved outside of the regions covered by the test data than polynomials and spherical harmonics (Wallace 2005). In any case, once the best mechanical fit has been derived for the telescope, additional spherical harmonics can be used to reduce harmonic terms arising from eccentricity in the drive systems and backlash (Buckman 2002). The WinTCS pointing program does not provide harmonic corrections, but more comprehensive computer packages do, such as TPOINT which was developed for the Anglo-Australian Telescope in the 1970s and has since been employed by professional observatories such as Keck, Gemini and ALMA (Wallace 2005).

Appendix C

Online 0.75m Upgrade Documentation

The following pages are screenshots of the online documentation provided by the author to support the 0.75m telescope upgrade and remote operation project and which are available on the SAAO's internal website.

Figure C.1: The 0.75m project's main page. The links lead to the TCS refurbishment page (top) and the remote operation project page (bottom) detailing the aspects of the remote operation software, procedures and tests.

Figure C.2: The TCS refurbishment home page with links to the 0.75m Technical Manual related technical documents page and related technical drawings page.

Figure C.3: The Technical Documents page (1). This provides links to all of the manuals and supplementary help documents relating to the 0.75m's subsystem's upgrade.

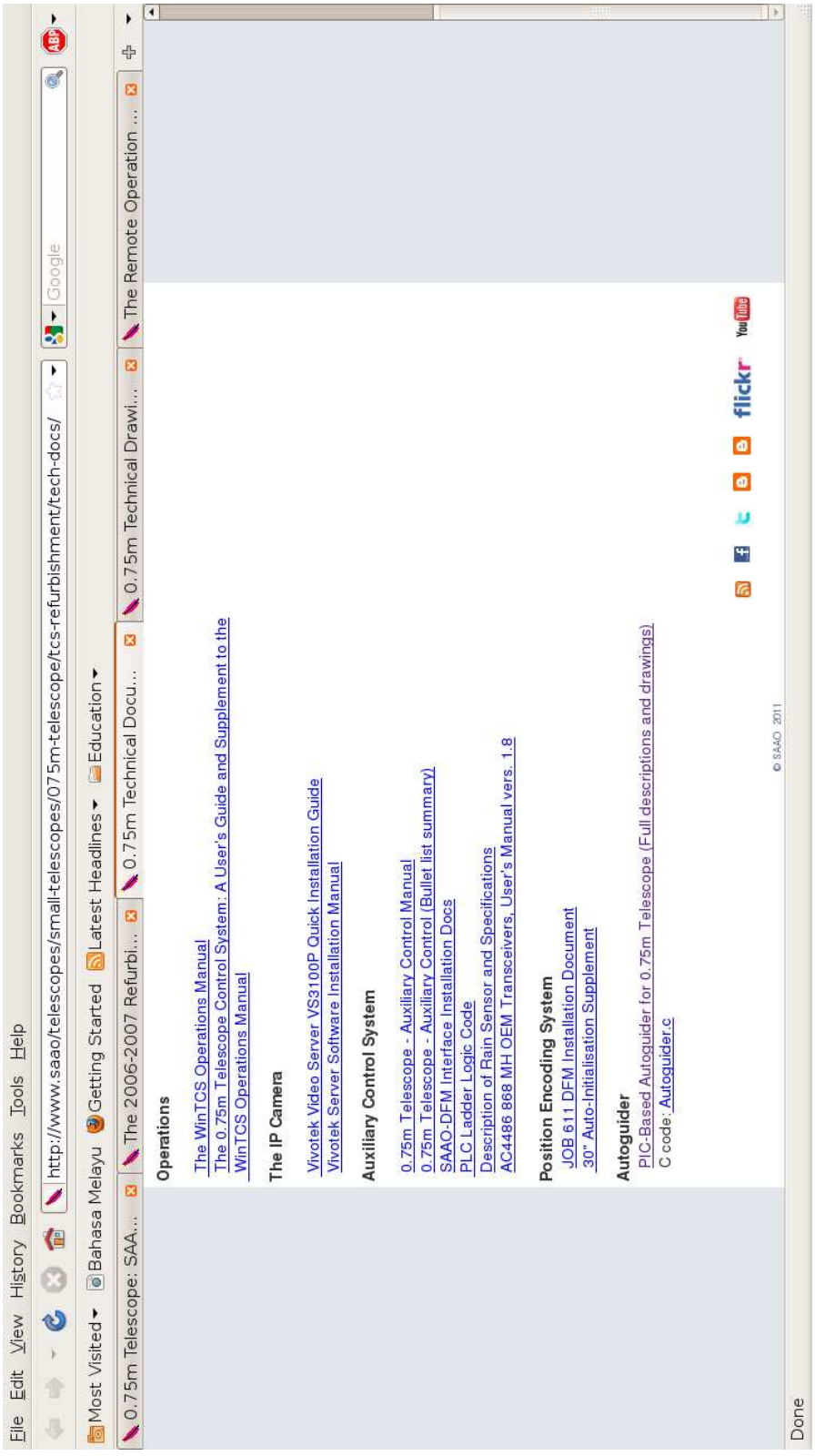

Figure C.4: The Technical Documents page (2)..

Figure C.5: The Technical Drawings page. This provides links to all of the design, mechanical and electronic drawings relating to the 0.75m's subsystem's upgrade.

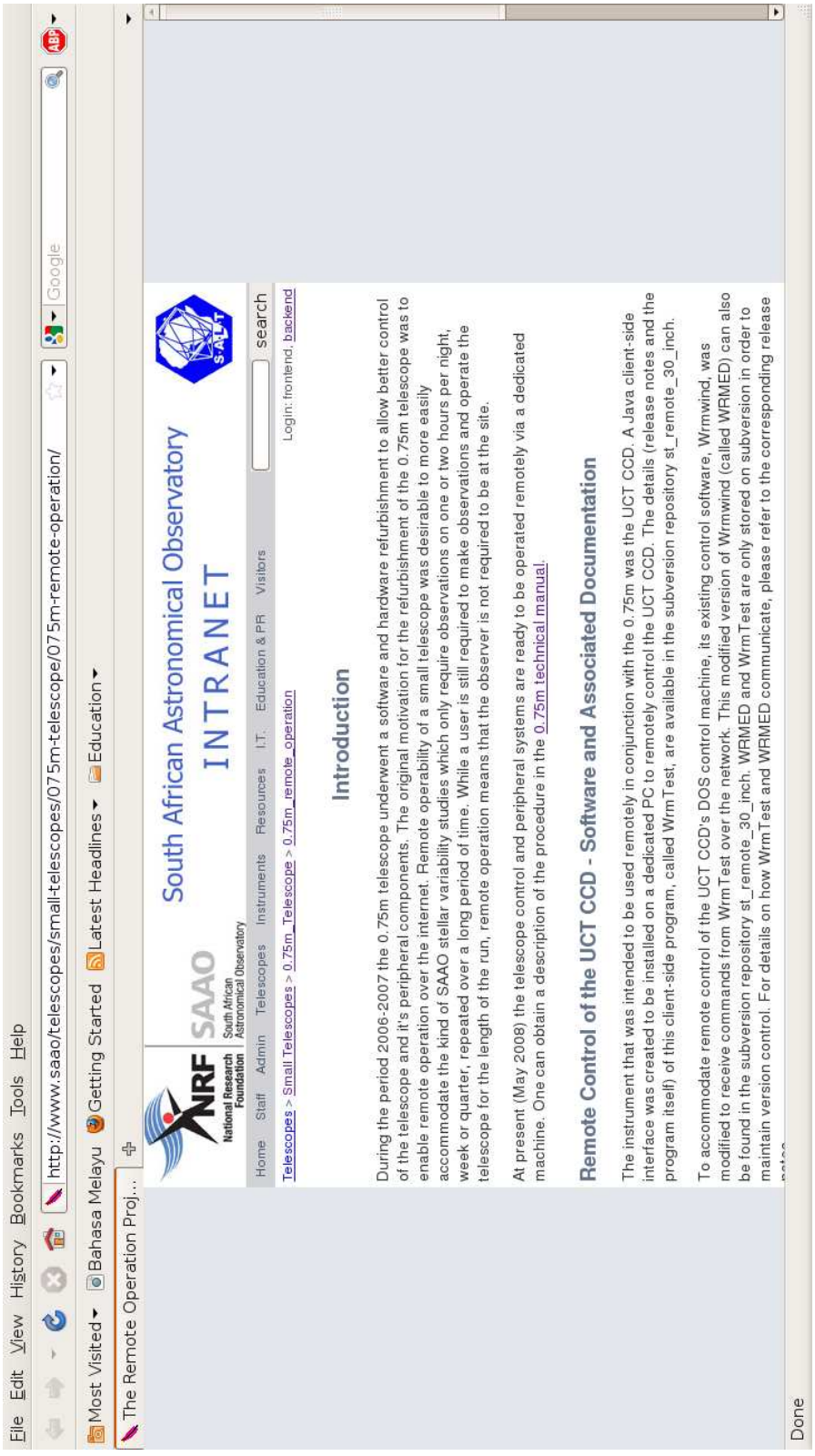

Figure C.6: The remote operation project page with links to the software and and associated documentation in the SAAO's SVN software repository.

Appendix D

RASNZ and AAVSO archival data

Amateur coverage of Z Cha and OY Car was obtained from the Royal Astronomical Society of New Zealand (RASNZ) Variable Star Section and the American Association of Variable Star Observers (AAVSO). The cleaned data sets spanning the period of observations presented in this work are shown in Figures D.1 and D.2. The data included observers' identification, confirmed visual magnitudes (verified by the AAVSO and RASNZ's quality assessment procedures, see RASNZ (VSS) 2011 and AAVSO 2011 for further details) and limiting or 'fainter than' magnitudes (see figure captions).

Visual estimates are quite noisy. To aid confident identification of outbursts, the peaks, and not the rise or onset of outburst, were searched for via visual inspection of the data. The data plotted were 'cleaned' for 'spurious' points by first only plotting confirmed visual magnitudes above a threshold value for each object. This threshold (T) was estimated from the known typical white light magnitudes for a target's normal and superoutbursts (Ritter & Kolb 2005) and was estimated by $T = M_N + 1/e * (M_N - M_q)$ where M_N is the peak magnitude of normal outburst and M_q is the quiescent out-of-eclipse magnitude. These thresholds roughly approximated to 13.6 and 13.4 visual magnitudes for OY Car and Z Cha respectively. Data above these thresholds were then considered 'events'.

Next, comparisons were made between the RASNZ and AAVSO data sets. Events were thereafter included for consideration as peak outbursts, only where there was more than one visual confirmation of the event, each with values within 0.5 magnitudes of each other. Visual confirmations for consecutive nights and, preferrably, from different observers were taken as the strongest cases for an outburst event.

Superoutbursts were relatively easy to identify, as can be seen in Figures D.1 and D.2. Their main criteria for selection was duration; any event recorded above normal outburst maximum for more than 3-5 days was identified as a superoutburst and, in nearly all cases, there was coverage of superoutburst events from both archives. Fortunately, over the period of my observations I had the benefit of many of the superoutbursts confirmed

by VSnet (Variable Star network) alerts which began circulation in 2005 (see VSNet 2011 for further details).

Normal outbursts were far more difficult to identify. An example of a difficult case has been left in the period 24513650-2453800 JD of Z Cha's coverage (Figure D.1). Over this period there are events which do not appear in both data sets; some recorded by different observers, some on consecutive nights, yet at significantly different magnitudes from one time instance to another. Serendipitiously, in most of these awkward cases, my own observations on the nights in question ruled out many false events. However, there is rarely this benefit for published data; unfortunately, such 'difficult' examples also appear during the periods of observation of the published data used in the analyses presented in Section 5.5. This is where comparison to limiting magnitudes and observer information can be critical; events which conflicted with limiting magnitude estimations on the same night or, secondarily, other observer's estimations, were ruled out as false positives.

Thus, the overall approach in the identification of outburst events has been conservative; if, application of all of the above selection criteria left a solitary data point as tenuous indication of an outburst event, this was also ruled out. Consequently, as mentioned in Section 5.5, where (normal) outburst could not be confidently identified, some radius measurements determined here, and in the literature, had to be left out of the final analysis.

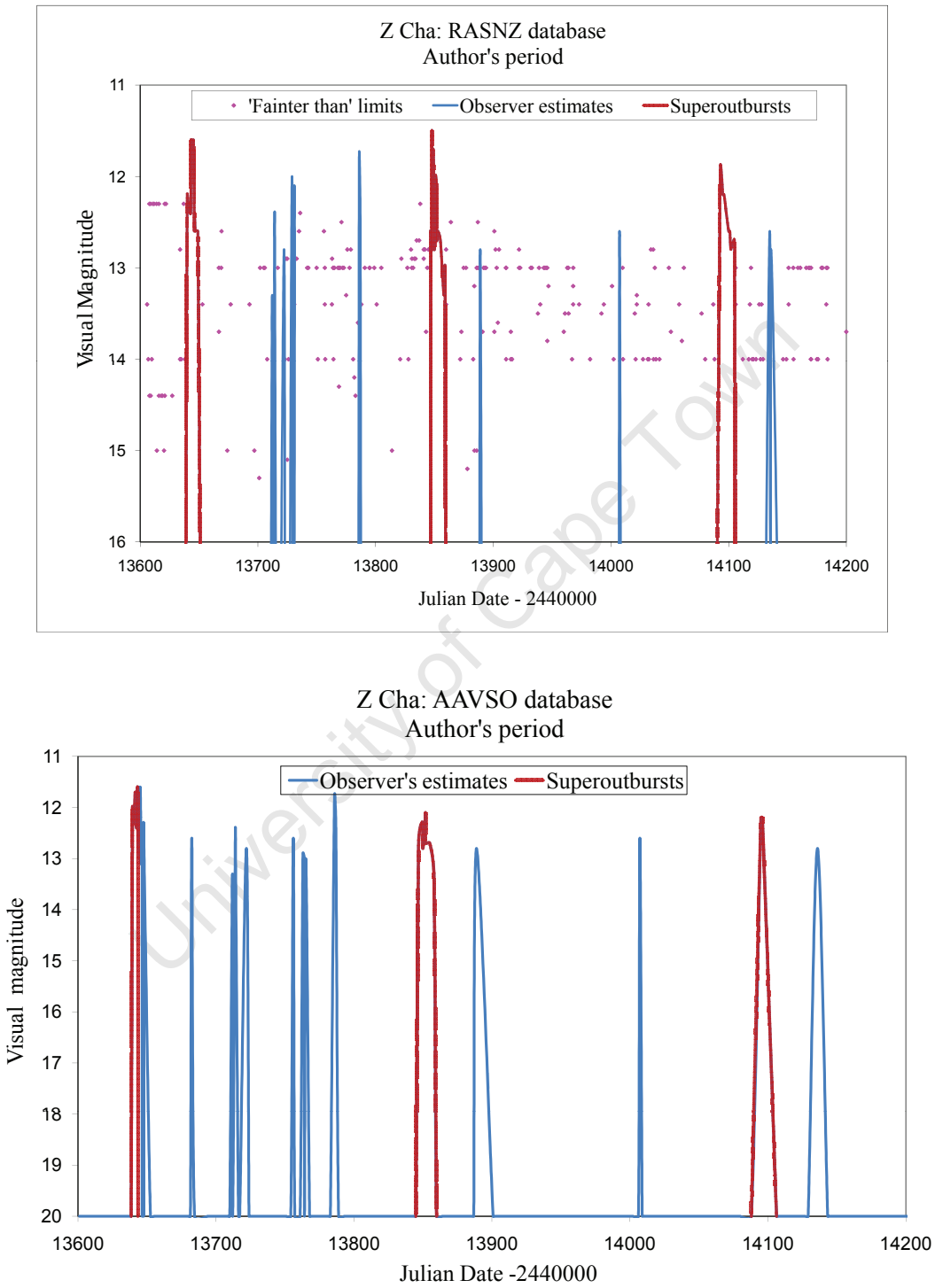

Figure D.1: (Top) Cleaned AAVSO archival data for Z Cha for JD 24513600-2454200. The candidate outburst events are plotted in blue as 'Observer estimates' where identified superoutburst events have been superimposed in red. (Bottom) Cleaned RASNZ archival data for Z Cha for JD 24513600-2454200. The candidate outburst events are plotted in blue as 'Observer estimates', identified superoutburst events superimposed in red. The 'fainter than' or limiting magnitudes (pink diamonds) have been included in this plot to give an idea of coverage.

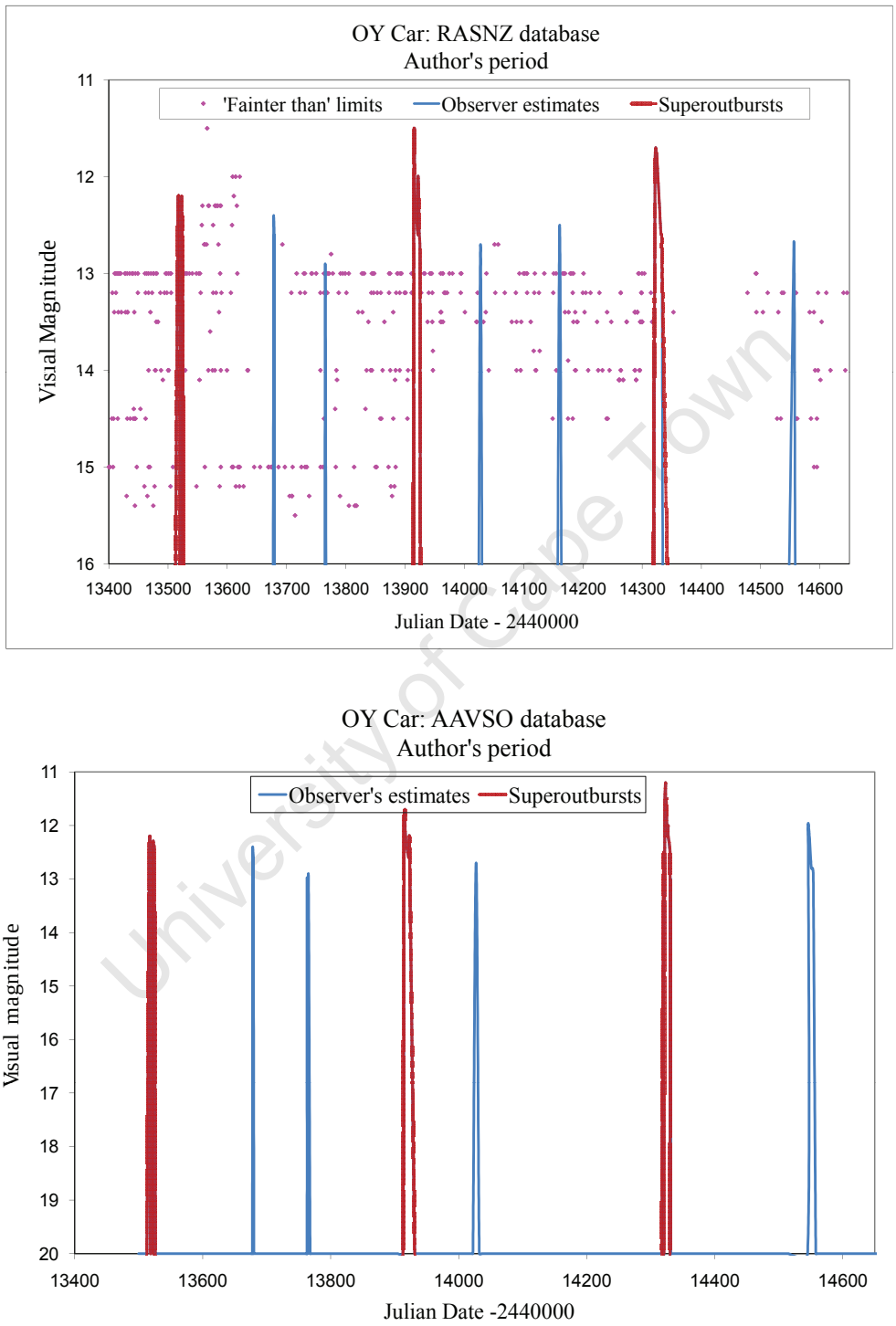

Figure D.2: (Top) Cleaned AAVSO archival data for OY Car for JD 24513400-2454600. The candidate outburst events are plotted in blue as 'Observer's estimates' where identified superoutburst events have been superimposed in red. (Bottom) Cleaned RASNZ archival data for OY Car for JD 24513400-2454600. The candidate outburst events are plotted in blue as 'Observer estimates', identified superoutburst events superimposed in red. The 'fainter than' or limiting magnitudes (pink diamonds) have been included in this plot to give an idea of coverage.

Bibliography

[1] AAVSO, 2011, http://www.aavso.org/what-we-do

[2] Aerocomm, 2007, *Ac4486 868 MH OEM Transceivers, User's Manual vers. 1.8*, http://www.aerocomm.com/rf_transceiver_modules/ac4486_868MHz_rf_transceiver.htm

[3] Agarwal, V., 2003, *Total Variation Regularization and L-curve method for the selection of regularization parameter*, http://imaging.utk.edu/people/former/vivek/EdgeTV.pdf

[4] Ak, T., Ozkan, M. T. and Mattei J. A., 2001, Astron. Astrophys., **369**, 882

[5] Allan, A., Hellier, C. and Ramseyer, T. F., 1996, Mon. Not. R Astron. Soc., **282**, 699

[6] Allan, A., Naylor, T., Steele, I. A. *and co-authors*, 2004 *eSTAR: Intelligent observing and rapid responses* SPIE, Vol. 5496, p. 313

[7] van Amerongen, S., Bovenschen, H. and van Paradijs, J., 1987, Mon. Not. R Astron. Soc., **229**, 245

[8] van Amerongen, S., Kuulkers, E. and van Paradijs, J., 1990, Mon. Not. R Astron. Soc., **242**, 522

[9] Anderson, N., 1988, Astrophys. J., **325**, 266

[10] Andronov, N., Pinsonneault, M. and Sills, A., 2003, Astrophys. J., **582**, 358

[11] Araujo-Betancor, S., Knigge, C., Long, K. S. *and co-authors*, 2003, Astrophys. J., **583**, 437

[12] ATC Innovations, 2010,*Software applications*, http://www.atcinnovations.com/what-we-do/software-applications/index.html

[13] Balestra, A., Santin, P., Sedmak, G., Comin, M., Raffi, G. and Wallander, A., 1992, Messenger No 69., p. 1

[14] Baptista, R., Steiner, J. E., and Cieslinski, D., 1994, Astrophys. J. **433**, 332

[15] Baptista, R., Catalán, M.S., Horne, K. and Zilli, D., 1998, Mon. Not. R Astron. Soc., **300**, 233

[16] Baptista, R., Catalán, M.S. and Costa, L., 2000, Mon. Not. R Astron. Soc., **316**, 529

[17] Baptista, R., Jablonski, F. and Oliveira, E., 2002, Mon. Not. R Astron. Soc., **335**, 75

[18] Baptista, R. and Bortoletto, A., 2004, Astron. J., **128**, 411

[19] Baptista, R., Santos, R. F., Faundez-Abans, M. and Bortoletto, A., 2007, Astron. J., **134**, 867

[20] Bath, G. T., 1973, Nature. Phys. Sci., **246**, 84

[21] Bailey, J., 1979, Mon. Not. R Astron. Soc., **187**, 645

[22] Berriman, G., 1984, Mon. Not. R Astron. Soc., **207**, 783

[23] Bierwirth, T., Szeifert, T., Dorigo, D., Nunes, P., Rejkuba, M., Baugh, K., Klein Gebbinck, M., Manning, A., Muravov D. and Vera, I., 2010, *New observing concepts for ESO survey telescopes*, SPIE Vol. 7737, p. 77370W

[24] Blomgren, P., Chan, T., and Mulet, P., 1997, *Extensions to total variation denoising*, SPIE, Vol. 3162, p. 367

[25] Borges, B. W. and Baptista, R., 2005, Astron. Astrophys. **437**, 235

[26] Borges, B. W., Baptista, R., Papadimitriou, C. and Giannakis, O., 2008, Astron. Astrophys. **480**, 481

[27] Bruch, A., 2000, Astron. Astrophys. **359**, 998

[28] Bruch, A. and Duschl, W., J., 1993, Astron. Astrophys. **275**, 219

[29] Buat-Ménard, V., Hameury, J.-M. and Lasota J.-P., 2001, Astron. Astrophys. **366**, 925

[30] Buckmann, A., 2002, *Telescope Pointing Errors and Corrections*, www.awrtech.co.uk/telerr.pdf

[31] Bus, S. J., Rayner, J. T., Tokunaga, A. T., and Tollestrup, E.V., 2009, *The NASA Infrared Telescope Facility (white paper)*

[32] Butler, R. F. and Forde, K., 2004, *Data reduction and analysis pipelines: the simple approach for the xFOSC family of instruments*, SPIE Vol. 5493, p. 502

[33] Caselles, V., Chambolle, A., Novaga, M., 2007, *The discontinuity set of solutions of the TV denoising problem and some extensions*, SIAM, Multiscale Modeling and Simulation, Vol. 6, No. 3, 879

[34] Chambolle A., 2003, *Total Variation Minimization and Applications*, Inverse Problems Workshop Series II, IPAM, UCLA

[35] Chambolle A., 2004, *An algorithm for total variation minimization and applications*, J. Math. Imag. Vis., **20(1-2)**,

[36] Chambolle A., Lions, P-L., 1997, *Image recovery via total variation minimization and related problems*, Numer. Math., **76**, 167

[37] Chan T. and Mulet P., 1999, *On the convergence of the lagged diffusivity fixed point method in total variation image restoration*, SIAM J. Appl. Math., **36**, 354

[38] Chan, T. and Esedoglu, S., Park, F. and Yip., A.,*Recent developments in total variation image restoration*, In Mathematical Models of Computer Vision, p 17-32 (Springer Verlag, 2005)

[39] Chan, T. and Esedoglu, S., 2005, *Aspects of total variation regularized $l1$ function approximation*, SIAM J. Appl. Math., **65**, 1817

[40] Chanan, G. A., Middleditch J. and Nelson E. J., 1976, Astrophys. J., **208**, 512

[41] Chartrand, R., 2005, *Numerical differentiation of noisy, nonsmooth data*, Los Alamos National Laboratory, http://math.lanl.gov/Research/Publications/Docs/chartrand-2005-numerical.pdf

[42] Cheng, F. H., Horne K., Marsh T. R., Hubeny I. and Sion E. M., 1992, Astrophys. J., **542**

[43] Cook, M. C., 1985a, Mon. Not. R Astron. Soc., **215**, 81

[44] Cook, M. C., 1985b, Mon. Not. R Astron. Soc., **216**, 219

[45] Cook, M. C. and Warner, B., 1984, Mon. Not. R Astron. Soc., **207**, 705

[46] Crawford, S. M., 2008, *Southern African Large Telescope: SLOTMODE manual*

[47] Czezowski, Adam *et al.*, 2005, ASP Conf. Ser., Vol. 351, 208

[48] Dai, Z., Qian, S. and Lajús, E., F., 2009, Astrophys. J., **703**, 109

[49] Darling, D., 2007, The Internet Encyclopedia of Science, *Equipotential Surface*, www.daviddarling.info/encyclopedia/E/equipotenitial_surface.html

[50] The DDMA Team, 2007, *A Primer on TV Abel Regularization*, http://ddma.lanl.gov/science/data2knowledge/inverse-problems/radiography/

[51] Diffraction Limited, 2010, http://www.cyanogen.com/

[52] Dhillon 2010 in *High Time Resolution Astrophysics (HTRA) IV - The Era of Extremely Large Telescopes*, workshop presentation

[53] O'Donoghue D., 1986, Mon. Not. R Astron. Soc., **220**, 230

[54] O'Donoghue D., Charles P. and Homer L., 1999, *The UCT CCD Photometer, Version 2.0.*

[55] O'Donoghue D., Buckley D. A. H., Balona L. A., Bester D. *and co-authors*, 2006, Mon. Not. R. Astron. Soc. **372**, 151

[56] Duschl, W., J. and Tscharnuter, W., M., 1991, Astron. Astrophys. **241**, 153

[57] Eaton, J. A., Henry, G. W., Fekel, C., 2001 *Advantages of Automated Observing with Small Telescopes*

[58] Edoh, K. and Roop, J. P, 2009, International Journal of Signal Processing, Image Processing and Pattern Recognition, Vol 2., No. 3, 57

[59] Eggleton, P., 1983, Astrophys. J. **268**, 368

[60] Elo, C. A., 2009, MSc Thesis, *Image Denoising Algorithms Based on the Dual Formulation of Total Variation*, Dept. Math., University of Bergen

[61] Fairborn 1990a, Seeds, M. A. and Richard, J. L. (eds) *Advances in Robotic Telescopes*(mesa: Fairborn Press)

[62] Fairborn 1990b, Baliunas S. and Richard J. L. (eds) *Robotic Observatories: Present and Future* (mesa: Fairborn Press)

[63] Feline, W. J., Dhillon, V. S., Marsh, T. S., Stevenson, M. J., Watson, C. A and Brinkworth, C. S., 2004a, Mon. Not. R. Astron. Soc. **347**, 1173

[64] Feline, W. J., Dhillon, V. S., Marsh, T. S. and Brinkworth, C. S., 2004b, Mon. Not. R. Astron. Soc. **355**, 1

[65] Flannery, B. P., 1975, Mon. Not. R Astron. Soc., **170**, 325

[66] Frank, J., King, A. and Raine, D. J., *Accretion Power in Astrophysics* (CUP, 1992)

[67] Fuchs, C., 2001, *DOS Frequently Asked Questions* http://www.drdos.net/faq/#p2_9

[68] Gajadhar, S., Vermeulen, T. and Cruise, W., 2011, *Retrofitting the Canada-France-Hawaii Telescope for remote operations* (paper), Telescopes from Afar Conference: An international conference on remotely operated, automated, or robotic ground based telescopes

[69] Gamma-ray bursts Coordinates Network, 2011 http://gcn.gsfc.nasa.gov/

[70] Gans, P., *Data Fitting in the Chemical Sciences* (Wiley, 1992)

[71] Gänsicke, 2005, B. T., ASP Conf. Ser., Vol. 330, 3

[72] Gänsicke, B. T., Dillon, M., Southworth, J. *and co-authors*, 2009, Mon. Not. R Astron. Soc., **397**, 217

[73] Gelderman, R., Strolger, L., Carini, M., Marchenko, S., Reddy Yaramala, S., Rumph, M., van Fleet, R., Wood, J. D., 2007, A. Astron. Soc., **211**, 1131

[74] Gerhensfield, N., *The Nature of Mathematical Modelling* (CUP, 1999)

[75] Greenhill, J. G., Hill, K. M., Dieters, S. *and co-authors*, 2006, Mon. Not. R Astron. Soc., **372**, 1129

[76] Hachisu, I. and Kato, M., 2001, Astrophys. J. **558**, 323

[77] Hameury, J.-M., Lasota, J.-P. and Warner, B., 2000, Astron. Astrophys. **353**, 244

[78] Hameury, J.-M., 2002, ASP Conference Series, Vol. 261, 377

[79] Hameury, J.-M., and Lasota, J.-P., 2005, Astron. Astrophys. **443**, 283

[80] Hanisch, R. J., Farris, A., Greisen, W. D. *and co-authors*, 2001, Astron. Astrophys. **376**, 359

[81] Hellier, C., 2001, *Cataclysmic Variable Stars: How and why they vary* (Springer-Praxis, 2001)

[82] Henden, A. A., 1990 in Proceedings of the 1990 11th Annual Smithsonian/Fairborn/I.A.P.P.P Symposium of Automatic Photoelectric Telescopes *Remote Observing with Large Telescopes* (Fairborn Press, 1990), p. 133

[83] Hessman, F. V., Gänsicke, B. T. and Mattei, J. A., 2000, Astron. Astrophys. **361**, 952

[84] Hilditch, R. W., 2001, *An Introduction to Close Binary Stars* (CUP, 2001), p. 250

[85] Hill, G., Hutchings, J. B., 1970, Ap. J., **162**, 265

[86] Horne, K., 1985, Mon. Not. R Astron. Soc., **213**, 129

[87] Horne, K. and Steining, R. F., 1985, Mon. Not. R Astron. Soc., **216**, 933

[88] Horne, K., Wood, J. H. and Steining, R. F., 1991, Astrophys. J., **378**, 271

[89] Howell S. B., Nelson, L. A. and Rappaport S., 2001, Astrophys. J., **550**, 897

[90] Howell S. B., Szkody, P., Kreidl T. J. and Dobrzycka D., 1991 PASP, **103**, 300

[91] Ichikawa, S. and Osaki Y., 1994, Pub. Astr. Soc. Japan, **46**, 621

[92] Ivanov, V. D., Caceres, C., Mason, E., 2009, *and co-authors* in *Science with the VLT in the ELT era*, Moorwood, A. (ed), Springer pub

[93] Jones, D.H., Saunders, W., Colless, M., et al., 2004, Mon. Not. R Astron. Soc., **355**, 747

[94] Kafka, S., 2005, PhD Thesis, *Exploring Stellar Activity on the Secondary Star of Ctaclysmic Variables*, Dept. Ast., Indiana Universitys

[95] Kamen, E. W., 1999, *Industrial Controls and Manufacturing*, p. 142 (Academic Press)

[96] Kippenhahn, R. and Wiegert, A., 1991, *Stellar Structure and Evolution* (Springer-Verlag, Berlin)

[97] Kopal, Z., 1959, *Close Binary Stars* (Wiley, 1959)

[98] Korte, R., 1997, *The Basics of Encoders* http://mmsonline.com/articles/049703.html

[99] Kuphaldt, T. R., 2009, *Lessons In Electric Circuits Vol. IV*, Chap. 6, http://openbookproject.net//electricCircuits/Digital/DIGI_6.html

[100] Lanza, A., F., 2006, Mon. Not. R. Astron. Soc. **369**, 1773

[101] Li, Y. and Santosa, F., 1996, IEEE Transactions on Image Processing, Vol. 5, No. 6, 987

[102] Lipunova, G. V. and Shakura, N. I., 2000, Astron. Astrophys., **356**, 363

[103] Livio, M. and Verbunt, F., 1988, Mon. Not. R Astron. Soc., **232**, 1

[104] Littlefair, S. P., Dhillon, V. S., Marsh, T. R., *and 3 co-authors*, 2007, Mon. Not. R. Astron. Soc. **381**, 827

[105] Littlefair, S. P., Dhillon, V. S., Marsh, T. R., *and 5 co-authors*, 2008, Mon. Not. R. Astron. Soc. **388**, 1582

[106] Lohninger H., 1999, *Teach Me Data Analysis: Savitzky-Golay Filter Coefficients* http://www.vias.org/tmdatanaleng/cc_savgol_coeff.html

[107] Lohninger H., 2006, *Fundamentals of Statistics : Savitzky-Golay Filter Coefficients* http://www.statistics4u.info/fundstat_eng/cc_savgol_coeff.html

[108] Las Cumbres Observatory Global Science Telescope (LCOGT) Network, 2011, *Science* http://lcogt.net/en/science

[109] Lubow, S. H. and Shu, F.H., 1975, Astrophys. J. **198**, 61

[110] Lucy, L. B., 1968a, Astrophys. J., **151**, 1123

[111] Lucy, L. B., 1968b, Astrophys. J., **153**, 877

[112] Li, J., Wu, K. and Wickrmashinge, D. T., 1994, Mon. Not. R Astron. Soc., **268**, 61

[113] Lynden-Bell, D. and Pringle J. E., 1974, Mon. Not. R Astron. Soc., **168**, 603

[114] Manly, A. A., 1990 in Proceedings of the 1990 11th Annual Smithsonian/Fairborn/I.A.P.P.P Symposium of Automatic Photoelectric Telescopes *The Observatory Controller* (Fairborn Press, 1990), p. 139

[115] Maran, S. P., 1967, Science, **158**, 867

[116] Marsh, T. R. and Pringle, J. E., 1990, Astrophys. J., **365**, 677

[117] Marquina, A. and Osher, S., 2000, *Explicit algorithms for a new time dependant model based on level set motion for nonlinear deblurring and noise removal*, SIAM J. Sci. Comput., **22**, No. 2, 387-405

[118] Melsheimer, F. M., 2005, *"Internet Telescope" Performance Requirements* www.dfmengineering.com/news/InternetTelescope.pdf

[119] Meyer, F. and Meyer-Hofmeister, E., 1979, Acta. Astr., **78**, 167

[120] Mineshige, S. and Wood, J., 1989, Mon. Not. R Astron. Soc., **241**, 259

[121] Mireles James, J.D., 2006, *Celestial Mechanics Notes Set 4: The Circular Restricted Three Body Problem* http://www.math.utexas.edu/users/jjames/hw4Notes.pdf

[122] Mochnacki, S W. and Doughty, N. A., 1972a, Mon. Not. R Astron. Soc., **156**, 51

[123] Mochnacki, S W. and Doughty, N. A., 1972b, Mon. Not. R Astron. Soc., **156**, 243

[124] Mountain, M. , 1996, *What is beyond the current generation of ground-based 8-m to 10-m class telescopes and the VLT-I ?*, SPIE Vol. 2871, p. 597

[125] NetworkCameraReviews.com, 2007, What is an IP network camera? http://www.networkcamerareviews.com

[126] Niemeyer, P. and Knudsen, J, 2005, *Learning Java* (O' Reilly Media, Inc, 2005)

[127] Nikunen, P., 2001, *Function Fitting* http://citeseer.ist.psu.edu/nikuneno/function.html

[128] Nguyen, N. C., 2006, *A Note on Tikhonov Regularization of Linear Ill-Posed Problems* http://www.mit.edu/ cuongng/Site/Publication_files/Tikhonov06.pdf

[129] Omega Lab, 2010, *Advanced Telescope Control and Auto Centre*, http://atcr.altervista.org/eng/atc.html

[130] OMRON, 2003, Cat. No. W353-E1-04, *Programmable Controllers, Programming Manual*

[131] Osaki, Y., 1974, Pub. Astron. Soc. Japan, **26**, 429

[132] Osaki, Y., 1989, Pub. Astron. Soc. Japan, **41**, 1005

[133] Osaki, Y. and Meyer, F., 2003, Astron. Astrophys., **401**, 325

[134] Osaki, Y. and Meyer, F., 2004, Astron. Astrophys., **428**, 170

[135] Osher, S., Solé, A. and Vese, L., 2003, Soc. Ind. App. Math, Vol. 1, No.3, 349

[136] Osher, S., Burger, M., Goldfarb, D., Xu, J. and Yin, W., 2005, *An iterative regularization method for total variation based image restoration*, Multiscale Model. and Simul., Vol 4., No. 2, 460

[137] Paczyński, B. and Sienkiewicz, R., 1972, Acta. Astr., **22**, 73

[138] Paczyński, 1977, B. Astrophys. J., **216**, 822

[139] Papaloizou, J. and Pringle, J.E., 1977, Mon. Not. R Astron. Soc., **181**, 441

[140] Patterson, J., Masi, G., Richmond, M. W. *and co-authors*, 2002, PASP, Vol. 114 **797**, 721

[141] Pearson, K. J., 2006, Mon. Not. R Astron. Soc., **371**, 235

[142] Peterson, C., 2001, Journal of Young Investigators, *How It Works: The Charged-Coupled Device, or CCD* http://www.jyi.org/volumes/volume3/issue1/features/peterson.html

[143] Pigulski, A. and Mischalska, G., 2002, IBVS, 5218

[144] Pollock, D. S. G., *Smoothing with Cubic Splines* (Queen Mary and Westfield College, Department of Economics, 1993), No. 291

[145] Pringle, J. E., 1977, Mon. Not. R Astron. Soc., **178**, 195

[146] Raffi, G. and Zeibell, M., 1986, Messenger No 44., p. 26

[147] RASNZ (VSS), 2011, http://www.variablestarssouth.org/index.php/information-and-resources/observing-a-reporting

[148] Rauscher, E., Menou, K., Seager, S. *and co-authors*, 2007, Astrophys. J., **664**, 1199

[149] Ritter, H., 1980, Astron. Astrophys., **91**, 161

[150] Ritter, H., 2008, Astrophys. J., Mem. S. A. It. Vol. 1, 1

[151] Ritter, H. and Kolb, U., 2005, *Catalogue of cataclysmic binaries, low mass X-ray binaries and related objects (Seventh edition)* http://physics.open.ac.uk/RKcat/.

[152] Ritter, H. and Schröder, 1979, Astron. Astrophys., **76**, 168

[153] Robinson, E. L., 1976, Ann. Rev. Astron. Astrophys.,**14**, 119

[154] Robinson, E. L., Wood, J. H., Bless, J. C. *and 8 co-authors*, 1995, Astroph. J., **443**, 295

[155] Rubenstein, E. L., Patterson, J. and Africano J. L., 1991, PASP **103**, 1258

[156] Rudin, L. I., Osher, S. and Fatemi, E., 1992, *Nonlinear total variation based noise removal algorithms*, Physica D, **60(1-4)**

[157] Ryan, O., 2006, *European Extremely Large Telescope Design Study*, HiTRI Study Report, European Community's Framework Programme 6

[158] Savitzky, A. and Golay, M., J., E., 1964, Anal. Chem., **36** (8): 1627

[159] Schechter, P. L., Mateo, M. and Saha, A., 1993, ASP Conference Series, Vol. 105, 1342

[160] Schreiber, M. R., Hameury, J.-M. and Lasota, J.-P., 2004, Astron. Astrophys., **427**, 621

[161] Schreiber, M. R., Hameury, J.-M. and Lasota, J.-P., 2005, ASP Conference Series, Vol. 330, 207

[162] Schreiber, M. R. and Lasota, J.-P., 2007, Astron. Astrophys., **473**, 897

[163] Shakura N.I. and Sunyaev R.A., 1973, Astron. Astrophys., **24**, 337

[164] Soloman, S., 2009 *Sensors Handbook*, 2nd Ed., p., 199 (McGraw-Hill Companies)

[165] Shporer, A., Brown, T., Lister, T. *and co-authors*, 2011, The Astrophysics of Planetary Systems Proceedings, IAU Symp. 276, A. Sozzetti, M. G. Lattanzi and A. P. Boss, eds.

[166] Silanten, S., 2009, *Inverse Problems*, University of Helsinki Lecture Notes

[167] Silber, A. D., Remillard, R. A., Horne, K. and Bradt., H. V., 1994, Astroph. J., **424**, 955

[168] Silva, D. *et al.* (eds), 2007, *Thirty Meter Telescope Detailed Science Case: 2007*, TMT Science Advisory Committee

[169] Sion, E. M., 2006, JAAVSO Vol. 35, Pt. 2B

[170] Skrutskie, M. F., Cutri, R. M., Stiening, R., Weinberg, M. D. *and co-authors*, 2006, Astron. J., **131**, 1163

[171] Smak, J., 1971. Acta. Astr. **21**, 15

[172] Smak, J., 1984. Acta. Astr. **34**, 93

[173] Smak J., 1986, Acta Astr., **36**, 211

[174] Smak, J., 1989. Acta. Astr. **39**, 41

[175] Smak, J., 1991. Acta. Astr. **41**, 269

[176] Smak, J., 2000., New Astronomy Review **44**, 171

[177] Smak, J., 2004a. Acta. Astr. **54**, 181

[178] Smak, J., 2004b. Acta. Astr. **54**, 429

[179] Smak, J., 2008. Acta. Astr. **58**, 55

[180] Smak, J., 2009. Acta. Astr. **59**, 103

[181] Smak, J., 2010. Acta. Astr. **60**, 1

[182] Software Bisque, 2010, http://www.bisque.com.

[183] Spruit, H. C. and Ritter, H., 1983, Acta. Astr., **124**, 267

[184] Steeghs, D., Perryman M. A. C., Reynolds, A., de Bruijne, J. H. J. *and co-authors*, 2003, Mon. Not. R Astron. Soc., **339**, 810

[185] Steele, I.A., Naylor, T., Allan, A. *and co-authors*, 2002, *A distributed telescope network*, SPIE, Vol. 4845, p. 13

[186] Szkody, P. and Howell S. B., 1992 Astroph. J., **78**, 537

[187] Szkody, P., Anderson, S. F., Hayden, M., *et al.*, 2009, Astrophys. J., **137**, 4011

[188] Taam, R. E. and Sandquist, E. L., 2000, Annu. Rev. Astron. Astrophys., **38**, 113

[189] Tikhonov, A. N., 1963, *Regularization of incorrectly posed problems*, Sov. Math. Dokl., **4**, 1035

[190] Tovmassian, G., Zharikov, S., Mennickent, R. and Greiner, J., 2004, ASP Conference Proceedings, Vol. 315, 15

[191] Truss, M. R., 2007, Mon. Not. R. Astron. Soc., **376**, 89

[192] Tsapras, Y., 2008, *The RoboNet-II project: Microlensing Anomaly Follow-up with the Las Cumbres Observatory Global Telescope Network* (poster), The Manchester Microlensing Conference: The 12th International Conference and ANGLES Microlensing Workshop

[193] Tsapras, Y., Street, R., Horne, K. *and co-authors*, 2009, *RoboNetII: Follow-up observations of microlensing events with a robotic network of telescopes*, Astronomische Nachrichte,n Vol. 330, p. 4

[194] Springer, W., Dawson, K., Gondolo, P. *and co-authors*, 2011, *Commissioning and development of remote operation capabilities of the Willard L. Eccles Telescope at the Frisco Peak Observatory* (paper), Telescopes from Afar Conference: An international conference on remotely operated, automated, or robotic ground based telescopes

[195] Tzen, S., 1998, *Optimizing DOS Memory*, http://www.knowplace.org/pages/morgue/optimizing_dos_memory.php

[196] Uemura, M., Kato, T., Matsumoto, K., *and co-authors*, 2000, PASJ, Vol. 52, L15

[197] Uemura, M., Kato, T., Ishioka, R. *and co-authors*, 2004, PASJ, **56**, S141

[198] VSNet, 2011, *VSNet: An International Mailing List on Variable Stars* http://www.kusastro.kyoto-u.ac.jp/vsnet/

[199] Vogt, N., 1982, Astrophys. J., **252**, 239

[200] Vogel and Oman M. E, 1996, *Iterative methods for total variation denoising*, SIAM J. Sci. Comput., Vol. 17, 1

[201] Vogel C. R., *Computational Methods for Inverse Problems*, Vol. 10, Society for Industrial and Applied Mathematics, Philadelphia (SIAM 2002)

[202] Waelkens, C., 1988, Messenger No 51., p. 18

[203] Wallace, P., 2005, *Telescope Pointing* www.tpsoft.demon.co.uk/pointing.htm

[204] Warner, B., *Cataclysmic Variable Stars* (CUP, 1995)

[205] Warner, B. and Peters, W. L., 1972, Mon. Not. R. Astron. Soc., **160**, 15

[206] Wheatley, P. J. and West, R. G., 2002, ASP Conference Series, Vol. 261, 433

[207] Wheatley, P. J. and West, R. G., 2003, Mon. Not. R. Astron. Soc., **345**, 1009

[208] White, R. R., Allan, A., Evans, S. *and co-authors*, 2006, *Interconnecting astronomical networks: evolving from single networks to meta-networks*, SPIE, Vol. 6274, p. 9

[209] White, R.R., Wren, J., Davis, H. *and co-authors*, 2004, *TALON - The Telescope Alert Operation Network System: Intelligent Linking of Distributed Autonomous Robotic Telescopes*, SPIE, Vol. 5496, p. 302

[210] Whitehurst, R., 1988, Mon. Not. R. Astron. Soc., **232**, 35

[211] Whitehurst, R. and King, A., 1991, Mon. Not. R Astron. Soc., **249**, 25

[212] Whitelock, P. A., 2004, *Optical Astronomy in Post-Apartheid South Africa: 1994 to 2004* Organizations and Strategies in Astronomy Vol. 5, p. 30

[213] Wikipedia contributors, 2009, Wikipedia, The Free Encyclopedia,*SavitzkyGolay smoothing filter* http://en.wikipedia.org/wiki/Savitzky_Golay_smoothing_filter

[214] Wilson, G., Czezowski, A., Hovey, G. R., *and co-authors*, 2005, ASP Conference Series, Vol. 347, 563

[215] Wilson, R. E. and Devinney, E. J., 1971, Ap. J. **166**, 605

[216] Wlodarczyk, K., 1986, Acta Astr., **36**, 395

[217] Wolf, S., Mantel, K. H., Horne K. *and co-authors*, 1993, Astron. Astrophys. **273**, 160

[218] Wood, J. H., 1986, Mon. Not. R. Astron. Soc. *PhD thesis*, University of Cambridge.

[219] Wood, J. H., 1987, Mon. Not. R. Astron. Soc. **228**, 797

[220] Wood, J., Horne, K., Berriman, G. and Wade, R. A. 1989a, Astrophys. J., **341**, 974

[221] Wood, J., Irwin, M. J. and Pringle, J. E., 1985, Mon. Not. R Astron. Soc., **214**, 475

[222] Wood, J. H., Horne K., Berriman, G. *and co-authors*, 1986, Mon. Not. R. Astron. Soc. **219**, 629

[223] Wood, J., Marsh, T. R., Robinson, E. L. *and co-authors*, 1989b, Mon. Not. R Astron. Soc., **239**, 809

[224] Wood, J. H. and Horne K., 1990, Mon. Not. R. Astron. Soc. **242**, 606

[225] Woudt P. A. and Warner B., 2001, Mon. Not. R. Astron. Soc. **328**, 159

[226] Yuan, J. and Qian, S., 2007, Astrophys. J., **669**, 93

[227] York, D.G., Adelman, J., Anderson, J.E. *and co-authors*, 2000, Astron. J., **120**, 1579

[228] Zach, C., Pock, T. and Bischof H., Proceedings of the 29th DAGM conference on Pattern recognition **p.214** *A duality based approach for realtime* $TV - L^1$ *optical flow* (Springer-Verlag Berlin, Heidelberg, 2007)

[229] Zhang, C. M., Wickramasinghe, D. T. and Ferrario, L., 2009, Mon. Not. R. Astron. Soc. **397**, 2208

[230] Zijlstra, A. A., Rodriguez, J. and Wallander, A., 1998, Messenger No 81., p 23

[231] Zola, S., 1989, Acta. Astr. **39**, 45